QUANTUM LIQUIDS AND QUANTUM CRYSTALS

Possible experimental test to determine the role of microscopic vortex rings in the λ transition in helium II

M. D. Tomchenko*

Institute of Theoretical Physics of the National Academy of Sciences of Ukraine, ul. Metrologicheskaya 14-b, Kiev 03143, Ukraine

(Submitted June 4, 2004; revised August 10, 2004)
Fiz. Nizk. Temp. **31**, 483–489 (May 2005)

An experimental test is proposed for determining the role of microscopic vortex rings (MVRs) in the λ transition in helium II. It is assumed that bulk He II contains an ensemble of vortex rings which initiate the λ transition and to a significant degree determine the value of T_λ. However, in very thin films of He II, such that the thickness d of the superfluid layer is less than the size d_0 of the smallest MVRs, the rings will not fit, and no MVR ensemble exists in them. Because of this, $T_\lambda(d)$ curve of helium II films on disordered substrates should have a feature in the form a jump at $d \approx d_0 \approx 6 \pm 4$ Å. The available experimental data on the heat capacity of thin films of He II are insufficiently complete and precise for drawing conclusions as to the presence of the proposed feature. © *2005 American Institute of Physics.*
[DOI: 10.1063/1.1924907]

1. INTRODUCTION

The microstructure of weakly excited states of helium II is mainly known,[1–5] but the important question of the microscopic nature of the λ transition in He II has still not been completely answered. The majority of authors consider that the λ transition in He II is accompanied (or caused) by destruction of the condensate, which is probably a composite containing not only the single-particle condensate but also two-particle and higher contributions.[3,6–9] In the Feynman approach[10] the λ transition is qualitatively similar to a phase transition in an ideal gas, although the condensate is not explicitly used in the model. Two-dimensional superfluid films of He II, in which the condensate is either absent entirely or is very small, are difficult to describe in the condensate approach. It is therefore possible that the superfluidity of He II is not due to the appearance of a condensate and that the λ transition in it is not equivalent to destruction of a condensate. According to a rather popular point of view an important role in the λ transition is played by an ensemble of microscopic vortex rings (MVRs),[3,11–15] the role of which is understood differently by different authors. It is possible that the rings contribute to depletion of the condensate. Both the condensate and vortex approaches can give a λ curve for the heat capacity.

In this paper an experiment is proposed that can determine whether or not the MVRs play an important role in the λ transition.

2. SOME PROPERTIES OF VORTEX RINGS IN He II

It is known from experiment[16,17] that vortex rings can indeed exist in He II and ''live'' for a long time without decaying. The stability of MVRs is due to the absence of viscosity in the medium and to their topological properties. Closed vortices have a core of radius $a \approx 0.8-1.5$ Å.[16,17] An exact microscopic description of the MVRs has not yet been constructed. Approximate models have been proposed[18,19] in which the MVRs are obtained as a solution of the Gross-Pitaevskii (GP) equation. However, for He II the GP equation has been obtained only in the mean field approximation,[20] and so the degree of accuracy and physical meaning of this equation for He II is not completely clear. According to the model proposed in Ref. 19 and also the experiments of Refs. 16, 17, first, the properties of the MVRs are qualitatively, and approximately quantitatively, similar to those of classical rings, and, second, the radius of the MVRs cannot be less than a certain smallest value R_0, where $R_0 \sim a \sim 1$ Å.

Let us make some estimates. Classical vortex rings with quantized circulation $\kappa = \hbar/m$ are described by the following formulas:[21]

$$v = \frac{\kappa}{2R}\left[\ln\frac{8R}{a} - \frac{1}{2} - f_1\left(\frac{a}{R}\right)\right], \tag{1}$$

$$E = 2\pi^2\rho^* R\kappa^2\left[\ln\frac{8R}{a} - 2 - f_2\left(\frac{a}{R}\right)\right], \tag{2}$$

$$P = 2\pi^2\rho^* R^2\kappa\left[1 - f_3\left(\frac{a}{R}\right)\right]. \tag{3}$$

Here v is the velocity, E the energy, P the momentum, and R the radius of the ring, m is the mass of an ^{4}He atom, and ρ^* is an effective density (see below). The corrections f_i describe the vortex core and are small for $R \gg a$. According to Eqs. (1)–(3), a ring of radius $R = 2.2$ Å has an energy of 9.83 K and a momentum of 2.07 Å^{-1}, while for $R = 3$ Å we get $E = 18.2$ K and $P = 3.85$ Å^{-1}. The MVR spectrum is shown

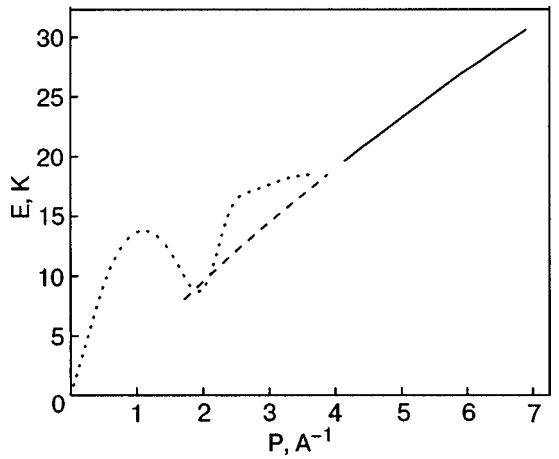

FIG. 1. Spectrum $E(P)$ of vortex rings according to Eqs. (2) and (3) for $f_2=f_3=0$, $\rho^*=\rho$. The dashed line is the spectrum of rings of radius $R=2-3$ Å; the solid line is the spectrum of rings of radius $R>3$ Å; rings with a similar spectrum probably exist in He II; the dotted curve shows the experimental spectrum of He II quasiparticles.

in Fig. 1 (for $\rho^*=\rho$, where ρ is the total density of He II); the solid curve shows the spectrum $E(P)$ of rings with $R>3$ Å, which may actually exist in He II.

The exact quantum formulas for the description of MVRs can also be written in the form (1)–(3), but the corrections f_i in this case are unknown. For small MVRs ($R\leqslant 5$ Å) these corrections can turn out not to be small. Several approximate models have been proposed for the description of MVRs,[14,18,19] but the smallest MVRs in them are described by different formulas. We therefore wondered what corrections f_i to use in Eqs. (1)–(3). This was decided by appeal to experiment. It has been found[17] that for vortex rings up to 5 Å in radius the classical formulas (1)–(3) with $f_i=0$ work in an approximate way. We therefore thought it most reasonable to use these simple classical formulas with $f_i=0$. We also made estimates assuming appreciably nonzero values of $f_i(a/R_0)$, of the order of 1, but this changed the estimate of R_0 by only 1 Å (see below).

Strictly speaking, for correct description of MVRs it is necessary to solve an N-particle Schrödinger equation taking into account the presence of phonons, rotons, the MVRs, and (for films) Berezinskii-Kosterlitz-Thouless (BKT) vortices in the system. This problem has not yet been solved. The MVRs can be described approximately by formulas (1)–(3), where ρ^* is an effective density that must be found from the exact microscopic equations. For description of macroscopic vortices (large rings of radius $R>100$ Å, BKT vortices) the relation $\rho^*=\rho_s$ is valid, but that relation does not hold for rings of radius $\sim 2-3$ Å; for them $\rho^*\neq\rho_s$, since the main contribution to the energy and momentum of such rings comes from the motion of helium atoms near the core of a given ring (far from a ring the fluid velocity induced by that ring decays rapidly with distance). That is, the other quasiparticles have little influence on the values of E, P, and v for the smallest MVRs, and therefore for the smallest rings ρ^* must not be replaced by ρ_s, but rather, ρ^* should be close to the total density ρ, even near T_λ.

As we shall see, if MVRs are described by formulas (1)–(3), then the smallest MVRs in He II should have a radius $R_0\geqslant 2.5$ Å, and in that case the energy of the rings will be few times greater than kT_λ. In the quantum model proposed in Ref. 19, the energy of the rings is also several times greater than kT_λ. Therefore, for an ensemble of noninteracting MVRs at $T<T_\lambda$ the equilibrium distribution is Boltzmann:[22]

$$dN_{vr}=\exp(-E(R)/kT)\,\frac{dVd\mathbf{P}(R)}{(2\pi\hbar)^3}. \tag{4}$$

Since the vortex rings can be created and annihilated (e.g., at the walls of the vessel), the chemical potential is assumed equal to zero. Taking Eqs. (1)–(3) into account, we obtain from (4) the number of MVRs per unit volume:

$$n_{vr}=8\pi\left(\frac{P_0}{2\pi\hbar}\right)^3\frac{kT}{E_0}\exp\left(-\frac{E_0}{kT}\right)g(T), \tag{5}$$

where

$$g(T)=e_0\int_1^\infty\left[\frac{\rho^*(x)}{\rho}\right]^3 x^5 \times\exp\left[e_0-e_0\frac{\rho^*(x)}{\rho}\left(x+\frac{x\ln x}{b}\right)\right]dx, \tag{6}$$

$$e_0=\frac{E(R_0)}{k_bT},\quad b=\ln\frac{8R_0}{a}-2,$$

P_0 and $E_0=E(R_0)$ are the momentum and energy of the smallest ring. For $R_0=2-3$ Å the value of g depends weakly on T, increasing from 0.5 to 0.7 as the temperature increases from 0 K to 2 K (see also Table I), but as $T\to T_\lambda$ the value of g increases without bound.

For the heat capacity and density of the normal component of an ensemble of rings we obtain

$$C=kn_{vr}\left(\frac{E_0^2}{(kT)^2}+2\frac{E_0}{kT}\left(1+g'\frac{T}{g}\right)+2+4g'\frac{T}{g}+g''\frac{T^2}{g}\right), \tag{7}$$

TABLE I. Parameters of vortex rings for different R_0.

R_0, Å	$n_{vr}^{-1/3}$, Å	d_{vr}, Å	$\overline{R}/R_0$	g
1	4.7	4	1.61	0.3
2	8.5	6	1.154	0.72
2.5	14.5	7	1.1	0.72
3	28.1	8	1.073	0.71
4	142	10	1.045	0.71
5	974	12	1.032	0.72
10	$2\cdot10^8$	22	1.012	0.74
20	10^{22}	42	1.005	0.76

Note: R_0 is the radius of the smallest vortex ring; $n_{vr}^{-1/3}$ is the mean distance between rings in the ensemble, according to Eq. (5); $d_{vr}=2R_0+2a$ is the "size" of the smallest ring; $\overline{R}$ is the mean radius of the rings in the ensemble; all for $T=2$ K, $a=1$ Å; $\rho*=\rho$ in Eqs. (2), (3).

$$\rho_n^{vr}=\frac{\langle P^2\rangle}{3kT}n_{vr}, \tag{8}$$

where $\langle\,\rangle$ is the average over the ensemble of rings. We note that the formulas for n_{vr}, $C(T)$, and ρ_n of a MVR ensemble are similar to those for a gas of rotons[23] as a result of the presence of a ''gap'' in both the MVR and roton spectra.

The behavior of the MVR ensemble near T_λ is interesting. For $T\to T_\lambda$ one has $\rho_s\sim[(T_\lambda-T)/T_\lambda]^{0.67}$. We set $\rho^*=\rho_s$ in (1)–(7). Then the integrand in (6) has a maximum at

$$x_m=\frac{5\rho}{\rho_s e_0\left(1+\dfrac{1}{b}+\dfrac{\ln x_m}{b}\right)}. \tag{9}$$

For temperatures very close to T_λ one has $x_m\gg 1$, and in that case the main contribution to the integral (6) is from rings of radius $R\gg R_0$, for which one must set $\rho^*=\rho_s$ in (1)–(7). For $T\to T_\lambda$ we obtain

$$g(T)\approx e_0(\rho_s/\rho)^3 x_m^6\exp(e_0-5)\sim(\rho_s/\rho)^{-3}\sim t^{-3\nu}\to\infty,$$

where $t\equiv(T_\lambda-T)/T_\lambda$, $\nu=0.67$. Because of the unbounded growth of g near T_λ the density of rings, the ensemble average radius of the rings $\overline{R}$, and the heat capacity of the MVR ensemble also increase without bound:

$$\frac{\overline{R}}{R_0}\simeq\frac{5\rho}{\varepsilon_0\rho_s},\quad n_{vr}\sim\rho_s^{-3},\quad C(T)\sim\frac{n_{vr}}{t^2}\sim t^{-3\nu-2}.$$

We neglect the quantity $\ln(\rho/\rho_s)\ll\rho/\rho_s$. Finally, infinite growth of the rings does not really occur: when the average distance between rings becomes smaller than the average size of the rings the formation of a vortex tangle occurs in He II. These estimates show that the MVR ensemble can cause a λ transition in He II. However, the phase transition is already partially built into the model, since we assume rather than deduce that $\rho_s\to 0$ at $T\to T_\lambda$.

It is seen from Table I that if the radius of the smallest vortices is small enough ($R_0\leqslant 2.5$ Å), then even far from T_λ, at $T=2$ K, the density of rings becomes high, and the rings almost touch. In this case it can be expected that for $T=T_\lambda$ the rings ''turbulize'' the medium,[11] and it is no longer necessary for $\rho_s(T_\lambda)=0$ to be built into the model. Thus it is seen that the λ transition in He II should be accompanied by the formation of a vortex tangle and, possibly, that it is the vortex rings that initiate the λ transition.

Let us estimate the value of the smallest vortex radius R_0. The radius of a vortex ring is defined as the distance from the center of the ring to the ''center'' of the cross section of the core.[24] Since the smallest ring looks like a torus with a very small hole, it is clear that R_0 should be around one to two core radii: $R_0\approx a-2a\approx 0.8-3$ Å. Such very small values of a and R_0 are physically reasonable, since a MVR is a vortex in a probability field and not in an ordinary classical medium, since the vortex core is the locus of points at which the probability of finding helium atoms is much less than outside the core (one can speak of the probability for an atom, since the size of the helium atom is much less than the diameter of the core). The smallest possible radius of a MVR is close to the radius of the core—such a solution is obtained for classical[24] and quantum[19] rings.

It is known that the temperature dependence of the heat capacity C of He II for $T<1.5$ K is determined mainly by the heat capacity of a gas of rotons and phonons,[25] and therefore at such temperatures an ensemble of MVRs should not contribute much to the heat capacity. According to Eqs. (1)–(7), for this it is necessary that $R_0\geqslant 2.5$ Å; then the MVR contribution to $C(T)$ will be less than the roton contribution by a factor of 10 or more.

According to the microscopic theory,[1–6] the observed spectrum of He II quasiparticles, including the roton minimum, is explained as a phonon spectrum. The observed spectrum has no branch corresponding to the spectrum of vortex rings (Fig. 1). With Eqs. (1)–(3) taken into account, this means that $R_0\geqslant 3$ Å.

Thus it follows from MVR theory[19,24] and the experimentally determined value $a\approx 0.8-1.5$ Å that $R_0\leqslant 3$ Å, and furthermore at such a value of R_0 there are sufficiently many vortex rings that they can influence the λ transition; on the other hand, it must be the case that $R_0\geqslant 2.5-3$ Å, since at such values of R_0 the contribution of the rings to the heat capacity of He II at $T<2$ K is small, in accordance with (1)–(7), and the spectrum of the rings lies outside the limits of the experimental spectrum of He II quasiparticles. Hence we obtain an estimate for the radius of the smallest MVRs: $R_0\approx 2.5-3$ Å. The smallest rings observed experimentally have a radius of the order of 5 Å or less.[17]

The use of the exact microscopic formulas for describing MVRs will, of course, correct our estimate of R_0 by 1–2 Å. For example, in the quantum model[19] a solution is obtained for vortex rings with normalization versions A and B. According to version A, $R_0\approx a\approx 1.1$ Å, the energy of the smallest ring $E_0\approx 15$ K; according to version B, $R_0\approx a\approx 0.5$ Å, one has $E_0\approx 7$ K. It is seen that the rings in this model are very small ($R_0\leqslant 1.5$ Å), but in this case the density and heat capacity of the MVR ensemble are an order of magnitude smaller than for the roton ensemble.

From the estimates presented we obtain an approximate value of the radius of the smallest vortex ring in He II:

$$R_0\simeq(2.5\pm 1.5)\text{Å}. \tag{10}$$

The error in (10) takes into account the fact that the f_i in (1)–(3) are unknown, as well as the inaccuracy in the determination of a.

Interestingly, the study of vortex formation at the λ transition in He II can give one a better understanding of the processes of formation of cosmic strings in the early universe.[26] The study of the attenuation of second sound in liquid ^{4}He at the transition through the λ point attests to the formation near T_λ of a dense vortex tangle with a cell size not greater than 10^3 Å (Ref. 26); however, those results were not confirmed in Ref. 27. We assume that microscopic vortex rings, i.e., rings of radius $R\leqslant 20$ Å, cannot be detected in such experiments, since second sound is sound in a gas of quasiparticles, while the MVRs themselves are quasiparticles and therefore cannot attenuate second sound.

We stress that there is no doubt as to the existence of an ensemble of MVRs in helium II; the only question is whether the smallest rings are small enough (or, equivalently, whether there are enough of them) that the MVR ensemble has an influence on the properties of He II and especially on the λ

transition. The above theoretical estimates and the experimental data indicate that such a possibility is quite probable.

3. EXPERIMENTAL TEST FOR THE λ TRANSITION: THE POSSIBILITY OF THE PRESENCE OF AN ANOMALY ON THE DEPENDENCE OF T_λ ON THE THICKNESS OF THE He II FILM

Let us consider the temperature dependence of the heat capacity $C(T)$ for He II films of different thickness. According to the experimental data,[28] there are two maxima on the $C(T)$ curve—a sharp one at $T=T_{KT}$, corresponding to the BKT transition, and a broad one at $T=T_c$. The relation $T_{KT}<T_c<T_\lambda^{3D}$ always holds. With increasing film thickness the values of T_c and T_{KT} approach $T_\lambda^{3D}=2.17$ K. We note that the sharp BKT peak on the $C(T)$ curve looks like a small hillock in comparison with the broader peak at $T=T_c$ (Refs. 30–33). This, in our opinion, means that a fundamental rearrangement of the medium on the micro level occurs at T_c. The dependence of the broad peak on the film thickness d (Refs. 30, 31, and 34) obviously indicates that this peak is inherited from the bulk λ transition. Therefore, although the helium film loses superfluidity at T_{KT} (because of the breaking of BKT vortex pairs),[35] the microstructure of the medium which is responsible for the superfluidity in the bulk is not destroyed at that temperature. This microstructure is destroyed only at $T=T_c$, and the λ transition occurs. Under this assumption the experimental dependence of $T_c(d)$ is explained well by finite-size scaling.[34]

We shall assume that the vortex rings cause the λ transition in bulk He II and therefore determine the value of T_λ (the mechanism is not important). We consider a He II film as the thickness d of the superfluid layer in it is decreased. When d becomes smaller than the size of the smallest ring, $d_0\approx 2R_0+2a\simeq 6\pm 4$ Å, the vortex rings clearly no longer fit in the film, and therefore the MVR ensemble ceases to exist in the system. For the system to undergo a λ transition for $d<d_0$ it is necessary that the number of remaining quasiparticles be larger than the number that would be required if MVRs existed in the system. This means that for $d\approx d_0$ the temperature of the λ transition should increase in a jump (see Fig. 2). The jump is somewhat ''smeared out'' on the large d side, since, according to Eqs. (3) and (4) and Table I, some of the rings have a radius $R>R_0$. The jump is also smoothed out because the finite-size scaling leads to a rather rapid decrease of T_c with decreasing d. Therefore, instead of the expected jump of T_c at $d\approx d_0$ there can be a ''step,'' $T(d)\approx$const, for a certain interval of d near d_0.

Let us estimate the value of the possible jump of T_c. We assume that the λ transition in He II is accompanied by complete depletion of the condensate. According to the calculation of Ref. 3, for $T=0$ the fraction of single-particle condensate $n_0=0.078$, and at $T=T_\lambda=2.17$ K one has $n_0=0.058$, i.e., the condensate is not completely depleted at $T=T_\lambda$, even though experimentally $n_0(T_\lambda)\approx 0$. In Ref. 3 it was assumed that the condensate is depleted of rotons—the number of atoms ''torn'' out of the condensate is proportional to the number of rotons. The authors of Ref. 3 assume that additional destruction of the condensate to a value $n_0(T_\lambda)=0$ occurs on account of vortex rings. Consequently, in the absence of vortex rings in helium II the rotons alone would be capable of completely destroying the condensate at a temperature for which the roton density is four times higher than at $T=2.17$ Å (then instead of $n_0=0.058$ we would have $n_0=0$). From the known formula for the free rotation density[23]

$$n_r=0.051\exp(-\Delta/T)\left(\frac{q_r}{1.925\ \text{Å}^{-1}}\right)^2\sqrt{\frac{\mu T}{0.14m_4K}}\ \text{Å}^{-3}$$

we find that this temperature is ≈3.12 K. It is seen that if the calculation of n_0 in Ref. 3 is correct, then the value of T_λ for He II in the absence of MVRs would be 0.95 K larger than the observed value 2.17 K. This is an estimated upper bound on the possible value of the jump of T_λ in the films.

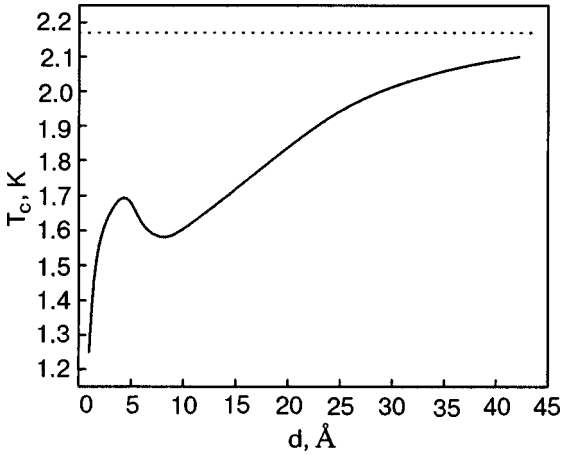

FIG. 2. Proposed $T_c(d)$ curve for He II films, with an anomaly at $d\simeq 6$ Å; T_c is the temperature of the broad peak on the curve of the heat capacity $C(T)$, and d is the thickness of the superfluid layer of the film. The values of T_c for $d<2.5$ Å and $d>10$ Å correspond to the crosses and squares in Fig. 3; the dotted line is T_λ for bulk He II.

Having estimates for d_0 and the value of the jump of T_c and also taking into consideration the smoothing of the jump, in Fig. 2 we show in an approximate way the proposed anomaly on the $T_c(d)$ curve. It is not yet possible to do a sufficiently exact calculation of the λ transition in He II films with all possible quasiparticles taken into account. However, our simple estimates are sufficient to predict the jump of T_λ and to indicate approximately the position and shape of the anomaly.

In Refs. 36 and 37 an estimate was observed for the core radius of BKT vortices: $a=12\pm 6$ Å for films of thickness $d\approx 10$–10^3 Å. For closed vortices in three dimensions $a\approx 1$ Å. The large value of the core radius of BKT vortices is apparently due to the fact that the BKT vortices are anchored to the substrate. In very thin films the MVRs are found close to the substrate, and the core radius of the MVRs can also grow. However, in films with thickness greater than twice the size of the smallest ring, i.e., $d\geqslant 12$ Å, the rings will no longer touch the substrate, and for such rings $a\approx 1$ Å. Therefore the possible growth of a for a MVR in very thin films increases the value of d_0 only to several angstroms: $d_0\approx 8\pm 4$ Å.

Since the core diameter of the BKT vortices is an order of magnitude greater than that of the rings, the energy of the BKT vortices is also an order of magnitude greater, and therefore BKT vortices and MVRs are excitations of differ-

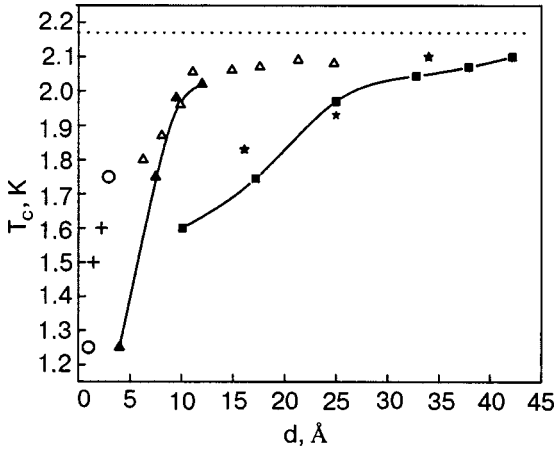

FIG. 3. Experimental $T_c(d)$ curve for He II films on substrates of jeweller's rouge[30] (*), Vycor[28,29] (▲), Vycor coated with an N_2 layer[29] (△), 2000 Å Nuclepore[31] (■), and Vycor[32] (+); the points with $T=1.25$ K and $T=1.75$ K from Refs. 28 and 29 against values of d renormalized according to Ref. 32; the dotted line is T_λ for bulk He II.

ent ''weight classes'' and can be considered approximately independent. The vanishing of the ensemble of MVRs at $d \approx d_0$ apparently leads to growth of ρ_s and, hence, to an increase in the energy of BKT vortices and a decrease of their density and heat capacity. This should lead to a slight jump on the $T_{BKT}(d)$ curve also, but we have not investigated this in detail.

Thus, if the bulk λ transition in He II is due to an ensemble of MVRs, then an anomaly should appear on the $T_c(d)$ curve at $d \approx 6 \pm 4$ Å, such as that illustrated in Fig. 2. And, if the MVRs do not play a key role in the λ transition and do not influence the value of T_λ, then such an anomaly on the $T_c(d)$ curve will not appear.

The $T_c(d)$ curve for He II has been measured previously[28–32] (see Fig. 3). The crosses in Fig. 3 show the values calculated according to Fig. 1 of Ref. 32, with the density of He II for the first superfluid layer assumed equal to 0.183 g/cm^3 (Ref. 28). In determining the thickness d from the data of Ref. 30 we assumed that the first layer is solid, and in determining d for Vycor coated with N_2 (the unfilled triangles in Fig. 3) we assumed a solid ^{4}He layer 1.5 Å thick (according to Fig. 11 of Ref. 29). In Ref. 30 the thickness was measured with an error not less than ± 4 Å.

We have the following notes in regard to the data in Fig. 3. The most accurate measurements of $C(T,d)$ are apparently those in Refs. 32 and 31. The data of Ref. 32 and Refs. 28 and 29, obtained for Vycor substrates, do not agree completely. According to Ref. 32, this is due to the inaccurate determination of d in Refs. 28 and 29, so that for $T_c = 1.25$ K the correct value is $d \approx 1$ Å rather than $d = 4$ Å, and for $T_c = 1.75$ K the value should be $d \cong 3$ Å and not ≈ 7 Å;[28,29] these ''renormalized'' curves are shown by circles in Ref. 3. If this is the case, then the Brewer curve is shifted to the left, and the points obtained in Ref. 32 lie on this curve. It is also seen that the data for Vycor[28,29,32] agree poorly with the data on $T_c(d)$ for substrates of Nuclepore[31] and jeweller's rouge.[30] This disagreement is possibly due to the inhomogeneity of the He II film on Vycor at $d > 8$ Å.[31]

On the whole, it is seen in Fig. 3 that the data of different studies do not agree very well, and there is a rather large scatter in the points.

The data in Fig. 3 do not permit us to determine whether the proposed anomaly on the $T_c(d)$ is present. More-precise measurements of $T_c(d)$ for different substrates, for d from 1 Å to 20 Å and with a small step $\Delta d \leqslant 1$ Å, are needed. To reveal the anomaly it is necessary that the He II film be superfluid at any thickness (at low T) and that the BKT effect be well observed. Therefore studies on substrates of the Mylar, Vycor glass, and Nuclepore type are needed (but not on graphite,[38] as helium on graphite substrates has complex properties and a tendency toward layer-by-layer crystallization).

Inasmuch as the observation or nonobservation of an anomaly on the $T_c(d)$ curve will convey information about the role of vortex rings in the λ transition in He II, it is of interest to have a precise measurement of the $T_c(d)$ curve.

CONCLUSION

We have proposed an experiment by which one can determine whether the λ transition in bulk He II is caused by microscopic vortex rings. If the rings largely determine the value of T_λ in bulk helium, then for thin films of superfluid helium the curve of T_λ versus the thickness d of the superfluid layer of the film should have a feature in the form a jump of T_λ at $d \approx 6 \pm 4$ Å (see Fig. 2). The available experimental data are insufficient to permit a conclusion as to the presence or absence of the predicted anomaly. Observation of an anomaly would be the first experimental evidence of the existence of an ensemble of MVRs as thermal excitations in He II.

The idea of this paper was also addressed in Ref. 39, where the nature of the broad peak on the $C(T)$ curve is discussed more completely and precisely.

The author thanks K. V. Krasnov for providing copies of Refs. 11 and 29.

*E-mail: mtomchenko@bitp.kiev.ua

[1] R. P. Feynman and M. Cohen, Phys. Rev. **102**, 1189 (1956).
[2] I. A. Vakarchuk and I. R. Yukhnovskiĭ, Teor. Mat. Fiz. **40**, 100 (1979); **42**, 112 (1980).
[3] L. Reatto, G. L. Masserini, and S. A. Vitiello, Physica B **197**, 189 (1994).
[4] É. A. Pashitskiĭ, S. I. Vilchinsky, and S. V. Mashkevich, Fiz. Nizk. Temp. **28**, 115 (2002) [Low Temp. Phys. **28**, 79 (2002)].
[5] M. D. Tomchenko, submitted to Zh. Éksp. Teor. Fiz. (JETP).
[6] N. N. Bogolyubov, J. Phys. USSR **11**, 23 (1947).
[7] O. Penrose and L. Onsager, Phys. Rev. **104**, 576 (1956).
[8] C. N. Yang, Rev. Mod. Phys. **34**, 694 (1962).
[9] Yu. A. Nepomnyashchii and E. A. Pashitskii, Zh. Éksp. Teor. Fiz. **98**, 178 (1990) [Sov. Phys. JETP **71**, 98 (1990)].
[10] R. P. Feynman, *Statistical Mechanics: a Set of Lectures*, Benjamin, Reading, Mass. (1972), Mir, Moscow (1978); D. ter Haar, Phys. Rev. **95**, 895 (1954).
[11] L. Onsager, Nuovo Cimento, Suppl. **6**, Suppl. 2, 249 (1949).
[12] E. Bycling, Ann. Phys. (N.Y.) **32**, 367 (1965).
[13] F. W. Wiegel, Physica (Amsterdam) **65**, 321 (1973).
[14] G. A. Williams, Phys. Rev. Lett. **59**, 1926 (1987); **68**, 2054 (1992); J. Low Temp. Phys. **89**, 91 (1992).
[15] F. Lund, A. Reisenegger, and C. Utreras, Phys. Rev. B **41**, 155 (1987).
[16] G. W. Rayfield and F. Reif, Phys. Rev. Lett. **11**, 305 (1963); Usp. Fiz. Nauk **83**, 755 (1964); Phys. Rev. **136**, A 1194 (1964).
[17] G. W. Rayfield, Phys. Rev. Lett. **19**, 1371 (1967); Phys. Rev. **168**, 222 (1968).

[18] D. Amit and E. P. Gross, Phys. Rev. **145**, 130 (1966).
[19] C. A. Jones and P. H. Roberts, J. Phys. A **15**, 2599 (1982).
[20] E. P. Gross, Nuovo Cimento **20**, 454 (1961); J. Math. Phys. **4**, 195 (1963).
[21] S. Patterman, *Superfluid Hydrodynamics*, North-Holland, Amsterdam (1974), Mir, Moscow (1978); V. V. Meleshko and M. Yu. Konstantinov, *Dynamics of Vortex Structures* [in Russian], Naukova Dumka, Kiev (1993); P. G. Saffman, Stud. Appl. Math. **49**, 371 (1970).
[22] L. D. Landau and E. M. Lifshitz, *Statistical Physics*, 3rd ed., Part 1, Pergamon Press, Oxford (1980), Nauka, Moscow (1976).
[23] E. M. Lifshitz and L. P. Pitaevskiĭ, *Statistical Physics* (3rd ed., Part 2 of L. D. Landau and E. M. Lifshitz), Pergamon Press, Oxford (1980), Nauka, Moscow (1978).
[24] J. Norbury, J. Fluid Mech. **57**, 417 (1973).
[25] R. J. Donnelly, J. A. Donnelly, and R. N. Hills, J. Low Temp. Phys. **44**, 471 (1981).
[26] P. C. Hendry, N. S. Lawson, R. A. M. Lee, P. V. E. McClintock, and C. D. H. Williams, Nature (London) **368**, 315 (1994); Physica B **210**, 209 (1995).
[27] M. E. Dodd, P. C. Hendry, N. S. Lawson, P. V. E. McClintock, and C. D. H. Williams, Phys. Rev. Lett. **81**, 3703 (1998); A. Ganshin, M. Mohazzab, and N. Mulders, J. Low Temp. Phys. **134**, 477 (2004).
[28] D. F. Brewer, A. J. Symonds, and A. L. Thomson, Phys. Rev. Lett. **15**, 182 (1965).
[29] D. F. Brewer, J. Low Temp. Phys. **3**, 205 (1970).
[30] H. P. R. Frederikse, Physica (Amsterdam) **15**, 860 (1949).
[31] T. P. Chen and F. M. Gasparini, Phys. Lett. A **62**, 231 (1977); F. M. Gasparini, T. P. Chen, and B. Bhattacharya, Phys. Rev. B **23**, 5797 (1981).
[32] D. Finotello, K. A. Gillis, A. Wong, and M. H. W. Chan, Phys. Rev. Lett. **61**, 1954 (1988).
[33] S. Q. Murphy and J. D. Reppy, Physica B **165–166**, 547 (1990).
[34] J. A. Nissen, T. C. P. Chui, and J. A. Lipa, J. Low Temp. Phys. **92**, 353 (1993).
[35] G. Agnolet, D. F. McQueeney, and J. D. Reppy, Phys. Rev. B **39**, 8934 (1989).
[36] K. Shirahama, M. Kubota, S. Ogava, N. Wada, and T. Watanabe, Phys. Rev. Lett. **64**, 1541 (1990).
[37] H. Cho and G. A. Williams, J. Low Temp. Phys. **101**, 463 (1995).
[38] M. Bretz, J. G. Dash, D. S. Hickernell, E. O. McLean, and O. E. Vilches, Phys. Rev. A **8**, 1589 (1973); P. A. Crowell and J. D. Reppy, Physica B **197**, 269 (1994).
[39] M. D. Tomchenko, J. Low Temp. Phys., in press.

Translated by Steve Torstveit

SUPERCONDUCTIVITY, INCLUDING HIGH-TEMPERATURE SUPERCONDUCTIVITY

Interaction of Abrikosov vortex with grain boundaries near H_{c1}. II. Magnetic and transport properties of polycrystalline high-T_c superconductors

L. V. Belevtsov*

A. A. Galkin Donetsk Physicotechnical Institute, ul. R. Lyuksemburg 72, Donetsk 84114, Ukraine
(Submitted April 1, 2003; revised July 20, 2004)
Fiz. Nizk. Temp. **31**, 490–499 (May 2005)

The magnetic and transport characteristics of a polycrystalline superconductor are investigated theoretically starting from the results on the energy distribution of an Abrikosov vortex in the vortex-laminar model [L. V. Belentsov, Low Temp. Phys. **31**, 116 (2005)]. It is shown that these properties depend largely on the normalized grain size, the intergrain coupling strength, the anisotropy, and the degree of surface smoothness (''specularity'') of the material. The first vortex entry field H_p, the first critical field H_{c1}, and the Gibbs free energy are calculated, and also the field dependence of the magnetization $M(H)$, pinning potential $U_p(H)$, and critical current density $J_c(H)$ near $H \sim H_{c1}$. The vortex-vortex interaction energy is found. © *2005 American Institute of Physics.* [DOI: 10.1063/1.1925347]

1. INTRODUCTION

Surface effects can play an important and even dominant role in the formation of the magnetic and transport characteristics of a type-II superconductor.[1–5] The vortex dynamics is intimately related to the magnetization.[6] Hysteretic phenomena are usually interpreted as proof of the finiteness of the critical currents owing to the bulk pinning of vortices. Experiments show that the existence of Bean-Livingston surface barriers[7] as possible sources of hysteretic behavior. In the framework of the critical-state approach Kuznetsov *et al.*[8] have estimated the enhancement of the magnetization of thin films with significant pinning owing to ''edge'' effects. Magnetization measurements by Zel'dova *et al.*[9] revealed a new ''geometric barrier'' for thin films which significantly enhanced the potential barrier in the presence of a Bean-Livingston barrier. Part I of this paper (see Ref. 10) described ''edge'' barriers in granular superconductors. It follows directly from the model used there that the vortex dynamics depends rather strongly not only on the value of the applied field but also on the normalized grain size, the intergrain coupling strength, the anisotropy, and the degree of surface smoothness of the material. In this part of the paper we shall examine how variation of these parameters influences the magnetic and transport properties of superconducting polycrystals in the mixed state at magnetic fields H near H_{c1}.

2. MAGNETIC PROPERTIES NEAR H_{c1}

In the mixed state the critical characteristics are specified by the energy distribution of the Abrikosov vortices. For a superconducting polycrystal the energy of an isolated vortex line localized at the point (x_0, z_0) has the form[10]

$$U(x_0,z_0)=\frac{\Phi_0}{4\pi}\left\{H_y^{\rm app}\exp(-x_0/\lambda_{ab})-H_y^{\rm app}+H_{c1}(\infty)+H_y^J(x_0,z_0)+\frac{\Phi_0}{4\pi\lambda_{ab}\lambda_c}\times\left[\sum_{\substack{n=-L\\(n\neq 0)}}^{L}P_n^S(x_0,x_0,z_0,z_0)+\sum_{n=-L}^{L}P_n^N(x_0,x_0,z_0,z_0)\right]\right\}, \quad (1)$$

where $\Phi_0=hc/2e$ is the magnetic flux quantum, $H_y^{\rm app}=(0,H_y,0)$ is the external magnetic field, and λ_{ab} and λ_c are the magnetic field penetration depths: the London depth along the ab plane and the crystallographic depth along the c axis, respectively. In our model λ_{ab} corresponds to penetration of the field into a grain from the surface side, and λ_c to penetration from the side of the Josephson junctions; K_0 is the zeroth-order Bessel function of imaginary argument;[11] $H_{c1}(\infty)$ is the first critical field of an infinite sample; L is degree of surface smoothness of the material;

$$H_y^J(x_0,z_0)=H_y^{\rm app}\int_0^\infty\frac{dk}{2\pi}\frac{4k\lambda_J^2}{1+\lambda_{ab}^2k^2}\times\frac{\sin(kx_0)\cosh[(1+\lambda_{ab}^2k^2)^{1/2}(z_0/\lambda_c)]}{\lambda_J^2k^2\cosh\gamma+(1+\lambda_{ab}^2k^2)^{1/2}\sinh\gamma} \quad (2)$$

is the value of the field at the point (x_0, z_0) due to the presence of Josephson coupling; here we have introduced the notation $\gamma=(1+\lambda_{ab}^2k^2)^{1/2}(a/2\lambda_c)$ and also

$$P_n^S(x,x_0,z,z_0)=(-1)^n K_0 \times\left(\sqrt{\frac{(x-x_0)^2+[z-(-1)^n z_0-na]^2}{\lambda_{ab}\lambda_c}}\right), \tag{3}$$

$$P_n^N(x,x_0,z,z_0)=(-1)^{n+1} K_0 \times\left(\sqrt{\frac{(x+x_0)^2+[z-(-1)^n z_0-na]^2}{\lambda_{ab}\lambda_c}}\right). \tag{4}$$

The dependence of the energy of a vortex line on the coordinates of its localization within a grain, $U(x_0,z_0)$, according to relation (1) contains a ''seed'' of all the main features of the magnetic and transport response of high-T_c superconducting (HTSC) polycrystals to variation of the parameters of the structurally nonuniform Josephson system and the applied field.

2.1. Critical fields

2.1.1. First vortex entry field

In the case when the barrier is suppressed by surface defects one would expect that the first vortex entry field H_p ($H_{c1}<H_p<H_c$) will be considerably higher than H_{c1}. In the case of the vortex-laminar model considered here, the surface of the grains is assumed to be rather smooth, and so $H_p=H_{c1}$ (Ref. 12). At this field the induced currents become large enough for the vortex to break away from its ''mirror images'' and to penetrate into the sample.[13] To find the field H_p one must minimize the vortex energy $U(x_0,z_0)$ at the grain surface. A vortex lines has its lowest energy along the OX axis at points $z=0$. On the other hand, we are interested in the case when the top of the barrier comes out onto the surface, i.e., $x_0=0$. But for $x_0\to 0$ one has $K_1(2x_0/\sqrt{\lambda_{ab}\lambda_c})\approx\sqrt{\lambda_{ab}\lambda_c}/2x_0$. At small x_0 we replace x_0 by ξ_{ab}, i.e., $K_1(2x_0/\sqrt{\lambda_{ab}\lambda_c})\approx\sqrt{\lambda_{ab}\lambda_c}/\xi_{ab}$. Hence, on the assumption $L\to\infty$, we obtain

$$H_p\approx\frac{\Phi_0}{\pi\lambda_c}\sum_{n=-\infty}^{+\infty}(-1)^{n+1}\frac{\xi_{ab}}{4\xi_{ab}^2+n^2a^2}[1-\Omega(\tau,\eta,\sigma)]^{-1}, \tag{5}$$

where

$$\Omega(\tau,\eta,\sigma)=\int_0^\infty\frac{dk}{2\pi}\frac{4k^2\lambda_J^2}{(1+\lambda_{ab}^2k^2)} \times\frac{\lambda_{ab}\cos(k\xi_{ab})}{\lambda_J^2k^2\cos\gamma+(1+\lambda_{ab}^2k^2)^{1/2}\sin\gamma}. \tag{6}$$

Relation (6) introduces a correction to the values of H_p when the grain boundaries are taken into account. In the limit $\lambda_J\to 0$ the problem goes over to that of the critical fields in a strongly coupled superconductor of the MgB_2 type. Here the first vortex penetration field is $H_p=\Phi_0/(\xi_{ab}\lambda_c)$, which in the isotropic case ($\xi_{ab}=\xi_c$, $\lambda_{ab}=\lambda_c$) will correspond to the known Bean-Livingston result. If it is assumed that $\xi\sim(1-T/T_c)^{-1/2}$ and $\lambda\sim(1-T/T_c)^{-1/2}$, then we obtain $H_p=[\Phi_0/4\pi\xi_{ab}^0\lambda_c^0](1-T/T_c)$, and thus, in the linear approximation this formula reproduces the result of Pissas *et al.*[14] for MgB_2. It is easy to see that H_p depends on the anisotropy.

2.1.2. First critical field H_{c1}

At a low density of vortex lines [low values of the induction $B\sim\Phi_0/(\xi_{ab}\xi_c)$] their interaction can be neglected. Then the first critical field H_{c1}, above which thermal equilibrium of the system corresponds to a finite density of vortices in the superconductor, can be found from the equation for the energy of a single vortex (1) under the condition $U(x_0,z_0)=0$. Since from the symmetry of the problem a vortex has its lowest energy at points $z=0$ and along the OX axis, the expression for the first critical field H_{c1} takes the form

$$H_{c1}(x_0,\tau,\eta,\sigma)=\frac{H_{c1}(\infty)-\dfrac{\Phi_0}{4\pi\lambda_{ab}\lambda_c}\left[\displaystyle\sum_{\substack{n=-\infty\\(n\neq 0)}}^{+\infty}P_n^S(x_0,x_0,0,0)+\sum_{n=-\infty}^{+\infty}P_n^N(x_0,x_0,0,0)\right]}{1-\exp\left(-\dfrac{x_0}{\lambda_{ab}}\right)-\displaystyle\int_0^\infty\frac{dk}{2\pi}\frac{4k\lambda_J^2}{(1+\lambda_{ab}^2k^2)}\frac{\sin(kx_0)}{\lambda_J^2k^2\cos\gamma+(1+\lambda_{ab}^2k^2)^{1/2}\sin\gamma}}. \tag{7}$$

The function $H_{c1}(x_0)$ is plotted in Fig. 1 for different anisotropy parameters and normalized grain sizes $\tau=a/2\lambda_c$. It is seen that together with an anisotropic potential barrier there exists an energy barrier which depends on τ. This barrier is greater the larger the value of τ. The results of Part I of this paper[10] confirm that even in the absence of a microscopic Bean-Livingston surface barrier an energy barrier can arise which depends on the normalized grain size. This type of barrier is somewhat analogous to the geometric barrier, where the field H_{c1} depends on the shape of the sample.[9] We note that relation (7) adequately describes the effect observed in Ref. 15 wherein the first critical field of the grains, H_{c1}^g, in a superfine-grained sample of the high-T_c superconductor $YBa_2Cu_3O_{7-\delta}$ was found to be significantly higher than the typical values for coarse-grained samples.

2.2. Interaction of vortex lines

In the mixed state in an ideal pinning-free superconductor the vortex-vortex interaction gives a contribution to the energy of the system through the dependence on the density of vortices. This leads to the well-known logarithmic

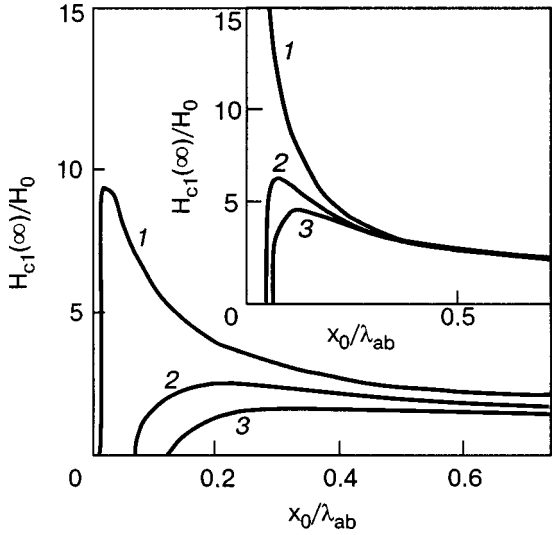

FIG. 1. Dependence of the local first critical field H_{c1} on the distance to the surface x_0 for various values of the anisotropy parameter η: 1.8 (*1*), 1.0 (*2*), and 0.8 (*3*). The main panel corresponds to the fine-grained limit ($\tau=0.5$), and the inset to the limit of large grains ($\tau=10$).

dependence of the field in the London theory for Abrikosov[12] and internal (pancake) vortices in layered superconductors.[16] To correctly describe the ''edge'' barriers one must take the vortex-vortex interaction into account. First, the energy of this interaction exceeds the barrier height. Second, the potential barrier should decrease on account of the vortex-antivortex interaction.

Let us generalize the formulation of the model to the case of many vortices. Suppose that the superconducting grain under consideration contains a system of N vortices, with axes along the Y axis and located at the points $R_1=(x_1,z_1)$, $R_2=(x_2,z_2),\ldots,$ $R_n=(x_n,z_n)$. Here the field of the vortices will satisfy the equation

$$\nabla\times[\lambda^2]J+\mathbf{H}=\Phi_0\mathbf{e}_y\left\{\sum_{k=1}^{N}\sum_{n=-\infty}^{+\infty}(-1)^n\delta(R-R_{nk}^{(+)})+(-1)^{n+1}\delta(R-R_{nk}^{(-)})\right\}, \tag{8}$$

where $\mathbf{e}_y$ is a unit vector along the OY axis; the index k refers to the kth vortex. The solution of equation (8) is presented in the form a sum of the fields for each vortex line of the system:

$$\mathbf{H}(R)=\mathbf{H}_1(\mathbf{R})+\mathbf{H}_2(\mathbf{R})+\ldots+\mathbf{H}_N(\mathbf{R}), \tag{9}$$

where

$$H_i(R)=\frac{\Phi_0}{2\pi\lambda_{ab}\lambda_c}\sum_{n=-\infty}^{+\infty}[P_n^S(x,x_i,z,z_i)+P_n^N(x,x_i,z,z_i)]. \tag{10}$$

After substitution of Eq. (8), taken at $k=1$, into the expression for the field distribution of an Abrikosov vortex penetrating a grain at a point (x_0,z_0),[10]

$$H_2(x,x_0,z,z_0)=\frac{\Phi_0}{2\pi\lambda_{ab}\lambda_c}\sum_{n=-\infty}^{+\infty}[P_n^S(x,x_0,z,z_0)+P_n^N(x,x_0,z,z_0)], \tag{11}$$

it is necessary to keep only the terms describing the contribution to the energy from the vortex-vortex interaction. Then the expression for a system of vortices is finally

$$U_{\rm int}=\frac{\Phi_0^2}{8\pi\lambda_{ab}\lambda_c}\sum_{\alpha,\beta}\sum_{n=-\infty}^{+\infty}[P_n^S(x_\alpha,x_\beta,z_\alpha,z_\beta)+P_n^N(x_\alpha,x_\beta,z_\alpha,z_\beta)]. \tag{12}$$

As is seen from Eq. (12), the vortex-vortex interaction energy depends on the normalized grain size $\tau=a/2\lambda_c$, the anisotropy $\eta=\lambda_c/\lambda_{ab}$, and the distance between vortices. Thus for description of the dynamics of the penetration of vortex lines into grains it is necessary to consider the the influence of the Lorentz force exerted on vortex i by vortex j, which is expressed as $-\nabla_i U(\mathbf{R}_i,\mathbf{R}_j)$, where

$$U(\mathbf{R}_i,\mathbf{R}_j)=U_{\rm int}(\mathbf{R}_i,\mathbf{R}_j)+U_{\rm self}(\mathbf{R}_i)+U_{\rm mirr}(\mathbf{R}_i). \tag{13}$$

Here $U_{\rm self}(\mathbf{R}_i)$ is the self-energy of the ith vortex, $U_{\rm int}(\mathbf{R}_i,\mathbf{R}_j)$ is the interaction energy between the ith and jth vortices of the vortex line, and $U_{\rm mirr}(\mathbf{R}_i)$ is the energy of interaction between the ith vortex line and its ''mirror images.''

Let us consider the case of two Abrikosov vortices. Let $d=\sqrt{(x_2-x_1)^2+(z_2-z_1)^2}$ be the distance between vortex lines. Then from expression (10) the interaction energy will have the form

$$U(d)=\frac{\Phi_0^2}{8\pi\lambda_{ab}\lambda_c}\times\sum_{n=-\infty}^{+\infty}\left[(-1)^nK_0\left(\sqrt{\frac{(x_1-x_2)^2+[z_1-(-1)^nz_2-na]^2}{\lambda_{ab}\lambda_c}}\right)+(-1)^{n+1}K_0\left(\sqrt{\frac{(x_1+x_2)^2+[z_1-(-1)^nz_2-na]^2}{\lambda_{ab}\lambda_c}}\right)\right]. \tag{14}$$

Expression (14) is valid for arbitrary d. It is easy to see that, like two-dimensional vortices in superconductors, the vortex lines under discussion demonstrate a logarithmic interaction law at large distances. Furthermore, the given model permits description of structural details of the vortex lattice. It should be noted that the vortex-antivortex interaction energy is of interest in consideration of the question of the possibility of a Berezinskii-Kosterlitz-Thouless vortex phase transition and in our notation will be expressed as $-U(d)$.

2.3. Magnetization

For a superconductor in an external field $H_y^{\rm app}$ the magnetization curve has a well-known triangular form. One of the manifestations of the ''edge'' barriers is represented in the form of the magnetization curve $M(H)$ in its sloping part near $M\approx 0$. Such behavior is due to the fact[17] that for $H=H_p$ both the screening currents and the potential barrier vanish, and the vortex lines can penetrate unimpeded into the grains. There is obviously also a substantial influence of the

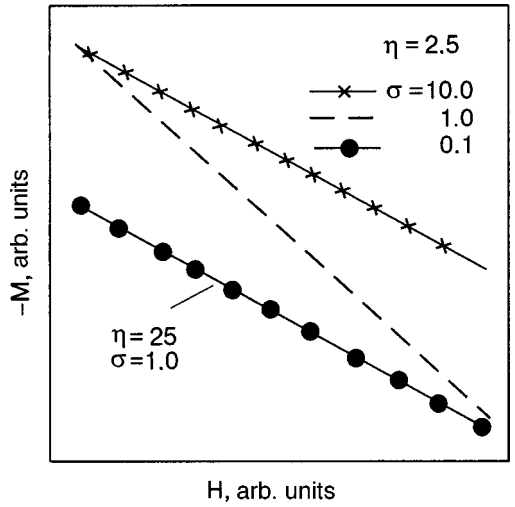

FIG. 2. Behavior of the low-field magnetization **M** as a function of the applied field H_y^{app} for different values of the anisotropy parameter η and intergrain coupling strength σ, taken at a normalized grain size $\tau=1.2$ and a degree of surface smoothness of the material $L=1$.

barrier on the magnetization curves $M(H)$ in a system of vortex lattices in an increasing field near H_{c1}, when the initial states are not yet ordered.

The magnetization **M** of an individual grain containing a vortex line will be described by the relation

$$4\pi M=\frac{1}{V}\int_V [B(r)-H]dV, \tag{15}$$

where V is the volume of the grain, and $B(r)$ and H are the local induction and the external magnetic field, respectively. In our case $B(r)\equiv H(x,z)$ is the field distribution in the grain,[10] and $H\equiv H_y^{app}$.

Let us consider how variation of the anisotropy parameter η and grain coupling strength σ will affect the low-field magnetization. For illustration Fig. 2 shows the calculated characteristics of the magnetization curves $M(H)$ for $H_{c1}\sim 300$ Oe. Two features are observed in this magnetic field region: 1) at a constant coupling strength parameter σ the value of $M(H)$ is smaller for larger η; 2) with decreasing σ the $M(H)$ curve rises. Thus the form of the magnetization curves depends directly on the anisotropy parameter, intergrain coupling strength, and reduced grain size. It should be noted that by varying these parameters one can evidently observe dia(para)magnetic transitions in polycrystalline HTSCs, which have been observed in numerous experiments.[18,19]

2.4. Gibbs free energy at $H \geqslant H_{c1}$

The Gibbs thermodynamic potential of a system of a large number of vortex lines has the form[20]

$$G=n_L F+\sum_{ij} U_{ij}-\frac{BH_y^{app}}{4\pi}, \tag{16}$$

where n_L is the number of lines per unit area, the first and third terms are due to the energy of an individual line and correspond to expression (1), and U_{ij} is the interaction energy between the ith and jth vortex lines, which is expressed by relation (12). The last term takes into account the influence of the external magnetic field H_y^{app}; this term makes large values of the induction B energetically favorable. In other words, the field H_y^{app} plays the role of an external pressure that tends to increase the density of Abrikosov vortices. Since each vortex line carries one flux quantum Φ_0, the induction B can be written in the form

$$B=n_L\Phi_0. \tag{17}$$

If the external field H_y^{app} is slightly greater than H_{c1} then it is (16) necessary to take into account the term describing interaction of vortices. Then the distribution of Abrikosov vortices will correspond to a periodic structure. As we know,[21] a triangular lattice of Abrikosov vortices is the most favorable. When the field is only slightly higher than H_{c1}, the equilibrium vortex density n_L is small, and the distance d between nearest vortex lines is large: $d>(\lambda_{ab}^2+\lambda_c^2)^{1/2}$. Therefore only the nearest-neighbor vortex pairs should be taken into account. Then the expression for the Gibbs free energy becomes

$$\begin{aligned} G=\frac{\Phi_0}{4\pi}\sum_{\alpha=1}^{n_L=B/\Phi_0}\Bigg\{ & H_y^{app}\exp(-x_\alpha/\lambda_{ab})-H_y^{app}+H_{c1}(\infty) \\ & +H_y^J(x_\alpha,z_\alpha)+\frac{\Phi_0}{4\pi\lambda_{ab}\lambda_c}\Bigg[\sum_{\substack{n=-\infty\\(n\neq 0)}}^{+\infty} P_n^S(x_\alpha,x_\alpha,z_\alpha,z_\alpha) \\ & +\sum_{n=-\infty}^{+\infty} P_n^N(x_\alpha,x_\alpha,z_\alpha,z_\alpha)\Bigg] \\ & +\frac{\Phi_0}{2\pi\lambda_{ab}\lambda_c}\sum_{\beta=1}^{\delta}\Bigg[\sum_{\substack{n=-\infty\\(n\neq 0)}}^{+\infty} P_n^S(x_\alpha,x_\beta,z_\alpha,z_\beta) \\ & +\sum_{n=-\infty}^{+\infty} P_n^N(x_\alpha,x_\beta,z_\alpha,z_\beta)\Bigg]\Bigg\}, \end{aligned} \tag{18}$$

where δ is the number of nearest neighbors of a given vortex line (for a triangular lattice $\delta=6$). The distance d is related to the induction B as

$$B\equiv n_L\Phi_0=\frac{2}{\sqrt{3}}\frac{\Phi_0}{d^2}. \tag{19}$$

It follows from the form of expression (18) that for $H_y^{app}>H_{c1}$ the initial slope $(\partial G/\partial B)_{B=0}$ is negative. With increasing induction the contributions of the interaction with the surface, Josephson junction, magnetic field, and the other Abrikosov vortices begin to grow. Thus the main contribution will be from the interaction of Abrikosov vortices with the Josephson link and the surface [the first term in (16)]. The other terms are small because they contain a term $\sim K_0(x)$, which for $d>\sqrt{\lambda_{ab}^2+\lambda_c^2}$ has the form $K_0(x)\sim\exp(-x)$. Consequently, at small values of B the interaction is small. At large values of B, however, this term gives the dominant contribution, leading to growth of the function $G(B)$. At a certain value $B=B(H)$ the function $G(B)$ reaches a minimum. Thus, unlike the case of a uniform superconductor, expression (16) demonstrates strong dependence on the normalized grain size τ, anisotropy η, and in-

tergrain coupling strength σ, and also on the degree of surface smoothness L in the case of a material with micrograin structure.

3. PINNING POTENTIAL AND CRITICAL CURRENT DENSITY

A type II superconductor has zero resistance if the magnetic vortices are pinned at defects or restricted of motion. In polycrystalline HTSCs the grain boundaries can serve as pinning centers.[22] At such sites the energy of a vortex line is so small that it becomes impossible for it to move through the sample. There are two characteristic quantities that determine how strongly an Abrikosov vortex is pinned at a defect: the pinning potential U_p and the critical current density J_c. A finite resistance appears when the binding energy of an Abrikosov vortex to a defect exceeds U_p or the current density exceeds J_c, leading to motion of the vortex lines. We shall show that the value of the ''edge'' barriers can play a substantial role and can determine the pinning potential and intragrain critical current density.[23]

3.1. Pinning potential

The mechanisms of pinning in granular superconductors are not yet fully understood. It remains an open question why the critical current densities of HTSC films are substantially higher than the values of J_c for the bulk HTSC materials. The key factor here is apparently the pinning of the vortices in an external magnetic field, which underlies the description of various phenomena involving the Abrikosov vortices such as the critical current, magnetization hysteresis, and the quantum tunneling of vortices. The problem of Abrikosov vortex pinning reduces to one of describing the elementary pinning force of an Abrikosov vortex—the interaction between the vortex and an isolated defect.

In comparison with the Bean-Livingston result,[7] expression (1) exhibits some differences of the barriers for Abrikosov vortices in granular superconductors. One of them—an energy barrier to the entry of the vortex into a grain from the side of the Josephson junction—can be interpreted as the pinning potential U_p. This is an obvious assumption, since defects are capable of pinning vortices, thereby lowering the order parameter locally in the superconductor, and this gives rise to a potential that inhibits the motion of the vortex line or internal vortex. Many experiments clearly indicate that even the well coupled grains of MgB_2, with a large misorientation angle θ of the boundary, can act as pinning centers at some values of the coherence length and lattice parameter.[22]

Taking relation (1) into account, we define the pinning potential per unit length of the vortex core as

$$U_p(x_0,L)=\lim_{z_0\to(a/2)} U(x_0,z_0,L). \tag{20}$$

The influence of the degree of smoothness L on the value of the pinning potential U_p is shown in Fig. 3 for $\tau=0.01$ (curve *1*) and $\tau=0.1$ (curve *2*). It is seen that in the case of large grains $\tau=0.1$, the influence of L on U_p is negligible; in the fine-grained case $\tau=0.01$, when $a\sim 1$ μm, the contribution from the next vortices-images for $L>1$ increases U_p by $\sim 16\%$ $(L\to\infty)$. Thus, if the pinning mechanism for the transport critical current is taken to be the dominant factor,

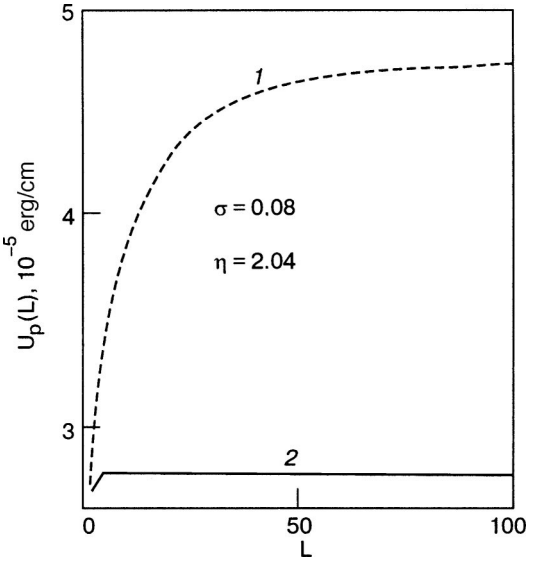

FIG. 3. Dependence of the pinning potential U_p on the degree of smoothness L of the material for $\tau=0.01$ (*1*) and 0.2 (*2*).

then the results agree with the experiments,[24] which show that the critical currents realized in fine-grain HTSCs are an order of magnitude larger than in samples with coarse grains. The pinning U_p is greater for smaller τ. Furthermore, the pinning potential in our model is an order of magnitude larger than the energy of an Abrikosov vortex at the grain center $(z_0=0)$.[10] This circumstance may be a direct indication of the possible similarity of the structure of vortex lattices in our model to that in a film under a parallel magnetic field,[25] where at fields $H\geqslant H_{c1}(d)$ $(d<\lambda$, where d is the film thickness and λ is the London penetration depth) the vortices are arranged in a row at the center of the film. As the field increases further, the structure of the lattice transforms to triangular.

Figure 4 shows the results of a numerical study of Eq. (20)—the dependence of the pinning energy on the reduced field $H_y^{\rm app}/H_{c1}(\infty)$ for $L\to\infty$ for values of the intergrain coupling parameter $\sigma=0.1$ and 10 and also (in the inset) for values of the anisotropy parameter $\eta=0.8$, 1.0, and 1.8. As is seen in the figure, in the limit of strong intergrain coupling the value of U_p falls off more rapidly with increasing field than in the weak-coupling limit. The inset shows the dependence of U_p on the anisotropy in the weak-coupling limit $\sigma=0.1$. It is easy to see that the pinning potential decreases with increasing η.

Thus the pinning potential is a function of many parameters: $U_p=U_p(H,\tau,\sigma,\eta,L)$. The approach developed in this paper can be used in a modified form in both strongly coupled (MgB_2) and weakly-coupled (HTSC) materials and also for studying the magnetic and transport properties of superconductors with a wide spectrum of grain sizes and anisotropy.

It should be noted that when the Lorentz force exerted on an Abrikosov vortex in an external magnetic field causes the vortex to move, the magnetic properties of the superconductor become reversible. Therefore the line of irreversibility on the $H-T$ phase diagram can be obtained from analysis of the $H-T$ dependence of the pinning energy U_p.

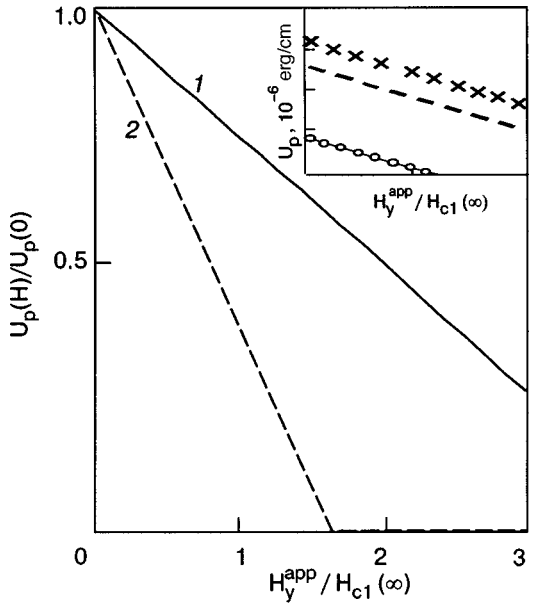

FIG. 4. Dependence of the pinning potential U_p on the applied field $H_y^{app}/H_{c1}(\infty)$ for $\sigma=0.1$ (*1*) and 10 (*2*), when $\tau\approx 1$. The inset shows the variation of U_p for $\eta=0.8$ (○), 1.0 (—), and 3.3 (×) in the weak-coupling limit $\sigma=0.1$.

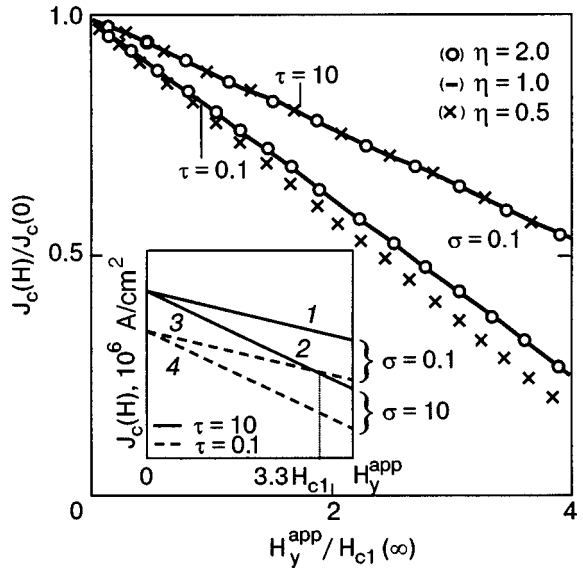

FIG. 5. Field dependence of the critical current density J_c for various values of the anisotropy parameter $\eta=0.5$, 1.0, and 2.0 for $\sigma=0.1$, $\tau=0.1$ and 10, and $L=1$. The inset shows the field dependence of J_c for values of the intergrain coupling $\sigma=0.1$ and 10. The solid and dashed lines correspond to the cases of large grains ($\tau=10$) and small grains ($\tau=0.1$), respectively.

3.2. Critical current density

Unlike the case of bulk untextured ceramic superconductors the field dependence of the critical current density $J_c(H_y^{app})$ in MgB_2 is determined by pinning and not by characteristic weak links. As in the case of HTSC materials, the pinning in MgB_2 depends strongly on field, being insignificant at low fields and forming a depinning line in fields near H_{c2}. Using relation (20), we find an expression for $J_c(H_y^{app})$ in the field region near H_{c1}. The current exerts on an Abrikosov vortex a force per unit length[26]

$$F_L=J/c. \tag{21}$$

Assuming that the force F_L in the critical state is counterbalanced by the pinning force, $F_p=F_L$, we obtain

$$F_p(H)=\frac{\Phi_0}{c}J_c(H). \tag{22}$$

In this expression the pinning force F_p is determined by the change of the pinning energy over distances of a scale ξ_c (ξ_c is the change of the order parameter at the grain boundary): $F_p=U_p/\xi_c$. Thus the local critical current density is a function of the external field H_y^{app} and the distance from the surface: $J_c(H_y^{app}, x_0, L)=(c/\Phi_0\xi_c)U_p(H_y^{app}, x_0, L)$. Averaging the current over the conducting cross section, we obtain an expression for the intragrain critical current density:

$$J_c(H_y^{app},L)=\frac{c}{\Phi_0\lambda_{ab}\xi_c}\int_0^{\lambda_{ab}}U_p(H_g^{app},x_0,L)dx_0. \tag{23}$$

Figure 5 shows the results of calculations of the field dependence of J_c for a coupling parameter $\sigma=0.1$, when $L\to\infty$ for various values of η and τ. It is seen in the main part of the figure that in the limit of large grains ($\tau=10$) the value of J_c is possibly independent of η, whereas in the small-grain limit ($\tau=0.1$) the value of J_c falls off with decreasing η. The inset shows the qualitative dependence of $J_c(H_y^{app})$ for coupling parameters $\sigma=0.1$ and 10 and also for normalized grain sizes $\tau=0.1$ and 10. The solid and dashed lines correspond to the limit of large and small grains, respectively. First off, one sees two extremal current states: $\sigma=0.1$, $\tau=10$ (curve *1*), and $\sigma=10$, $\tau=0.1$ (curve *4*), which correspond to the largest and smallest values of J_c for a given η. In fields $H_y^{app}\approx 3.3H_{c1}$ the current states with $\sigma=0.1$ and 10 are practically indistinguishable in the limit of small (curves *3* and *4*) and large (curves *1* and *2*) grain sizes. Thus in fields approximately equal to $3.3H_{c1}$ the value of J_c depends mainly on the grain sizes and is practically independent of the intergrain coupling strength σ. In fields $H_y^{app}\gg 3.3H_{c1}$, however, it can happen that the fine-grained structures have higher J_c than the coarse-grained structures (curves *2* and *3*). It is seen in the figure that the steepest drop of J_c is characteristic for the fine-grained, strongly coupled surfaces (curve *4*).

It is shown in the inset that the calculated value $J_c\sim 10^6$ A/cm^2. However, it follows from the experimental results that $J_c\sim 10^5$ A/cm^2 at $T\sim 10$ K. The discrepancy may be due to the fact that the pinning potential at the grain boundaries has a collective nature. This should lower the value of J_c. Thus the calculated value of J_c describes satisfactorily the main features of the transport in polycrystalline superconductors. This is a direct indication that the grain boundaries are the factor governing the transport properties. The grain boundaries ''anchor'' the Abrikosov vortices, creating pinning centers. The dependence on the anisotropy is substantial. Thus the technique of texturing may be used to optimize the technological process of making materials with large J_c.

It should be noted that in considering the question of the intragrain critical current density we have assumed that there is one pinning center for each grain. In other words, were are studying transport properties governed by the elementary

vortex pinning force F_p^i. In real materials, however, the pinning potential U_p is a sum of the energies of the pinning centers: $U_p = \Sigma_i U_p^i$ (or the vortex density at the grain boundaries, n_p),[27] i.e., $U_p \propto n_p \propto H_y^{app}$. Taking into account that $J_c \propto U_p \propto n_p$, one can conclude that as soon as the external magnetic field increases, so do the number of Abrikosov vortices and, hence, the density of pinning centers.[28] Thus with increasing field the value of J_c is determined by the pinning on the set of defects, which can support large currents to high fields. In the case of fields $H_{c1} \ll H \ll H_{c2}$ every vortex line is coupled with a vortex lattice, which should increase U_p. Therefore the dependence of U_p on H and, hence, $J_c(H)$ are weakened, as is is seen from the experimental results of transport measurements.

4. CONCLUSIONS

The results obtained show that the grains play a substantial, even dominant role in the formation of the magnetic and transport properties in polycrystalline superconductors at magnetic fields H close to H_{c1}. Apparently the role of the boundaries will be significant in both ceramic and single-crystal HTSCs. The normalized grain size τ, the intergrain coupling strength σ, the anisotropy η, and the degree of smoothness of the material all shape the potential barrier that impedes both the entry and exit of a vortex line and can enhance or weaken the Bean–Livingston barrier. These parameters should be taken into account in a realistic analysis of the questions of the first vortex entry field H_p, the lower critical field H_{c1}, hysteresis effects, and also the pinning potential and the intragrain critical current density J_c. The results of this study can be applied for analysis of the question of stability of the vortex lattice and also in the study of the Berezinskii–Kosterlitz–Thouless vortex phase transition. The proposed model can account for the difference in the transport behavior of different samples with a weakly coupled Josephson structure (HTSCs) and strongly coupled materials (MgB_2, LiBC) with different degrees of graininess and anisotropy. The degree of surface smoothness of the materials also has an important bearing on these questions, since our results directly imply such a dependence of the critical parameters in the case of fine-grained samples.

The author expresses his deep gratitude to A. I. D'yachenko, Yu. V. Medvedev, and A. A. Abramov for helpful discussions of the results of this study.

*E-mail: apmath@dgma.donetsk.ua

[1] E. H. Brandt, Phys. Rev. B **60**, 11939 (1999).
[2] E. H. Brandt, Fiz. Nizk. Temp. **27**, 980 (2001) [Low Temp. Phys. **27**, 723 (2001)].
[3] L. Burlachkov, Phys. Rev. B **47**, 5830 (1993).
[4] I. L. Maksimov and A. E. Elistratov, Appl. Phys. Lett. **72**, 1650 (1998).
[5] I. L. Maksimov and G. M. Maksimova, JETP Lett. **65**, 423 (1997).
[6] S. Senoussi, J. Phys. III (France) **2**, 1041 (1992).
[7] M. Konczykowski, L. I. Burlachkov, Y. Yeshurun, and F. Holtzberg, Phys. Rev. B **43**, 13707 (1991); C. P. Bean and J. D. Livingston, Phys. Rev. Lett. **12**, 14 (1964).
[8] A. V. Kuznetsov, D. V. Eremenko, and V. N. Trofimov, Phys. Rev. B **59**, 1507 (1999).
[9] E. Zeldov, A. I. Larkin, V. B. Geshkenbein, M. Konczykowski, D. Majer, B. Khaykovich, V. M. Vinokur, and H. Shtrikman, Phys. Rev. Lett. **73**, 1428 (1994).
[10] L. V. Belevtsov, Fiz. Nizk. Temp. **31**, 155 (2005) [Low Temp. Phys. **31**, 116 (2005)].
[11] P. M. Morse and H. Feshbach, *Methods of Theoretical Physics*, McGraw-Hill, New York (1953), Izd-vo Inostr. Lit., Moscow (1960), Chapter 10.
[12] J. Pearl, Appl. Phys. Lett. **5**, 65 (1964).
[13] P. G. de Gennes, Solid State Commun. **3**, 127 (1965).
[14] M. Pissas, E. Moraitakis, D. Stamopoulos, G. Papavassilio, V. Psycharis, and S. Kountandos, cond-mat/0108153 **v1**, Preprint 2001.
[15] L. G. Mamsurova, K. S. Pigal'skiĭ, A. V. Shlyakhtina, and L. G. Shcherbakova, Fiz. Nizk. Temp. **18**, 238 (1992) [Sov. J. Low Temp. Phys. **18**, 164 (1992)].
[16] Yu. M. Ivanchenko, L. V. Belevtsov, Yu. A. Genenko, and Yu. V. Medvedev, Physica C **193**, 291 (1992).
[17] A. M. Campbell and J. E. Evetts, *Critical Currents in Superconductors*, Taylor and Francis, London (1972), Mir, Moscow (1975).
[18] P. Singha Deo, V. A. Schweigert, and F. M. Peeters, Phys. Rev. B **59**, 6039 (1999).
[19] P. Singha Deo, F. M. Peeters, and V. A. Schweigert, Superlattices Microstruct. **25**, 1195 (1995).
[20] P. G. de Gennes, *Superconductivity of Metals and Alloys* (Benjamin, New York, 1966), Mir, Moscow (1968).
[21] W. H. Kleiner, L. M. Roth, and S. H. Autler, Phys. Rev. A **133**, 1226 (1964).
[22] B. A. Glowacki, M. Majoros, M. Vickers, J. E. Evetts, Y. Shi, and I. McDougall, Semicond. Sci. Technol. **14**, 193 (2001).
[23] J. R. Clem, in *Proceeding of 13th Conference on Low Temperature Physics (LT13)*, K. D. Timmerhaus, W. J. O'Sullian, and E. F. Hammel (eds.), Plenum, New York (1974), Vol. **3, p.** 102.
[24] A. S. Krasil'nikova, L. G. Mamsurova, N. G. Trusevich, A. V. Shlyakhtina, and L. G. Shcherbakova, Fiz. Nizk. Temp. **18**, 302 (1992) [Low Temp. Phys. **18**, 208 (1992)].
[25] S. H. Brongersma, E. Verwej, N. J. Koeman, D. G. de Groot, and R. Griessen, Phys. Rev. Lett. **71**, 2319 (1993).
[26] V. V. Shmidt and G. S. Mkrtchyan, Usp. Fiz. Nauk **112**, 459 (1974) [Sov. Phys. Usp. **17**, 170 (1974)].
[27] N.-C. Yeh, Phys. Rev. B **40**, 4566 (1989).
[28] E. H. Brandt and U. Essmann, Phys. Status Solidi B **144**, 13 (1987).

Translated by Steve Torstveit

Superconductivity in nonadiabatic systems with an "extended" singularity in the electron energy spectrum

M. E. Palistrant*

Institute of Applied Physics of the Academy of Sciences of Moldova, Academy St. 5, Cishinau 2028, Moldova

(Submitted July 12, 2004)
Fiz. Nizk. Temp. **31**, 500–506 (May 2005)

An equation for determining the superconducting transition temperature T_c is obtained in the linear approximation in the nonadiabaticity for a system with a square-root singularity in the electron density of states. The vertex function is calculated and analytical expressions are obtained for T_c in the limiting cases $T_c \ll \mu_1$ and $\mu_1 = 0$ (μ_1 is the singular point) and also an expression for the coefficient of the isotope effect. It is shown that the contribution of nonadiabatic effects to T_c is significant and decreases on approach to the singular point $\mu_1 = 0$, and the smallness of the isotope effect is due to the presence of such a singularity in the electron energy spectrum and the nonadiabaticity of the system. © *2005 American Institute of Physics.* [DOI: 10.1063/1.1925348]

1. INTRODUCTION

Materials with high-temperature superconducting properties (oxide ceramics, fullerenes, organic compounds) are very complex systems. They have a rich set of properties, the consistent consideration and understanding of which will help reveal the answer to the central question of the mechanism of high-temperature superconductivity. Many properties inherent to these materials have now been discovered—in particular, the singularity in the electron energy spectrum that promotes the elevation of the superconducting transition temperature T_c.

Experimental studies[1] of the electronic structure of $YBa_2Cu_3O_{6.9}$ and $YBa_2Cu_4O_8$ reveal the presence of an "extended" saddle-point singularity in the band corresponding to the CuO_2 plane. A simple model for the formation of this singular point was proposed in Ref. 1. Under certain conditions imposed on the parameters of the theory, one can obtain a one-dimensional electron density of states, which diverges as the square-root of the energy:

$$N(\varepsilon) = N_0 \sqrt{\frac{E}{\varepsilon - \varepsilon_0}}, \tag{1}$$

where E is a quantity of the order of the electron energy, and ε_0 is the singular point. The presence of an "extended" singularity makes it possible to reach high T_c independently of the mechanism of superconductivity (phonon or nonphonon). Abrikosov[1,2] constructed a theory based on the BCS-Migdal model, which is applicable for describing superconductivity in metals. For them $\varepsilon_F \gg \omega_0$ (ε_F is the Fermi energy and ω_0 is a characteristic phonon frequency). However, the yttrium compounds in which the above singularity is observed are nonadiabatic systems. This inequality does not hold in them, but instead $\varepsilon_F \sim \omega_0$. In this case the Migdal theorem[3] is violated and it is necessary to construct a theory of superconductivity for systems with an "extended" singularity, going beyond the framework of the Migdal theorem and taking into account additional many-particle processes. The technique for taking such processes into account, proposed, e.g., in Refs. 4 and 5, has since been used by us to study the thermodynamic properties of nonadiabatic superconductors with a variable density of charge carriers in clean[6,7] and dirty[8,9] systems. The studies reported in those papers showed that effects due to nonadiabaticity of the system and to strong electron correlations promote the formation of superconductivity at high temperatures. In systems with a magnetic impurity they delay the decline of T_c with increasing impurity concentration and increase the region of the gapless state and the coexistence region of superconductivity and ferromagnetism. They have a substantial influence on the crossover from the scenario of BCS superconductivity to Bose condensation of local pairs (the Schaffroth scenario) in the region of low charge carrier densities.[6]

The goal of the present study is to construct a theory of superconductivity for systems with inherent nonadiabaticity ($\varepsilon_F \sim \omega_0$ or $\varepsilon \ll \omega_0$) which have an "extended" singularity in the energy spectrum, i.e., a one-dimensional electron density of states (1). Such properties are possessed, in particular, by the yttrium ceramics mentioned above.

This paper is arranged as follows. In Sec. 2 we give the basic definitions, write expressions for the mass operators and Green's functions (normal and anomalous) in the approximation linear in the nonadiabaticity, and calculate the vertex function. In Sec. 3 we obtain an equation for determining the superconducting transition temperature in the weak-coupling approximation ($T_c \ll \omega_0$) and find analytical solutions in two limiting cases. In Sec. 4 we give an expression for the coefficient of the isotope effect, α. In the last Section we present numerical solutions of the equation determining T_c at all possible values of the parameter μ_1/ω_0. The coefficient α is also calculated, and the results obtained are analyzed.

2. BASIC OPERATIONS. VERTEX FUNCTIONS

We start from a Hamiltonian describing an electron-phonon system and use perturbation theory[10] to determine

the Matsubara Green's functions (normal and anomalous). The perturbation series for the self-energy operators (diagonal $\Sigma_N(\mathbf{p}\Omega)$ and nondiagonal $\Sigma_S(\mathbf{p}\Omega)$) takes into account the diagrams in all orders of perturbation theory in the electron-phonon interaction, as is done in the case of adiabatic systems, and additional diagrams containing vertex corrections and corresponding to the crossing of two electron-phonon interaction lines. A justification for this approximation is given in Refs. 4 and 5 (see also Refs. 6 and 7). Thus we obtain for the mass operators Σ_N and Σ_S

$$\Sigma_N(\mathbf{p}\Omega)=\frac{1}{\beta V}\sum_{\mathbf{p}_1\Omega_1} V_N(pp_1)G(\mathbf{p}_1\Omega_1), \tag{2}$$

$$\Sigma_S(\mathbf{p}\Omega)=\frac{1}{\beta V}\sum_{\mathbf{p}_1\Omega_1} V_S(pp_1)F(\mathbf{p}_1\Omega_1), \tag{3}$$

where

$$V_N(pp_1)=-g^2D(\Omega-\Omega_1)[1+\lambda_0P_V(\mathbf{pp}_1\Omega\Omega_1)], \tag{4}$$

$$V_S(\mathbf{pp}_1)=-g^2D(\Omega-\Omega_1)[1+2\lambda_0P_V(\mathbf{pp}_1\Omega\Omega_1) +\lambda_0P_C(\mathbf{pp}_1\Omega\Omega_1)]. \tag{5}$$

Here $D(\Omega-\Omega_1)$ corresponds to the phonon Green's function

$$D(\omega)=-\frac{\omega_0^2}{\omega^2+\omega_0^2}, \tag{6}$$

g^2 is the electron-phonon interaction constant, $\lambda_0=N_0g^2$, and P_V and P_C are the vertex and crossing functions, respectively:

$$P_V(\mathbf{pp}_1\Omega\Omega_1)=-\frac{g^2}{\beta V}\sum_{\mathbf{p}_2\Omega_2} D(\Omega-\Omega_2)G(\mathbf{p}_2\Omega_2) \times G(\mathbf{p}_1+\mathbf{p}_2-\mathbf{p},\quad \Omega_1+\Omega_2-\Omega),$$

$$P_C(\mathbf{pp}_1\Omega\Omega_1)=-\frac{g^2}{\beta V}\sum_{\mathbf{p}_2\Omega_2} D(\Omega-\Omega_2)G(\mathbf{p}_2\Omega_2) \times G(\mathbf{p}_2-\mathbf{p}-\mathbf{p}_1,\quad \Omega_2-\Omega-\Omega_1). \tag{7}$$

We shall henceforth consider a temperature region close to the critical temperature T_c. In this case for the functions G and F we can limit consideration to the expressions

$$G(\mathbf{p}\Omega)=\frac{1}{Zi\Omega-\tilde{\varepsilon}_p},\quad F(\mathbf{p}\Omega)=\frac{\Sigma_S(\Omega)}{Z^2\Omega^2-\tilde{\varepsilon}_p^2}, \tag{8}$$

where

$$Z=1-\lim_{\Omega\to0}\frac{1}{\Omega}\operatorname{Im}\Sigma_N(\Omega);\quad \tilde{\varepsilon}_p=\varepsilon_p+\operatorname{Re}\Sigma_N(0); \tag{9}$$

$$\Sigma_N(\Omega)=\Sigma_N(\mathbf{p}_F\Omega);\quad \Sigma_S(0)=\Sigma_S(\mathbf{p}_F0).$$

We note that expressions (2) and (3) contain the total Green's functions with the electron-phonon interaction taken into account in all orders of perturbation theory. The approximation consists in taking into account only the approximation linear in the nonadiabaticity, which corresponds to keeping diagrams with an intersection of two electron-phonon interaction lines (the presence of the vertex function P_V and crossing function P_C in Eqs. (4) and (5)). This allows one in calculating functions P_V and P_C to use the Green's function (8), setting in it $Z=1$ and $\tilde{\varepsilon}_p=\varepsilon_p$. As in the previous papers,[6–9] here we perform the summation over Ω_2 in expressions (7) in the weak-coupling approximation ($T_c\ll\omega_0$), which is equivalent to integration over frequency at $T=0$. We then pass from a summation over $\mathbf{p}_2$ to integration over energy in accordance with the presence of an "extended" singularity in the system[1]

$$\frac{1}{V}\sum_{\mathbf{p}_2}\cdots\to\int_0^W N(\xi_{p_2})d\xi_{p_2}=\int_{-\mu_1}^{W-\mu_1}N(\varepsilon_{p_2}+\mu)d\varepsilon_{p_2}. \tag{10}$$

Here the electron density of states $N(\varepsilon)$ is given by relation (1). We use the method of direct evaluation, analogous to the calculations done in Refs. 3–6. Because of the one-dimensional dispersion relation for the energy of the electrons and their "forward" scattering, we have $\mathbf{p}\to p_x\sim p_{1x}\sim p_{2x}=p_F$, which makes it possible to replace $\varepsilon_{\mathbf{p}_2-\mathbf{p}+\mathbf{p}_1}$ and $\varepsilon_{\mathbf{p}_2-\mathbf{p}-\mathbf{p}_1}$ by $\varepsilon_{\mathbf{p}_2}$. This substitution simplifies the calculation substantially in comparison with three-dimensional and two-dimensional systems,[6–9] since in this case there is no integration over angle variables.

We obtain

$$\operatorname{Re}P_V(0\Omega_1)=\operatorname{Re}P_C(0\Omega_1)=\frac{\omega_0\sqrt{E}}{2\Omega_1}[\varphi_++\varphi_-], \tag{11}$$

where

$$\varphi_+=\frac{A_+}{A_+^2+B_+^2}\left[\arctan\frac{B_+}{A_+-\sqrt{\mu_1}}-\arctan\frac{B_+}{\sqrt{\mu_1}+A_+}\right] -\frac{B_+}{A_+^2+B_+^2}\frac{1}{2}\ln\frac{(A_+-\sqrt{\mu_1})^2+B_+^2}{(A_++\sqrt{\mu_1})^2+B_+^2},$$

$$\varphi_-=\frac{B_-}{A_-^2+B_-^2}\left[\frac{1}{2}\ln\frac{(W^{1/2}+A_-)^2+B_-^2}{(W^{1/2}-A_-)^2+B_-^2} -\frac{1}{2}\ln\frac{(\sqrt{\mu_1}+A_-)^2+B_-^2}{(\sqrt{\mu_1}-A_-)^2+B_-^2}\right]-\frac{A_-}{A_-^2+B_-^2} \times\left[\arctan\frac{B_-}{W^{1/2}-A_-}+\arctan\frac{B_-}{W^{1/2}+A_-} -\arctan\frac{B_-}{\sqrt{\mu_1}+A_-}+\arctan\frac{B_-}{A_--\sqrt{\mu_1}} -\pi\Theta(A_--\sqrt{\mu_1})\right]. \tag{12}$$

The quantities $A_\pm$ and $B_\pm$ are given by the expressions

$$A_\pm=\frac{1}{\sqrt{2}}[\sqrt{(\mu_1\pm\omega_0)^2+\Omega_1^2}+(\mu_1\pm\omega_0)]^{1/2},$$

$$B_\pm=\frac{\operatorname{sgn}\Omega_1}{\sqrt{2}}[\sqrt{(\omega_0\pm\mu_1)^2+\Omega_1^2}-(\mu_1\pm\omega_0)]^{1/2}. \tag{13}$$

It is easy to see on the basis of formulas (11)–(31) that the relation $\operatorname{Re}P_V(0\Omega_1)=\operatorname{Re}P_V(0-\Omega_1)$. Here we have not given

the expression for $\mathrm{Im}\,P_V(0\Omega_1)$. We note, however, that $\mathrm{Im}\,P_V(0\Omega_1)=-\mathrm{Im}\,P_V(0-\Omega_1)$. This circumstance allows us to avoid considering this expression below, since it does not contribute to the self-energy equations (2), (3). We substitute definitions (4), (6), and (8) into Eq. (2) and perform the summation over Ω_1 in the standard way, replacing it by integration at $T=0$. We then go over to integration over the energy ε_{p_1}, using the two-dimensional electron density of states (1).

As a result of these calculations we obtain

$$\lim_{\Omega\to 0}\frac{1}{\Omega}\mathrm{Im}\sim\Sigma_N(\Omega)=-\frac{\omega_0\sqrt{E}\lambda_z^0}{2}\left\{-\frac{\sqrt{W}}{(\mu_1-\omega_0)(W-\mu_1+\omega_0)}+\frac{\sqrt{\mu_1}}{\omega_0}\left(\frac{1}{\mu_1+\omega_0}+\frac{1}{\mu_1-\omega_0}\right)-\frac{1}{2(\mu_1+\omega_0)^{3/2}}\ln\frac{\sqrt{\mu_1+\omega_0}-\sqrt{\mu_1}}{\sqrt{\mu_1+\omega_0}+\sqrt{\mu_1}}-\frac{1}{2}\frac{1}{(\mu_1-\omega_0)^{3/2}}\left[\ln\frac{\sqrt{W}-\sqrt{\mu_1-\omega_0}}{\sqrt{W}+\sqrt{\mu_1-\omega_0}}-\ln\frac{\sqrt{\mu_1}-\sqrt{\mu_1-\omega_0}}{\sqrt{\mu_1}+\sqrt{\mu_1-\omega_0}}\right]\Theta(\mu_1-\omega_0)+\frac{1}{(\omega_0-\mu_1)^{3/2}}\left[\arctan\sqrt{\frac{W}{\omega_0-\mu_1}}-\arctan\sqrt{\frac{\mu_1}{\omega_0-\mu_1}}\right]\Theta(\omega_0-\mu_1)\right\},\tag{14}$$

$$\mathrm{Re}\,\Sigma_N(0)=-\frac{\lambda_z^0\omega_0\sqrt{E}}{2}\left\{\frac{1}{\sqrt{\mu_1-\omega_0}}\left[\ln\frac{\sqrt{W}-\sqrt{\mu_1-\omega_0}}{\sqrt{W}+\sqrt{\mu_1-\omega_0}}-\ln\frac{\sqrt{\mu_1}-\sqrt{\mu_1-\omega_0}}{\sqrt{\mu_1}+\sqrt{\mu_1-\omega_0}}\right]\Theta(\mu_1-\omega_0)+\frac{2}{\sqrt{\omega_0-\mu_1}}\left[\arctan\sqrt{\frac{W}{\omega_0-\mu_1}}-\arctan\sqrt{\frac{\mu_1}{\omega_0-\mu_1}}\right]\Theta(\omega_0-\mu_1)+\frac{1}{\sqrt{\mu_1+\omega_0}}\ln\frac{\sqrt{\mu_1+\omega_0}-\sqrt{\mu_1}}{\sqrt{\mu_1+\omega_0}+\sqrt{\mu_1}}\right\},\tag{15}$$

where

$$\lambda_z^0=\lambda_0[1+\lambda_0 P_V(0\omega_0)],\tag{16}$$

and $\Theta(x)=1$ for $x>0$ and 0 for $x<0$.

3. SUPERCONDUCTING TRANSITION TEMPERATURE

We start from the expression for the mass operator Σ_S (3), substitute definitions (4) and (8) into that formula, and take the expression P_V out from under the summation over Ω_1 at the points $\Omega=0$, $\Omega_1=\omega_0$ (Refs. 4 and 5). We then use the approximation that is used in the theory of superconductivity with electron-phonon interaction:[11,12]

$$\frac{\omega_0^2}{(\Omega-\Omega_1)^2+\omega_0^2}\to\frac{\omega_0^2}{\Omega^2+\omega_0^2}\frac{\omega_0^2}{\Omega_1^2+\omega_0^2}.\tag{17}$$

These operation lead to the expression

$$\Sigma_S(\Omega)=\lambda_\Delta^0\frac{\omega_0^2}{\Omega^2+\omega_0^2}\frac{1}{\beta V}\sum_{\mathbf{p}_1\Omega_1}\frac{\omega_0^2}{\Omega_1^2+\omega_0^2}\frac{\Sigma_S(\Omega_1)}{\tilde{\varepsilon}_{p_1}^2+\Omega_1^2+\Omega_1^2Z^2},\tag{18}$$

where

$$\lambda_\Delta^0=\lambda_0[1+3\lambda_0 P_V(0\omega_0)].\tag{19}$$

We write Eq. (18) in the form

$$\Sigma_S(\Omega)=\lambda_\Delta^0\frac{\omega_0^2}{\Omega^2+\omega_0^2}A.\tag{20}$$

Substituting (17) and (20) into (18) and using formula (1), we obtain equations for determining the superconducting transition temperature in a nonadiabatic system with an ''extended'' singularity in the energy spectrum:

$$1=\lambda_\Delta^0\int_{-\mu_1}^{W-\mu_1}d\varepsilon_{p_1}\frac{\sqrt{E}}{\sqrt{\varepsilon_{p_1}+\mu_1}}\frac{1}{\beta}\sum_{\Omega_1}\frac{\omega_0^2}{(\Omega_1^2+\omega_0^2)}\times\left[1-\frac{\Omega_1^2}{\Omega_1^2+\omega_0^2}\right]\frac{1}{\tilde{\varepsilon}_{p_1}^2+Z^2\Omega_1^2}.\tag{21}$$

We do the summation over Ω_1 in (21) in the standard way. Changing from the sum to an integral, we obtain the expression

$$\frac{Z}{\lambda_\Delta^0}=\frac{\omega_0}{2}\int_{-\bar{\mu}_1}^{\bar{W}-\bar{\mu}_1}\frac{\sqrt{E}d\bar{\varepsilon}_{p_1}}{\sqrt{Z\bar{\varepsilon}_{p_1}+\tilde{\mu}_1}}\times\left[-\frac{\omega_0\tanh\dfrac{\beta_c\bar{\varepsilon}_{p_1}}{2}}{\bar{\varepsilon}_{p_1}}+1\right]\frac{1}{\bar{\varepsilon}_{p_1}^2-\omega_0^2}-\frac{\omega_0}{4}\int_{-\bar{\mu}_1}^{\bar{W}-\bar{\mu}_1}\frac{\sqrt{E}d\bar{\varepsilon}_{p_1}}{\sqrt{Z\bar{\varepsilon}_{p_1}+\tilde{\mu}_1}}\frac{1}{(\omega_0+|\bar{\varepsilon}_{p_1}|)^2},\tag{22}$$

where $\bar{\varepsilon}_{p_1}=\varepsilon_{p_1}/Z$, $\bar{W}=W/Z$, and $\bar{\mu}_1=\tilde{\mu}_1/Z$.

We set $T_c=0$ in all terms in (22) except the one containing the logarithmic singularity with respect to that quantity. Such an approximation is valid in the weak-coupling approximation ($T_c\ll\omega_0$). After doing the integration over energy in the terms not containing T_c, we bring Eq. (22) to the form

$$\frac{Z}{\lambda_\Delta^0}\sqrt{\frac{\mu_1}{E}}=\frac{\sqrt{\mu_1}}{2}\int_{-\bar{\mu}_1}^{\bar{W}-\bar{\mu}_1}\bar{\varepsilon}_{p_1}\frac{d\bar{\varepsilon}_{p_1}\tanh\dfrac{\beta_c\bar{\varepsilon}_{p_1}}{2}}{\sqrt{Z\bar{\varepsilon}_{p_1}+\tilde{\mu}_1}}-\Phi(\omega_0\tilde{\mu}_1W),\tag{23}$$

$$\Phi(\omega_0\mu_1 W)=+\frac{1}{4}\left[\frac{\tilde{\mu}_1}{\tilde{\mu}_1+Z\omega_0}+\frac{\tilde{\mu}_1}{\tilde{\mu}_1-Z\omega_0}\right]-\frac{\omega_0\sqrt{W\tilde{\mu}_1}}{4(\omega_0+\overline{W}-\tilde{\mu}_1)(\tilde{\mu}_1-Z\omega_0)}+\frac{1}{2}\left[1+\frac{Z\omega_0}{4(\tilde{\mu}_1+Z\omega_0)}\right]\times I_1+\frac{1}{2}\left[1-\frac{Z\omega_0}{4(\tilde{\mu}_1-Z\omega_0)}\right]I_2, \tag{24}$$

$$I_1=-\frac{\sqrt{\tilde{\mu}_1}}{\sqrt{\tilde{\mu}_1+Z\omega_0}}\ln\frac{-\sqrt{\tilde{\mu}_1}+\sqrt{\tilde{\mu}_1+Z\omega_0}}{\sqrt{\tilde{\mu}_1+Z\omega_0}+\sqrt{\tilde{\mu}_1}},$$

$$I_2=-\frac{\sqrt{\tilde{\mu}_1}}{\sqrt{\tilde{\mu}_1-Z\omega_0}}\left[\ln\frac{\sqrt{W}-\sqrt{\tilde{\mu}_1-Z\omega_0}}{\sqrt{W}+\sqrt{\tilde{\mu}_1-Z\omega_0}}-\ln\frac{\sqrt{\tilde{\mu}_1}-\sqrt{\tilde{\mu}_1-Z\omega_0}}{\sqrt{\tilde{\mu}_1}+\sqrt{\tilde{\mu}_1-Z\omega_0}}\right]\Theta(\tilde{\mu}_1-Z\omega_0)+\frac{2\sqrt{\tilde{\mu}_1}}{\sqrt{Z\omega_0-\tilde{\mu}_1}}\left[\arctan\sqrt{\frac{W}{Z\omega_0-\tilde{\mu}_1}}-\arctan\frac{\sqrt{\tilde{\mu}_1}}{\sqrt{Z\omega_0-\tilde{\mu}_1}}\right]\Theta(Z\omega_0-\tilde{\mu}_1). \tag{25}$$

An analytical expression for T_c can be obtained from (23) in two limiting cases, namely, $\overline{W}$, $\overline{\mu_1}\gg T_c$, and at the singular point $\mu_1=0$.

After separating out the logarithmic singularity with respect to T_c in (23) for W, $\mu_1\gg T_c$, we obtain

$$T_c=\frac{8\overline{\mu_1}\gamma}{\pi}\left[\frac{\sqrt{\overline{W}}-\sqrt{\tilde{\mu}_1}}{\sqrt{\overline{W}}+\sqrt{\tilde{\mu}_1}}\right]^{1/2}\times\exp\left\{-Z/\lambda_D^0\sqrt{\frac{\tilde{\mu}_1}{E}}-\Phi(\omega_0\tilde{\mu}_1 W)\right\}. \tag{26}$$

At the point $\mu_1=0$ we obtain from (23)

$$T_c=\frac{A^2}{2Z_0}\left[\frac{Z_0}{\lambda^0_{\Delta_0}\sqrt{E}}+\frac{1}{\sqrt{W}}+\frac{\sqrt{W}}{4(Z_0\omega_0+W)}+\frac{5}{4}\frac{1}{\sqrt{\omega_0 Z_0}}\arctan\sqrt{\frac{W}{Z_0\omega_0}}\right]^{-2}, \tag{27}$$

where

$$A=\int_0^\infty\frac{dx}{\sqrt{x}\cosh^2 x}=1.906;\quad Z_0=Z|_{\mu_1=0};$$

$$\lambda^0_{\Delta_0}=\lambda^0_\Delta|_{\mu_1=0}.$$

In the limit $W\to\infty$, $P_V=0$, $\omega_0\to\infty$ we obtain from (26) and (27) the following expressions at $T_c\ll\mu_1$ and $\mu_1=0$:

$$T_{c_0}=\frac{8\mu_1\gamma}{\pi}\exp(-1/\lambda_0\sqrt{\mu_1/E}), \tag{28}$$

$$T^0_{c_0}=\frac{A^2}{2}\lambda_0^2 E. \tag{29}$$

These formulas correspond to the case of an adiabatic system with an ''extended'' singularity in the energy spectrum without allowance for retardation and corresponds to the results of Ref. 1.

From a comparison of Eq. (26) with (28) and Eq. (27) with (29) it can be concluded that in a nonadiabatic system, as in an adiabatic one, T_c increases with decreasing chemical potential (as it approaches the singular point ε_0). A renormalization of the parameters of the theory takes place on account of effects of nonadiabaticity, and an additional term, $\Phi(\omega_0\tilde{\mu}_1 W)$, also appears in the exponent on the right-hand side of (26) on account of retardation.

4. ISOTOPE EFFECT

The coefficient of the isotope effect is determined by the relation

$$\alpha=-\partial\ln T_c/\partial\ln M, \tag{30}$$

where M is the mean ionic mass. In ordinary superconductors with an electron-phonon mechanism of superconductivity one has $\alpha=1/2$.

The presence of van Hove singularities in the electron density of states leads to a significant increase of this coefficient.[2,12] This decrease is explained by the replacement of the Debye frequency, which cuts off the electron-phonon interaction, by a certain electron energy that is independent of the mass of the ion. Furthermore, the coefficient α falls off with increasing Migdal parameter ($m=\omega_0/\varepsilon_F$) and can reach small values[5–7] in nonadiabatic systems.

In this Section we determine the joint influence of the extended singularity in the electron density of states and of nonadiabaticity effects on the isotopic coefficient α. We consider the case $\mu_1\gg T_c$ starting from the expression for the superconducting transition temperature (26). For simplicity we set $W\to\infty$, $\overline{\mu_1}\approx\mu_1$ and introduce the variable $x=\omega_0/\mu_1$. We obtain

$$\alpha(x)=\frac{1}{2}\frac{\partial\ln T_c}{\partial\ln x}=\frac{1}{2}x\frac{\partial\ln T_c}{\partial x}, \tag{31}$$

where

$$\frac{\partial\ln T_c}{\partial x}=-\left[\frac{1}{Z}+\sqrt{\frac{\mu_1}{E}}\frac{1}{\lambda^0_\Delta}\right]\frac{\partial Z}{\partial x}+\sqrt{\frac{\mu_1}{E}}\frac{Z}{{\lambda^0_\Delta}^2}\frac{\partial\lambda^0_\Delta}{\partial x}-\frac{\partial}{\partial x}\Phi(\omega_0\mu_1\infty), \tag{32}$$

$$Z=1+\lambda_z^0 f_z,\quad \frac{\partial Z}{\partial x}=\lambda_0^2 f_z\frac{\partial P_V}{\partial x}+\lambda_z^0\frac{\partial f_z}{\partial x},$$

$$\frac{\partial\lambda^0_\Delta}{\partial x}=3\lambda_0^2\frac{\partial P_V}{\partial x}, \tag{33}$$

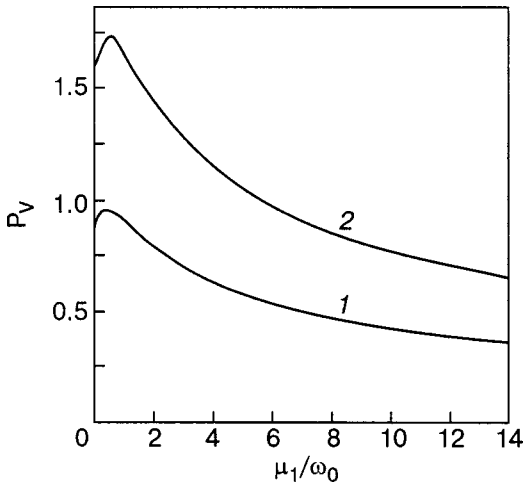

FIG. 1. Dependence of the vertex function P_V on the ratio μ_1/ω_0 at values of $E/\omega_0=3$ (*1*) and 10 (*2*).

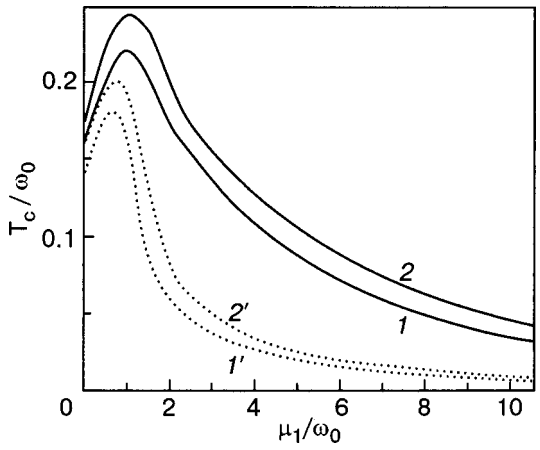

FIG. 2. Dependence of the critical temperature T_c on the parameter μ_1/ω_0: $E/\omega_0=3$, $\lambda_0=0.5$ (*1*) and (*1′*); $E/\omega_0=10$, $\lambda_0=0.3$ (*2*) and (*2′*). The solid curves correspond to a nonadiabatic and the dotted curves to an adiabatic system.

$$f_z=f_z^{(1)}+f_z^{(2)},$$

$$f_z^{(1)}=\frac{1}{2}\sqrt{\frac{E}{\mu_1}}\left\{\frac{1}{1+x}+\frac{1}{1-x}-\frac{x}{2(x+1)^{3/2}}\ln\frac{\sqrt{1+x}-1}{\sqrt{1+x}+1}\right\},$$

$$f_z^{(2)}=\frac{1}{2}\sqrt{\frac{E}{\mu_1}}\frac{x}{2(1-x)^{3/2}}\ln\frac{1-\sqrt{1-x}}{1+\sqrt{1-x}}\Theta(1-x)+\frac{1}{2}\sqrt{\frac{E}{\mu_1}}\frac{x}{2(x-1)^{3/2}}\times\left[\frac{\pi}{2}-\arctan\sqrt{\frac{1}{x-1}}\right]\Theta(x-1). \quad (34)$$

The quantities λ_z^0, λ_Δ^0, P_V, and Φ are given by formulas (16), (19), (11), and (24), respectively.

5. ANALYSIS OF THE RESULTS

The presence of a square-root singularity in the electron density of states (1) due to the two-dimensional dispersion relation for the electron energy plays a dual role in the formation of superconductivity in nonadiabatic systems at high temperatures. First, this singularity in itself leads to a high T_c near the singular point $\mu_1=0$. Second, because of the two-dimensional motion of the electrons and their ''forward'' scattering the momentum transfer in the electron-phonon interaction is small. This circumstance leads to a large positive value of the vertex function and hence a significant increase of the electron-phonon interaction constant and superconducting transition temperature T_c.

Figure 1 shows the vertex function P_V (11) versus the ratio μ_1/ω_0 for different values of the ratio of E to ω_0. As is seen from the figure, near the point $\mu_1=0$ the function P_V reaches a maximum, making for an increase of the parameters λ_z (16) and λ_Δ (19).

The solution of Eq. (23) for the superconducting transition temperature T_c is plotted as a function of μ_1/ω_0 in Fig. 2. The analytical formulas (26) and (27) were also used in the calculations. The maximum value of T_c both in the case of a nonadiabatic system (curves *1* and *2*) and adiabatic (curves *1′* and *2′*) is reached at $\mu_1\approx\omega_0$ and not at the point $\mu_1=0$, as is stated in Ref. 1. The cause of such behavior is easily seen from Eq. (22). In particular, at $W\to\infty$ the value of the lower limit of integration on the right-hand side of this equation decreases with decreasing μ_1, while the integrand increases. The competition between these two factors leads to a shift of the maximum of T_c to the right in relation to the singular point $\mu_1=0$.

In our opinion, in a nonadiabatic system the electron energy E cannot be significantly larger than the phonon energy ω_0, as happens in ordinary superconductors, and, hence, values of $T_c\sim 100$ K and higher can be achieved at small values of λ_0 if both effects are taken into account: the presence of a singular point in momentum space, which leads to a square-root singularity in the electron density of states, and the nonadiabaticity effects, which violate the Migdal theorem ($P_V>0$).

The contribution of nonadiabaticity to the value of T_c depends largely on the parameters of the theory and is substantial at all values of the ratio μ_1/ω_0, increasing with distance from the singular point $\mu_1=0$. As is seen in Fig. 1, in the nonadiabatic systems under consideration it is easy to reach values of T_c characteristic of materials with high-temperature superconductivity. We note that the solutions we have obtained are underestimated because of the factorization of the phonon Green's function (see approximation (17)). In systems with a constant electron density of states the value of T_c is lowered on account of the use of approximation (17) by a factor of $e_0^{-1/2}$ (where e_0 is the base of natural logarithms).[4,6,14] In our case for a system with a square-root singularity in the electron density of states the corresponding factor is on average equal to 0.45.

Figure 3 shows the dependence of the isotope-effect coefficient α on the ratio ω_0/μ_1 obtained on the basis of the above formulas (31)–(34). One observes a substantial decrease of the isotope effect as the singular point $\mu_1=0$ is approached (in adiabatic systems, curves *1′* and *2′*). The

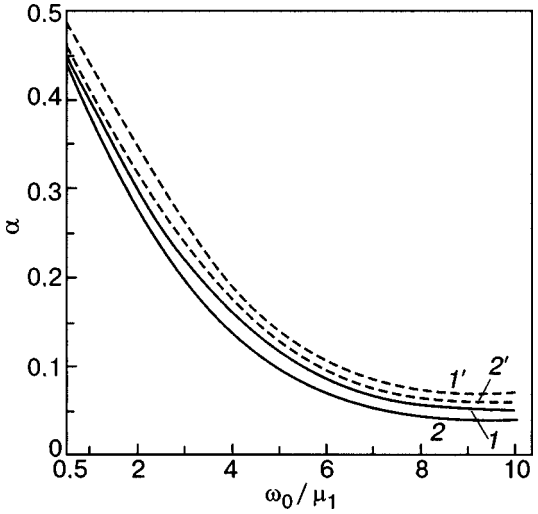

FIG. 3. Dependence of the isotopic coefficient on ω_0/μ_1: $E/\omega_0=3$, $\lambda_0=0.5$ (*1*) and (*1′*); $E/\omega_0=10$, $\lambda_0=0.3$ (*2*) and (*2′*). The solid curves correspond to a nonadiabatic and the dashed curves to an adiabatic system.

qualitative picture in this case agrees with the result of Ref. 1. Together with this an additional decrease arises due to the effect of nonadiabaticity (curves *1* and *2*).

Thus it can be assumed that the smallness of the isotope-effect coefficient in yttrium ceramics may be interpreted as a combined effect of the presence of an ''extended'' singularity in the electron energy spectrum and the nonadiabaticity of these systems.

The author is sincerely grateful to V. Ursu for assistance in the numerical calculations and to S. A. Palistrant for the layout of this paper.

*E-mail: statphys@asm.md

[1] A. A. Abrikosov, Y. C. Campuzano, and K. Gofron, Physica C **214**, 73 (1993).
[2] A. A. Abrikosov, Physica **238**, 191 (1994); Phys. Rev. B **51**, 11955 (1995); *ibid.* **52**, R15738 (1995); *ibid.* **53**, R8910 (1996).
[3] A. B. Migdal, Zh. Éksp. Teor. Fiz. **34**, 1438 (1958) [Sov. Phys. JETP **7**, 996 (1958)].
[4] L. Pietronero, S. Strassler, and C. Grimaldi, Phys. Rev. B **52**, 10516 (1995).
[5] C. Grimaldi, L. Pietronero, and S. Strassler, Phys. Rev. B **52**, 10530 (1995).
[6] M. E. Palistrant, Fiz. Nizk. Temp. **26**, 557 (2000) [Low Temp. Phys. **26**, 407 (2000)]; Fiz. Nizk. Temp. **29**, 1173 (2003). [Low Temp. Phys. **29**, 889 (2003)].
[7] M. E. Palistrant and F. G. Kochorbe, J. Phys.: Condens. Matter **12**, 2217 (2000).
[8] M. E. Palistrant, Teor. Mat. Fiz. **119**, 455 (1999); Fiz. Nizk. Temp. **28**, 157 (2002) [Low Temp. Phys. **28**, 109 (2002)]; Teor. Mat. Fiz. **135**, 137 (2003).
[9] M. E. Palistrant and F. G. Kochorbe, J. Supercond.: Incorporating Novel Magnetism **15**, 113 (2002); J. Phys.: Condens. Matter **15**, 3267 (2003); Int. J. Mod. Phys. B **17**, 2545 (2003).
[10] A. A. Abrikosov, L. P. Gor'kov, and I. E. Dzyaloshinskiĭ, *Methods of Quantum Field Theory in Statistical Physics*, Prentice-Hall, Englewood Cliffs, N.J. (1963), Nauka, Moscow (1962).
[11] W. L. McMillan, Phys. Rev. **167**, 331 (1968).
[12] D. E. Morris, R. M. Kuroda, A. G. Markelz, J. H. Nickel, and J. Y. T. Wei, Phys. Rev. B **37**, 5936 (1988).
[13] J. Labbe and J. Bok, Europhys. Lett. **3**, 1225 (1987).
[14] R. Combescot, Phys. Rev. B **42**, 7810 (1990).

Translated by Steve Torstveit

LOW-TEMPERATURE MAGNETISM

EPR spectrum and magnetic ordering of copper orotate

K. V. Kutko,* A. I. Kaplienko, and E. P. Nikolova

B. Verkin Institute for Low Temperature Physics and Engineering, National Academy of Sciences of Ukraine, pr. Lenina 47, Kharkov 61103, Ukraine

A. G. Anders

V. N. Karazin Kharkov National University, pl. Svobody 4, Kharkov 61077, Ukraine

O. V. Shishkin and R. I. Zubatuk

Institute of Scintillation Materials, NTK "Institute for Single Crystals" of the National Academy of Sciences of Ukraine, pr. Lenina 60, Kharkov 61001, Ukraine

(Submitted July 19, 2004; revised September 27, 2004)
Fiz. Nizk. Temp. **31**, 507–512 (May 2005)

An x-ray diffraction study and measurements of the EPR spectrum of a copper orotate single crystal $[Cu(C_5H_3N_2O_4)(H_2O)_2]$ are carried out. At room temperature a one-center EPR spectrum of orthorhombic symmetry is observed. The extremal values of the g factors are determined. Low-temperature broadening of the resonance lines is observed. It is assumed that it is due to the formation of short-range antiferromagnetic order, which arises when the temperature approaches the Néel point $T_N = 3.2$ K. © *2005 American Institute of Physics.* [DOI: 10.1063/1.1925349]

1. INTRODUCTION

Orotic acid is a precursor of the pyrimidine bases of nucleic acids in their biosynthesis. Bioconversion reactions of orotic acid occur in the presence of enzymes. Their activation and normal functioning require metal ions. For this reason a number of papers devoted to the interaction of metal ions with orotic acid and its derivatives have appeared in recent years.[1,2] Attention has been devoted mainly to the interrelation between the chemistry of the metal ions and their role in the life of organisms.

Copper orotate dihydrate $[Cu(C_5H_3N_2O_4)(H_2O)_2]$ belongs to the family of metalorganic substances which are accepted in medicine as compounds having enzymatic properties. To elucidate the general regularities of enzymatic reactions it is necessary to establish the equilibrium structures of the given metalorganic complexes. Here the most informative studies are of the EPR spectra of Cu^{2+} ions in these metalorganic compounds.

In this paper we report x-ray diffraction studies of a copper orotate dihydrate crystal and measurements of the angular and temperature dependences of the EPR spectra of Cu^{2+} ions in this crystal. In view of the weak coupling between the molecules of the complexes in the crystalline state, it can be assumed that the coordination of the Cu^{2+} ions in orotate crystals and in biological solution are only slightly different.[3] Therefore the spectra of the Cu^{2+} ions in a crystal and in a biological solution can be assumed similar.

The method of growth of the single-crystal samples of a complex of Cu^{2+} with orotic acid differs from the methods used in Refs. 1 and 2. In those studies $[Cu(Oro)(H_2O)_2]$ and $[Cu(Oro)_2(H_2O)_3]$ complexes were obtained either via methyl orotate (orotic acid methyl ester) or by boiling down a mixture of aqueous solutions of $CuCl_2$ and potassium orotate at room temperature. In our case the initial mixture of $CuCl_2$ solutions and potassium orotate were filtered off from a precipitate at room temperature and held at $T = 5$ °C for a week. The crystals obtained were quite perfect in shape, blue-green in color, and were in the form of elongated slabs with beveling of the opposite sides.

To refine the type of complex and the parameters of the local environment of Cu^{2+} we did an x-ray study of the crystals obtained.

2. X-RAY ANALYSIS OF COPPER OROTATE

An X-ray study of copper orotate (empirical formula $C_5H_6N_2O_6Cu$, molecular weight 253.66 a.u.) was done at room temperature on a Siemens P3/PC automatic diffractometer (Mo$K\alpha$ radiation, wavelength 0.71073 Å, graphite monochromator, $2\theta/\theta$ scanning, $2\theta_{max} = 60°$). The unit cell parameters were $a = 9.503(3)$ Å, $b = 6.915(2)$ Å, $c = 11.851(3)$ Å, $\beta = 95.22(2)°$, $V = 775.5(3)$ Å^3, space group $P2_1/n$, four formula units per unit cell, calculated density of the crystal 2.824 mm^{-1}, and linear coefficient of absorption for Mo$K\alpha$ 2.824 mm^{-1}.

The structure was solved by a direct method and refined with the SHELX97 software package.[4] The structure was refined according to the squares of the structure amplitudes F^2 by a full matrix least-squares method in the anisotropic approximation for the nonhydrogen and in the isotropic approximation for the hydrogen atoms. Absorption was taken into account empirically by the method of Ref. 5. The final divergence factors are $wR_2 = 0.074$ for 2194 reflections and

TABLE I. Relative coordinates ($\times 10^4$) and the equivalent isotropic thermal parameters U(eq) ($Å^2 \cdot 10^3$) of the nonhydrogen atoms, and the coordinates ($\times 103$) and isotropic thermal parameters U(eq) ($Å^2 \cdot 10^3$) of the hydrogen atoms in the copper orotate structure.

	x/a	y/b	z/c	U(eq)
Cu(1)	1510(1)	7113(1)	9022(1)	18(1)
O(1)	3610(1)	8548(2)	11276(1)	26(1)
O(2)	7826(2)	7147(3)	9995(1)	36(1)
O(3)	4079(1)	5043(2)	6879(1)	26(1)
O(4)	2138(1)	5949(2)	7658(1)	22(1)
O(5)	950(2)	8062(3)	10453(1)	36(1)
O(6)	−379(1)	6179(3)	8536(1)	31(1)
N(1)	5689(2)	7922(2)	10564(1)	19(1)
N(2)	3553(1)	7319(2)	9479(1)	16(1)
C(1)	4235(2)	7946(2)	10462(1)	17(1)
C(2)	6527(2)	7216(3)	9770(2)	21(1)
C(3)	5771(2)	6557(3)	8741(1)	20(1)
C(4)	4340(2)	6624(2)	8660(1)	15(1)
C(5)	3479(2)	5815(2)	7635(1)	18(1)
H(5OA)	230(3)	8530(4)	10670(3)	40(7)
H(5OB)	1620(5)	8160(5)	10880(3)	59(11)
H(6OA)	−960(3)	6280(5)	8930(3)	51(9)
H(6OB)	−640(3)	6190(4)	7800(2)	39(7)
H(1N)	6190(3)	8340(5)	11220(3)	47(8)
H(2)	6290(2)	6080(3)	8174(1)	16(5)

TABLE II. Bond lengths (Å) in the copper orotate structure.

Cu(1)–O(5)	1.937(2)
Cu(1)–O(6)	1.945(1)
Cu(1)–O(4)	1.947(1)
Cu(1)–N(2)	1.973(2)
Cu(1)–O(3)*	2.335(1)
O(1)–C(1)	1.250(2)
O(2)–C(2)	1.239(2)
O(3)–C(5)	1.227(2)
O(4)–C(5)	1.281(2)
N(1)–C(2)	1.376(2)
N(1)–C(1)	1.377(2)
N(2)–C(1)	1.352(2)
N(2)–C(4)	1.365(2)
C(2)–C(3)	1.432(2)
C(3)–C(4)	1.355(2)
C(4)–C(5)	1.509(2)

*Note:** The coordinates of the atom were obtained with the use of the symmetry operation $(-x+0.5,\ y+0.5,\ -z+1.5)$.

$R_1 = 0.028$ for 1897 reflections having absolute intensity greater than twice the error of its determination,[4] and the goodness of the least-squares fit $S = 1.049$. The coordinates of the atoms are listed in Table I, and the bond lengths and valence angles are presented in Tables II and III. The molecular structure of copper orotate and the structure with respect to the axes a, b, c are presented in Figs. 1 and 2, respectively.

Thus the structural parameters of our crystals agreed with the parameters of copper orotate used in Ref. 6.

The copper orotate crystal has polymer chains along a twofold translation axis (the (010) crystallographic direction) on account of the additional coordination of the copper atom. These chains are coupled to each other by stacking interactions between the pyrimidine cycles of the molecules [the symmetry operation $(1-x,\ 1-y,\ 2-z)$]. Because of these interactions the ligands form centrosymmetric dimers; the N(2) atom is located almost directly below the C(2) atom, and the planes of the aromatic cycles lie parallel to each other a distance 3.26 Å apart. In the crystal the polymer chains are also connected by a three-dimensional network of intermolecular hydrogen bonds: N(1)–H(1N)...O(4) $(0.5+x, 1.5-y, 0.5+z)$ (H...O 1.91 Å, N–H...O 172°), O(5)–H(5OA)...O(3) $(-0.5+x, 1.5-y, 0.5+z)$ (H...O 2.15 Å, O–H...O 158°), O(6)–H(6OA)...O(2) $(-1+x, y, z)$ (H...O 1.88 Å, O–H...O 170°), and O(6)–H(6OB)...O(1) $(-0.5+x, 1.5-y, -0.5+z)$ (H...O 1.88 Å, O–H...O 170°). Thus according to the x-ray diffraction data the local environment of the copper ion consists of five ligand atoms: an oxygen of the carboxyl group of the pyrimidine ring, the oxygen atoms of two molecules of the water of crystallization, the nitrogen atom N(2) of the pyrimidine heterocycle, and an oxygen atom of the carboxyl group of the adjacent pyrimidine ring.

3. EPR SPECTRUM OF COPPER OROTATE

The EPR spectra were investigated at room temperature on a JEOL type YES-ME-3x spectrometer ($\lambda = 3.2$ cm). The EPR spectra at low temperatures were obtained in the temperature interval 2–50 K with the use of a millimeter-wave spectrometer ($\lambda = 4$ mm). The external magnetic field was produced by a superconducting solenoid. The measurement error did not exceed 10^{-3} of the nominal value, and the uncertainty in temperature was not more than 0.1 K on the segment 2–5 K and not over 0.5 K for $T > 5$ K.

Because at room temperature the copper orotate crystal belongs to the monoclinic class with space group $C_{2h}^2 = P_{2_1}/n$ and contains four molecules per unit cell, so that the unit cell and primitive cell coincide, the local symmetry C_1 of the Cu^{2+} ions[7] results in the formation of two inversion-related pairs of copper ions in the unit cell. This last circumstance makes for the formation of two magnetically inequivalent copper-ion EPR centers in the unit cell, with a symmetric rotation of the principal axes of the spectroscopic splitting (g) tensors with respect to the C_2 axis (the b axis) of the crystal.

However, one center is observed in the EPR spectrum. This is apparently due to the smallness of the angle of rotation of the local axes of the two centers with respect to the C_2 axis of the crystal, so that at the rather significant width of the resonance line (~ 50 Oe at room temperature) the

TABLE III. Valence angles (degrees) in the copper orotate structure.

O(5)–Cu(1)–O(6)	93.03(7)	C(4)–N(2)–Cu(1)	111.7(1)
O(5)–Cu(1)–O(4)	174.78(7)	O(1)–C(1)–N(2)	123.2(1)
O(6)–Cu(1)–O(4)	87.76(6)	O(1)–C(1)–N(1)	118.7(2)
O(5)–Cu(1)–N(2)	94.41(7)	N(2)–C(1)–N(1)	118.1(1)
O(6)–Cu(1)–N(2)	164.59(6)	O(2)–C(2)–N(1)	119.5(2)
O(4)–Cu(1)–N(2)	83.65(6)	O(2)–C(2)–C(3)	125.7(2)
O(5)–Cu(1)–O(3)*	91.89(7)	N(1)–C(2)–C(3)	114.7(2)
O(6)–Cu(1)–O(3)*	88.63(6)	C(4)–C(3)–C(2)	118.2(2)
O(4)–Cu(1)–O(3)*	93.29(5)	C(3)–C(4)–N(2)	125.0(2)
N(2)–Cu(1)–O(3)*	104.57(5)	C(3)–C(4)–C(5)	120.8(1)
C(5)–O(3)–Cu(1)**	127.1(1)	N(2)–C(4)–C(5)	114.2(1)
C(5)–O(4)–Cu(1)	115.3(1)	O(3)–C(5)–O(4)	125.2(2)
C(2)–N(1)–C(1)	125.6(2)	O(3)–C(5)–C(4)	119.7(1)
C(1)–N(2)–C(4)	118.3(1)	O(4)–C(5)–C(4)	115.1(1)
C(1)–N(2)–Cu(1)	130.0(1)		

*Note:** The coordinates of the atom were obtained by applying the symmetry operation $(-x+0.5,\ y+0.5,\ -z+1.5)$.
** The coordinates of the atom were obtained by applying the symmetry operation $(-x+0.5,\ y-0.5,\ -z+1.5)$.

components of these centers could not be resolved in the angular dependence.

Thus a one-center spectrum of orthorhombic symmetry is observed in this compound; it is described by an effective Hamiltonian

$$\hat{H}=g\mu_B\mathbf{H}\hat{S}, \tag{1}$$

where μ_B is the Bohr magneton and **H** is the magnetic field.

It is known[8,9] that for a spin value of the Cu^{2+} ion $S=1/2$ (i.e., the absence of fine structure of the spectrum) the EPR spectrum should be described by Hamiltonian (1) in the case of a crystal-field symmetry not higher than orthorhombic. The difference between an orthorhombic spectrum and a monoclinic or triclinic one will consist in the orientation of the principal axes of the g-factor tensor—in the orthorhombic case these axes should coincide with the a, b, and c directions of the lattice, while in the monoclinic case only one of the axes coincides, and in the triclinic case none of them does. In the case of copper orotate the monoclinic angle is very close to $\pi/2$ and therefore the differences in the directions of the axes are also expected to be small.

For an orthorhombic Hamiltonian the angular dependence of the effective g factor should be described by the expression

$$g^2=g_z^2\cos^2\theta+g_x^2\sin^2\theta\cos^2\varphi+g_y^2\sin^2\theta\sin^2\varphi, \tag{2}$$

where θ is the angle between the external field and the monoclinic axis C_2, and φ lies in the basal plane (the b axis).

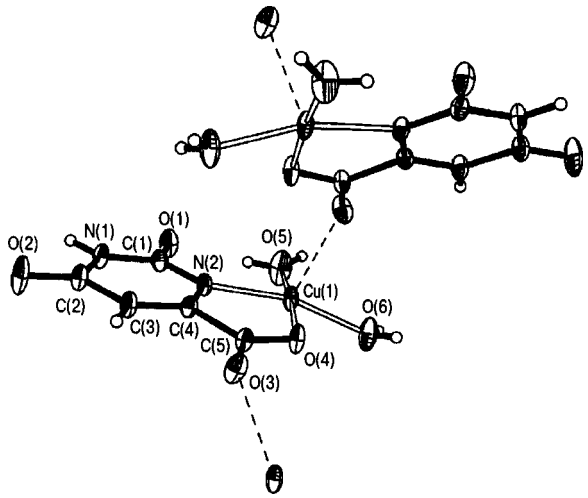

FIG. 1. Molecular structure of copper orotate according to the data of x-ray structural analysis. The ellipsoids of thermal vibrations of the nonhydrogen atoms are shown at the 50% probability level of their localization.

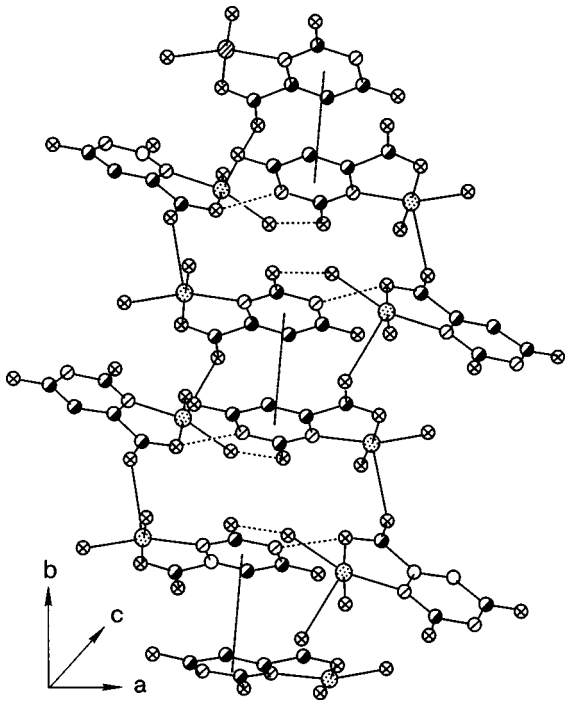

FIG. 2. Structure of copper orotate with respect to the axes a, b, c. The dotted lines indicate hydrogen bonds also the stacking interactions between pyrimidine rings.

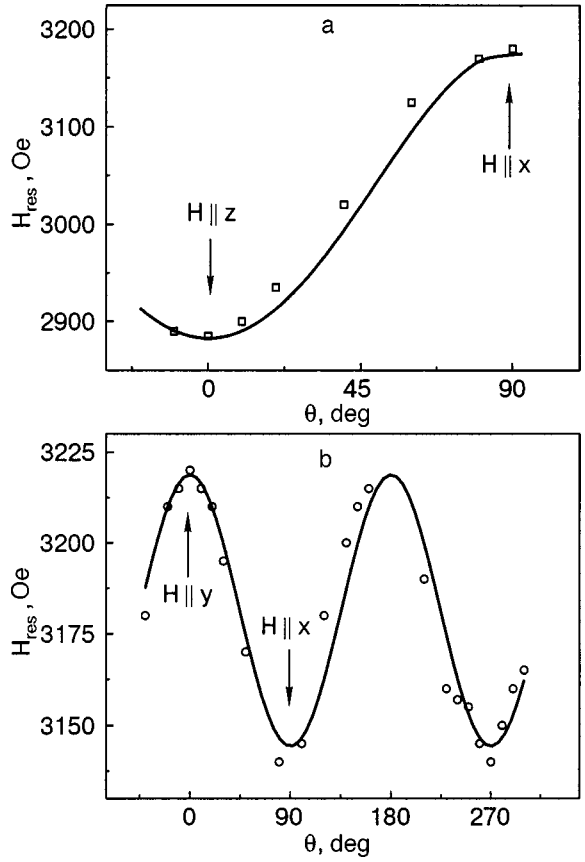

FIG. 3. Angular dependence of the EPR spectra in the ab (a) and ac (b) planes at room temperature ($\nu = 9.4$ GHz).

Figure 3 shows the angular dependences of the EPR spectra in the ab (a) and ac (b) planes at room temperature. The extremal values of the g factor are: $g_z = 2.32$, $g_x = 2.14$, and $g_y = 2.09$.

The relationship found among the parameters of the effective g factor correspond to a rhombically distorted octahedral environment of the divalent copper ion. It is known[8] that in the case of an ''elongated'' octahedron the orbital ground state of this ion is the Kramers doublet $|x^2-y^2\rangle$, characterized by angular distribution of the electron density in the equatorial plane with maxima in the directions of the ligand atoms. For this state the components of the effective g factor are expressed as

$$g_\parallel = 2 - 8\lambda/\Delta, \quad g_\perp = 2 - 2\lambda/\Delta, \tag{3}$$

where $g_\parallel = g_z$, $g_\perp = (g_x^2 \cos^2\varphi + g_y^2 \sin^2\varphi)^{1/2}$, λ is the parameter of the spin-orbit interaction (for a free ion $\lambda = -830$ cm^{-1}), and Δ is the parameter describing the splitting of the term by the cubic component of the crystal field. A typical value of the ratio $\lambda/\Delta = -0.05$,[8] and so the inequality $g_\parallel > g_\perp$ should hold, with $(g_\parallel - 2)/(g_\perp - 2) \approx 4$.

We see that the ratio of the components of the g factor corresponds to conditions in which the local octahedron is elongated in the direction of the b axis. The five-coordinated local environment of the Cu^{2+} ion in our case corresponds precisely to the extremal axial distortion of the octahedron.

With decreasing temperature the extremal directions and values of the effective g factor components are preserved, attesting to the absence of structural phase transitions in the system. At the same time, the resonance line is noticeably broadened at $T < 24$ K. This broadening may be due to critical fluctuations in the region of short-range magnetic order preceding the point T_N of the transition to the antiferromagnetically ordered state. On this temperature interval the linewidth can be written in the form[10]

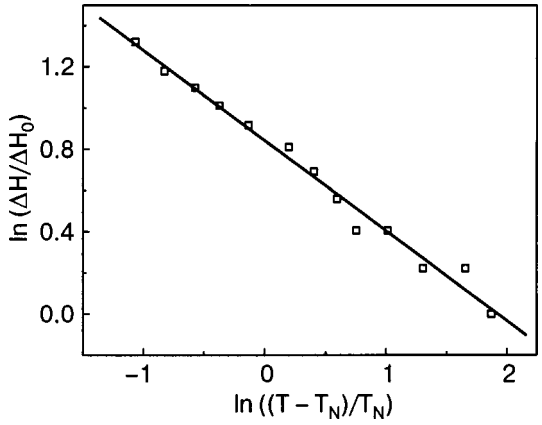

FIG. 4. Temperature dependence of the EPR linewidth in copper orotate ($\nu = 72.81$ GH, the ab plane). The points are the experimental data, the solid line is calculated according to relation (4). ΔH_0 is the resonance linewidth at $T = 24$ K.

$$\Delta H \sim (T - T_N)^{-n}. \tag{4}$$

The optimal description of the critical broadening process shown in Fig. 4 is obtained for $n = 0.44$, which is a typical value of the exponent for a three-dimensional magnetic system. The three-dimensional magnetic ordering attests to the absence of pronounced chains or planes of exchange-coupled copper ions in this crystal structure. A description of the experimentally obtained low-temperature broadening (Fig. 4) in accordance with Eq. (4) for all temperatures in the region $T < 24$ K yielded a value $T_N = 3.2 \pm 0.5$ K. A processing of the experimental results by the least-squares method was carried out for the whole range of critical broadening. The temperature 3.2 K corresponds to the minimum of the total rms deviation, and the error of determination of T_N is given for a 10% deviation of that quantity.

4. CONCLUSIONS

These studies have established the following.

The orbital ground state of the Cu^{2+} ion in copper orotate is $|x^2-y^2\rangle$. This state corresponds to the case of an elongated octahedron. The five-coordinated configuration of ligands in this compound can be regarded as a variant of an extremely elongated octahedron. Copper orotate is a three-dimensional low-temperature antiferromagnet with a Néel temperature $T_N = 3.2 \pm 0.5$ K.

*E-mail: kkutko@ilt.kharkov.ua

[1] T. B. Tam Ha, A. M. Larsonneur-Galibert, P. Castan, and J. Jaud, J. Chem. Cryst. **29**, 565 (1999).
[2] G. Maistralis, A. Koutsodimou, and N. Katsaros, Trans. Met. Chem. **25**, 166 (2000).
[3] N. N. Vlasova and N. K. Davidenko, Koord. Khimiya **9**, 1470 (1983).

[4] G. M. Sheldrick, *SHELX97. Programs for Crystal Structure Analysis (Release 97-2)*, University of Göttingen, Germany (1997).
[5] N. W. Alcock, *Crystallographic Computing*, F. R. Ahmed, S. R. Hall, and C. P. Huber (eds.), Munksgaard, Copenhagen (1970), p. 271.
[6] S. Parkin, B. Moezzi, and H. Hope, J. Appl. Crystallogr. **28**, 53 (1995).
[7] *International Tables for X-Ray Crystallography*, Birmingham (1952), p. 101.
[8] A. Abragam and B. Bleaney, *Electron Paramagnetic Resonance of Transition Ions*, Clarendon Press, Oxford (1970), Mir, Moscow (1972).
[9] S. A. Altshuler (Al'tshuler) and B. M. Kozyrev, *Electron Paramagnetic Resonance in Compounds of Transition Elements*, Halsted, New York (1975), Nauka, Moscow (1972).
[10] H. Mori and K. Kawasaki, Prog. Theor. Phys. **26**, 971 (1962).

Translated by Steve Torstveit

Frustrated states of the spin-glass type in diluted ferrimagnetic oxides

N. N. Efimova*

V. N. Karazin Kharkov National University, pl. Svodoby 4, Kharkov 61077, Ukraine
(Submitted October 1, 2004; revised November 3, 2004)
Fiz. Nizk. Temp. **31**, 513–529 (May 2005)

The results of comprehensive experimental research on two model frustrated systems of dilute ferrimagnetic oxides—the slightly anisotropic cubic spinels $Li_{0.5}Fe_{2.5-x}Ga_xO_4$ and the highly anisotropic hexagonal $BaFe_{12-x}Ga_xO_{19}$—are reviewed and summarized. The concentration x-T phase diagrams constructed for this class of magnets for the first time are discussed, the mechanisms of formation of disordered states of the spin-glass type (with the role of the exchange interaction and anisotropy taken into account) are examined, and the structure of the states and the influence of spatial inhomogeneity of the cluster type are considered. It is shown for the example of the Li–Ga spinels that in this class of anisotropic Heisenberg magnets with short-range exchange the form of the x-T diagram differs from the canonical form for spin-glass systems: in the reentrant region ($0.9 \leqslant x \leqslant 1.5$) one observes a new cooperative frustrated state and a line of first-order phase transitions $T_1(x)$ terminating in a critical point at $x = 0.8$. © *2005 American Institute of Physics.* [DOI: 10.1063/1.1925350]

INTRODUCTION

Spin-glass physics as a new field of research is customarily considered to date from a paper published in 1975 by Canella and Mydosh, who, in studying an Au–Fe alloy with an RKKY exchange interaction of alternating sign, observed a cusp on the temperature dependence of the low-frequency dynamic susceptibility $\chi_{ac}(T)$ at low fields at a temperature T_f (also denoted T_g).[1–3] The existence of unusual magnetic properties, different from those of the previously known magnets, at $T<T_f$ was grounds for postulation of the existence of a new magnetic state with a phase transition at $T=T_f$.

The experimental "portrait" of the spin glasses (SGs), based on the results of a large number of studies, includes the following hallmarks:[1–4] the presence of features on the temperature dependence of the linear and nonlinear parts of the low-frequency dynamic susceptibility $\chi_{ac}(T)$ and on the temperature dependence of the linear susceptibility components $\chi'(T)$ and $\chi''(T)$, with $\chi''(T)\neq 0$ in the entire region $T<T_f$; dependence of T_f on the external magnetic field and frequency; the absence of anomalies on the temperature dependence of the magnetic contribution to the heat capacity C at $T=T_f$ and its linear trend for $T<T_f$; dependence of the magnetic properties on the prehistory of the sample—cooling to $T<T_f$ in the absence (ZFC) or presence (FC) of magnetic field; the presence of relaxation processes on a scale from 10^{-12} s the macroscopically large (~astronomical) times; the presence of aging effects; the appearance of unidirectional anisotropy after cooling in the FC regime.

The transition to a state of the SG type, identifiable by the set of phenomenological hallmarks listed above, can occur not only from a paramagnetic (PM) state but also from ferro- or antiferromagnetic (FM, AFM) phases. Such a transition and the state realized for $T<T_f$ are commonly called reentrant. For $T<T_f$ in Heisenberg systems a mixed state of a ferromagnetic spin glass (FSG) wherein two types of order parameter, FM and CC, coexist.[1–3]

A significant step in the development of the modern concepts of the nature of SG states was taken in theoretical studies in the Ising model with an infinite radius of interaction, starting with the paper by Sherrington and Kirkpatrick (SK).[5] At the present time essentially the only consistent theory of the spin glass is mean field theory.[5–7] Despite the progress in understanding the nature of SG states and explaining the characteristic SG properties, strictly speaking such a theory is applicable only to classical spin glasses—highly dilute alloys of noble and transition metals with long-range RKKY exchange. The fact that the same phenomenological hallmarks of the SG state are observed in systems with a short-range interaction as in classical spin glasses undoubtedly attests to a common nature of these disordered states. However, to all appearances this does not extend to the mechanisms of their formation.[2,3,6,7]

The use of numerical methods and computer simulation, which are widely employed for studying the properties of SGs with short-range interactions, has shown that in the framework of an exchange mechanism the transition to the SG state at a finite temperature $T_f>0$ K is possible only for Ising spins.[8] For Heisenberg systems it is stably found[1–3] that the lower critical dimension $d_c>3$. This contradiction is reconciled to some degree if the presence of random anisotropy is taken into account: for the Heisenberg model with a nearest-neighbor interaction a finite transition temperature $T_f \sim J(D/J)^{1/4}$, where J and D are the standard deviations of the exchange and anisotropy distributions, respectively, was obtained in Ref. 9. Serious problems also arise in connection with the spatial inhomogeneity of the magnetic states, which cannot in principle be eliminated in dilute magnetic systems with short-range interaction.[1] In such a situation it is hard to expect that only individual spins will act as structural units. In general the shape of the phase diagram in the reentrant region cannot be regarded as established.[2,6,10,11] For example, the existence region of the regular noncollinear structures that can form for $T<T_C$ (the Curie point) was not found in

those studies.[12] Recently more and more attention is being paid to frustrated FMs and AFMs, but their study is essentially still limited to theoretical models. Thus at present there is still a wide range of open questions concerning the SG state in Heisenberg systems with short-range interaction.

In this paper we present a review and summary of experimental results on anisotropic Heisenberg SG systems with short-range interaction from research done at the V. N. Karazin Kharkov National University. As model objects in this research we have used two systems of diluted ferrimagnetic oxides: the slightly anisotropic $Li_{0.5}Fe_{2.5-x}Ga_xO_4$ (Ga_xS, $0.7 \leqslant x \leqslant 2.0$) and the highly anisotropic $BaFe_{12-x}Ga_xO_{19}$ (Ga_xM, $4.0 \leqslant x \leqslant 9.0$). These were chosen with allowance for the results of a study of the exchange interaction in two- and five-sublattice ferrites in the framework of the molecular field model with the use of the method of diamagnetic substitutions[13] and also for published data on the sources and mechanisms of anisotropy.[14]

It is of interest to study these objects in their own right, since it would fill a gap in the SG data base. Historically almost all of the known x-T-H phase diagrams of SG systems have a ferromagnetic or antiferromagnetic state, and not a ferrimagnetic one, at the start of the concentration axis (at $x=0$). It is hard to say *a priori* what type of phase diagram will be obtained for a sublattice structure with competing antiferromagnetic exchange interactions in combination with the presence of spontaneous magnetization.

1. CHOICE OF MODEL OBJECTS AND THE PROGRAM OF STUDIES

The overall task of the research was to determine the form of the concentration phase diagrams in ferrimagnetic oxides with a disturbed exchange and to use them as an example to investigate the mechanisms of formation of disordered states of the SG type in Heisenberg systems with short-range interaction. Guided by this, we chose as the initial compounds the simplest and best-studied ferrimagnetic oxides with a single kind of magnetic ions (Fe^{3+}): the two-sublattice lithium spinel $Li_{0.5}Fe_{2.5}O_4$ (S), with a cubic structure, and the five-sublattice barium ferrite $BaFe_{12}O_{19}$ (M), with a hexagonal structure of the magnetoplumbite type. These compounds are insulators, and the dominant interaction in them is the short-range Kramers–Anderson superexchange between the magnetic ions (Me) via the oxygen anions, i.e., the pair exchange integral J_{nk} depends on the $Me_n-O^{2-}Me_k$ angles and distances.[15] For Fe^{3+} ions $J_{nk}<0$ for any geometry of the exchange bonds;[15] this was shown in Ref. 13 for the lithium spinel and the M-ferrite. Even in the initial compounds the inter- and intrasublattice negative exchange interactions compete with each other. As a result of the strong intersublattice exchange in the two compounds a collinear ferrimagnetic ordering is formed, with magnetic moments at 0 K equal to 2.5 (S) and 20 (M) Bohr magnetons; the Curie temperatures T_C are 913 and 733 K, respectively.[13]

We chose the simplest way of disturbing the exchange—diamagnetic substitution in which the number of nearest neighbors is altered. This condition is satisfied to a sufficient degree by the substitution $Ga^{3+} \rightarrow Fe^{3+}$, since the ionic radii are close, 0.62 and 0.67 Å, respectively. In both systems there exists a continuous series of solid solutions all the way to nonmagnetic gallates. An important consideration is that initially ($x<6.0$) the Ga^{3+} ions do not have a tendency toward preferential substitution of positions in the R block of the hexagonal structure (sublattices $2b$ and $4f_2$),[16] which play a very important role in the formation of the magnetic structure of magnetoplumbite.[13] This allows one to assume that the disturbance of the exchange is of the same type, although not completely identical, in both systems. The question of the onset of frustration in substituted spinels was considered in Ref. 17. Since the M type of crystal structure contains spinel S blocks as elements, the conclusions of Ref. 17 can be extended to the substituted compounds Ga_xM as well.

The anisotropy energy in spinels and M-ferrites is one to two orders of magnitude smaller than the exchange energy. The values of the anisotropy constants K_1 at $T=0$ K are 1.25×10^5 erg/cm^3 for the lithium spinel and 4.5×10^6 erg/cm^3 for the M-ferrite.[14] In spinels the anisotropy is of a single-ion character. The contribution of each ion is determined by the L-S coupling and the crystalline field, which has cubic point symmetry, but with uniaxial components for the octahedral sublattice.[14] In magnetoplumbite there are two microscopic sources of anisotropy: the dipole–dipole and spin–orbit interactions of the Fe^{3+} ions (in the low-symmetry $2b$ positions).[14] The two contributions are comparable in value, but the first leads to an easy plane ($K_1<0$) and the second (the dominant one) to an easy axis ($K_1>0$). In Ga_xS the easy axes correspond to directions of the [111] type.

Thus the choice of the diluted systems Ga_xS and Ga_xM as model objects allows one to study the x-T diagrams over a wide range of concentrations and to investigate the role of exchange and anisotropy in the formation of the SG and FSG states. Based on the fact that SG systems of the most diverse kinds, including the comprehensively investigated system with short-range interaction (Eu–Sr)S, exhibit a set of properties predicted by mean field theory, the first order of business was to study the above-listed canonical hallmarks of the SG state. In the magnetic measurements only static and low-frequency fields were used. To observe and identify states of different types and the phase transitions between them, calorimetric studies were carried out along with the magnetic studies. Most of the experimental results that will be presented and discussed below were published in Refs. 18–25. The techniques of the measurements and the methods of sample preparation and monitoring of their stoichiometry and single-phasedness are described in those papers.

In view of the fact that the first step in the proposed program of studies is to reveal the ''mean-field hallmarks'' of states of the SG type, a brief discussion of the main concepts of the SG in reference to the SK mean field theory[1–6] is in order.

2. SPIN GLASS IN THE SHERRINGTON-KIRKPATRICK MEAN FIELD MODEL

The first theoretical treatment of the spin glass was carried out by Edwards and Anderson (EA),[26] who proposed a mechanism for its formation, a model of the spin structure, and the type of order parameter q_{EA}. All together this in

essence constituted the first definition of the SG state. According to Ref. 26, the transition to the SG state at a temperature $T=T_f$ is due to the appearance of a random local magnetization at the sites occupied by magnetic ions: $\mathbf{m}_i=\langle \mathbf{S}_i\rangle_T\neq 0$ but $\Sigma_i^N \mathbf{m}_i=0$ (here $\langle \mathbf{S}_i\rangle_T$ is the thermodynamic mean). The freezing of the spins ($\mathbf{m}_i\neq 0$) is due to the presence of competing exchange interactions of random magnitude and sign. The value of T_f is determined by the standard deviation J of the exchange.

The results of subsequent theoretical and experimental studies showed that the definition of the SG state in the EA model does not reflect its physical essence. The fundamental distinguishing characteristics of the spin glass, as was first shown in the SK model, are due to features of the energy spectrum, viz., to a high degree of degeneracy of the ground state and to nonergodicity.[1–6] The degeneracy is due to a high concentration of frustrated exchange bonds, i.e., bonds for which there are no spin configurations that lead to an absolute (unique) minimum of energy.

At the transition to the SG state the phase space breaks up into a large number of valleys separated by activation barriers, the height of which in the limit $N\to\infty$ (N is the number of spins) becomes infinite.[1–6] Thus the system is always found in a restricted region of phase space—a valley. Because of this, an average over all possible configurations *à la* Gibbs is not equivalent to an average over time, which corresponds to the configuration average only in the limits of a single valley. Importantly, the fractionation of phase space with the formation of all the new infinite barriers that starts at T_f continues all the way to 0 K.[6] There are also activation barriers of finite height within the valleys, and they are responsible for the very broad spectrum of relaxation times. The long-term relaxation effects (magnetic viscosity) observed experimentally in SGs on a time scale of $10^{-12}-10^4$ s are, according to the conclusions of mean field theory, due to intravalley transitions, i.e., to overcoming of the barriers of finite height.

The order parameter q_{EA} introduced in Ref. 26 is also single-valley. Its equivalent in the SK theory is the parameter q:

$$q_{EA}=\lim_{t\to\infty}\langle\langle \mathbf{s}_i(0)\mathbf{s}_i(t)\rangle_T\rangle_C, \quad q_{EA}=q=\langle\langle \mathbf{s}_i\rangle_T^2\rangle_C, \tag{1}$$

where $\langle\ldots\rangle_C$ is the configuration average; $q_{EA}=0$ for $T>T_f$ and has a finite value for $T<T_f$. It is the same for all valleys and characterizes the degree of freezing of the spins in any of them. Thus q is in some sense an experimentally reproducible quantity: on cooling ($T\leqslant T_f$) the system can get stuck in any valley, but this does not affect the value of q_{EA} and its behavior at $T>0$ K.[3,6]

Meanwhile, it is perfectly obvious that a single-value order parameter cannot be used for an adequate description of the SG state. The role of the order parameter is played more successfully by the so-called Parisi function $q(x)$, defined on the interval $0\leqslant x\leqslant 1$, which is the solution in the SK model with broken replica symmetry.[3,6] The physical meaning of the function $q(x)$ as the SG order parameter is that it is the inverse probability of overlapping of the valleys, i.e., the degree of correlation of the states in phase space: $x(q)=\int_0^q P(q')dq'$, $P(q)$ is the distribution function of the overlaps $q^{\alpha\beta}$, α and β are valleys. For uncorrelated states $q^{\alpha\beta}=0$, and for completely correlated states $q^{\alpha\beta}=q^{\alpha\alpha}=q(1)$. The latter means that the system is imprisoned in one of the valleys, i.e., $q^{\alpha\beta}=q_{EA}$.

The order parameters q_{EA} and $q(x)$ can be related to the nonequilibrium χ_{neq} and equilibrium χ_{eq} susceptibilities, which are usually identified with the experimentally measured χ_{ZFC} and χ_{FC} (Ref. 3):

$$\chi_{\text{neq}}=T^{-1}[1-q_{FA}(T)], \quad \chi_{\text{eq}}=T^{-1}\left[1-\int_0^x q(x)dx\right]. \tag{2}$$

It follows from (2) that the dependence of the magnetic properties of a SG on the prehistory (magnetic irreversibility: $\chi_{ZFC}(T)\neq\chi_{FC}$) is due to the nonergodicity of the SG state, and the difference of their susceptibilities can serve as a measure of this.[3]

The results obtained in the pioneering work of Sherrington and Kirkpatrick[5] correspond to the replica-symmetric approximation, in which there is no phase transition to the SG state in the presence of magnetic field. Below we shall establish that such a transition at $H\neq 0$ does exist and is manifested in breaking of the replica symmetry.[1–3] The lines of instability of the replica-symmetric solution—the Almeida–Thouless (AT) line—has the form

$$T_f(H)=J\left[1-\frac{3}{4}\left(\frac{H}{J}\right)^2\right]^{1/3}, \quad H\ll J,$$

$$T_f(H)=(3\sqrt{2\pi})^{-1}J\exp\left[-\frac{H^2}{2J^2}\right], \quad H>J. \tag{3}$$

For a Heisenberg SG (n-component vector SG) the PM–SG transition is described in the general case by several order parameters.[3] In the isotropic case for $H\neq 0$ the situation simplifies. Initially at $T_f(H)$ the spin component transverse to H freezes ($q_\perp\neq 0$)—the Gabey–Toulouse (GT) line. For $H<J$ the function $T_f(H)$ has the form

$$T_f(H)=J\left[1-\frac{23}{110}\left(\frac{H}{J}\right)^2\right]. \tag{4}$$

As in the case of an Ising SG [see Eq. (3)] the transition at $T_f(H)$ along the GT line is a transition to a nonergodic state, when the corresponding order parameters are Parisi functions. At higher values of H, i.e., lower temperatures, the longitudinal spin components freeze. This process is described by a line of critical behavior analogous to the AT line in Ising systems. That this stepwise freezing is a realistic picture is not in doubt. For example, it was shown theoretically in Ref. 27 that the two lines coincide. Experimentally in the vast majority of cases for Heisenberg systems an AT line $\tau\propto H^{2/3}$ is observed at low fields and a GT line $\tau'\propto H^2$ at high fields.[1–3] Such behavior is explained by the influence of random anisotropy, which, according to Ref. 28, makes the transition Ising-like.

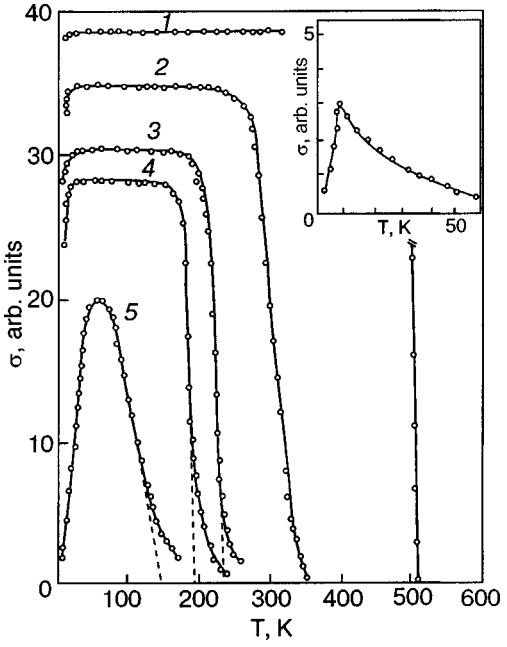

FIG. 1. Temperature dependence of the magnetization of Ga_xS samples for different concentrations x: 0.9 (*1*), 1.2 (*2*), 1.3 (*3*), 1.35 (*4*), 1.4 (*5*). In the inset $x=1.7$, $H=50$ Oe.

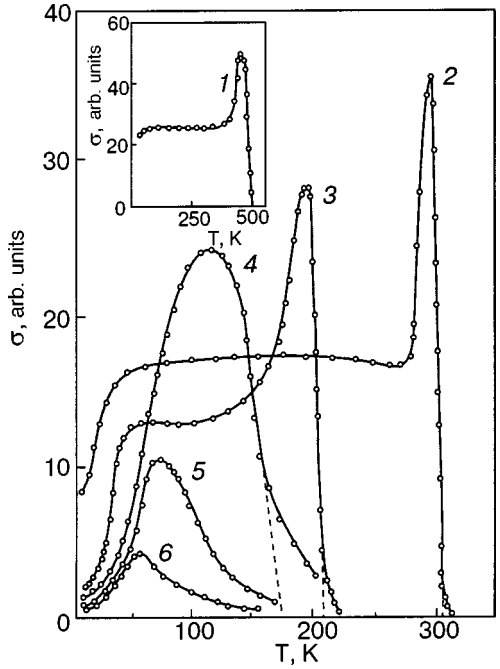

FIG. 2. Temperature dependence of the magnetization of Ga_xM samples at different concentrations x: 4.0 (*1*), 6.0 (*2*), 7.0 (*3*), 7.5 (*4*), 8.0 (*5*), 8.5 (*6*); $H=50$ Oe.

3. CONSTRUCTION OF THE *x*-*T* CONCENTRATION PHASE DIAGRAMS

3.1. Temperature dependence of the low-field magnetization and dynamic susceptibility

It is well to begin the discussion of the results on the magnetic properties used to construct the concentration phase diagrams for the systems Ga_xS and Ga_xM with the temperature dependence of the low-field static susceptibility $\chi_{dc}(T)$ or magnetization $\sigma_H(T)$, since those functions directly give a clear picture of the changes in the magnetic subsystem of these objects when the concentration of nonmagnetic ions in them is increased.

Figures 1 and 2 show $\sigma_H(T)$ for the Ga_xS and Ga_xM systems, measured in a static field $H=50$ Oe on heating of the samples after they had been cooled down beforehand to 4.2 K at $H=0$ (the ZFC regime). First of all, it is well seen from the data of Figs. 1 and 2 that the substitution $Ga^{3+} \rightarrow Fe^{3+}$ leads to a decrease of the Curie temperature T_C, which can nevertheless be reliably determined by extrapolation to the T axis of the segments with maximum derivative $\partial\sigma/\partial T$ to $x=1.35$ (Ga_xS) and $x=7.0$ (Ga_xM). Except for the low-temperature region, the $\sigma_H(T)$ curves for Ga_xS at $x<1.4$ are typical for magnetically soft materials, for which the shape anisotropy is dominant. Unlike Ga_xS, in the Ga_xM system a maximum at $T \rightarrow T_C$ (the Hopkinson effect) is clearly visible, which is observed, as a rule in the presence of strong crystallographic anisotropy.[29] This means that the Ga_xM system remains highly anisotropic upon the substitution $Ga^{3+} \rightarrow Fe^{3+}$. From the standpoint of observation of the SG states in this concentration region the behavior of the magnetization in the low-temperature region is significant: for $T \rightarrow 0$ K both systems exhibit the decrease of $\sigma_H(T)$ typical for SG states, this decrease being sharper the higher the concentration of Ga^{3+}.

Further, at practically identical concentrations of nonmagnetic ions $c \geqslant 60\%$ [Ga^{3+} in Ga_xM and ($xGa^{3+} + 0.5Li^{+}$) in Ga_xS] the $\sigma_H(T)$ curves in both systems are bell-shaped initially and then develop a cusp (see the inset in Fig. 1). The position of the cusp on the temperature scale depends on x.

The behavior of the temperature dependence of the low-frequency dynamic susceptibility χ and its real part χ' are analogous to the $\sigma_H(T)$ curve. It has been established that there exists a minimum concentration (for Ga_xS it is $x=0.9$) at which the $\chi''(T)$ curves in the temperature region $T \ll T_C$ begin to exhibit maxima, the position and even the existence of which depends on the value of the alternating field h. For illustration of the results obtained in this series of studies Fig. 3 shows the $\chi''(T)$ curves for Ga_xS samples with $x=0.9$ and 1.35.

3.2. Dependence of the magnetic properties on the prehistory—magnetic irreversibility

The main features of the behavior of the magnetization due to its dependence on the prehistory are illustrated by the data shown in Figs. 4 and 5 for the Ga_xS and Ga_xM systems, respectively. The character of the $\sigma_{ZFC}(T)$ and $\sigma_{FC}(T)$ curves presented in Fig. 4 is typical for the concentration interval $x \leqslant 1.35$ in the Ga_xS system and for $x \leqslant 6.0$ in the Ga_xM system.[18,19] It is seen that in both systems irreversibility exists in a wide range of temperatures, i.e., its presence is observed at temperatures much higher than the position of the maximum on the $\chi''(T)$ curves. With increasing field this interval narrows, and at a certain value H the irreversibility vanishes: for example, at $H=100$ Oe for $Ga_{0.9}S$ and at $H>10^3$ Oe for Ga_6M. The magnetization σ_{FC} in the concentration region under discussion is independent of temperature in Ga_xS and increases weakly with temperature in Ga_xM.

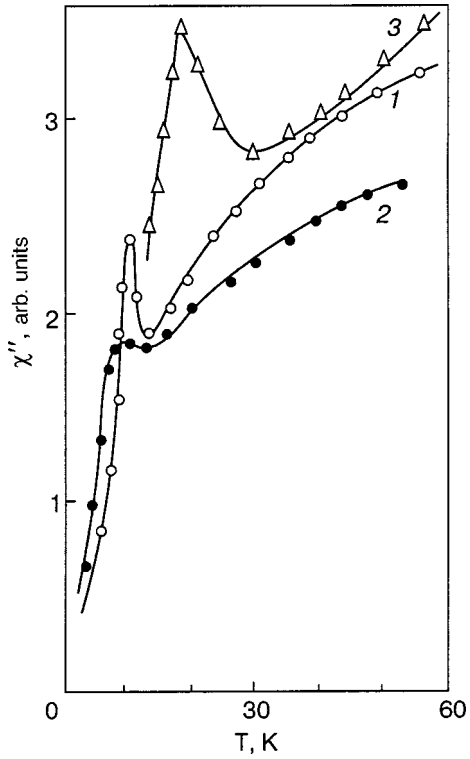

FIG. 3. Temperature dependence of the imaginary part of the dynamic susceptibility $\chi''(T)$ for Ga_xS samples: curves *1*,2—$x=0.9$ ($f=120$ Hz, $h_0=1.4$ Oe (*1*), 6.4 Oe (*2*)); curve *3* is for $x=1.35$ ($f=60$ Hz, $h_0=1$ Oe).

The manifestation of irreversibility different from that predicted theoretically is also observed at higher concentrations of nonmagnetic ions: $x\geqslant 1.5$ (Ga_xS) and $x\geqslant 8.0$ (Ga_xM). As is seen in Fig. 5, at comparatively weak fields irreversibility is manifested at any temperature to which the sample is heated during measurements of the $\sigma_{ZFC}(T)$ curve. The magnetization σ_{FC}, like $\sigma_{ZFC}(T)$, depends on temperature, but unlike the latter it tends toward a finite limit as $T\to 0$ K. With increasing field H irreversibility becomes a

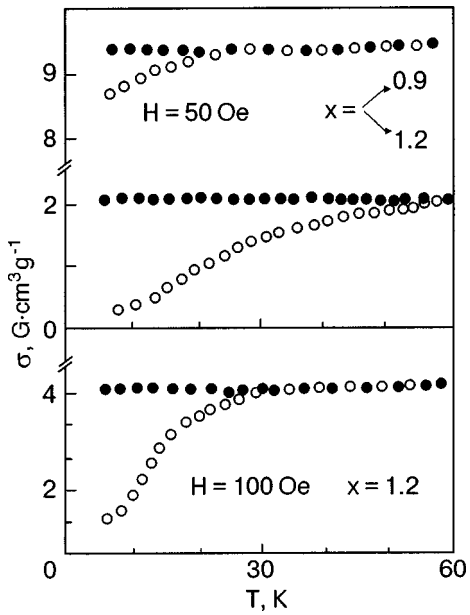

FIG. 4. Magnetization polytherms of Ga_xS samples with different concentrations x. ZFC regime (○) and FC regime (●).

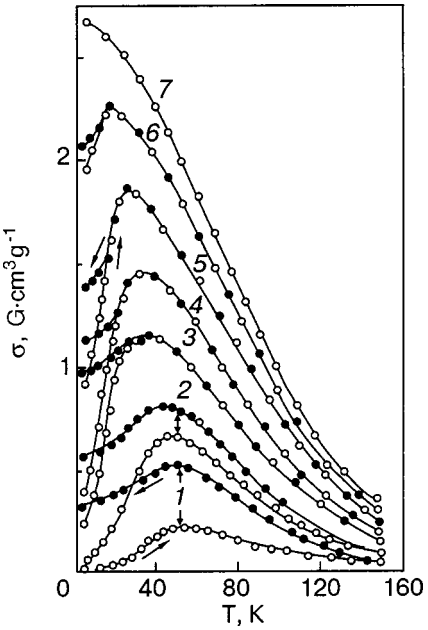

FIG. 5. Magnetization polytherm for Ga_xM samples with $x=8.25$ in different fields H [Oe]: 50 (*1*), 200 (*2*), 750 (*3*), 10^3 (*4*), 3×10^3 (*5*), 5×10^3 (*6*), 8.25×10^3 (*7*). The ZFC (○) and FC (●) regimes.

low-temperature effect, i.e., it exists in the region $T\leqslant T_f$, if T_f is defined as the position of the maximum on the $\chi''(T)$ curve. Such a deviation from the predictions of the SK model is only natural, since this model does not take into account the real structure of the samples: the existence of regions of short-range atomic and magnetic order[1] and the presence of domain structure with preservation of the long-range FM order, i.e., in FSG states. These factors, which have no direct bearing on the transition to a state of the SG type, make it possible for irreversibility effects to appear in a very wide range of temperatures.[30]

3.3. Long-term relaxation of the nonequilibrium magnetization σ_{ZFC} (magnetic viscosity); line of critical behavior $T_f(H)$

The relaxation processes are well described by a logarithmic law: the time dependence of the nonequilibrium magnetization σ_{ZFC} at constant values of the field H and temperature $T\leqslant T_f$ has the form:[4] $\sigma_{ZFC}(t)=\sigma_{ZFC}(0)+S\ln(t/t_0)$, where $t_0\sim 10$ s, $\sigma_{ZFC}(0)$ is the value of the magnetization at a time t_0 after the field is switched on (the first measurement), $S(T,H)$ is the coefficient of magnetic viscosity, and $S_H(T)\to 0$ for $T\to T_f$ and $T\to 0$ K.

The behavior of the coefficient $S=S(T,H)$ is illustrated by the data presented in Figs. 6 and 7. The results of Fig. 6 demonstrate the characteristic manifestations of magnetic viscosity effects for Ga_xS samples in the concentration interval $0.9\leqslant x\leqslant 1.2$. It must be noted that for this concentration region the magnetic viscosity has been studied successfully only with the use of a SQUID magnetometer (the measurements were made at the B. Verkin Institute for Low Temperature Physics and Engineering, National Academy of Sciences of Ukraine, Kharkov in collaboration with V. A. Desnenko and A. S. Panfilov).[31] The changes $\Delta\sigma_{ZFC}(t)\sim 10^{-3}$ $G\cdot cm^3\,g^{-1}$ over a time of 3.6×10^4 s. The high sensitivity of

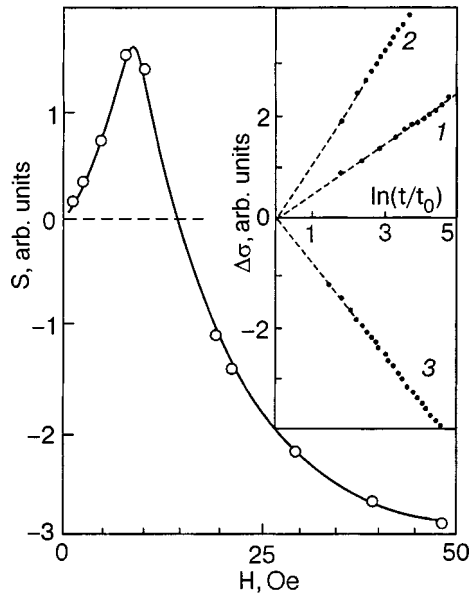

FIG. 6. Magnetic-field dependence of the logarithmic viscosity coefficient S_T for a $Ga_{0.9}S$ sample at 4.2 K. The inset shows the $\Delta\sigma_{ZFC}-\ln(t/t_0)$ relation in a field $H=4$ Oe at different temperatures T [K]: 4.2 (*1*), 8 (*2*), 11 (*3*).

the method made it possible to record not only the vanishing but also the change of sign of $S_T(H)$ or $S_H(T)$. The temperature corresponding to the sign change of $S_H(T)$ agrees within the experimental error with the value of T at which the maximum occurs on the $\chi''(T)$ curves (see Fig. 3). Taking into account that the long-range FM order and, accordingly, the domain structure are plainly still preserved in the concentration region $x\leqslant 1.5$, the relaxation of the magnetization, described by a logarithmic law with $S<0$, is obviously due to the system of domain walls. At a high Ga^{3+} concentration the $S(T,H)$ relations can be investigated on a ballistic magnetometer (sensitivity 10^{-3} G·cm^3 g^{-1}). Figure 7 shows the $S_H(T)$ curves for Ga_8M and $Ga_{1.3}S$ samples. It is seen that

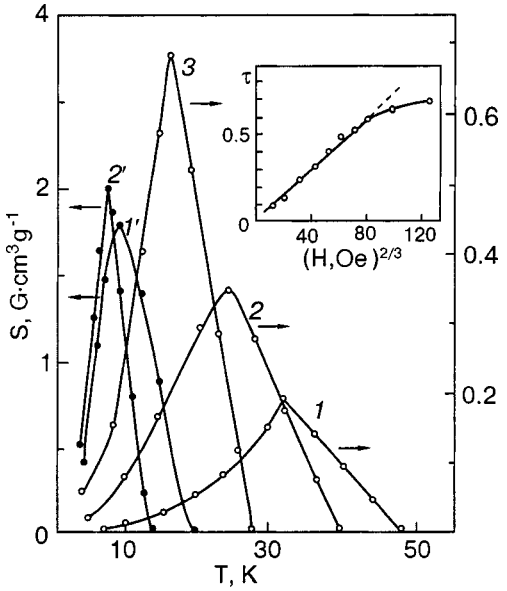

FIG. 7. Temperature dependence of S_H for a Ga_8M sample at different fields H [Oe]: 50 (*1*), 200 (*2*), 500 (*3*); for a $Ga_{1.3}S$ sample at fields H [Oe]: 70 (*1′*), 100 (*2′*). The inset shows $\tau=f(H^{2/3})$ for Ga_8M; $\tau=[T_f(0)-T_f(H)]/T_f(0)$.

these curves, like $S_T(H)$, are nonmonotonic and have maxima in the interval between 0 K and $T_f(H)$. The position of these maxima is not accidental: for the Ga_xS system the maxima are found at $T=0.4T_f(H)$, and for the Ga_xM system, at $T=0.6T_f(H)$ [$T_f(H)$, the temperature at which the viscosity coefficient $S_H(T)$ goes to zero, is by definition the temperature of the phase transition to a state of the SG type in a magnetic field $H\neq 0$]. The trend of the $S_T(H)$ and $S_H(T)$ curves obtained for diluted Ga_xS and Ga_xM systems is completely analogous to that for a SG with RKKY exchange. In our case, however, the values of the viscosity coefficient are an order of magnitude or two higher, especially at concentrations $\sim(60-70)\%$.[18,32]

A study of the $S_H(T)$ curves over a wide range of fields made it possible to determine the $T_f(H)$ lines, and from a mathematical processing of the latter with allowance for Eqs. (3) and (4) one can determine the form of the lines of critical behavior in a magnetic field, $\tau=f(H)$, where $\tau=1-T_f(H)/T_f(0)$. In all cases the critical behavior predicted by mean field theory for Heisenberg systems with random anisotropy[28] is observed. In the low-field limit (the regime of strong anisotropy) this is the Almeida–Thouless line, $\tau\propto H^{2/3}$. At high fields (the weak anisotropy regime) this is the Gabey–Toulouse line $\tau'\propto H^2$; $\tau'=1-T_f(H)/T_f'(0)$, where $T_f'(0)$ is the temperature at which the high-field parts of the $T_f(H)$ curves extrapolate for $H\to 0$. The strong and weak anisotropy regimes are determined by the conditions $d\gg h^{3/2}$ and $d\ll h^{5/3}$, respectively. The parameters d and h depend on the relationships among H, the standard deviation J of the exchange and the standard deviation D of the anisotropy: $d=D/J$, $h=\mu H/D$, where μ is the magnetic moment. It should be noted that the values of $T_f(H)$ determined independently from the conditions $S_H(T)=0$ and $\sigma_{ZFC}(T,H)\neq\sigma_{FC}(T,H)$ agree within 1–2 K.

In the context of mean field theory the presence of lines of critical behavior and the ''relaxation'' method of determining $T_f(H)$ in combination with magnetic irreversibility effects at low temperatures and the presence of maxima on the $\chi''(T)$ curves attest to the occurrence of a transition to disordered states of the SG type in the Ga_xS and Ga_xM systems in the low-temperature region. Figure 8 shows the x-T concentration phase diagrams of these systems, which were constructed not only from determination of the $T_f(0)$ lines but also from additional studies. The goal of those studies was to identify and determine the structure of the magnetic states. In particular, much attention was devoted to the question of the existence of a thermodynamic limit at the Curie point for $c\to c_0$.

3.4. Concentration region of the existence of long-range FM order. Temperature dependence of the magnetic contribution to the heat capacity

In determining the existence region of long-range FM order in terms of the concentration (especially in the ''hard'' region, i.e., near c_0) an approach based on observation of the phase transition at the Curie point was used. For this, in addition to measurement of the temperature dependence of the low-field magnetization (see Figs. 1 and 2), studies of the critical behavior in magnetic field were carried out[22,33] with the use of an equation of state of the form $(H/\sigma)^{1/\gamma}=A(T$

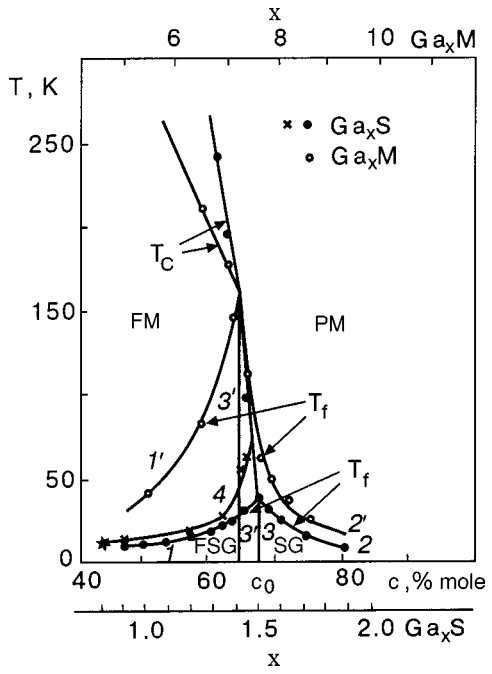

FIG. 8. x-T phase diagram of the slightly anisotropic system $Li_{0.5}Fe_{2.5-x}Ga_xO_4$ and the highly anisotropic $BaFe_{12-x}Ga_xO_{19}$. The $T_f(x)$ lines *1* and *1′* correspond to transition to a ferrimagnetic spin glass state, the $T_f(x)$ lines *2* and *2′* to the transition to a spin-glass state, and the vertical lines *3* and *3′* to the concentration transition FSG→SG; line *4* is the line of first-order transitions $T_1(x)$ in the slightly anisotropic system Ga_xS. The lines labeled T_C are lines of Curie points.

$-T_C)/T_C+B\sigma^{1/\beta}$. For the example of the Ga_xS sample with $x=1.45$ it was shown for the first time that for $c\to c_0$ (i.e., $x_0=1.5$) the values of the critical exponents depend on the value of the field H. The mean field values of the exponents, namely, $\gamma=1$, $\beta=0.5$, and $\delta=3$ for the critical isotherm $\sigma \propto H^{1/\delta}$ at low fields $H<500$ Oe gives way to the values $\gamma=1.33$, $\beta=0.4$, and $\delta=4.41$ in the interval 1.5–8.0 kOe. The value of T_C remains unchanged: 97 ± 2 K. When the magnetization isotherms for samples with $x\geqslant1.5$ (Ga_xS) and $x\geqslant7.75$ (Ga_xM) were processed by the same procedure for as for $Ga_{1.45}S$ it was found that for $c\geqslant c_0$ the spontaneous magnetization $\sigma_s=0$ in the whole range of temperatures.

This conclusion is in good agreement with the results on the temperature dependence of the magnetic contribution to the heat capacity $C(T)$ for the Ga_xS system. The magnetic contribution is obtained from the total heat capacity of a sample by direct subtraction of the heat capacity of the nonmagnetic gallate $Li_{0.5}Ga_{2.5}O_4$. The latter was measured independently and was taken equal to the lattice heat capacity.[21,23] By comparing the trend of the $C(T)$ curves for samples with $x=1.45$ and 1.6, shown in Figs. 9 and 10, respectively, one notices the absence of any features on the $C(T)$ curve for $x=1.6$. The trend of that curve corresponds completely to the canonical spin-glass behavior of $C(T)$.[1–3] For $x=1.45$ the characteristic maximum corresponding to a second-order phase transition at the Curie point is observed at $T\sim97$ K. The nature of the maxima observed for samples with $x=1.2$ and 1.45 (Fig. 9) at temperatures below T_C and also the irregularities in the trend of the $C(T)$ curve for $x=1.2$ will be discussed below.

The linear dependence of $C(T)$ typical for SG states is

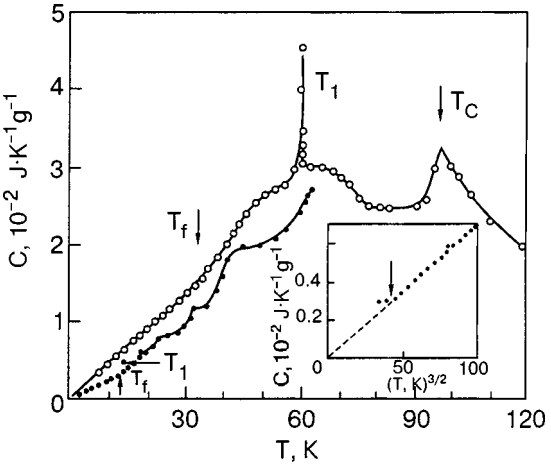

FIG. 9. Temperature dependence of the magnetic part of the heat capacity $C(T)$ for $Ga_{1.45}S$ and $Ga_{1.2}S$ samples. The inset shows a plot of $C(T^{3/2})$ for $Ga_{1.2}S$ at $T>T_f$. T_f is the temperature of the transition to the FSG state, T_1 is a first-order phase transition, and T_C is the Curie point.

obtained at $T<T_f$ for all samples of the Ga_xS system with $x\geqslant0.9$.[21,23] For $x=1.2$ and 1.45 this is seen from the data presented in Fig. 9. The measurements in the temperature interval 4.2–120 K were made by us in collaboration with V. A. Pervakov, N. Yu. Tyutryumova, and V. I. Ovcharenko (V. N. Karazin Kharkov National University) and for temperatures $T=2-20$ K with A. G. Anderson, A. M. Gurevich, and V. N. Yeropkin (B. Verkin Institute for Low Temperature Physics and Engineering, National Academy of Sciences of Ukraine, Kharkov). The $C(T)$ curves for the Ga_xM system were not investigated.

Thus in the Ga_xS and Ga_xM systems the long-range FM order is destroyed at critical concentrations c_0 which are very close in value. For $T<T_f$ a mixed FSG state is realized in the concentration region $c<c_0$, i.e., a spontaneous magnetization exists in the whole temperature range from 0 K to T_C.

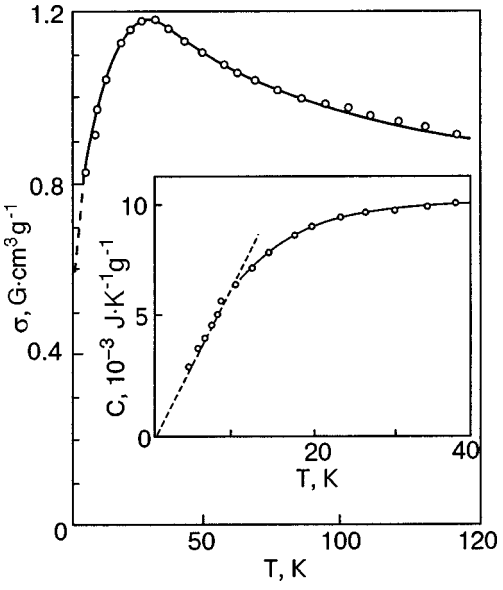

FIG. 10. Temperature dependence of the low-field magnetization $\sigma_{ZFC}(T)$ for $H=50$ Oe and the magnetic contribution to the heat capacity at $H=0$ (inset) for the sample $Ga_{1.6}S$.

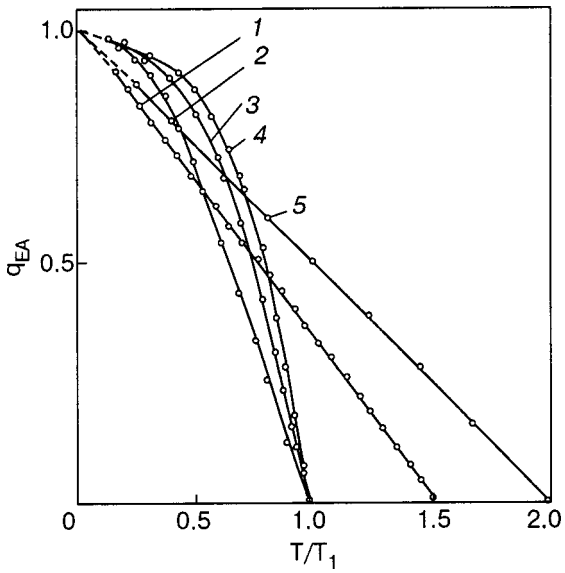

FIG. 11. Experimental dependence of $q_{EA}(T)$ for samples of the system Ga_xS at various x: 1.50 (*1*), 1.55 (*2*), 1.60 (*3*), 1.90 (*4*) for Ga_xM with $x=8.25$ (*5*).

3.5. Order parameter q_{EA}

In the SK model the PM–SG transition is a phase transition with respect to the order parameter q_{EA}. In Heisenberg SGs in the limit of high anisotropy the mixing of the longitudinal and transverse components of the spin causes the n-component SG order parameter to become an isotropic one-component order parameter that coincides with the single-valley parameter q_{EA}.[3,28] Near the AT instability line (the transition at $H\neq 0$) one can write q_{EA} in the form of a power series in the reduced temperature $\tau=1-T/T_f(0)$: $q_{EA}(\tau)=\tau+\tau^2-\tau^3$. The parameter $q_{EA}(T)$ is related to the experimentally determined values as[1]

$$q_{EA}(T)=1-T[C_{\chi\,ZFC}^{-1}(T)+\Theta]^{-1},$$

where C is the Curie constant and Θ is the paramagnetic Curie temperature.

The results of a calculation of $q_{EA}(T)$ with the use of this relation are presented in Fig. 11.[18] The parameters C and Θ are defined in the PM region near T_f, where the Curie–Weiss law $\chi=C/(T-\Theta)$ holds. It is seen that for all Ga_xS samples with $x\geqslant 1.55$ a PM–SG transition occurs with respect to the parameter q_{EA}. The temperature dependence $q_{EA}(T)$ is linear to $\tau=0.2$, and for $\tau>0.2$ the quadratic term becomes dominant.

For the Ga_xM system an analogous calculation of q_{EA} leads to dependences like curve *5* in Fig. 11, i.e., q_{EA} cannot serve as the order parameter for the PM–SG transition. Analyzing the causes of this according to the formal characteristics, viz., the values of the parameters C and Θ, which are presented in Table I, one notices the following. The parameter q_{EA} fails to describe the PM–SG transition in all cases when $\Theta>0$: for $x=x_0=1.5$ in Ga_xS and for $x\geqslant x_0\approx 7.75$ in Ga_xM. If it is assumed that $\Theta>0$ corresponds to nonzero mean FM exchange, then the differences of the Ga_xS and Ga_xM systems in respect to the possibility of describing the PM–SG transition in them for $c>c_0$ by the order parameter q_{EA} reduce to the circumstance that in one case $J_0=0$ and in the other $J_0\neq 0$. Such a situation is in principle possible since the chosen systems, while close, are by no means completely identical in the sense of the exchange disturbance. For $J_0\neq 0$, including in the FSG states, a more complex single-valley order parameter is probably needed.

3.6. FCC–CC concentration transition

On the basis of the results presented above it has been established that the slightly and highly anisotropic systems under study have the same type of x-T phase diagrams, on which regions of FM and PM states and also two types of spin glasses exist. For $c<c_0$, where the long-range FM order is preserved down to 0 K and for $T<T_f$ coexists with a spin-glass state, this is a mixed FSG state. For $c>c_0$, where the spontaneous magnetization $\sigma_s=0$, a "pure" SG state is realized. The concentration transition from the FSG (ferrimagnetic spin-glass) to the SG state is characterized by the vanishing of the FM order parameter σ_s at $c=c_0$ and the appearance of the SG order parameter q_{EA} (for Ga_xS). According to the conclusions of mean field theory, this transition corresponds to vertical lines *3* and *3′* on the x-T diagram (see Fig. 8). Such a position of lines *3* and *3′* shows that a sequence of transitions of the PM–FM–FSG–SG or PM–SG–FSG type, etc. does not exist. In mean field theory only PM–FM–SG (Ising model) or PM–FM–FSG (Heisenberg model) transitions, which have been observed

TABLE I. Values of the Curie constant C and the paramagnetic Curie temperature Θ for the Ga_xS and Ga_xM systems in the PM region near T_f and also the values of $d=D/J$, $T_0\sim J$, and ΔT_f the anisotropy contribution to T_f.

x	Ga_xS					x	Ga_xM				
	C,K	Θ,K	d	T_0,K	ΔT,K		C,K	Θ,K	d	T_0,K	ΔT,K
1.4	–	–	0.51	25	3	6.0	–		0.38	35	5
1.45	–	–	0.53	26	7	7.0	–		0.58	62	18
1.5	190	49	0.47	30	7	7.5	–		0.65	107	38
1.55	190	2	0.5	26	6	7.75	86	123	0.48	90	20
1.6	190	−56	0.47	18	4	8.0	55	108	0.49	43	9
1.7	46	−37	–			8.25	27	96	0.49	39	8
1.9	5	−4	–			8.5	–	–	0.50	29	6

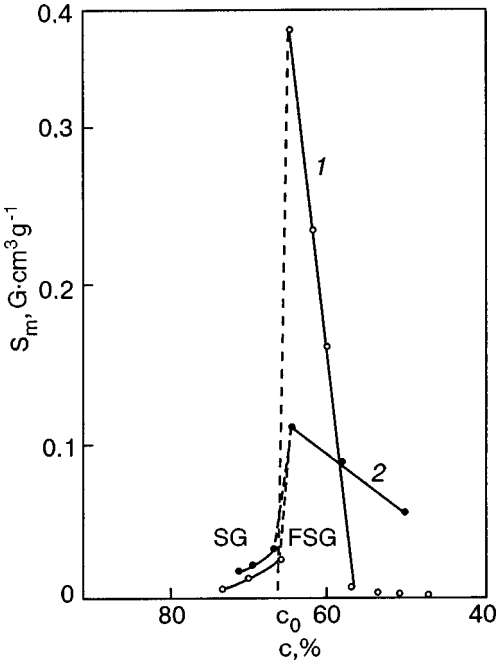

FIG. 12. Concentration dependence of the magnetic viscosity coefficient $S_m(x)$ for the systems Ga_xS (*1*) and Ga_xM (*2*) in a field $H=50$ Oe at temperatures of $0.4T_f(H)$ and $0.6T_f(H)$, respectively.

experimentally,[1–3] are possible in the reentrant region. In the SG region these are only PM–SG transitions.

We succeeded in observing yet another, previously unmentioned manifestation of the FSG–SG concentration transition.[18] It is particularly noteworthy as being a direct consequence of the experimentally observed properties of the SG. We are referring to the change of the trend of the concentration dependence of the magnetic viscosity coefficient, which decreases sharply (in a jump) at the transition to the SG state. Figure 12 shows the concentration dependence $S_m(x)$ at temperatures $T=0.4T_f(H)$ for Ga_xS and $T=0.6T_f(H)$ for Ga_xM in a field $H=50$ Oe. Such a jump-like change of $S(T,H)$ at $c=c_0$ also takes place at other temperatures. The jump of $S(T,H)$ at $c=c_0$ means that the system dynamics, which is determined by the height of the intravalley energy barriers, is different in the SG and FSG states. Furthermore, the critical concentration c_0 separates regions on the x-T diagram differing strongly not only in the value but also in the concentration dependence of $S(x)$: in the SG region ($c>c_0$) the coefficient of magnetic viscosity decreases weakly with increasing x, while in the reentrant region, FSG, it increases sharply for $c\to c_0$.

4. MECHANISMS OF FORMATION OF THE SPIN-GLASS STATES IN DILUTED FERRIMAGNETIC OXIDES

4.1. Influence of anisotropy

Summing up the foregoing results, we can conclude that the slightly anisotropic and highly anisotropic systems of diluted ferrimagnetic oxides with short-range exchange considered above display the behavioral features predicted by mean field theory for Heisenberg SG systems with random anisotropy. On the quantitative level the most noticeable difference is between the dynamic behavior of the systems Ga_xM and Ga_xS and also the position of the $T_f(x)$ lines on the x-T phase diagrams. This is manifested with particular clarity in the FSG region, where the $T_f(x)$ line for the Ga_xM system lies much higher than for Ga_xS, especially as the multicritical point x_0 of the x-T diagram is approached. In contrast, the value of the viscosity coefficient $S(x)$, which in both systems grows for $x>x_0$, is much higher in Ga_xS than in Ga_xM. This shows that the anisotropy raises the height of the intravalley activation barriers. Clearly, however, the fact that $S(x)$ grows is itself not directly related to the anisotropy.

Upon transition to the SG state the difference in the behavior of the two systems is smoothed out. The trends of the concentration curves $S(x)$ and the values of S in the two systems are very similar, i.e., the contribution of the anisotropy to the total barrier heights, if it exists at all, is insignificant. The fact that the lines $T_f(x)$ draw together sharply in the SG region (see Fig. 8) is an important experimental result.

In discussing the trend of the $T_f(x)$ lines it should be mentioned first that the crucial fact in explaining the mechanisms of formation of states of the SG type is that the concentration boundaries of the different magnetic states on the x-T diagrams of the two systems practically coincide. This is a clear indication that the leading role in the formation of spin-glass states is played by the disturbance of the exchange interaction.

We have attempted to estimate the influence of the random anisotropy using the conclusions of mean field theory,[28] according to which:

$$T_f'(0)=T_f(0)[1-(n+2)d/2(n+1)^{1/2}], \tag{5}$$

$$T_f(0)=T_0[1+(n-1)d^2]^{1/2}, \tag{6}$$

where $T_f'(0)$ and $T_f(0)$ are the experimentally determined values (see the critical behavior), $T_0\sim J$ is the transition temperature determined by the standard deviation of the exchange, $n=3$ (for classical Heisenberg spins), and $d=D/J$. The results of a calculation of d and T_0 are presented in Table I.

As is seen from the tabulated data, in the framework of the approximation used it is found that the random anisotropy influences the value of the transition temperature in both the FSG and SG states. Its influence becomes weaker with increasing distance from the critical concentration for the existence of long-range FM order, c_0, but it is rather pronounced in the close vicinity of that concentration.

It is interesting to note that crude estimates in the framework of the mean field model lead to the same result as in the theory[9] of Heisenberg systems with short-range interaction: the value of the anisotropy has a weak effect on the value of T_f in the SG states. Nevertheless, the same estimates (in the framework of mean field theory) for the FSG region show that differences in the positions of the $T_f(x)$ lines remain even when the anisotropy (or more precisely, its standard deviation, which can be larger in Ga_xM than in Ga_xS because of the presence of competing mechanisms) is taken into account; see Table I. To all appearances in considering the mechanisms of formation of states of the SG type (especially FSG) in diluted ferrimagnets several other factors must also be taken into consideration: the short-range character of the exchange, the sublattice structure, and the distribution of nonmagnetic cations over sublattices and the spatial inhomo-

geneity of their arrangement in the crystal. All of these influence the structure of the states, their spatial inhomogeneity, the possibility of formation of noncollinear structures of different types, etc.

4.2. Structure of the magnetic states. Effects of spatial inhomogeneity

The use of diamagnetic substitution to disturb the exchange in systems with short-range interaction inevitably leads to spatial inhomogeneity of the exchange and magnetization. There are two reasons for this: the short-range character of the exchange directly, and the presence of regions of short-range atomic order.[1] In the case of a collinear ferromagnetic structure, initially groups of canted spins with a weakened exchange—regions of local noncollinearity (RLNs)—appear. Isolated RLNs are inhomogeneities in the collinear FM structure which can serve as pinning centers for domain walls and can lead to magnetic irreversibility effects. As was shown by Villain,[17] as a result of an interaction analogous to the Suhl–Nakamura interaction of nuclear spins, the deviation of the spins (polarization) propagates a finite distance from the diamagnetic impurity. Because of this, at a certain concentration of diamagnetic impurities the RLNs interact, i.e., overlap. Since the interaction potential between the RLNs varies with distance in proportion to r^{-3}, then for $T\to 0$ K, overlap of the RLNs can be expected even at comparatively low concentrations of diamagnetic impurities. In the presence of frustration the appearance of long-range correlations between the transverse components of the spins in the XY plane can correspond to a transition to a mixed FSG state with a spontaneous magnetization parallel to the Z axis. Its structure is analogous to the structure of the mixed state obtained by Gabey and Toulouse for Heisenberg magnets in the mean field model.

For $T>T_f$ the RLNs again become isolated. The presence of such inhomogeneities can give rise to additional degrees of freedom in the magnetic subsystem.[17] Indeed, for $0.9\leqslant x\leqslant 1.2$ in the region near T_f $(T>T_f)$ the temperature dependence of the magnetic part of the heat capacity displays broad, smeared maxima against the background of the $C(T)\propto T^{3/2}$ Bloch law trend.[19] Such behavior is illustrated by the results presented in Fig. 9 for $x=1.2$. As is seen from these data, with increasing distance from T_f new maxima appear and, on the whole, these irregular $C(T)$ curves lie lower than would be implied by a $T^{3/2}$ law.

With increasing degree of dilution the canted fraction of the spins increases, and ultimately the inhomogeneities become regions (clusters) with strong exchange, the linear dimensions of which can reach hundreds of angstroms.[19] Such a spatially inhomogeneous structure can be represented as two exchange-coupled subsystems—a matrix of frustrated spins with a weakened exchange and clusters with a strong internal exchange embedded in it. The type of magnetic ordering in the crystal is determined by the state of the matrix and can be of any sort—PM, FM, FSG, or SG.

In the Ga_xS and Ga_xM systems under discussion the signs of inhomogeneity are initially manifested as smearing of the trend of the low-field magnetization polytherms $\sigma_H(T)$ in the T_C region (see Figs. 1 and 2). The spatial inhomogeneity of all types of states is especially pronounced

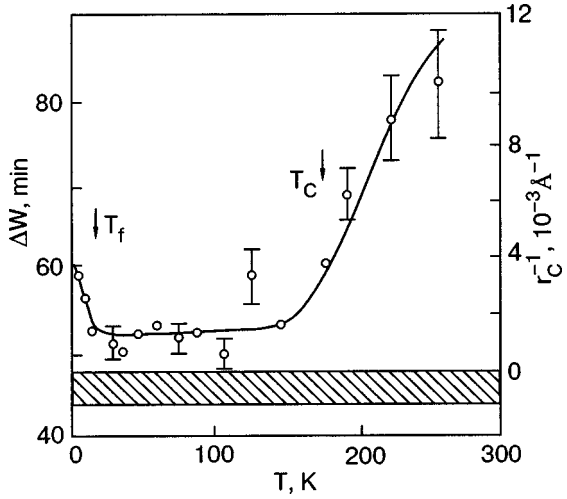

FIG. 13. Temperature dependence of the half-width of the magnetic reflection (111) for a $Ga_{1.35}S$ sample. The shaded region corresponds to the instrumental width with the error taken into account.

for concentrations x close to the multicritical point of the x-T diagram. For this reason in a very wide range of temperatures (certainly encompassing the PM region) both for $c<c_0$ and for $c>c_0$, the magnetization isotherms $\sigma_T(H)$ have exactly the same visual appearance: their shape is similar to the magnetization curve of a superparamagnet.[19]

An interesting effect confirming that the cluster model gives a realistic picture of the spatial inhomogeneity of the FM state was successfully observed in a $Ga_{1.4}S$ sample. For $T_f<T<T_C$ a relaxation of the magnetization is observed wherein, depending on the experimental (T-H) window the decrease of the magnetization could be either exponential or follow a logarithmic law with $S<0$ (Ref. 34). Such behavior is characteristic of an ensemble of superparamagnetic particles described by a broad but not monotonic distribution function $F(M)$.[35]

The correctness of the model in question is also confirmed by neutron diffraction data, both from the literature[2] and from a study which we carried out in collaboration with G. A. Takzeĭ and his co-workers at the Institute of Nuclear Research of the National Academy of Sciences of Ukraine for a $Ga_{1.35}S$ sample.[25] Figure 13 shows the temperature dependence of the half-width of the structural magnetic reflection, ΔW, which is proportional to the inverse correlation radius: $r_C=0.94\lambda/\Delta W\cos\theta$, where $\lambda=1.22$ Å, and θ is the neutron scattering angle. It is seen that as the temperature approaches T_C^+ (here the value of T_C is still quite well defined; see Fig. 1) the inverse correlation radius r_C^{-1} decreases in a practically linear manner but remains finite even for $T\leqslant T_C$ ($r_C\sim 600$ Å). Neutron diffraction results of this kind raised doubts as to the possibility that long-range FM order can exist in spatially inhomogeneous systems, even though the data of magnetic research in the majority of doubtful situations indicate that such order is preserved.

To resolve this contradiction an heuristic model based on the results of computer simulations was proposed in Ref. 36, according to which

$$r_C^{-1}(T)=r_0^{-1}(\Delta x)+r_{CT}^{-1}(T), \tag{7}$$

where $r_0(\Delta x)$ determines the mean size of a percolation cluster and depends on the proximity Δx of the concentration to the percolation threshold, and $r_{CT}(T)$ is the thermal correlation radius. The quantity $r_0^{-1}(\Delta x)$ remains finite in the whole temperature region $T \leqslant T_C$, and the transition at T_C, with the formation of long-range FM order, is due to the variation of $r_{CT}^{-1}(T)$.

The process of formation of states of the SG type is reflected by the low-temperature part of the $\Delta W(T)$ curve in Fig. 13. It is seen that for $T \to 0$ K a gradual decrease of $r_0(\Delta x)$ occurs, starting at T_f. This means that an ever greater number of spins are disordered, passing over from the cluster subsystem to the matrix subsystem of frustrated spins. However, inhomogeneities in the form of rather large ($l \sim 10^2$ Å for $x = 1.35$ in Ga_xS) ferrimagnetic clusters persist down to 0 K. For Ga_xS the FSG state for $0.9 \leqslant x < 1.2$ can probably be considered homogeneous in the sense that its structural units are individual frustrated spins. Only in this region of concentrations can the process of transition in temperature to the FSG state be considered as freezing of the transverse components of the spins in random directions. At a large Ga^{3+} concentration, i.e., $1.2 < x < 1.5$, the freezing process entails not only the spins of the frustrated matrix but also the clusters exchange-coupled to it, the sizes of which decrease for $T \to 0$ K. The freezing of the magnetic moments of the clusters for $T < T_f$ differs from the "superparamagnetic" process, since it is governed mainly by exchange forces and not by anisotropy. We note that the growth of $S(x)$ in the FSG region can evidently be regarded as an effect due to the influence of spatial inhomogeneity on the height of the intravalley energy barriers and the participation of clusters in SG relaxation processes.

For $c > c_0$, when the long-range FM order no longer present, "superparamagnetic" behavior is also observed for $1.5 < x \leqslant 1.7$ in the PM region near T_f. This means that the same spin-freezing process takes place in the SG states as that presented in Fig. 13. The data in Table I suggest that the Curie constant C, i.e., the size of the clusters in the PM region, begins to decrease sharply at $x > 1.6$. Consequently, the spatial inhomogeneity of the SG states also decreases. At $x = 1.9$ the SG can be considered homogeneous starting practically at the freezing temperature. However, for $x < 1.9$ the PM→SG transition is a transition between spatially inhomogeneous cluster states. With decreasing temperature in the interval $0\text{ K} < T < T_f$ the SG state becomes more and more homogeneous. The behavior in Ga_xM apparently follows the same general pattern.

4.3. New frustrated state and line of first-order thermodynamic phase transitions in the reentrant region of the *x*-*T* diagram

The causes of the different position of the $T_f(x)$ lines for Ga_xS and Ga_xM in the reentrant region of the x-T diagram is hard to explain in the conceptual framework discussed above. Of the distinguishing features of the model systems considered, almost no attention has been paid to their sublattice structure. Meanwhile, in many-sublattice ferrimagnetic oxides, diamagnetic substitution in different sublattices leads to unequal disturbance of the exchange.[13] As we have mentioned, a large role in the formation of the magnetic structure

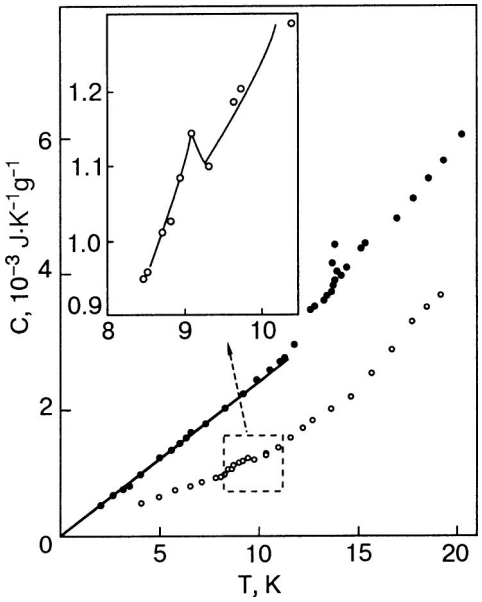

FIG. 14. Temperature dependence of the magnetic part of the heat capacity C for $Ga_{0.9}S$ (●) and $Ga_{0.8}S$ (○) samples. The inset shows a fragment of $C(T)$ for the $Ga_{0.8}S$ sample in the region of the second-order phase transition (the critical point on the $T_1(x)$ line; Fig. 8).

in the M-ferrite is played by magnetic ions of the R block (sublattices $2b$ and $4f_2$). They are separated by spinel blocks S containing 75% of the total number of magnetic ions. There are two possible ways that the substitution of the Fe^{3+} ions in the $2b$ sublattice in Ga_xM can influence the value of $T_f(x)$. The first of them is essentially within the framework of the traditional approach: removing the $2b$ ions from the exchange leads to an appreciable increase in the standard deviation J of the exchange in comparison with substitution in the spinel block. The second presupposes a qualitative rather than just quantitative influence of this substitution: weakening of the exchange coupling between spinel blocks can lead to a change in the type of spin ordering, namely, to the formation of a noncollinear structure. Such a change has been observed by neutron diffraction in the system $Ba_{12-x}In_xO_{19}$ (In_xM) for $x \geqslant 3.0$, when around 70% of the $2b$ positions are occupied by the nonmagnetic In^{3+} ions.[37] As a result of this, at $T \sim 110$ K a structure of the block spiral type is formed. We have done studies which show that in $In_{3.6}M$ at $T_f = 85$ K a transition to a cluster spin-glass state (PM–SG) occurs which exhibits the whole set of canonical hallmarks of the SG state which were listed above.[38–40]

This suggested the hypothesis that in the FSG region there should exist, in addition to the $T_C(x)$ and $T_f(x)$ lines, a third line of phase transitions, between the collinear (in the macroscopic sense) structure and a regular noncollinear FM structure. According to this hypothesis, the different behavior of the $T_f(x)$ lines for the Ga_xS and Ga_xM systems is due to two causes: different types of noncollinear structures that form on dilution; different stability of these noncollinear structures against the effects of frustration. For an experimental check of these hypotheses we first chose the simpler Ga_xS system and used the classical method of observing thermodynamic phase transitions—study of the temperature dependence of the magnetic part of the heat capacity. As is seen from the data in Figs. 9, 14, and 15, in the temperature

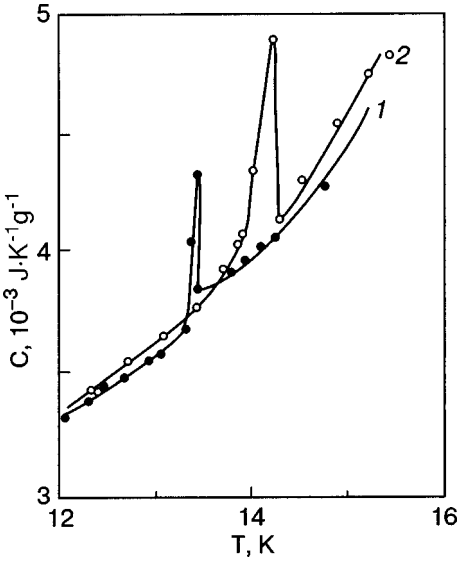

FIG. 15. Fragments of the $C(T)$ curves for $Ga_{0.9}S$ (curve *1*) and $Ga_{1.2}S$ (curve *2*) in the region of the first-order phase transition.

interval between T_f and T_C at $T_1(x)$ there indeed exists a first-order phase transition (PT-I) which is manifested as a very narrow and sharp peak on the $C(T)$ curve.[19,24] For $x=1.45$ and 1.4 at these same temperatures a sharp change of the magnetization is observed.[19] The $T_1(x)$ line on the phase diagram in Fig. 8 terminates in a critical point at $x=0.8$, since the phase transition at $x=0.8$ has the features of a second-order phase transition (PT-II); see Fig. 14. In particular, here there is no longer any hysteresis: the trend of $C(T)$ is the same on heating and cooling. For $T\to 0$ K the $C(T)$ curve obeys a spin-wave law $T^{3/2}$ rather than a linear law as for $x\geqslant 0.9$. For a $Ga_{0.7}S$ sample no anomalies on the $C(T)$ curves which would indicate the presence of a phase transformation are observed in the region 4.2–20 K.

The results obtained here confirm our hypothesis that a third line of phase transitions is present in the reentrant region of the x-T diagram. However, the observed PT-I in Ga_xS cannot be attributed to the formation of a regular noncollinear structure. The fact that the $T_1(x)$ line terminates in a critical point ($x=0.8$) means that it separates phases with the same symmetry. But at $T>T_1(x)$ this is an FM state with statistical noncollinearity (RLNs). Thus the results not only attest to the presence of a previously unknown PT-I line on the x-T diagram but also to the formation of some new frustrated thermodynamic phase at a lower temperature, a precursor in temperature to the FSG state. This radically alters the concepts of the mechanisms of formation of the FSG states developed in mean field theory and may serve as a stimulus for further theoretical and experimental research on frustrated magnetic states of the SG type.

We note in conclusion that although for Ga_xS ordered noncollinear structures are not realized in the entire concentration region, in the many-sublattice system Ga_xM such a variant cannot be completely ruled out *a priori*. Our results show that the concentration phase diagrams of frustrated systems can be much more complex than would follow from mean field theory. Further study of frustrated states in many-sublattice magnetic oxides are very promising in this connection.

CONCLUSION

As a result of a comprehensive study of magnetic and thermal properties of model frustrated systems of diluted ferrimagnetic oxides—the slightly anisotropic two-sublattice $Li_{0.5}Fe_{2.5-x}Ga_xO_4$ (Ga_xS) system and the highly anisotropic five-sublattice $BaFe_{12-x}Ga_xO_{19}$ (Ga_xM) system, which belong to the class of Heisenberg magnets with short-range interaction, we have obtained the following results.

For both systems there exists an interval of concentrations x with a distinct lower boundary within which the canonical hallmarks of states of the SG type are observed. In the presence of magnetic field the transition to these states at a temperature $T_f(H)$ occurs along lines of critical behavior which are predicted in mean field theory with an infinite radius for Heisenberg systems with random anisotropy: $\tau \propto H^{2/3}$ at low fields, and $\tau' \propto H^2$ at high fields.

We have obtained explicit evidence that all types of magnetic states have a spatially inhomogeneous structure of the cluster type at nonmagnetic ion concentrations of the order of 60–70%. In spite of this, the overall shape of the x-T concentration phase diagrams constructed on the basis of the results on canonical SG properties and the determination of the existence region of long-range FM order agree with the predictions of mean field theory. The x-T diagram has regions of FM and PM states and also two types of disordered states of the SG type: a mixed FSG state, in which FM and SG order coexist for $T<T_f$, and a "pure" spin glass, where the spontaneous magnetization $\sigma_s=0$. For the Ga_xS system the PM$\to$SG transition at $T=T_f$ can be described by a one-component order parameter q_{EA}. It is found that the concentration transition FSG$\to$SG at a concentration c_0 (the multicritical point of the x-T diagram) is accompanied not only by the vanishing of the FM order parameter (the spontaneous magnetization goes to zero) but also by a change in trend of the $S(x)$ curves—a jump-like change of the value of the magnetic viscosity coefficient, which is related to the height of the intravalley activation barriers and characterizes processes of long-term logarithmic relaxation of the nonequilibrium magnetization σ_{ZFC}.

The coincidence of the concentration boundaries of the disordered states of both types on the x-T diagrams for the slightly anisotropic and highly anisotropic systems attests to an exchange mechanism of formation of the spin-glass states, which, according to the results of a theoretical analysis, in Heisenberg systems with short-range interaction can be realized only in the presence of anisotropy. The $T_f(x)$ lines, the position of which in the FSG region ($c<c_0$) is noticeably different for Ga_xS and Ga_xM, draw together sharply with increasing distance from c_0 into the SG region ($c>c_0$). This confirms the theoretical conclusion that anisotropy does not have a large influence on the value of T_f in Heisenberg systems with short-range interaction. That value is determined mainly by the standard deviation J of the exchange.

We have established that the form of the x-T phase diagram of the Ga_xS system can be more complex than the canonical one. In the reentrant (FSG) region of the phase diagram between the lines of Curie points and $T_f(x)$ a new line of first-order thermodynamic phase transitions $T_1(x)$, terminating in a critical point at $x=0.8$, is observed. Thus between the FM and FSG states there exists a previously

unknown frustrated phase whose symmetry coincides with the symmetry of the FM state that precedes it in temperature.

The results of comprehensive studies of model frustrated systems based on diluted ferrimagnetic oxides have shown that the study of this class of magnets is very promising from the standpoint of extending the concepts of frustrated systems in general and of the mechanisms of formation of states of the SG type in particular.

*E-mail: Alexander.V.Vankevich@univer.kharkov.ua

[1] K. M. Fischer, Phys. Solid State **116**, 357 (1983); **130**, 13 (1985).
[2] K. Binder and A. P. Young, Rev. Mod. Phys. **58**, 801 (1986).
[3] I. Ya. Korenblit and E. F. Shender, Usp. Fiz. Nauk **157**, 267 (1989) [Sov. Phys. Usp. **32**, 139 (1989)].
[4] S. L. Ginzburg, *Irreversible Phenomina in Spin Glasses* [in Russian], Nauka, Moscow (1989).
[5] S. Kirkpatrick and D. Sherrington, Phys. Rev. Lett. **35**, 1792 (1975); Phys. Rev. B **17**, 4384 (1978).
[6] V. S. Dotsenko, Usp. Fiz. Nauk **163**, 1 (1993).
[7] C. M. Newman and D. L. Stein, J. Phys.: Condens. Matter **15**, R1319 (2003).
[8] A. T. Ogielski, Phys. Rev. B **32**, 7384 (1985).
[9] B. W. Morris, S. G. Colborne, M. A. Moore, A. J. Bray, and J. Canisius, J. Phys. C **19**, 1157 (1986).
[10] W. M. Saslow and G. Parker, Phys. Rev. Lett. **56**, 1074 (1986).
[11] J. R. Tomson, Hong Guo, D. Y. Ruan, M. J. Zuckerman, and M. Grant, Phys. Rev. B **45**, 3129 (1992).
[12] S. M. Zhilyakov, Izvestiya Vyssh. Uchebn. Zaved., Ser. Fizika **27**, 105 (1984).
[13] N. N. Efimova, *Author's Abstract of Candidate's Dissertation* [in Russian and Ukrainian], Kharkov (1977).
[14] M. I. Darby and E. D. Isaac, IEEE Trans. Magn. **MAG-10**, 259 (1974).
[15] J. B. Goodenough, *Magnetism and the Chemical Bond*, Interscience, New York (1963), Metallurgiya, Moscow (1968).
[16] G. Albanese, Nuovo Cimento Soc. Ital. Fis., B **58**, 480 (1968).
[17] J. Villain, Z. Phys. B: Condens. Matter **33**, 31 (1979).
[18] N. N. Efimova, Yu. A. Popkov, and N. V. Tkachenko, Zh. Éksp. Teor. Fiz. **90**, 1413 (1986) [Sov. Phys. JETP **63**, 827 (1986)]; Zh. Éksp. Teor. Fiz. **97**, 1208 (1990) [Sov. Phys. JETP **70**, 678 (1990)]; Fiz. Nizk. Temp. **14**, 981 (1988) [Sov. J. Low Temp. Phys. **14**, 539 (1988)]; Fiz. Nizk. Temp. **15**, 1055 (1989) [Sov. J. Low Temp. Phys. **15**, 585 (1990)]; Fiz. Nizk. Temp. **16**, 1565 (1990) [Sov. J. Low Temp. Phys. **16**, 881 (1990)]; Phys. Status Solidi **154**, 333 (1989).
[19] N. N. Efimova, Zh. Éksp. Teor. Fiz. **113**, 1039 (1998) [JETP **86**, 731 (1998)]; JETP Lett. **67**, 329 (1998); Fiz. Nizk. Temp. **23**, 1067 (1997) [Low Temp. Phys. **23**, 802 (1997)]; Fiz. Nizk. Temp. **24**, 1063 (1998) [Low Temp. Phys. **24**, 797 (1998)].
[20] N. N. Efimova, N. V. Tkachenko, and I. I. Bokovoĭ, Fiz. Tverd. Tela (Leningrad) **31**(6), 254 (1989) [Sov. Phys. Solid State **31**, 1059 (1989)].
[21] N. N. Efimova, V. A. Pervakov, V. I. Ovcharenko, and M. Yu. Tyutryumova, Fiz. Tverd. Tela (St. Petersburg) **35**, 2838 (1993) [Phys. Solid State **35**, 1405 (1993)].
[22] N. N. Efimova and M. B. Ustimenkova, Zh. Éksp. Teor. Fiz. **114**, 2065 (1998) [JETP **87**, 1122 (1998)].
[23] N. N. Efimova, S. R. Kufterina, A. G. Anders, S. V. Startsev, A. M. Gurevich, and V. N. Eropkin, Fiz. Nizk. Temp. **24**, 337 (1998) [Low Temp. Phys. **24**, 255 (1998)].
[24] A. G. Anders, N. N. Efimova, S. R. Kufterina, A. M. Gurevich, and V. N. Eropkin, Visnik KhDU im. V. N. Karazina, No. 558, Seriya Fizika, vip. **6**, 67 (2002).
[25] N. N. Efimova, Yu. A. Popkov, G. A. Takzeĭ, A. B. Surzhenko, and A. M. Dvoeglazov, Fiz. Tverd. Tela (St. Petersburg) **36**, 490 (1994) [Phys. Solid State **36**, 271 (1994)].
[26] S. F. Edwards and P. W. Anderson, J. Phys. F: Met. Phys. **5**, 965 (1975).
[27] F. V. Goltsev, Phys. Solid State **B126**, 537 (1984).
[28] K. H. Fischer, Z. Phys. B: Condens. Matter **60**, 151 (1985).
[29] S. V. Vonsovskiĭ, *Magnetism*, Vols. 1 and 2, Wiley, New York (1974), Nauka, Moscow (1971).
[30] L. V. Kirenskiĭ, A. I. Drokin, and D. A. Lapteĭ, *Temperature Magnetic Hysteresis of Ferromagnets and Ferrites* [in Russian], Sibirsk. Otd. Akad Nauk SSSR (1965).
[31] N. N. Efimova, V. B. Valiĭov, S. R. Kufterina, M. B. Ustimenkova, V. A. Desnenko, and A. S. Panfilov, Visnik KhDU im. V. N. Karazina, Seriya Fizika, No. 440, 119 (1999).
[32] C. N. Guy, J. Phys. F: Met. Phys. **8**, 1309 (1978).
[33] F. Arrott and J. E. Noaker, Phys. Rev. Lett. **19**, 786 (1967).
[34] N. N. Efimova and M. B. Ustimenkova, J. Magn. Magn. Mater. **185**, 360 (1998).
[35] Yu. I. Petrov, *Physics of Small Particles* [in Russian], Nauka, Moscow (1982).
[36] R. J. Birgeneau, R. A. Cowley, G. Shirane *et al.*, Phys. Rev. B **21**, 317 (1980).
[37] M. I. Namtalishvili, O. P. Aleshko-Ozhevskiĭ, and I. I. Yamzin, Fiz. Tverd. Tela (Leningrad) **13**, 2543 (1971) [Sov. Phys. Solid State **13**, 2137 (1972)].
[38] N. N. Efimova, N. V. Tkachenko, and A. V. Borisenko, Fiz. Tverd. Tela (Leningrad) **29**, 1331 (1987) [Sov. Phys. Solid State **29**, 762 (1987)].
[39] N. N. Efimova and N. V. Tkachenko, Fiz. Tverd. Tela (Leningrad) **33**, 1583 (1991) [Phys. Solid State **33**, 891 (1991)].
[40] A. G. Anders, N. N. Efimova, V. B. Valiev, S. R. Kufterina, A. M. Gurevich, A. I. Krivchikov, A. V. Terekhov, and T. V. Chagovets, Fiz. Tverd. Tela (St. Petersburg) **29**, 406 (2003) [Phys. Solid State **29**, 305 (2003)].

Translated by Steve Torstveit

Magnetic resonance studies of the low-dimensional magnet $NaFe(WO_4)_2$

K. G. Dergachev, M. I. Kobets, and E. N. Khatsko*

B. Verkin Institute for Low Temperature Physics and Engineering, National Academy of Sciences of Ukraine, pr. Lenina 47, Kharkov 61103, Ukraine

(Submitted August 20, 2004; revised September 7, 2004)
Fiz. Nizk. Temp. **31**, 530–535 (May 2005)

Magnetic resonance studies of the low-dimensional monoclinic compound $NaFe(WO_4)_2$ are carried out in the frequency range 25–142 GHz and temperature range 1.8–300 K. The EPR data near the phase transition attest to the two-dimensionality of the magnetic structure of $NaFe(WO_4)_2$. The frequency-field relation of the AFMR spectrum shows that this compound is a biaxial antiferromagnet. The characteristic parameters of the AFMR energy spectrum are determined: the values of the energy gaps $\nu_1=141$ GHz and $\nu_2=168.7$ GHz, the anisotropy fields $H_{a1}=10.5$ kOe and $H_{a2}=15$ kOe, and the exchange field $H_e=121$ kOe. The ratio of the intralayer to the interlayer exchange is estimated. Additional absorption is observed due to local modes caused by destruction of the translational order of the magnetic structure. © *2005 American Institute of Physics.* [DOI: 10.1063/1.1925387]

INTRODUCTION

The double molybdates and tungstenates $MR(XO_4)_2$, where M is a monovalent alkali-metal ion, R is a rare-earth or transition-metal ion, and X is molybdenum or tungsten, form a wide class of substances that includes a number of families of different symmetry of the crystal structure, from tetragonal to triclinic. This class of compounds is of interest because of a number of features due to the low symmetry of the crystal lattice, the relatively small value of the exchange, the substantial role of the dipole-dipole interaction of the magnetic ions, and, most often, the low dimensionality of the magnetic structure and the competition of the magnetic and electric interactions, which determines the energy spectrum of the magnetic ion.

Iron sodium double tungstenate $NaFe(WO_4)_2$ belongs to the monoclinic system $P2/c$. The unit cell parameters are $a=9.88$ Å, $b=5.72$ Å, $c=4.94$ Å, $\beta=(90\pm5)°$ (Ref. 1). Unlike the other transition-metal double tungstenate compounds, the $NaFe(WO_4)_2$ single crystal has a layered crystal structure (Fig. 1a). The magnetic ion is iron Fe^{3+} with a ground state $^6S_{5/2}$ ($L=0$, $S=5/2$). The Na^+ and Fe^{3+} ions form layers of identical ions in planes parallel to the bc plane, and the layers of iron and sodium alternate along the a direction (Fig. 1b). Along the c axis in the layer the Fe^{3+} ions form zigzag chains with a shortest $Fe^{3+}-Fe^{3+}$ distance equal to 3.085 Å (see Fig. 1). The $Fe^{3+}-Fe^{3+}$ distance along the b axis in the bc plane is 5.72 Å, which is almost twice as large as the shortest $Fe^{3+}-Fe^{3+}$ distance in the chain. The distance between the nearest magnetic ions along the a direction (9.88 Å) is considerably larger than in the other crystallographic directions. This makes for a two-dimensional *crystallographic* structure with a chain structure in the layer. Measurements of the temperature dependence of the principal values of the magnetic susceptibility of the $NaFe(WO_4)_2$ single crystal[2] have shown that a magnetic phase transition to an ordered state occurs at a temperature $T_N=4$ K. The magnetic axis y coincides with a twofold axis directed along the crystallographic b axis, while the directions of the magnetic axes x and z in the basal plane ac depend on temperature, and below the magnetic ordering point they are turned by 45° with respect to the a and c crystallographic axes. At high temperatures the susceptibility is well described by a Curie–Weiss law with a negative Curie constant $\Theta=-19$ K. This attests to the antiferromagnetic character of the exchange. Above the Néel point a broad maximum of the susceptibility is observed ($T_{max}\approx15$ K), characteristic for low-dimensional magnets. The circumstances described above made this compound an interesting object for study of its resonance properties in both the paramagnetic and ordered regions, and, moreover, the comparatively high Néel point (4 K) made it possible to carry out an AFMR study in a convenient temperature range for our experimental setup.

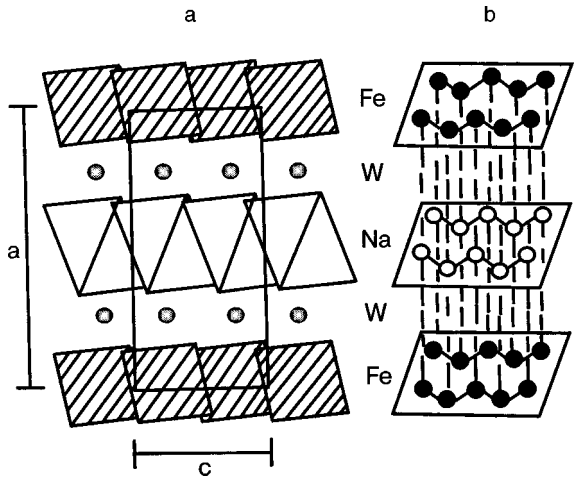

FIG. 1. a—Fragment of the crystal structure of $NaFe(WO_4)_2$ in the ac plane.[1] One can see the octahedral chains of Fe ($x=0$) and Na ($x=0.5$). b—Layers of the magnetic Fe^{3+} ions separated by layers of the nonmagnetic Na^+ ions.

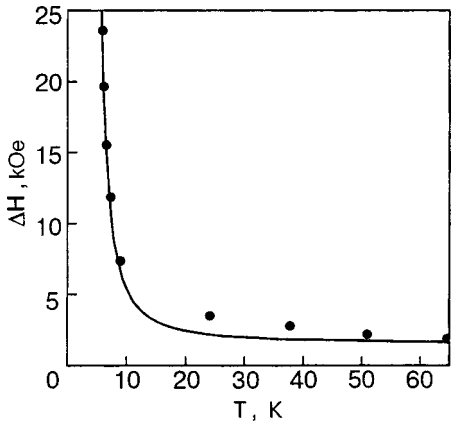

FIG. 2. Temperature dependence of the EPR spectrum in $NaFe(WO_4)_2$. The solid curve corresponds to Eq. (2) with the parameter values given in the text.

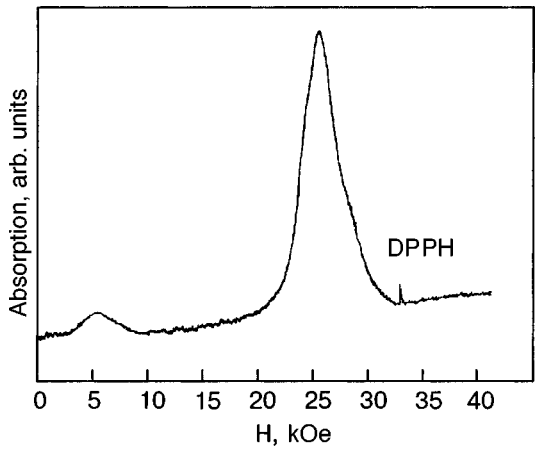

FIG. 3. Shape of the absorption spectrum of the AFMR in $NaFe(WO_4)_2$ for $\mathbf{H}\|\mathbf{l}$ and $T=1.8$ K at a frequency of 97.48 GHz. DPPH is the reference absorption line of diphenylpicrylhydrazyl.

RESULTS AND DISCUSSION

The measurements were made on a forward-gain radio spectrometer in the frequency range 25–142 GHz, in the temperature interval 1.8–100 K, and in magnetic fields up to 80 kOe. In the paramagnetic region for refinement of the magnetic phase transition temperature T_N at a frequency of 78.1 GHz we carried out temperature measurements of the EPR spectrum of the Fe^{3+} ion in $NaFe(WO_4)_2$. The transition temperature determined from the vanishing of the EPR line is equal to $T_N=3.8\pm0.1$ K, in good agreement with the susceptibility data.[2] The experimental temperature dependence of the EPR linewidth is shown in Fig. 2. The broadening of the EPR line with decreasing temperature as the magnetic ordering temperature is approached is due to growth of critical fluctuations of the short-range magnetic order near T_N. Such a mechanism of broadening of the EPR linewidth near the transition temperature can be described in the three-dimensional case by an expression of the form

$$\Delta H=\Delta H_\infty\left(\frac{T-T_N}{T}\right)^{-\alpha}, \tag{1}$$

where ΔH_∞ is the linewidth in the high-temperature limit.

For $NaFe(WO_4)_2$ the parameters in this formula have the values $\Delta H_\infty=1.5$ kOe and $\alpha=2.5$.

Although the theoretical curve (1) describes the experiment quite satisfactorily in the temperature range $T_N<T<15$ K, such a large value of the exponent α is atypical for a three-dimensional magnet. Since the crystallographic two-dimensionality most likely causes lowering of the magnetic dimension, let us try to describe the behavior of the EPR linewidth in the model of a two-dimensional antiferromagnet. Such a model has been considered in the papers by Huber and Seehra,[3] Richards,[4] and others. According to the theory of Ref. 3, the expression for the EPR linewidth for a two-dimensional antiferromagnet near T_c has the form

$$\Delta H=\Delta H_\infty\left[1+C\left(\frac{T-T_N}{T_N}\right)^{-p}\right], \tag{2}$$

where C is a constant, and the exponent p lies in the range 1.5–1.71.

In our case $p=1.5$ (the solid curve in Fig. 2), indicating a low dimension of the magnetic system. Furthermore, the wide temperature interval (in comparison with T_N) in which the EPR linewidth is described by expression (2) (see Fig. 2) is also typical for low-dimensional magnets.

Further resonance studies of the $NaFe(WO_4)_2$ single crystal were carried out in the magnetically ordered state at a temperature of 1.8 K. The frequency-field curves of the AFMR spectrum were investigated in the frequency range 25–142 GHz at magnetic fields up to 60 kOe. An example of the recorded absorption spectrum at a frequency of 97.48 GHz is shown in Fig. 3. The form of the frequency-field curve of the AFMR along the easy axis z, which lies in the ac plane and is turned 45° with respect to the a and c axes, is shown in Fig. 4. At $H=0$ there is a gap $\nu_1=141\pm1$ GHz in the spin-wave spectrum. We used the value of the gap in zero field to determine the value of the effective magnetic anisotropy field by the known formula

$$\nu_1=(2H_{a1}H_e)^{1/2}. \tag{3}$$

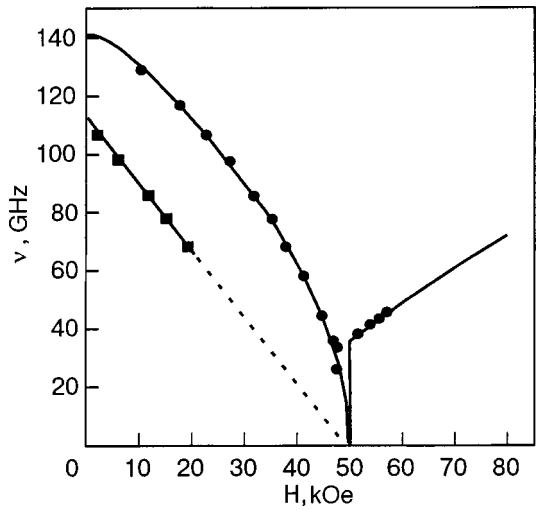

FIG. 4. Frequency-field diagram of the AFMR spectrum along the easy axis for $T=1.8$ K: ●—AFMR in the collinear and canted phases; ■—local mode. The solid lines correspond to Eqs. (6), (7), and (9) for the parameter values indicated in the text. The dashed line is the extension of relation (9) for convenience of inspection.

We could not see an exchange branch even with the use of a pulsed technique (maximum field $H \approx 220$ kOe), and therefore the value of H_e was determined from magnetic measurements.[2]

One can determine the value of the ''strong'' exchange interaction from an estimate for the case of a plane Heisenberg lattice and spin 5/2 (Ref. 5):

$$\frac{kT_{\chi\,\max}}{JS(S+1)} = 2.05, \tag{4}$$

where $T_{\chi\,\max}$ is the temperature of the maximum on the susceptibility curve $\chi(T)$, k is Boltzmann's constant, J is the exchange, and S is the spin. When the values are put in we obtain $J = 0.815$ K.

Let us now estimate the exchange field H_e using the standard expression

$$H_e = 2\frac{z_i J_i S}{g\mu_B}, \tag{5}$$

where H_e is the exchange field acting on an atom, z_i is the number of ith-nearest neighbors of a given atom, g is the g factor, and μ_B is the Bohr magneton. We obtain the estimates $H_e \approx 121$ kOe and, from expression (3), $H_{a1} = 10.5$ kOe.

The observed frequency-field curve of the resonance along the easy axis z, shown in Fig. 4, agrees with the theoretical description of the branches of the spectrum in the collinear and spin-flop phase for a biaxial antiferromagnet for an orientation of the external magnetic field **H** along the antiferromagnetic vector **l**.

When the external magnetic field H is less than the field of the spin-flop transition, $H_{sf} = \sqrt{2H_{a1}H_e}$, the observed AFMR in the collinear phase ($\mathbf{H} \| \mathbf{l}$; $\mathbf{m} = 0$) for the descending branch is described by an expression of the form[7]

$$(\nu/\gamma)^2 = \frac{1}{2}\{H^2 + C_1 + C_2 - [H^4 + 2H^2(C_1 + C_2) + (C_2 - C_1)^2]^{1/2}\}, \tag{6}$$

where $\gamma = \mu_B g$, $C_1 = 2H_{a1}H_e$, and $C_2 = 2H_{a2}H_e$.

At the field $H = H_{sf}$ a first-order magnetic phase transition is observed; the reorientation of the antiferromagnetic vector occurs by a jump in the layer plane ac toward an intermediate axis.

Above the spin-flop field, $H > H_{sf}$, the field dependence of the frequency has the form

$$(\nu/\gamma)^2 = H^2 - H_{sf}^2. \tag{7}$$

Expressions (6) and (7) give a satisfactory description of the experimental $\nu(H)$ curves (see Fig. 4) with the following parameter values: $H_e = 121$ kOe, $H_{a1} = 10.5$ kOe, $H_{a2} = 15$ kOe.

The second anisotropy field H_{a2} found in this way permits determination of the second gap in the AFMR spectrum: $\nu_2 = \sqrt{2H_{a2}H_e} = 168.7$ GHz. Of course, for our experimental capabilities (maximum frequency ≈ 140 GHz and magnetic fields not over 80 kOe) we could not measure the frequency-field curve of the AFMR spectrum for the magnetic field orientation along the x and y axes for observation of the high-frequency gap.

For the description of the magnetic and resonance properties of highly anisotropic low-dimensional compounds it is important to determine the value of the interaction constant for the strong intralayer exchange in relation to that for the weak interlayer interaction, which stabilizes the long-range magnetic order. In Refs. 8 and 9 relations were found between the critical temperature of the transition to the ordered state and the exchange constants for an anisotropic low-dimensional Heisenberg magnet. Let us estimate the value of the interlayer exchange interaction J' using the following relation from Ref. 9:

$$1 \approx \frac{S^2 J'}{T_N}\exp\left[4\pi\left(\frac{zS^2 J}{T_N} - 1\right)\right], \tag{8}$$

where J is the exchange integral in the plane and J' is the interplane exchange integral. Substitution of the corresponding parameters gives a value $J' \sim 10^{-6}J$. Estimates for low-dimensional magnets[10] give values of the ratio J'/J in the range 10^{-3}–10^{-20}, and so, in spite of its small value, the estimate obtained for the ratio J'/J is reasonable.

For the existence of a phase transition in a low-dimensional Heisenberg magnets the presence of single-ion anisotropy is important, since for an isotropic low-dimensional Heisenberg magnet there is no transition at finite temperatures.[11]

Therefore the magnetic ordering in $NaFe(WO_4)_2$ at a relatively high temperature ($T_N = 3.8$ K) is due to substantial intralayer anisotropy. Here the ordering is of a two-dimensional character. The magnetic structure of the given compound consists of very weakly coupled (almost independent) layers whose structure is determined by the large ($H_e = 121$ kOe) intralayer exchange and anisotropy ($H_{a1} = 10.5$ kOe, $H_{a2} = 15$ kOe), i.e., the dynamic properties of such a magnet are close to those of the static model of independent ordered layers.

Such a state is rarely uniform; a domain structure arises at the transition to the ordered state, and for a low-dimensional structure, unlike a three-dimensional one, the width of a domain wall is of the order of the interatomic distances. In this case the domain boundaries can be treated as topological defects. In the case of a two-dimensional (or one-dimensional) antiferromagnet it is possible to have statistical metastable destruction of the ideal translational order of the magnetic structure: a domain wall, an inverted layer, and other such magnetic translational defects. This gives rise to additional absorption lines, the so-called local AFMR modes. They are due to the ''incorrect'' orientation of the antiferromagnetic vector in one or several layers. The physical cause of the local modes is the proximity of the energies of the magnetic interactions establishing the mutual orientation of the magnetic moments of neighboring layers (or within a layer) and the energies of the different sorts of imperfections that fix a given orientation of the antiferromagnetic vector. According to a theoretical treatment[13] for a layered antiferromagnet the presence of translational defects leads to an additional absorption line with a frequency below the main resonance frequency.

Such lines have indeed been observed in experiment. As is seen in Fig. 4, besides the resonance, which we interpret as an acoustic mode of antiferromagnetic resonance, an addi-

tional broad line has been observed at magnetic fields below the resonance field of the acoustic mode. In our opinion the additional absorption observed can be attributed to the magnetic defects described above. The integrated intensity of the additional line, which is nearly 100 times weaker than the acoustic mode, and also its width depend on the quality of the sample and the cooling conditions. The optimal polarization for the local mode of AFMR is $\mathbf{h}\|\mathbf{H}$. In zero magnetic field at a temperature of 1.85 K the frequency of the gap of the additional excitation is equal to $\nu_{0L}=113\pm1$ GHz. Although the angular dependence of the additional line parallels the acoustic mode of AFMR and does not cross it anywhere, its frequency-field relation, unlike that of the acoustic mode, is described by an expression linear in the field, of the type

$$\nu_L=\nu_{0L}-cH. \tag{9}$$

It is seen (Fig. 4) that the frequency of the local mode should go to zero at the same field as the acoustic mode. With decreasing frequency this line decreases in intensity, becoming hard to observe, and at frequencies below 60 GHz it vanishes. It can be assumed that the number of magnetic defects decreases with increasing external magnetic field.

Generally speaking, the presence of an additional line can be due to other causes such as impurities, a spin-cluster resonance, and two-magnon subthreshold absorption.

Let us consider these possibilities.

In the presence of a magnetic impurity an additional absorption line should be observed in the paramagnetic state also, but it was not observed in the experiment. In the case that the frequency of the impurity line at zero magnetic field lies below the frequency of the main resonance (as in our case), its presence also leads to destruction of the translational symmetry of the crystal, giving rise to what is known in the literature as localized impurity states (see the monograph by Izyumov and Medvedev).[14] The condition of localization of impurity excitations is that they be far enough away in energy from the excitations of the host. In the case when they approach the AFMR line a coupled state arises—the impurity line is enhanced and splitting of the absorption line is observed, accompanied by a transfer of intensity from one line to another, but we observed no such modification of the spectrum, either.

The spin-cluster resonance is observed only in highly anisotropic Ising systems. We are dealing with a Heisenberg magnet.

The formation of this absorption line in the AFMR spectrum at $T=1.8$ K may also have its origin in subthreshold two-magnon absorption (STA), which is specific to low-dimensional magnets. Without going into details, we note that, according to the papers by Anders, Zvyagin, *et al.*,[15,16] in low-dimensional magnets STA bands with both the sum $(\nu_1+\nu_2)$ and difference $(\nu_1-\nu_2)$ frequencies can be observed. When the external magnetic field **H** is oriented along the easy axis only the difference STA bands can be observed below the magnon gap. In our case the lower boundary for the appearance of the STA is 28 GHz, which is far from the experimentally observed lines. In addition, the frequency of the STA lines increases with increasing field, whereas in our case the situation is the opposite (Fig. 4).

Therefore, in view of what we have said above, the first explanation of the cause of the additional absorption line is to be preferred—a local mode caused by the destruction of the translational order in the magnetic system.

CONCLUSIONS

1. The EPR spectrum investigated in the vicinity of the phase transition attest to the two-dimensionality of the magnetic structure of $NaFe(WO_4)_2$.

2. The frequency-field dependence of the AFMR in $NaFe(WO_4)_2$, measured in the ordered phase at $T=1.8$ K, shows that this compound is a biaxial antiferromagnet.

3. The characteristic parameters of the AFMR energy spectrum have been determined: the energy gaps $\nu_1=141$ GHz and $\nu_2=168.7$ GHz, the anisotropy fields $H_{a1}=10.5$ kOe and $H_{a2}=15$ kOe, and the energy field $H_e=121$ kOe. The ratio of the intra- and interlayer exchange constants has been estimated.

4. Additional absorption has been observed which is due, we believe, to local modes resulting from the destruction of the translational order of the magnetic structure.

In closing the authors thank A. S. Kovalev for a helpful discussion of the results of this study and for useful ideas for their interpretation, and A. A. Stepanov for support and interest in this study.

*E-mail: khatsko@ilt.kharkov.ua

[1] P. V. Klevtsov and R. F. Klevtsova, J. Solid State Chem. **2**, 278 (1970).
[2] A. G. Anders, A. I. Zvyagin, P. S. Kalinin, E. N. Khats'ko, and V. G. Yurko, Fiz. Nizk. Temp. **1**, 1013 (1975) [Sov. J. Low Temp. Phys. **1**, 485 (1975)].
[3] D. L. Huber and M. S. Seehra, Phys. Lett. **43**, 311 (1973).
[4] P. M. Richards, Solid State Commun. **13**, 253 (1973).
[5] L. J. de Jongh, in *Magnetism and Magnetic Materials*, in *Proceedings of the 18th Annual Conference, Denver, 1972*, edited by C. D. Graham and J. Rhyne, AIP Conf. Proc. **10**, 561 (1972).
[6] J. S. Smart, *Effective Field Theories of Magnetism*, Saunders, London (1966), Mir, Moscow (1968).
[7] T. Nagamiya, K. Yosida, and R. Kubo, Adv. Phys. **4**, 1 (1955).
[8] S. B. Khokhlachev, Zh. Eksp. Teor. Fiz. **70**, 265 (1976) [Sov. Phys. JETP **43**, 137 (1976)].
[9] V. A. Slyusarev and R. P. Yankelevich, Fiz. Nizk. Temp. **3**, 1175 (1977) [Sov. J. Low Temp. Phys. **3**, 570 (1977)].
[10] L. J. de Jongh and A. R. Miedema, Adv. Phys. **23**, 1 (1974).
[11] N. D. Mermin and H. Wagner, Phys. Rev. Lett. **17**, 1133 (1966).
[12] A. A. Stepanov and D. A. Yablonskii, Fiz. Nizk. Temp. **15**, 215 (1989) [Sov. J. Low Temp. Phys. **15**, 122 (1989)].
[13] A. N. Goncharuk, A. A. Stepanov, and D. A. Yablonskiĭ Fiz. Tverd. Tela (Leningrad) **31**(12), 132 (1989) [Sov. Phys. Solid State **31**, 2099 (1989)].
[14] Yu. A. Izyumov and M. V. Medvedev, *Magnetically Ordered Crystals Containing Impurities*, Consultants Bureau, New York (1973), Nauka, Moscow (1971), Russ. p. 271.
[15] A. G. Anders, A. I. Zvyagin, Yu. V. Pereverzev, A. I. Petutin, and A. A. Stepanov, J. Phys. (Paris) **39**, Suppl. II, C6-739 (1978).
[16] A. G. Anders, A. I. Zvyagin, and A. I. Petutin, Fiz. Nizk. Temp. **6**, 491 (1980) [Sov. J. Low Temp. Phys. **6**, 234 (1980)].

Translated by Steve Torstveit

On the theory of electromagnetic fields radiated by an elastic wave in a ferromagnet

Yu. A. Kolesnichenko* and D. I. Stepanenko

B. Verkin Institute for Low Temperature Physics and Engineering, National Academy of Sciences of Ukraine, pr. Lenina 47, Kharkov 61103, Ukraine

(Submitted September 13, 2004)
Fiz. Nizk. Temp. **31**, 536–541 (May 2005)

The generation of electromagnetic oscillations by a sound wave in a substance having magnetic order is investigated under conditions of the normal skin effect. The amplitude of the electric field and the phase difference of the electromagnetic and sound waves are calculated as functions of the saturation magnetization, anisotropy energy, magnetostriction constants, and other parameters characterizing the magnetic material. © *2005 American Institute of Physics.*
[DOI: 10.1063/1.1925367]

Interest in the theoretical study of the interconversion of electromagnetic and sound waves in ferromagnetic metals has heightened in the last decade in connection with the discovery of a family of rare-earth (R) nickel borocarbides (RNi_2B_2C),[1–4] a significant number of which have magnetic order. With the same crystal structure, the borocarbides can exhibit a transition to the superconducting state (R=Y, Lu), possess heavy-fermion properties (R=Yb), or demonstrate coexistence of superconductivity and magnetism (R=Tm, Er, Ho, Dy) or only magnetic ordering (R=Tb, Gd). The superconducting borocarbides are among the so-called unconventional superconductors, the order parameter in which corresponds to $s+g$ symmetry,[5–7] in contrast to the isotropic s-wave pairing in ordinary metals. Experimental and theoretical study of the magnetoacoustic processes in magnetic borocarbides in the normal state can elucidate the influence of the magnetic order on their kinetic and thermodynamic characteristics. Besides the mechanisms of interconversion of the boson branches of the spectrum which are inherent to normal metals,[8,9] magnetic materials have specific mechanisms of excitation and interaction of sound, spin, and electromagnetic waves. Because of the magnetoelastic interaction, the propagation of elastic waves in ferromagnets and antiferromagnets is accompanied by oscillations of the magnetization. Although magnetoacoustic oscillations have been widely studied theoretically (see, e.g., Refs. 10 and 11) those studies were limited to the approximation of magnetostatics, and the electric fields were not considered in them. In the present paper we study the generation of electromagnetic oscillations by a sound wave in substances having magnetic order. We consider the case realized in practice wherein the electrons responsible for the magnetic properties are localized in lattice atoms, and the mean free time of the conduction electrons τ_e is short in relation to the frequencies of the alternating fields and the electron cyclotron frequency in the external magnetic field.

We start from the following expression for the energy density of a ferromagnet:

$$w_\Sigma = w_e(\mathbf{M}^2) + w_a(\mathbf{M}) + \frac{1}{2}\alpha_{ik}\frac{\partial \mathbf{M}}{\partial x_i}\cdot\frac{\partial \mathbf{M}}{\partial x_k} + \frac{\mathbf{H}^{(m)^2}+\mathbf{E}\cdot\mathbf{D}}{8\pi} - \mathbf{M}\cdot\mathbf{H}^{(\mathrm{ext})} + \frac{1}{2}\rho\dot{\mathbf{u}}^2 + \frac{1}{2}\eta_{iklm}u_{ik}u_{lm} + f_{ik}(\mathbf{M})u_{ik} + \mathcal{E}(\mathbf{r},t). \quad (1)$$

Here $w_e(\mathbf{M}^2)$ is the exchange energy, $w_a(\mathbf{M})$ is the anisotropy energy, the third term is the exchange energy due to the nonuniformity of the magnetic moment density $\mathbf{M}$. The fourth and fifth terms are the energy of the electromagnetic field and the energy of the magnetic moment in an external uniform magnetic field $\mathbf{H}^{(\mathrm{ext})}$; $\mathbf{H}^{(m)}$ is the magnetic field produced by the magnetization, $\mathbf{E}$ and $\mathbf{D}$ are the electric field and electric displacement, respectively. The next three terms determine the elastic and magnetostriction energies; ρ is the density of the ferromagnet, $\mathbf{u}$ is the displacement vector of the lattice points with coordinates $\mathbf{r}$ at time t, $\dot{\mathbf{u}}$ is the time derivative, η_{iklm} is the tensor of elastic constants, u_{ik} is the strain tensor, and f_{ik} is the tensor characterizing the magnetostriction.

The energy of the system of conduction electrons with a dispersion relation $\varepsilon_0(\mathbf{p})$ can be written in the form[12]

$$\mathcal{E}(\mathbf{r},t) = \int \frac{2d^3p}{(2\pi\hbar)^3}[\varepsilon_0(\mathbf{p}) + \delta\varepsilon(\mathbf{r},\mathbf{p},t)]f(\mathbf{r},\mathbf{p},t), \quad (2)$$

where $\delta\varepsilon(\mathbf{r},\mathbf{p},t) = \lambda_{ik}(\mathbf{p})u_{ik} - (\mathbf{p} - m\partial\varepsilon_0/\partial\mathbf{p})\dot{\mathbf{u}}$ is the additional energy of an electron in the field of a sound wave, $\lambda_{ik}(\mathbf{p})$ is the deformation potential,[13] and m is the free electron mass. The distribution function $f(\mathbf{r},\mathbf{p},t)$ of the electronic system perturbed by alternating fields is conveniently represented as the sum of an instantaneous equilibrium distribution function and a nonequilibrium admixture:

$$f(\mathbf{r},\mathbf{p},t) = f_0(\varepsilon_0(\mathbf{p}) + \delta\varepsilon(\mathbf{r},\mathbf{p},t) - \delta\mu) - \psi(\mathbf{r},\mathbf{p},t)\frac{\partial f_0(\varepsilon_0)}{\partial\varepsilon_0}, \quad (3)$$

where $f_0(\varepsilon_0(\mathbf{p}))$ is the Fermi function, $\delta\mu = u_{ik}\langle\lambda_{ik}\rangle/\langle 1\rangle$ is the variation of the chemical potential determined from the condition of conservation of electron density, and the angle brackets

$$\langle\ldots\rangle = \int \frac{2d^3p}{(2\pi\hbar)^3}\left(-\frac{\partial f_0}{\partial\varepsilon_0}\right)\ldots$$

denotes averaging over the Fermi surface.

The equation of motion of the magnetic moment density has the form[10,14]

$$\frac{d\mathbf{M}(\mathbf{r},t)}{dt} = g[\mathbf{M}(\mathbf{r},t)\times\mathbf{H}^{\text{eff}}] + \mathbf{R}, \tag{4}$$

where $g = -\gamma 2\mu_B/\hbar$, $\mu_B = |e|\hbar/2mc$ is the Bohr magneton, and γ is the gyromagnetic ratio of the ferromagnet. The effective magnetic field $\mathbf{H}^{\text{eff}}(\mathbf{r},t)$ is written as a functional derivative of the energy of the ferromagnet with respect to $\mathbf{M}(\mathbf{r},t)$:

$$\mathbf{H}^{\text{eff}}(\mathbf{r},t) = -\frac{\delta W}{\delta\mathbf{M}(\mathbf{r},t)}, \quad W = \int w_\Sigma d^3r. \tag{5}$$

The relaxation term $\mathbf{R}$, according to Ref. 10, can be written in the form

$$\mathbf{R} = \frac{1}{\tau_2}\left(\mathbf{H}^{\text{eff}} + \frac{1}{2g}\,\text{curl}\;\dot{\mathbf{u}}\right) - \frac{1}{\tau_1}\left\{\mathbf{m}\times\left[\mathbf{m}\times\left(\mathbf{H}^{\text{eff}} + \frac{1}{2g}\,\text{curl}\;\dot{\mathbf{u}}\right)\right]\right\}, \tag{6}$$

where $\mathbf{m} = \mathbf{M}/M$, and τ_1 and τ_2 are the temperature-dependent relaxation time of the direction and magnitude of the magnetic moment.

It follows from expressions (1) and (5) that

$$H_i^{\text{eff}} = H_i^{(\text{in})} - \frac{\partial w_a(\mathbf{M})}{\partial M_i} - 2M_i w_e'(\mathbf{M}^2) + \alpha_{lk}\frac{\partial^2 M_i}{\partial x_l \partial x_k} - u_{lk}\frac{\partial f_{lk}(\mathbf{M})}{\partial M_i}, \tag{7}$$

$\mathbf{H}^{(\text{in})} = \mathbf{H}^{(\text{ext})} + \mathbf{H}^{(m)}$ is the field inside the ferromagnet.

The equilibrium state corresponds to a minimum of the energy of the ferromagnet, and therefore the equation $\mathbf{H}^{\text{eff}}(\mathbf{r}) = -\delta W/\delta\mathbf{M}(\mathbf{r}) = 0$ together with the equations of magnetostatics determines the equilibrium values of the magnetization $\mathbf{M}(\mathbf{r})$ and field $\mathbf{H}^{(m)}(\mathbf{r})$. We shall ignore effects deriving from the existence of domain structure, assuming that the equilibrium magnetization is uniform and is found from the equation

$$H_i^{(\text{in})} - \frac{\partial w_a(\mathbf{M})}{\partial M_i} - 2M_i w_e'(\mathbf{M}^2) = 0. \tag{8}$$

Equation (4) must be supplemented by the equation of motion of the elastic medium[10,12]

$$\rho\ddot{u}_i = \eta_{iklm}\frac{\partial u_{lm}}{\partial x_k} + \frac{\partial f_{ik}(\mathbf{M})}{\partial M_l}\frac{\partial M_l}{\partial x_k} + \mathbf{M}\cdot\frac{\partial \mathbf{H}^{\text{eff}}}{\partial x_i} + \frac{1}{2g}(\text{curl}\;\mathbf{R})_i + \frac{1}{c}[\mathbf{j}\times\mathbf{B}]_i - \frac{m}{e}\frac{\partial j_i}{\partial t} + \frac{\partial}{\partial x_k}\langle\Lambda_{ik}\psi\rangle \tag{9}$$

and Maxwell's equations

$$\text{curl}\;\mathbf{H}^{(\text{in})} = \frac{4\pi}{c}\mathbf{j}, \quad \text{curl}\;\mathbf{E} = -\frac{1}{c}\frac{\partial\mathbf{B}}{\partial t}, \quad \text{div}\,\mathbf{B} = 0, \quad \text{div}\,\mathbf{j} = 0. \tag{10}$$

Here

$$\mathbf{j} = e\langle\mathbf{v}\psi\rangle \tag{11}$$

is the current density, $\mathbf{B} = \mathbf{H}^{(\text{in})} + 4\pi\mathbf{M}$ is the magnetic induction, $\Lambda_{ik} = \lambda_{ik} - \langle\lambda_{ik}\rangle/\langle 1\rangle$, and $\mathbf{v} = \partial\varepsilon_0/\partial\mathbf{p}$.

The system of equations of the problem is closed by the kinetic equation in the τ approximation for the equilibrium component of the distribution function:

$$\frac{\partial\psi}{\partial t} + \mathbf{v}\frac{\partial\psi}{\partial\mathbf{r}} + \frac{e}{c}[\mathbf{v}\times\mathbf{B}]\frac{\partial\psi}{\partial\mathbf{p}} + \frac{\psi}{\tau_e} = e\mathbf{v}\tilde{\mathbf{E}} - \Lambda_{ik}\dot{u}_k, \tag{12}$$

where $\tilde{\mathbf{E}} = \mathbf{E} + 1/c\,[\dot{\mathbf{u}}\times\mathbf{B}] - (m/e)\ddot{\mathbf{u}} - \nabla\delta\mu/e$ is the effective electric field.

In the local limit we can easily obtain from Eqs. (11) and (12) an expression for the current density:

$$j_l = \tau_e e^2\langle v_l v_k\rangle\tilde{E}_k - \tau e\langle v_l\Lambda_{ik}\rangle\dot{u}_{ik} \equiv \sigma_{lk}\tilde{E}_k + \gamma_{lik}\dot{u}_{ik}, \tag{13}$$

which is a sum of the electronic current and the deformation current due to the lattice displacement.

The system of equations (4), (7), (9)–(12) together with the boundary conditions determines the electromagnetic and acoustic fields arising in an elastically strained ferromagnet.

Let us consider a ferromagnet with a cubic crystal lattice in a magnetic field $\mathbf{H}^{(\text{ext})} = (0,0,H^{(\text{ext})})$ occupying the half space $z > 0$. In the case when the x, y, and z axes are directed along the edges of a cube, the anisotropy energy can be written in the form

$$w_a(\mathbf{M}) = -\frac{1}{2}\beta(M_x^4 + M_y^4 + M_z^4) \tag{14}$$

(we have neglected the influence of the magnetostrictive strains on the crystal structure). For $\beta > 0$ the crystal has three equivalent directions of easy magnetization along the x, y, and z axes, and the equilibrium magnetization $\mathbf{M}_0$ will be parallel to the vector $\mathbf{H}^{(\text{ext})}$. We set

$$\mathbf{M}(\mathbf{r},t) = \mathbf{M}_0 + \tilde{\mathbf{M}}(\mathbf{r},t), \quad \mathbf{H}^{(\text{in})}(\mathbf{r},t) = \mathbf{H}_0 + \mathbf{h}(\mathbf{r},t), \tag{15}$$

where $\tilde{\mathbf{M}}(\mathbf{r},t)$ and $\mathbf{h}(\mathbf{r},t)$ are small deviations from the equilibrium values. Noting that for a cubic crystal $\alpha_{ik} = \alpha\delta_{ik}$, one can easily obtain from formulas (7) and (8) a linearized expression for the effective magnetic field:

$$H_i^{\text{eff}} = h_i + \alpha\frac{\partial^2\tilde{M}_i}{\partial x_k^2} - \left(\frac{H_0}{M_0} + 2\beta\mathbf{M}_0^2\right)\tilde{M}_i - 4M_{0_i}w_e''(\mathbf{M}_0^2)\times(\tilde{\mathbf{M}}\mathbf{M}_0) - u_{lk}\frac{\partial f_{lk}(\mathbf{M}_0)}{\partial M_{0_i}}. \tag{16}$$

Under experimental conditions the elastic wave usually propagates along the normal $\mathbf{n}$ to the surface, and the displacement at the boundary is assumed to be specified:

$$\mathbf{u}(0,t)=\mathbf{u}_0 e^{-i\psi t}, \quad \mathbf{u}_0 \perp \mathbf{n}. \tag{17}$$

The character of the processes occurring over a sufficiently extended time interval is determined by the boundary regime, since the influence of the initial conditions is weakened because of the dissipation inherent to all real systems. For steady-state oscillations the time dependence of all the alternating quantities has the form $e^{-i\omega t}$.

Assuming that the elastic and magnetostriction properties of the ferromagnet are isotropic, we use the following expressions[10,15] for the tensors η_{iklm} and f_{ik}:

$$\eta_{iklm}=\rho(s_l^2-2s_t^2)\delta_{ik}\delta_{lm}+\rho s_t^2(\delta_{il}\delta_{km}+\delta_{im}\delta_{kl}),$$
$$f_{ik}=f_1 M_i M_k+f_2 M^2\delta_{ik}, \tag{18}$$

where s_t and s_l are the velocities of transverse and longitudinal sound, and f_1 and f_2 are the magnetostriction constants. Neglecting effects due to anisotropy of the charge carrier dispersion relation, we can write the conductivity tensor σ_{ik} and the renormalized deformation potential Λ_{ik} in the form

$$\sigma_{ik}=\tau e^2\langle v_l v_k\rangle=\sigma\delta_{ik},$$
$$\Lambda_{ik}=\Lambda(\varepsilon_0)\left(v_i v_k-\frac{1}{3}v^2\delta_{ik}\right), \tag{19}$$

where $\Lambda(\varepsilon_0)$ depends only on the electron energy. Under these conditions $\gamma_{lik}=0$, and the strain contribution to the current is equal to zero, while the circular components $u_+=u_x+iu_y$, $h_+=h_x+ih_y$ of the vectors $\mathbf{u}$, $\mathbf{h}$, $\mathbf{E}$, and $\mathbf{M}^{\sim}$ satisfy the equations

$$\left[\overline{\psi}_0\left(\frac{H_0}{M_0}+2\beta\mathbf{M}_0^2\right)-\omega\right]M_+^{\sim}-\overline{\omega}_0\alpha\frac{\partial^2 M_+^{\sim}}{\partial z^2}$$
$$=\overline{\omega}_0 h_+-\left(f_1\overline{\omega}_0 M_0+\frac{i\omega}{2g\tau}\right)\frac{\partial u_+}{\partial z}, \tag{20}$$

$$-\omega^2 u_+-s_t^2\frac{\partial^2 u_+}{\partial z^2}=\frac{f_1 M_0}{\rho}\frac{\partial M_+^{\sim}}{\partial z}+\frac{B_0}{4\pi\rho}\left(1+\frac{\omega}{\omega_B}\right)\frac{\partial h_+}{\partial z}$$
$$+\frac{i}{2\rho g}\frac{\partial R_+}{\partial z}, \tag{21}$$

$$-\frac{\partial^2 h_+}{\partial z^2}=i\frac{4\pi\sigma\omega}{c^2}(h_++4\pi M_+^{\sim})$$
$$-i\frac{4\pi\sigma\omega}{c^2}B_0\left(1+\frac{\omega}{\omega_B}\right)\frac{\partial u_+}{\partial z}, \tag{22}$$

$$E_+=-i\frac{\omega}{ck}B_+^{\sim}, \quad B_+^{\sim}=h_++4\pi M_+^{\sim}. \tag{23}$$

Here $\overline{\omega}_0=\omega_0-i\tau^{-1}$, $\omega_0=gM_0$, $\tau^{-1}=\tau_2^{-1}+\tau_1^{-1}$, $B_0=H_0+4\pi M_0$, and $\omega_B=|e|B_0/mc$.

The boundary conditions for the electric and magnetic fields satisfying system (20)–(23) reduce to continuity of the components h_+ and E_+ at the boundary of the ferromagnet with free space. Continuity of the normal component of the energy flux density at the surface of the ferromagnet and formula (1) imply the following boundary condition for the magnetization:

$$\frac{\partial M_+^{\sim}(0)}{\partial z}=0. \tag{24}$$

In the case when the inequality $\max(B_0^2/8\pi\rho s_t^2, f_1 M_0^2/\rho s_t^2)\ll 1$ holds, the nondissipative terms on the right-hand side of equation (21) constitute a small correction. Taking them into account leads to renormalization of the sound velocity and rotation of the plane of polarization of the vector $\mathbf{u}$. If over the time of passage of the wave through the sample the angle of rotation of the amplitude of the displacement vector is small, then in neglect of dissipative effects the acoustic field can be assumed equal to the external field

$$u_+(z,t)=u_{0_+}e^{-i\omega t+iqz}, \quad q=\frac{\omega}{s_t}, \tag{25}$$

and Eqs. (20), (22) and (23) can be regarded as independent of Eq. (21).

The solution of the inhomogeneous system of differential equations (20), (22), (23) should be sought in the form of a sum of the solution of the corresponding homogeneous system and an induced solution describing the field induced by the sound wave. The induced solution of equations (20) and (22) is a plane wave, $M_+^{\sim}(z,q)=M_+^{\sim}qe^{iqz}$, $h_+(z,q)=h_+(q)e^{iqz}$ with wave number q and amplitudes

$$h_+(q)=\frac{qu_{0_+}}{D}\left[\overline{B}_0+\frac{4\pi\left(f_1\overline{\omega}_0 M_0+\frac{i\omega}{2g\tau}\right)}{d_1}\right], \tag{26}$$

$$M_+^{\sim}(q)=\frac{qu_{0_+}}{d_1}\left[\frac{\overline{\omega}_0}{D}\overline{B}_0-i\left(f_1\overline{\omega}_0 M_0+\frac{i\omega}{2g\tau}\right)\right.$$
$$\left.\times\left(1+i\frac{4\pi\overline{\omega}_0}{d_1 D}\right)\right], \tag{27}$$

where

$$d_1\equiv d_1(\omega,q)=\overline{\omega}_0\left(\frac{H_0}{M_0}+2\beta\mathbf{M}_0^2+\alpha q^2\right)-\omega,$$
$$D=(q\delta)^2-i\left(1+\frac{4\pi\overline{\omega}_0}{d_1}\right),$$

$\delta=c/\sqrt{4\pi\sigma\omega}$ is the depth of the skin layer, $\overline{B}_0=B_0(1+\omega/\omega_B)$.

From Eqs. (23) it is easy to find the ac electric field

$$E_+(z,q)=E_+(q)e^{iqz},$$

$$E_+(q)=-i\frac{\omega}{c}u_{0_+}\left\{\frac{\overline{B}_0}{D}\left(1+\frac{4\pi\overline{\omega}_0}{d_1}\right)\right.$$
$$-i\frac{4\pi\left(f_1\overline{\omega}_0 M_0+\frac{i\omega}{2g\tau}\right)}{d_1}$$
$$\left.\times\left[1+\frac{i}{D}\left(1+\frac{4\pi\overline{\omega}_0}{d_1}\right)\right]\right\}, \tag{28}$$

induced by the sound wave. In the limit $q\delta\to 0$ we obtain $E_+^{(0)}(q)=u_+\overline{B}_0\omega/c$, and the effective field

$$\tilde{E}_+ = E_+ - \frac{\omega}{c} u_+ \overline{B}_0 \tag{30}$$

goes to zero. The conduction current and the field $\tilde{\mathbf{E}}$ is produced by the following term in the expansion of (28) in powers of $(q\delta)^2$:

$$\tilde{E}_+(q) = -i(q\delta)^2 \frac{\omega}{c} u_{0_+} \frac{\overline{B}_0 d_1 + 4\pi\left(f_1 \overline{\omega}_0 M_0 + \dfrac{i\omega}{2g\tau}\right)}{d_1 + 4\pi\overline{\omega}_0}. \tag{31}$$

Separating Eq. (31) into real and imaginary parts,

$$\tilde{E}_+(q) = -\frac{i(q\delta)^2 \omega u_{0_+}}{c[\Omega^2 + (\zeta + 4\pi)^2 \tau^{-2}]} \times \left\{ \Omega[\overline{B}_0(\omega_0\zeta - \omega) + 4\pi f_1 \omega_0 M_0] + (\zeta + 4\pi)\tau^{-2}\left(\overline{B}_0\zeta + 4\pi f_1 M_0 - \frac{2\pi\omega}{g}\right) - i4\pi\omega\tau^{-1}\left[\overline{B}_0 - \left(f_1 + \frac{1}{2}(\zeta + 4\pi)\right) M_0 + \frac{\omega}{2g}\right] \right\}, \tag{32}$$

we find the phase difference of the electromagnetic and sound waves:

$$\varphi = -\frac{\pi}{2} - \arctan \frac{4\pi\omega\tau^{-1}\left[\overline{B}_0 - \left(f_1 + \dfrac{1}{2}(\zeta + 4\pi)\right) M_0 + \dfrac{\omega}{2g}\right]}{\Omega[\overline{B}_0(\omega_0\zeta - \omega) + 4\pi f_1 \omega_0 M_0] + (\zeta + 4\pi)\tau^{-2}\left(\overline{B}_0\zeta + 4\pi f_1 M_0 - \dfrac{2\pi\omega}{g}\right)}. \tag{33}$$

Here

$$\Omega = \omega_0(\zeta + 4\pi) - \omega = \mathrm{Re}(d_1 + 4\pi),$$

$$\zeta = \frac{H_0}{M_0} + 2\beta\mathbf{M}_0^2 + \alpha q^2.$$

For the asymptotic representation of the magnetic field and magnetization for $(q\delta)^2 \ll 1$ it is sufficient to consider only the zeroth approximation in the small parameter $(q\delta)^2$:

$$h_+^{(0)}(q) = iqu_{0_+} \frac{\overline{B}_0 d_1 + 4\pi\left(f_1 \overline{\omega}_0 M_0 + \dfrac{i\omega}{2g\tau}\right)}{d_1 + 4\pi\overline{\omega}_0}, \tag{34}$$

$$M_+^{(0)\sim}(q) = iqu_{0+} \frac{\overline{B}_0 \overline{\omega}_0 - \left(f_1 \overline{\omega}_0 M_0 + \dfrac{i\omega}{2g\tau}\right)}{d_1 + 4\pi\overline{\omega}_0}. \tag{35}$$

The solutions of the homogeneous system of differential equations corresponding to (20), (22), and (23) describe modes which are damped at distances of the order of the skin depth. Assuming that the spatial dependence of all the variable quantities is of the form e^{ikz}, we obtain from (20), (22), and (23) the dispersion relation giving the wave number as a function of frequency:

$$D(\omega,k) = (\delta k)^2 - i\left(1 + \frac{4\pi\overline{\omega}_0}{d_1(\omega,k)}\right) = 0. \tag{36}$$

In the case $\alpha\delta^2 \ll H_0/M_0 + 2\beta\mathbf{M}_0^2$ equation (36) takes the form

$$k^2(\omega) = \frac{i}{\delta^2}\left(1 + 4\pi \frac{(\omega_0^2 + \tau^{-2})\zeta - \omega_0\omega + i\omega\tau^{-1}}{(\omega_0\xi - \omega)^2 + \xi^2\tau^{-2}}\right), \tag{37}$$

where $\xi = H_0/M_0 + 2\beta\mathbf{M}_0^2$. From the two roots it is necessary to choose the solution for which the mode is damped at $z \to \infty$.

Applying the boundary condition (24) and using Maxwell's equations, we can easily express the amplitudes of the skin solutions,

$$M_+^s(k,q) = -\frac{q}{k} M_+^{\sim}(q),$$

$$h_+^s(k,q) = -\frac{q}{k} \frac{d_1(\omega,k)}{\overline{\omega}_0} M_+^{\sim}(q), \tag{38}$$

$$E_+^s(k,q) = i\frac{\omega q}{k^2 c} \frac{d_1(\omega,k) + 4\pi\overline{\omega}_0}{\overline{\omega}_0} M_+^{\sim}(q)$$

in terms of the amplitude of the displacement at the boundary of the ferromagnet. Here $M_+^{\sim}(q)$ is determined by formula (27). It follows from expressions (38) for $q = \omega/s_t \ll |k| \sim \delta^{-1}$ that the amplitudes of the skin-effect modes are small compared to the amplitudes of the forced oscillations.

The electromagnetic waves radiated by the sound wave (25) in a ferromagnetic insulator are determined by the equation of motion of the magnetization (20) and the wave equation, which for a ferromagnetic insulator with dielectric constant ε becomes

$$-\frac{\partial^2 h_+}{\partial z^2} = \varepsilon \frac{\omega^2}{c^2}(h_+ + 4\pi M_+^{\sim}). \tag{39}$$

It follows from this equation that the magnetic field excited by a sound wave with wave number $q = \omega/s_t$ is significantly less than the ac magnetization:

$$h_+ \approx 4\pi\varepsilon \frac{s_t^2}{c^2} M_+^{\sim} \ll M_+^{\sim} = -i\frac{q}{d_1}\left(f_1 \overline{\omega}_0 M_0 + \frac{i\omega}{2g\tau}\right) u_+. \tag{40}$$

The electric field induced by the sound wave in a ferromagnetic insulator and the phase difference of the electromagnetic and sound waves are determined by the expressions

$$E_+^{\sim}=4\pi\frac{\omega}{kc}M_+^{\sim}=-i\frac{4\pi\omega}{d_1 c}\left(f_1\overline{\omega}_0 M_0+\frac{i\omega}{2g\tau}\right)u_+, \tag{41}$$

$$\varphi=-\frac{\pi}{2}-\arctan\frac{\tau^{-1}\omega\left[-f_1 M_0+\frac{1}{2g}(\omega-\zeta\omega_0)\right]}{f_1 M_0[\zeta(\tau^{-2}+\omega_0^2)-\omega\omega_0]-\frac{1}{2g}\zeta\tau^{-2}\omega}. \tag{42}$$

From the homogeneous system of equations of the problem it is easy to obtain the dispersion relation that determines the spectrum of free oscillations of the electromagnetic field:

$$k^2=\varepsilon\frac{\omega^2}{c^2}\left(1+\frac{4\pi\overline{\omega}_0}{d_1(\omega,k)}\right). \tag{43}$$

It follows from the boundary condition (24) that the amplitudes of the free oscillations of the electromagnetic field and magnetization M_+^f in a ferromagnetic insulator substantially exceed the amplitude of the induced oscillations: $M_+^f \simeq (c/\varepsilon s_t)M_+^{\sim}$.

The electric fields produced by a sound wave in a substance having magnetic order depends substantially on the magnetostriction constants and magnetization relaxation times. In the case when the relaxation times of the magnitude and direction of the magnetization are large, $\tau^{-1}\equiv\tau_1^{-1}+\tau_2^{-1}<\omega|\omega_0|$, the phase difference $\Delta\varphi$ of the electromagnetic and sound waves tends toward $-\pi/2$. The deviation $\Delta\varphi$ from $-\pi/2$ is maximum for frequencies of the order of $\omega\sim|\omega_0|\sim\tau^{-1}$.

The authors thank V. D. Fil' for calling their attention to the importance of the problem. This study was supported by the CRDF program (Grant No. UPI-2566-KH-03).

*E-mail: kolesnichenko@ilt.kharkov.ua

[1] C. Mazumdar, R. Nagarajan, C. Godart, L. C. Gupta, M. Latroche, S. K. Dhar, C. L. Clement, B. D. Padalia, and R. Vijayaraghavan, Solid State Commun. **87**, 413 (1993).
[2] R. Nagarajan, C. Mazumdar, Z. Hossain, S. K. Dhar, K. V. Gopalakrishnan, L. C. Gupta, C. Godart, B. D. Padalia, and R. Vijayaraghavan, Phys. Rev. Lett. **72**, 274 (1994).
[3] R. J. Cava, H. Takagi, B. Batlogg, H. W. Zandbergen, J. J. Krajewski, W. F. Peck, Jr., R. B. van Dover, R. J. Felder, T. Siegrist, K. Mizahashi, J. O. Lee, H. Eisaki, S. A. Carter, and S. Uchida, Nature (London) **367**, 146 (1994).
[4] R. J. Cava, H. Takagi, H. W. Zandbergen, J. J. Krajewski, W. F. Peck, Jr., T. Siegrist, B. Batlogg, R. B. van Dover, R. J. Felder, K. Mizuhashi, J. O. Lee, H. Eisaki, and S. Uchida, Nature (London) **367**, 252 (1994).
[5] P. Pairor and M. B. Walker, Phys. Rev. B **65**, 064507 (2002).
[6] K. Maki, P. Thalmeier, and H. Won, Phys. Rev. B **65**, 140502R (2002).
[7] Hyun C. Lee and Han-Yong Choi, Phys. Rev. B **65**, 174530 (2002).
[8] A. N. Vasil'ev and Yu. P. Gaĭdukov, Usp. Fiz. Nauk **141**, 431 (1983) [Sov. Phys. Usp. **26**, 952 (1983)].
[9] V. D. Fil', Fiz. Nizk. Temp. **27**, 1347 (2001) [Low Temp. Phys. **27**, 993 (2001)].
[10] A. I. Akhiezer, V. G. Bar'yakhtar, and S. V. Peletminskii, *Spin Waves*, North-Holland, Amsterdam (1968), Nauka, Moscow (1967).
[11] E. A. Turov and V. G. Shavrov, Usp. Fiz. Nauk **140**, 429 (1983) [Sov. Phys. Usp. **26**, 593 (1983)].
[12] V. M. Kontorovich, Zh. Éksp. Teor. Fiz. **45**, 1638 (1963) [Sov. Phys. JETP **18**, 1125 (1964)].
[13] A. I. Akhiezer, Zh. Éksp. Teor. Fiz. **8**, 1318 (1938).
[14] E. S. Borovik, A. S. Mil'ner, and V. V. Eremenko, *Lectures on Magnetism* [in Russian], Izdatel'stvo Kharkovskogo Universiteta, Kharkov (1972).
[15] A. I. Akhiezer, V. G. Bar'yakhtar, and S. V. Peletminskiĭ, Zh. Éksp. Teor. Fiz. **35**, 228 (1958) [Sov. Phys. JETP **8**, 157 (1959)].

Translated by Steve Torstveit

ELECTRONIC PROPERTIES OF METALS AND ALLOYS

Magnetic absorption of electromagnetic waves by a small metallic particle of ellipsoidal form

N. I. Grigorchuk*

N. N. Bogolyubov Institute of Theoretical Physics of the National Academy of Sciences of Ukraine, Metrologichna St. 14-b, Kyiv 03143, Ukraine

P. M. Tomchuk

Institute of Physics of the National Academy of Sciences of Ukraine, Nauka Ave. 46, Kyiv 03028, Ukraine
(Submitted July 10, 2004; revised September 23, 2004)
Fiz. Nizk. Temp. **31**, 542–552 (May 2005)

The magnetic absorption of electromagnetic waves by a small metallic particle of ellipsoidal form is investigated in frequency regions both higher and lower than the characteristic frequency of the free passage of an electron between walls of the particle. The boundary conditions chosen are diffuse reflection of the electron from the inner surface of the particle. For the case when the thickness of the skin layer is large compared to the characteristic size of the particle, analytical expressions are obtained which permit determination of the dependence of the energy absorbed by a particle on its shape and orientation with respect to the direction of incidence of the radiation. The low-frequency absorption by small metallic particles is analyzed in detail for the first time. For particles in the form of oblate or prolate ellipsoids of revolution it is shown at particle sizes and what initial polarizations of the incident wave that the magnetic absorption becomes dominant over electric absorption. [DOI: 10.1063/1.1925368]

1. INTRODUCTION

The study of the properties of small metallic particles (SMPs) is not only of purely scientific interest but also of practical importance in certain applications. For example, when paints containing such particles are applied to a solid surface, the absorption or reflection of electromagnetic (EM) waves in a certain range of frequencies can be affected appreciably. In outer space, SMPs can form layers of dusty plasma that can pose a hazard to spacecraft. By studying the features of the absorption of radiation by such particles one can learn to control their behavior by means of lasers.

The electromagnetic properties of SMPs differ substantially from those of metals.[1,2] A criterion of smallness for a particle is that its size be comparable to the wavelength λ of the incident EM wave. If the characteristic particle size d becomes comparable to or smaller than λ, a number of features will be observed in the transport, optical, and thermodynamic properties of the particles; these are usually attributed to manifestation of size effects.[3]

The ratio of d to the thickness δ of the skin layer (the skin depth) is extremely important, as is also the ratio of d to the electron mean free path l. As a rule, particles for which $d<\delta\ll\lambda$ are considered. Subject to this condition the variants $d\gg l$ and $d\ll l$ are both possible. In the latter case a sharp decrease in the energy exchange between electrons and the lattice has been observed, and that can lead to a ''gap'' between the lattice temperature and electron temperature when power is fed into the SMP.[4] The electrons, gaining a large energy, become ''hot,'' and this leads to a number of interesting observable effects.[5] A clear feature of SMPs is a strong dependence of the infrared absorption on the polarization of the wave and the shape of the particle.[6–9] It was found that for equal flux the power absorbed by particles of equal volume but of different shape can differ by several orders of magnitude. This served as an impetus for the development of a theory not only for spherical particles[10–13] but also for particles in the form of cylinders,[6,14,15] ellipsoids,[16] and other shapes.[3] Although the spherical particle model has been the most thoroughly studied,[1] the ellipsoidal particle model has turned out to be more informative for investigating the influence of the shape of the SMPs on their optical properties. An ellipsoidal shape is convenient primarily because it provides a simple way (by varying the ratio of the semiaxes of the ellipsoid) to model a rather wide class of particles of most of the real forms they are known to take (from disk-like to antenna-like). Furthermore, changing the ratio of the semiaxes has a strong influence on the depolarizing factors that determine the internal (local) fields induced inside the particle by an EM wave and thereby influences the scattering of electrons and optical absorption.

The optical properties of SMPs has been studied for a long time now, and the results are fully reflected in monographs.[1,17–19] However, for nonspherical particles, especially for $d\ll l$ there have been relatively few attempts to calculate the energy of incident radiation absorbed by a particle. For cylindrical particles of finite length the magnetic absorption cross section was calculated quite recently in Refs. 14 and 15. General expressions for electric and mag-

netic absorption by an ellipsoidal particle have been obtained in Ref. 16, but there the electric absorption was considered in more detail, and magnetic absorption was treated schematically and incompletely. In particular, the low-frequency absorption (when $\omega < \omega_{\text{fl}}$, where ω_{fl} is the frequency of the electron's oscillation between the walls (inverse time of flight); we shall refer to this below as the transit frequency) is not investigated. In this frequency region, however, magnetic absorption, as will be shown below, is already comparable to the electric frequency for a particle with a radius of 50 Å, and it increases with increasing radius of the particle. This growth can be increased significantly by deformation of the particle to an oblate or prolate form.

The goal of this study is to examine in detail the magnetic absorption of SMPs of ellipsoidal form for arbitrary orientation of the particle with respect to the direction of propagation of the incidence wave at frequencies both above and below the characteristic frequency of free passage of the electron between walls of the particle.

In this paper we do not take into account the influence of the ensemble of SMPs on an individual particle under consideration, an effect which is of importance in its own right[20] and can alter the value of the internal field in the particle severalfold, but this effect remains secondary to the influence of the shape of the individual particle itself.[16] The results obtained by us for a single particle can easily be generalized to an ensemble of identical weakly interacting particles all oriented in the same way. For an ensemble of particles of different shapes and orientations it is not always justifiable to introduce effective mean values (for example, in calculating the emission of electrons,[5] where the value of the effect depends exponentially on the intensity of the absorption, which in turn is sensitive to the shape of the particle and the polarization of the wave).

The rest of this paper is laid out as follows. In Sec. 2 we describe the model and the initial principles of the problem. In Sec. 3 we write a basic formula for the energy absorbed by an SMP. Sections 4 and 5 are devoted to analysis of the low- and high-frequency limits of the problem. Finally, in Sec. 6 we present the main results and conclusions of this study.

2. MODEL AND INITIAL PRINCIPLES

For describing the interaction of radiation with a spherical particle in the framework of classical electrodynamics one usually uses Mie theory.[19] However, Mie theory applies only for particles with $d \gg l$. Therefore, we shall start from the kinetic theory of electrons without imposing any restrictions on the size of the particle.

Suppose that we have an ellipsoidal metal particle on which is incident an electromagnetic wave

$$\begin{pmatrix} \mathbf{E} \\ \mathbf{H} \end{pmatrix} = \begin{pmatrix} \mathbf{E}_0 \\ \mathbf{H}_0 \end{pmatrix} \mathrm{e}^{-i(\mathbf{k}\cdot\mathbf{r}-\omega t)}. \tag{1}$$

Here $\mathbf{E}$ and $\mathbf{H}$ are its electric and magnetic components, ω and $\mathbf{k}$ are its frequency and wave vector, and $\mathbf{r}$ and t describe the spatial coordinate and time. We assume that $d \ll \lambda$. This allows us to treat the particle as immersed in spatially uniform $\mathbf{E}$ and $\mathbf{H}$ fields which are oscillatory in time. The electric component of the EM wave induces in the SMP along the jth direction (in the principal axes of the ellipsoid) a local electric field[21]

$$E_{\text{in}}^{j} = \frac{E_0^j}{1 + L_j(\varepsilon(\omega) - 1)}, \tag{2}$$

that is specified in terms of the depolarizing factor L_j and the permittivity (dielectric function) of the particle, $\varepsilon(\omega)$. The magnetic component of the EM wave induces an eddy electric field E_{ed}. Since the depolarizing factor, which varies, depending on the shape of the particle, from 0 to 1, appears as a cofactor with the dielectric function (which has a rather large value for metals in the infrared), it turns out that particles of the same volume but different shapes absorb amounts of energy per unit time which, depending on the frequency of the light, can differ by orders of magnitude.

If the skin depth $\delta_H \gg d$, then $\mathbf{H}_0$ can also be regarded as a uniform static field, and we can write Maxwell's equations for $\mathbf{E}_{\text{ed}}$:

$$\operatorname{curl}\mathbf{E}_{\text{ed}} = i\frac{\omega}{c}\mathbf{H}_0, \quad \operatorname{div}\mathbf{E}_{\text{ed}} = 0, \tag{3}$$

with the boundary conditions at the surface of the particle

$$\mathbf{E}_{\text{ed}}\mathbf{n}\big|_s = 0, \tag{4}$$

where $\mathbf{n}_s$ is the normal to the surface S of the ellipsoid. Then the contribution of the eddy currents to the absorption will be maximum. The field E_{ed}, when the fact that the right-hand side of Eq. (3) is constant for $\delta_H \gg d$ is taken into account, can be written as a linear function of the coordinates:

$$(E_{\text{ed}})_j = \sum \alpha_{jk} x_k, \quad (x_1 = x, x_2 = y, x_3 = z). \tag{5}$$

The matrices α_{ij} are easily determined from Eqs. (3) and condition (4):

$$\left.\begin{aligned} \alpha_{xy} &= -i\frac{\omega}{c}\frac{R_x^2}{R_x^2+R_y^2}H_z, \quad \alpha_{yx} = i\frac{\omega}{c}\frac{R_y^2}{R_y^2+R_x^2}H_z \\ \alpha_{xz} &= i\frac{\omega}{c}\frac{R_x^2}{R_x^2+R_z^2}H_y, \quad \alpha_{zx} = -i\frac{\omega}{c}\frac{R_z^2}{R_z^2+R_x^2}H_y \\ \alpha_{zy} &= i\frac{\omega}{c}\frac{R_z^2}{R_z^2+R_y^2}H_x, \quad \alpha_{yz} = -i\frac{\omega}{c}\frac{R_y^2}{R_y^2+R_z^2}H_x \end{aligned}\right\}, \tag{6}$$

where R_x, R_y, and R_z are the semiaxes of the ellipsoid along the x, y, and z axes. For convenience, here and below the subscript 0 has been dropped from the notation for the components of the external magnetic field. Then for the x component of the eddy field, for example, we finally have

$$E_{\text{ed}}^{x} = \frac{i\omega}{c}\left(\frac{zH_y}{R_z^2+R_x^2} - \frac{yH_z}{R_x^2+R_y^2}\right)R_x^2. \tag{7}$$

The other two components of the field can easily be obtained by a cyclic permutation of the indices in Eq. (7). Having determined the field $\mathbf{E}_{\text{ed}}$, we can use the formula

$$W = \frac{1}{2}\Re\mathrm{e}\int_V d\mathbf{r}\mathbf{j}_m(\mathbf{r})\cdot\mathbf{E}_{\text{ed}}^{*}(\mathbf{r}) \tag{8}$$

to find the value of the power absorbed, provided we know the current $\mathbf{j}_m(\mathbf{r})$.

For particles of size $d \gg l$ the currents are usually related to the field by the expression $\mathbf{j}_m = \sigma \mathbf{E}_{\text{ed}}$, with $\sigma = \omega\varepsilon''/4\pi$, where ε'' is the imaginary part of the permittivity. In this case the bulk scattering of electrons is dominant and, as is easily shown, using Eq. (7), for SMPs having the form of ellipsoids of revolution

$$W = V\frac{\varepsilon''\omega^3}{80\pi c^2} R_\perp^2 \left[\mathbf{H}_\parallel^2 + \frac{2R_\parallel^2}{R_\parallel^2 + R_\perp^2} \mathbf{H}_\perp^2 \right], \tag{9}$$

where V is the volume of the particle, and

$$\mathbf{H}_\parallel^2 = \mathbf{H}_z^2, \quad \mathbf{H}_\perp^2 = \mathbf{H}_x^2 + \mathbf{H}_y^2,$$

$$R_x = R_y = R_\perp, \quad R_z = R_\parallel. \tag{10}$$

Formula (9) generalizes the known expression for the energy of magnetic absorption by a spherical particle,[21]

$$W_M = \frac{V}{80\pi}\omega c'' \left(\frac{\psi R}{c} \right)^2 |\mathbf{H}_0|^2, \tag{11}$$

in which for a metal

$$\varepsilon'' = \frac{\nu}{\omega}\frac{\omega_p^2}{\nu^2 + \omega^2}, \tag{12}$$

where ν is the collision frequency and ω_p is the plasma frequency.

If for estimation we take $\omega_p \approx 5\times 10^{15}\ \text{s}^{-1}$, $\nu \approx 10^{13}\ \text{s}^{-1}$, $\omega(\text{CO}_2) \approx 2\times 10^{14}\ \text{s}^{-1}$ (which give $\varepsilon' \approx -622$, $\varepsilon'' \approx 31$) and the minimum radius allowable in the framework of the approximation $2R \gg l$ is $R = 460$ Å,[1)] then, as is easily computed using expression (5) of Ref. 16, the magnetic absorption will be approximately four times higher than the corresponding absorption due to the electric field. With decreasing radius of the particle the magnetic absorption falls off quadratically. As we shall see below, this estimate can change substantially at other frequencies.

Let us consider the opposite case, when $d \ll l$. Now the absorption of power from the wave occurs only on account of collisions of the electrons with the inner surface of the particle. It is customary to say[12] that the surface scattering of electrons is dominant in this case. Now the calculation of the current must be done by a microscopic approach, in accordance with which

$$\mathbf{j}_m(\mathbf{r}) = 2e\left(\frac{m}{2\pi\hbar} \right)^3 \int\int\int \mathbf{v}(\mathbf{r}) f(\mathbf{r},\mathbf{v}) d^3(v), \tag{13}$$

where $f(\mathbf{r},\mathbf{v})$ is the distribution function of the electrons over coordinates $\mathbf{r}$ and velocities $\mathbf{v}$, and e and m are the charge and mass of the electron. The integration is over all frequencies. The field $\mathbf{E}_{\text{ed}}$ causes a deviation from the equilibrium Fermi distribution of the electrons. Therefore the total distribution function $f(\mathbf{r},\mathbf{v})$ is found in the form of a sum of an equilibrium function $f_0(\varepsilon)$ (dependent only on the kinetic energy ε of the electron) and a nonequilibrium admixture $f_1(\mathbf{r},\mathbf{v})$, which in the linear approximation in the external field is determined from the kinetic equation[22]

$$(\nu - i\omega) f_1(\mathbf{r},\mathbf{v}) + \mathbf{v}\frac{\partial f_1(\mathbf{r},\mathbf{v})}{\partial \mathbf{r}} + e(\mathbf{E}_{\text{in}} + \mathbf{E}_{\text{ed}})\mathbf{v}\frac{\partial f_0(\mathbf{r},\mathbf{v})}{\partial \varepsilon} = 0 \tag{14}$$

with the boundary conditions

$$f_1(\mathbf{r},\mathbf{v})|_S = 0, \quad v_n < 0, \tag{15}$$

for diffuse reflection of the electrons from the inner walls of the particle,[2)] where v_n is the electron velocity component normal to the surface S.

The collision integral in Eq. (14) is written in the relaxation time approximation ($\tau = 1/\nu$).

If we transform to the deformed coordinates and velocities according to the rule

$$x_j \Rightarrow \frac{R_j}{R}x_j', \quad v_j \Rightarrow \frac{R_j}{R}v_j', \quad R = (R_1R_2R_3)^{1/3}, \tag{16}$$

and solve the partial differential equation (14) by the method of characteristics,[25] then we can obtain a solution for the function $f_1(\mathbf{r},\mathbf{v})$ in the form

$$f_1(\mathbf{r},\mathbf{v}) = -e\frac{\partial f_0}{\partial \varepsilon}\left[\mathbf{v}\cdot\mathbf{E}_{\text{in}} + \sum_{i,j=1}^{3} \alpha_{ij} v_i \left(\frac{x_j' R_j}{R} + v_j \frac{\partial}{\partial(\nu - i\omega)} \right) \right] \left(\frac{1 - \exp[-(\nu - i\omega)t']}{\nu - i\omega} \right). \tag{17}$$

The parameter t', which is is equal to

$$t' = \frac{1}{v'^2}[\mathbf{r}'\cdot\mathbf{v}' - \sqrt{(R^2 - r'^2)v'^2 + (\mathbf{r}'\cdot\mathbf{v}')^2}], \tag{18}$$

characterizes the position of the electron along the trajectory $\mathbf{r}' = \mathbf{v}'t' + \mathbf{R}$. The radius vector $\mathbf{R}$ gives the position of the point on the surface at which the trajectory begins (at $t' = 0$). We recall that after the deformation (16) the ellipsoidal shape of the particle becomes spherical (with radius R).

3. ENERGY ABSORBED

Using Eqs. (7), (8), (13), and (17), after integrating over the coordinates as in Ref. 16, we can write the magnetic-field energy absorbed by the particle in the general case as

$$W = \frac{\pi e^2 m^3 R^3}{2(2\pi h)^3} \Re\text{e}\left\{ \frac{1}{\overline{\nu}} \int d^3v\, \delta(\varepsilon - \mu) \times \left[\psi_1(v') \sum_{i,j=1}^{3} |\alpha_{ij}|^2 R_j^2 v_i^2 + 2\psi_2(v') R^2 \times \sum_{i,j=1}^{3} |\alpha_{ij} + \alpha_{ji}|^2 \frac{v_i^2 v_j^2}{v'^2} \right] \right\}, \tag{19}$$

where $\overline{\nu} = \nu - i\omega$, and we have taken into account that $\partial f_0/\partial\varepsilon \approx -\delta(\varepsilon - \mu)$, where μ is the Fermi energy. If we denote $q = \overline{\nu} 2R/v'$, then the remaining notation in (19) is

$$\psi_1(v') = \frac{8}{15} - \frac{1}{q} + \frac{4}{q^3} - \frac{24}{q^5} + \frac{8}{q^3}\left(1 + \frac{3}{q} + \frac{3}{q^2} \right) \text{e}^{-q}, \tag{20}$$

$$\psi_2(v') = \frac{2}{5} - \frac{1}{q} + \frac{8}{3q^2} - \frac{6}{q^3} + \frac{32}{q^5} - \frac{2}{q^2}\left(1 + \frac{5}{q} + \frac{16}{q^2} + \frac{16}{q^3} \right) \text{e}^{-q} - \frac{3}{4}\psi_1(v'). \tag{21}$$

For SMPs of spherical shape, owing to the skew-symmetry of the matrix α_{ij}, the last term in (19) vanishes. Expression (19) determines the magnetic absorption of a particle in general form and describes both electron scattering processes taking place in the bulk (in collisions with phonons, impurity centers, lattice defects, etc.) and also surface processes. For each of them separately one can obtain simple analytical expressions from Eq. (19). The specifics of the scattering mechanism are incorporated in the parameters q and $\nu - i\omega$. For example, if it is assumed that $|q| \gg 1$, then $\psi_1 \approx 8/15$, $\psi_2 \approx 0$, and it is easy to verify that the magnetic absorption is governed by an expression that coincides exactly with the formula (9) obtained above for the case of bulk scattering. If, on the contrary, the parameter $|q| \ll 1$, then the governing role in the absorption of energy from the wave is played by electron scattering on the surface of the SMP. Let us discuss it in more detail. It is convenient to separate the analysis into low-frequency ($\omega \ll \omega_{\text{fl}}$) and high-frequency ($\omega \gg \omega_{\text{fl}}$) absorption, where $\omega_{\text{fl}} = v_F/2R$ is the transit frequency and v_F is the velocity of an electron on the Fermi surface.

4. LOW-FREQUENCY ABSORPTION

As one can readily verify, in this case

$$\mathfrak{Re}\left\{\frac{1}{\nu}\psi_1(v)\right\} \approx \frac{1}{3}\frac{R}{v'}, \mathfrak{Re}\left\{\frac{1}{\nu}\psi_2(v)\right\} \approx \frac{1}{36}\frac{R}{v'}, \tag{22}$$

and Eq. (19) can be rewritten as

$$W_{LF} = \frac{\pi e^2 m^2 R^4}{6(2\pi\hbar)^3}\int \frac{d^3v}{v'}\,\delta(v^2 - v_F^2)\left[\sum_{i,j=1}^{3}|\alpha_{ij}|^2 R_j^2 v_i^2 + \frac{R^2}{6}\sum_{i,j=1}^{3}|\alpha_{ij}+\alpha_{ji}|^2\frac{v_i^2 v_j^2}{v'^2}\right]. \tag{23}$$

For a particle in the form of an ellipsoid of revolution the sum in Eq. (23), on the basis of Eq. (6), becomes

$$\sum_{i,j=1}^{3}|\alpha_{ij}|^2 R_j^2 v_i^2 = \left(\frac{\omega}{c}R_\perp\right)^2\left\{\mathbf{H}_\parallel^2\frac{v_\perp^2}{4} + \frac{R_\parallel^4}{(R_\parallel^2+R_\perp^2)^2}\times\left[\mathbf{H}_\perp^2 v_\parallel^2 + \left(\frac{R_\perp}{R_\parallel}\right)^2(\mathbf{H}_x^2 v_y^2 + \mathbf{H}_y^2 v_x^2)\right]\right\} \tag{24}$$

$$\sum_{i,j=1}^{3}|\alpha_{ij}+\alpha_{ji}|^2 v_i^2 v_j^2 = 2\left(\frac{\omega}{c}\right)^2\frac{|R_\parallel^2 - R_\perp^2|^2}{(R_\parallel^2+R_\perp^2)^2}v_\parallel^2(\mathbf{H}_x^2 v_y^2 + \mathbf{H}_y^2 v_x^2), \tag{25}$$

where it should be kept in mind that $v_x^2 + v_y^2 = v_\perp^2$ and $\mathbf{H}_\parallel$, $\mathbf{H}_\perp$ are the magnetic field components along and transverse to the axis of revolution of the ellipsoid.

Taking (24) and (25) into account, we can easily evaluate the integrals over velocities, and we finally get

$$W_{LF} = \frac{3}{64}V\frac{ne^2}{mv_F}\left(\frac{\omega}{c}\right)^2 R_\perp^3\left[\rho_L(e_p)\mathbf{H}_\parallel^2 + \eta_L^M(e_p)\times\left(\frac{R_\parallel^2}{R_\parallel^2+R_\perp^2}\right)^2\mathbf{H}_\perp^2\right], \tag{26}$$

where

$$n = \frac{8\pi}{3}\left(\frac{mv_F}{2\pi\hbar}\right)^3, \quad v_F = \sqrt{\frac{2\mu}{m}}, \tag{27}$$

$$\rho_L(e_p) = \begin{cases} \dfrac{1}{2e_p^2}\sqrt{1-e_p^2} + \dfrac{1}{e_p}\left(1 - \dfrac{1}{2e_p^2}\right)\arcsin e_p, & R_\perp < R_\parallel \\ -\dfrac{1}{2e_p^2}\sqrt{1+e_p^2} + \dfrac{1}{e_p}\left(1 + \dfrac{1}{2e_p^2}\right)\ln(e_p + \sqrt{1+e_p^2}), & R_\perp > R_\parallel \end{cases}, \tag{28}$$

$$\eta_L^M(e_p) = \begin{cases} -\left(2 + \dfrac{1}{e_p^2}\right)\sqrt{1-e_p^2} + \dfrac{1}{e_p}\left(4 + \dfrac{1}{e_p^2} - \dfrac{8}{3}e_p^2\right)\arcsin e_p, & R_\perp < R_\parallel \\ \left(-2 + \dfrac{1}{e_p^2}\right)\sqrt{1+e_p^2} + \dfrac{1}{e_p}\left(4 - \dfrac{1}{e_p^2} + \dfrac{8}{3}e_p^2\right)\ln(e_p + \sqrt{1+e_p^2}), & R_\perp > R_\parallel \end{cases} \tag{29}$$

are functions that depend on the eccentricities of the ellipsoid, which for the prolate ($R_\perp < R_\parallel$) or oblate ($R_\perp > R_\parallel$) ellipsoids considered in the problem are

$$e_p^2 = \begin{cases} 1 - R_\perp^2/R_\parallel^2, & R_\perp < R_\parallel \\ R_\perp^2/R_\parallel^2 - 1, & R_\perp > R_\parallel \end{cases}. \tag{30}$$

The superscript M in Eq. (29) indicates that this function arises only for magnetic fields. In the limiting cases the functions mentioned behave as follows:

$$\rho_L(e_p) = \begin{cases} \dfrac{1}{4}\pi, & R_\perp \ll R_\parallel, \\ \dfrac{2}{3}, & R_\perp = R_\parallel, \\ \dfrac{R_\parallel}{R_\perp}\left(\ln\left(2\dfrac{R_\perp}{R_\parallel}\right) - \dfrac{1}{2}\right), & R_\perp \gg R_\parallel \end{cases} \tag{31}$$

$$\eta_L^M(e_p)=\begin{cases}\pi\left(1+\dfrac{1}{6}\right), & R_\perp \ll R_\parallel,\\ \dfrac{8}{3}, & R_\perp = R_\parallel \equiv R,\\ \dfrac{R_\perp}{R_\parallel}\left(\dfrac{8}{3}\ln\left(2\dfrac{R_\perp}{R_\parallel}\right)-2\right), & R_\perp \gg R_\parallel.\end{cases}$$

This allows us to rewrite the expression for the power absorbed (26) for the cases of highly prolate or highly oblate ellipsoids, respectively, as

$$W_{LF}\approx\frac{3\pi}{4.64}V\frac{ne^2}{mv_F}\left(\frac{\omega}{c}\right)^2 R_\perp^3\{\mathbf{H}_\parallel^2+5\mathbf{H}_\perp^2\},\quad R_\perp\ll R_\parallel. \tag{32}$$

$$W_{LF}\approx\frac{3}{64}V\frac{ne^2}{mv_F}\left(\frac{\omega}{c}\right)^2 R_\parallel^3\left[\ln\left(2\frac{R_\perp}{R_\parallel}\right)-\frac{1}{2}\right]\times\left\{\left(\frac{R_\perp}{R_\parallel}\right)^2\mathbf{H}_\parallel^2+4\mathbf{H}_\perp^2\right\},\quad R_\perp\gg R_\parallel. \tag{33}$$

In particular, it follows from Eq. (32) that for SMPs in the form highly prolate ellipsoids the magnetic absorption in the case when the magnetic field direction is perpendicular to the axis of revolution, under otherwise equal conditions, is five times greater than in the case when the field is oriented along this axis.

Having a general expression (23) for the magnetic absorption of a SMP of ellipsoidal form, one can without difficulty, by analogy with the electric absorption, write an expression for the absorption in the case of low-frequency scattering in terms of the components of the optical conductivity tensor, which in this case is due to the magnetic component of the EM wave (we denote it by the subscript M):

$$W_{LF}=\frac{V}{2}[\sigma_{M,\parallel}^{LF}\mathbf{H}_\parallel^2+\sigma_{M,\perp}^{LF}\mathbf{H}_\perp^2], \tag{34}$$

where

$$\sigma_{M,\parallel}^{LF}=\frac{3}{32}\frac{ne^2}{mv_F}\left(\frac{\omega}{c}\right)^2 R_\perp^3\rho_L(e_p),$$

$$\sigma_{M,\perp}^{LF}=\frac{3}{32}\frac{ne^2}{mv_F}\left(\frac{\omega}{c}\right)^2 R_\perp^3\left(\frac{R_\parallel^2}{R_\parallel^2+R_\perp^2}\right)^2\eta_L^M(e_p) \tag{35}$$

are its longitudinal and transverse components. In the case of a spherical particle ($R_\parallel=R_\perp\equiv R$) it becomes a scalar quantity:

$$\sigma_M^{LF}=\frac{1}{16}\frac{ne^2}{mv_F}\left(\frac{\omega}{c}\right)^2 R^3. \tag{36}$$

In the general case of nonspherical particles σ_M^{LF} is a tensor quantity that depends considerably on the shape of the particle. Figure 1 (curve *1*) shows how the ratio of conductivities along mutually perpendicular directions depends on the shape of the ellipsoid, specified by the ratio of the lengths of its semiaxes $R_\perp/R_\parallel$. The dependence is constructed in accordance with formulas (35). Using this figure, one can trace how the ratio of conductivities changes in an oblate SMP in comparison with a prolate particle.

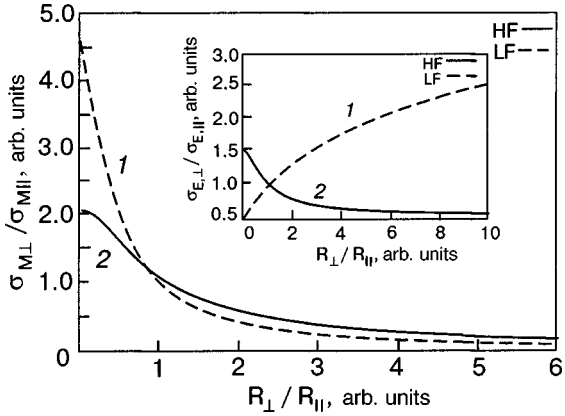

FIG. 1. Dependence of the ratio of optical conductivity transverse to and along the axis of revolution of the ellipsoid on the ratio of the semiaxes of the SMP of ellipsoidal shape for the case of low $\omega\ll\omega_{\text{fl}}$ (*1*) and high $\omega\gg\omega_{\text{fl}}$ (*2*) frequencies. The inset shows the same dependence for the optical conductivity due to the electric component of the EM wave.[16]

5. HIGH-FREQUENCY ABSORPTION

In this case also we shall assume that $\omega\gg\nu$. Then

$$\Re\mathrm{e}\left\{\frac{1}{\nu}\psi_1(v)\right\}\approx\frac{v'}{2R\omega^2},\Re\mathrm{e}\left\{\frac{1}{\nu}\psi_2(v)\right\}\approx\frac{v'}{8R\omega^2}, \tag{37}$$

and Eq. (19) can be rewritten as

$$W_{HF}\cong\frac{\pi e^2m^3R^2}{4(2\pi\hbar)^3\omega^2}\int d\mathbf{v}\delta(\varepsilon-\mu)\left[\sum_{ij}^{3}|\alpha_{ij}|^2R_j^2v_i^2v'+\frac{R^2}{2}\sum_{ij}^{3}|\alpha_{ij}+\alpha_{ji}|^2\frac{v_i^2v_j^2}{v'}\right]. \tag{38}$$

After integration over $\mathbf{v}$ with allowance for Eqs. (24) and (25) we obtain the following expression for the magnetic absorption in the high-frequency case:

$$W_{HF}=\frac{9}{128}V\frac{ne^2}{mc^2}v_FR_\perp\left[\rho_H(e_p)\mathbf{H}_\parallel^2+\eta_H^M(e_p)\times\left(\frac{R_\parallel^2}{R_\parallel^2+R_\perp^2}\right)^2\mathbf{H}_\perp^2\right]. \tag{39}$$

Here the functions that depend on the eccentricity of the ellipsoid are

$$\rho_H(e_p)=\begin{cases} \dfrac{1}{8e_p^2}(1+2e_p^2)\sqrt{1-e_p^2}-\dfrac{1}{8e_p^2}(1-4e_p^2)\arcsin e_p, & R_\perp<R_\parallel, \\ -\dfrac{1}{8e_p^2}(1-2e_p^2)\sqrt{1+e_p^2}+\dfrac{1}{8e_p^3}(1+4e_p^2)\ln(e_p+\sqrt{1+e_p^2}), & R_\perp>R_\parallel. \end{cases} \tag{40}$$

$$\eta_H^M(e_p)=\begin{cases} -\dfrac{1}{4e_p^2}(1-8e_p^2+4e_p^4)\sqrt{1-e_p^2}+\dfrac{1}{4e_p^3}(1+2e_p^2)\arcsin e_p, & R_\perp<R_\parallel, \\ \dfrac{1}{4e_p^2}(1+8e_p^2+4e_p^4)\sqrt{1+e_p^2}-\dfrac{1}{4e_p^3}(1-2e_p^2)\ln(e_p+\sqrt{1+e_p^2}), & R_\perp>R_\parallel. \end{cases} \tag{41}$$

in the limiting cases they behave as follows:

$$\rho_H(e_p)=\begin{cases} \dfrac{3}{16}\pi, & R_\perp \ll R_\parallel, \\ \dfrac{2}{3}, & R_\perp=R_\parallel,, \\ \dfrac{1}{4}\dfrac{R_\perp}{R_\parallel}, & R_\perp \gg R_\parallel. \end{cases}$$

$$\eta_H^M(e_p)=\begin{cases} \dfrac{\pi}{4}\left(1+\dfrac{1}{2}\right), & R_\perp \ll R_\parallel, \\ \dfrac{8}{3}, & R_\perp=R_\parallel\equiv R, \\ \left(\dfrac{R_\perp}{R_\parallel}\right)^3, & R_\perp \gg R_\parallel. \end{cases} \tag{42}$$

This allows us to determine the energy absorbed by a SMP having the form of a prolate ellipsoid, a sphere, or a disk, for which we find, respectively:

$$W_{HF}\approx\frac{27\pi}{8.128}V\frac{ne^2v_F}{mc^2}R_\perp\left\{\frac{1}{2}\mathbf{H}_\parallel^2+\mathbf{H}_\perp^2\right\}, \quad R_\perp \ll R_\parallel. \tag{43}$$

$$W_{HF}\approx\frac{3}{64}V\frac{ne^2v_F}{mc^2}R\mathbf{H}_0^2, \quad R_\perp=R_\parallel\equiv R, \tag{44}$$

$$W_{HF}\approx\frac{9}{128}V\frac{ne^2v_F}{mc^2}R_\parallel\left\{\left(\frac{R_\perp}{2R_\parallel}\right)^2\mathbf{H}_\parallel^2+\mathbf{H}_\perp^2\right\}, \quad R_\perp \gg R_\parallel. \tag{45}$$

Similarly to the previous case, we find from formula (43), in particular, that the magnetic absorption of a SMP in the form a highly prolate ellipsoid with its axis of revolution oriented perpendicular to the external magnetic field, is a factor of two greater than in the case of its orientation along the field.

If, by analogy with Eq. (34), the energy absorbed is expressed in terms of the tensor components corresponding to the optical conductivity due to the magnetic field, then for the high-frequency case we obtain

$$\sigma_{M,\parallel}^{HF}=\frac{9}{64}\frac{ne^2}{mc^2}v_FR_\perp\rho_H(e_p),$$

$$\sigma_{M,\perp}^{HF}=\frac{9}{64}\frac{ne^2}{mc^2}v_FR_\perp\left(\frac{R_\parallel^2}{R_\parallel^2+R_\perp^2}\right)^2\eta_H^M(e_p). \tag{46}$$

Curve *2* in Fig. 1 illustrates the dependence of the ratio of the tensor components of the high-frequency conductivity along mutually perpendicular directions on the ratio of the lengths of the semiaxes of the ellipsoid. The dependence is constructed in accordance with formulas (46). Comparing this result with the result obtained in the low-frequency case (curve *1*), we see that for oblate particles in the interval $1<R_\perp/R_\parallel<6$ the high-frequency transverse conductivity is slightly higher than the low-frequency conductivity. For the case of a prolate form it is just the opposite—the low-frequency transverse conductivity becomes noticeably higher. For a spherical particle the low-frequency and high-frequency conductivities are the same. The inset shows the analogous curves for the optical conductivity due to the electric component of the EM wave.[16]

Using the results of Ref. 16 for the electric absorption W_E and expression (26) for the magnetic absorption, one can compare their relative contributions in the low-frequency case as well. For this it is necessary to choose a particular one of the possible polarizations. The polarization for which the vector of the electric wave is directed along the major axis of the ellipsoid ($\mathbf{E}\|\mathbf{E}_\parallel$, $\mathbf{E}_\perp=0$) or, accordingly, the vector of the magnetic wave $\mathbf{H}=\mathbf{H}_\perp$, $\mathbf{H}_\parallel=0$, we shall call the EL-MT polarization. If, on the contrary, the vector of the electric wave is along the minor axis of the ellipsoid ($\mathbf{E}\|\mathbf{E}_\perp$, $\mathbf{E}_\parallel=0$), then there are two possible directions of the vector of the magnetic wave: along the major axis of the ellipsoid ($\mathbf{H}=\mathbf{H}_\parallel$, $\mathbf{H}_\perp=0$) or along the minor axis ($\mathbf{H}=\mathbf{H}_\perp$, $\mathbf{H}_\parallel=0$). The first of these possibilities we shall call the ET-ML polarization, while the second will be called the ET-MT polarization. For the EL-MT and ET-ML polarizations the ratio of the energy absorbed in the low-frequency case is given by the relation

$$\left.\frac{W_{LF}^M}{W_{LF}^E}\right|_{\substack{EL\text{-}MT\\ ET\text{-}ML}}=\frac{1}{12}\left(\frac{\omega}{c}R_\perp\right)^2 \times\frac{\rho_L(e_p)\mathbf{H}_\parallel^2+[1+(R_\perp/R_\parallel)^2]^{-2}\eta_L^M(e_p)\mathbf{H}_\perp^2}{\dfrac{\eta_L^E(e_p)}{L_\parallel(e_p,\omega)}\mathbf{E}_\parallel^2+\dfrac{\rho_L(e_p)}{L_\perp(e_p,\omega)}\mathbf{E}_\perp^2}, \tag{47}$$

and for the ET-MT polarization

$$\left.\frac{W_{LF}^M}{W_{LF}^E}\right|_{ET\text{-}MT}=\frac{1}{12}\left(\frac{\omega}{c}R_\perp\right)^2\frac{\eta_L^M(e_p)L_\perp(e_p,\omega)\mathbf{H}_\perp^2}{\rho_L(e_p)[1+(R_\perp/R_\parallel)^2]^2\mathbf{E}_\perp^2}, \tag{48}$$

where for the electric field

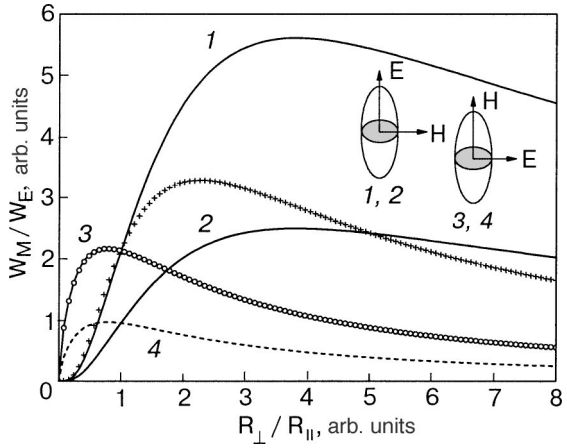

FIG. 2. Dependence of the ratio of the energy absorbed from the magnetic and electric fields on the ratio of the semiaxes of a SMP having the form of an ellipsoid of revolution, at frequencies $\omega \ll \omega_{fl}$ and for two polarizations of the incident wave: EL-MT (*1,2*) and ET-ML (*3,4*). Curves (*1*) and (*3*) are for a particle with $R=75$ Å, and curves (*2*) and (*4*) for $R=50$ Å. The results for a particle with $R=300$ Å at frequencies $\omega \gg \omega_{fl}$ are shown for the EL-MT polarization by the crosses ($\times$) and for the ET-ML polarization by circlets ($\bigcirc$) (they are coincident with curve (*3*)). The insets show the polarization of the EM wave relative to the ellipsoid.

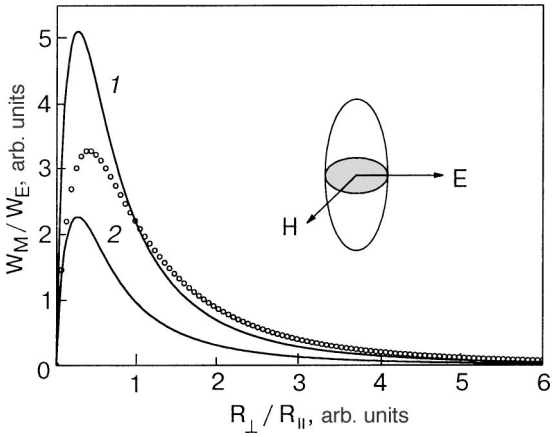

FIG. 3. Dependence of the ratio of the energy absorbed from the magnetic and electric fields on the ratio of the semiaxis of a SMP having the form of an ellipsoid of revolution, for $\omega \ll \omega_{fl}$ and for the orientation of the electric field along the minor axis of the ellipsoid in the MT polarization of the magnetic vector. Curve (*1*) corresponds to a particle with $R=75$ Å and curve (*2*) to a particle with $R=50$ Å. The results for a particle with $R=300$ Å at frequencies $\omega \gg \omega_{fl}$ in this same polarization of the electric and magnetic vectors are shown by circlets ($\bigcirc$).

$$\eta_L^E(e_p)=\begin{cases} -\dfrac{1}{e_p^2}\sqrt{1-e_p^2}+\dfrac{1}{e_p^3}\arcsin e_p, & R_\perp<R_\parallel \\ \dfrac{1}{e_p^2}\sqrt{1+e_p^2}-\dfrac{1}{e_p^3}\ln(e_p+\sqrt{1+e_p^2}), & R_\perp>R_\parallel \end{cases}, \tag{49}$$

and the internal electric field is expressed in terms of the external field with the use of the factor

$$L_{\parallel,\perp}(e_p,\omega)=1+L_{\parallel,\perp}(e_p)[\varepsilon'(\omega)-1]^2 +[L_{\parallel,\perp}(e_p)\varepsilon''(\omega)]^2, \tag{50}$$

$$L_\perp(e_p)=\frac{1}{2}(1-L_\parallel(e_p)), \quad L_\parallel(e_p) =\begin{cases} \dfrac{1-e_p^2}{2e_p^3}\left(\ln\dfrac{1+e_p}{1-e_p}-2e_p\right), & R_\perp<R_\parallel \\ \dfrac{1+e_p^2}{e_p^3}(e_p-\arctan e_p), & R_\perp>R_\parallel \end{cases}, \tag{51}$$

and the remaining notation is the same as introduced previously.

Figure 2 shows how W_{LF}^M/W_{LF}^E depends on the shape of the ellipsoid for two polarizations (EL-MT and EL-ML). It is seen that while for a spherical particle of radius 50 Å the contribution to the absorption of the electric and magnetic components are approximately equal, for particles with $R=75$ Å the contribution of the magnetic component is already twice as large. In the high-frequency case (e.g., for $\omega=2\times10^{14}$ s^{-1}; Ref. 16) such growth becomes possible (independently of polarization) only for particles of radius 300 Å. The trend of W_{LF}^M/W_{LF}^E as a function of the ratio $R_\perp/R_\parallel$ for this case is shown by the crosses in Fig. 2. For the ET-ML polarization it follows exactly the curve for particles with $R=75$ Å. As the shape of the particle changes from spherical to antenna-like the magnetic absorption decreases in the polarizations EL-MT and ET-ML, although when the particle passes to a disk-like form the magnetic absorption increases for the EL-MT polarization and decreases for the ET-ML polarization. We note that the largest value of the ratio W_{LF}^M/W_{LF}^E is reached in the EL-MT polarization for particles of oblate shape at $R_\perp/R_\parallel\approx4$ (independently of the radius of the particle prior to its deformation), while for the ET-ML polarization W_{LF}^M/W_{LF}^E reaches a maximum value for prolate particles, the value being only slightly greater than the corresponding value for a spherical particle.

Figure 3 shows the same dependence for the remaining polarization of the EM wave, ET-MT. For the same ratio of the energy absorbed in the spherical particle, the effect observed when its shape is changed in this case is opposite to that described above for the EL-MT polarization: the magnetic absorption increases in comparison with the electric absorption in the prolate SMP and falls in comparison with it in the oblate. Here the growth of W_{LF}^M/W_{LF}^E reaches a maximum for a prolate shape (independently of the initial radius of the particle), at a radius ratio $R_\perp/R_\parallel\approx0.25$, and with decrease of this ratio the contribution of the magnetic absorption falls in relation to that of the electric absorption.

Thus it is seen from the calculations illustrated in Figs. 2 and 3 that if the magnetic absorption in a spherical particle is, say, twice as large as the electric absorption, then by deformation of such a particle by a factor of four (to an oblate or prolate shape) one can achieve an increase of the magnetic absorption for certain polarizations by more than a factor of five.

6. CONCLUSION

For SMPs in the form of ellipsoids with sizes much smaller than the wavelength of the incident EM wave and the skin depth we have calculated the energy of magnetic absorption at frequencies both above and below the characteristic frequency of the free passage of an electron between walls of the particle. We have considered both the case when

the electron mean free path is larger than the size of the particle and the case when it is smaller. It was assumed that the electrons reflect from the inner surface of the particle in a diffuse manner.

Under conditions for which the bulk or surface scattering of electrons is dominant we have obtained analytical expressions that can be used to determine the dependence of the energy absorbed by a particle on its shape and orientation with respect to the direction of the incident radiation. We have shown that for nonspherical particles the optical conductivity caused by the magnetic component of the EM wave, in contrast to the classical Drude case, becomes a tensor quantity. For particles having the shape of ellipsoids of revolution we have found the components of this tensor and investigated their dependence on the deviation of the particle shape from spherical. Simple analytical expressions were obtained for the energy absorbed by highly prolate or oblate particles.

A feature of SMPs of low symmetry was found wherein the magnetic absorption can be larger than or smaller than the electric absorption, depending on the shape of the particle and its orientation with respect to the direction of the incident EM radiation. It was shown, in particular, that for spherical particles of radius 50 Å at frequencies below the transit frequency of the electron between walls the magnetic absorption in three different polarizations is already comparable in value to the electric absorption, and as the radius of the particle is increased further the magnetic absorption begins to exceed the electric. We have found that when the shape of the particle deviates from spherical to the oblate side, one can obtain growth of the magnetic absorption if $\mathbf{E}_0$ is directed along the major axis of the ellipsoid. If $\mathbf{E}_0$ is directed along the minor axis, then for particles of prolate shape significant growth of the magnetic absorption (in comparison with the spherical particle) can be achieved in the MT polarization and a small amount of growth in the ML polarization. For oblate particles the electric absorption is dominant in these polarizations.

*E-mail: ngrigor@bitp.kiev.ua

[1)]For a typical metal with an electron density $\sim 10^{22}$ cm^{-3} one has $v_F \approx 0.8\times 10^8$ cm/s, and for the value of η given above, $l \sim 800$ Å. Consequently, the radius of the particle cannot be smaller than 400 Å.

[2)]The other known case—specular reflection of electrons from the surface—is more typical of semimetals.[2,23] In ''good'' metals the reflection is close to the specular only for ''glancing'' electrons colliding with the surface at small angles.[24] The fraction of electrons falling into that category can be determined from the dependence of the resistance on magnetic field. Since the wavelength of the conduction electrons is of the order of the interatomic distances, while the characteristic size of the roughnesses always present on the inner surface of an ellipsoidal SMP is much larger than that, in the given case we have decided in favor of diffuse reflection, in which the correlation between the incident and reflected electrons is lost. Diffuse reflection is also preferred in the study of SMPs of cylindrical form.[14,15]

[1] C. F. Bohren and D. R. Huffman, *Absorption and Scattering of Light by Small Particles*, Wiley, New York (1983), Mir, Moscow (1986).
[2] I. M. Lifshits, M. Ya. Azbel', and M. I. Kaganov, *Electron Theory of Metals*, Consultants Bureau, New York (1973), Nauka, Moscow (1971).
[3] D. M. Wood and N. W. Ashcroft, Phys. Rev. B **25**, 6255 (1982).
[4] P. M. Tomchuk, Metallofiz. Noveishie Tekhnol. (Kiev) **25**, 1233 (2003).
[5] A. A. Benditskiĭ, L. V. Viduta, V. I. Konev, S. M. Pimenov, A. M. Prokhorov, P. M. Tomchuk *et al.*, Poverkhnost' **10**, 48 (1988).
[6] R. Ruppin and H. Yaton, Phys. Status Solidi B **74**, 647 (1976).
[7] R. Ruppin, Phys. Rev. B **19**, 1318 (1979).
[8] A. J. Glick and E. D. Yorke, Phys. Rev. B **18**, 2490 (1978).
[9] H. J. Trodahl, Phys. Rev. B **19**, 1316 (1979).
[10] D. B. Tanner, Phys. Rev. B **30**, 1042 (1984).
[11] A. Kawabata and R. Kubo, J. Phys. Soc. Jpn. **21**, 1765 (1966).
[12] É. A. Manykin, P. P. Poluéktov, and Yu. G. Rubezhnyĭ, Zh. Éksp. Teor. Fiz. **70**, 2117 (1976) [Sov. Phys. JETP **43**, 1105 (1976)].
[13] A. G. Lesskis, V. E. Pasternak, and A. A. Yushkanov, Zh. Éksp. Teor. Fiz. **83**, 310 (1982) [Sov. Phys. JETP **56**, 170 (1982)].
[14] É. V. Zavitaev, A. A. Yushkanov, and Yu. I. Yalamov, Zh. Éksp. Teor. Fiz. **124**, 1112 (2003) [JETP **97**, 996 (2003)].
[15] É. V. Zavitaev and A. A. Yushkanov, Opt. Spektrosk. **97**, 131 (2004); Pis'ma Zh. Tekh. Fiz. **30**, 74 (2004) [Tech. Phys. Lett. **30**, 697 (2004)].
[16] P. M. Tomchuk and B. P. Tomchuk, Zh. Éksp. Teor. Fiz. **112**, 661 (1997) [JETP **85**, 360 (1997)].
[17] H. C. van de Hulst, *Light Scattering by Small Particles*, Wiley, New York (1957), Izd-vo Inostr. Lit., Moscow (1961).
[18] Yu. I. Petrov, *Physics of Small Particles* [in Russian], Nauka, Moscow (1982).
[19] M. Born and E. Wolf, *Principles of Optics*, 4th ed., Pergamon Press, Oxford (1969), Nauka, Moscow (1973).
[20] C. Pecharroman and J. E. Iglesias, Phys. Rev. B **49**, 7137 (1994).
[21] L. D. Landau and E. M. Lifshitz, *Electrodynamics of Continuous Media*, 2nd ed., rev. and enl., by E. M. Lifshitz and L. P. Pitaevskii, Pergamon Press, Oxford (1984), Nauka, Moscow (1982).
[22] V. P. Silin and A. A. Rukhadze, *Electrodynamic Properties of Plasma and Plasma-like Media* [in Russian] Gosatomizdat, Moscow (1961), Sec. 17.
[23] V. G. Peschanskiĭ and M. Ya. Azbel', Zh. Éksp. Teor. Fiz. **55**, 1980 (1968) [Sov. Phys. JETP **28**, 1045 (1969)].
[24] A. F. Andreev, Usp. Fiz. Nauk **105**, 113 (1971) [Sov. Phys. Usp. **14**, 609 (1972)].
[25] R. Courant, ''Partielle Differentialgleichungen,'' in R. Courant and D. Hilbert, *Methoden der Mathematischen*; published in translation as *Uravneniya s Chastnymi Proizvodnymi*, Mir, Moscow (1964), Chapter 2.

Translated by Steve Torstveit

PHYSICAL PROPERTIES OF CRYOCRYSTALS

Isochoric thermal conductivity of solid nitrogen

V. A. Konstantinov,* V. G. Manzhelii, V. P. Revyakin, and V. V. Sagan

B. Verkin Institute for Low Temperature Physics and Engineering of the National Academy of Sciences of Ukraine, 47 Lenin Ave., Kharkov 61103, Ukraine

(Submitted July 8, 2004)
Fiz. Nizk. Temp. **31**, 553–557 (May 2005)

The isochoric thermal conductivity of solid nitrogen is investigated on four samples of different densities in the temperature interval from 20 K to the onset of melting. In α-N_2 the isochoric thermal conductivity exhibits a dependence weaker than $\Lambda \propto 1/T$; in β-N_2 it increases slightly with temperature. The experimental results are discussed within a model in which the heat is transported by low-frequency phonons or by ''diffusive'' modes above the mobility edge. The growth of the thermal conductivity in β-N_2 is attributed to the decreasing ''rotational'' component of the total thermal resistance, which occurs as the rotational correlations between the neighboring molecules become weaker. © *2005 American Institute of Physics.*
[DOI: 10.1063/1.1925369]

INTRODUCTION

The thermal conductivity of simple molecular crystals is determined by both translational and orientational motion of molecules in the lattice sites. This motion can be either oscillatory or rotational depending on the relation between the noncentral force and the rotational kinetic energy. Except for rare cases (quantum crystals), the motion of molecules at rather low temperatures is inherently oscillatory: the molecules execute orientational vibrations about equilibrium directions. As the temperature rises, the root-mean-square (rms) amplitudes of the librations increase and the molecules can jump over some accessible orientations. This may lead to a phase transition because the long-range orientation order dissappears. By choosing crystals with different molecular interaction parameters and varying the temperature, it is possible to change the degree of the orientational order and investigate the effect of the molecule rotation upon the thermal conductivity.

Owing to their rather simple and largely similar physical properties,[1,2] the N_2-type crystals (N_2, CO, N_2O, and CO_2) consisting of linear molecules come as suitable objects for such studies. In these crystals the noncentral part of the molecular interaction is determined mostly by the quadrupole force. At low temperatures and pressures, these crystals have a cubic lattice with four molecules per unit cell. The axes of the molecules are along the body diagonals of cube. In N_2 and CO_2, which have equivalent diagonal directions, the crystal symmetry is $Pa3$, for the noncentrosymmetrical molecules CO and N_2O the crystal symmetry is $P2_13$.

In CO_2 and N_2O the noncentral interaction is very strong and the long-range orientational order can persist up to their melting temperatures. In N_2 and CO the barriers impeding the rotation of the molecules are an order of magnitude lower; as a result, orientational disordering phase transitions occur at 35.7 and 68.13 K, respectively. In the high-temperature phases, the N_2 and CO molecules occupy the sites of the hcp lattice of the space group $P6_3/mmc$.

For a correct comparison with theory, the thermal conductivity must be measured at constant density, which excludes the thermal expansion effect. Such investigations were made on CO_2 and N_2O in Ref. 3. Significant deviations from the dependence $\Lambda \propto 1/T$ were observed at $T \geqslant \Theta_D$. It was shown that these departures occurred when the thermal conductivity was approaching its lower limit. The concept of the lower limit of thermal conductivity[4] is based on the following: the mean free paths of the oscillatory modes participating in heat transfer are essentially limited, and the site-to-site heat transport proceeds as a diffusive process.

The goal of this study was to investigate the isochoric thermal conductivity of solid nitrogen in both orientationally ordered and orientationally disordered phases. Earlier, the thermal conductivity of nitrogen was investigated only under saturated vapor pressure.[5–7]

EXPERIMENTAL TECHNIQUE

Constant-volume investigations are possible for molecular solids having a comparatively low thermal pressure coefficient $(dP/dT)_V$. Using a high-pressure cell, it is possible to grow a solid sample of sufficient density. In subsequent experiments it can be cooled with practically unchanged volume, while the pressure in the cell decreases slowly. In samples of moderate densities the pressure drops to zero at a certain characteristic temperature T_0 and the isochoric condition is then broken; on further cooling, the sample can separate from the walls of the cell. In the case of a fixed volume, melting occurs in a certain temperature interval, and its onset shifts towards higher temperatures with increasing density of the sample. This is seen, for example, in the V-T phase diagram[2] of solid N_2 in Fig. 1. The deviations from the constant volume caused by the thermal and elastic deformation of the measuring cell were usually no more than 0.3% and could be taken into account.

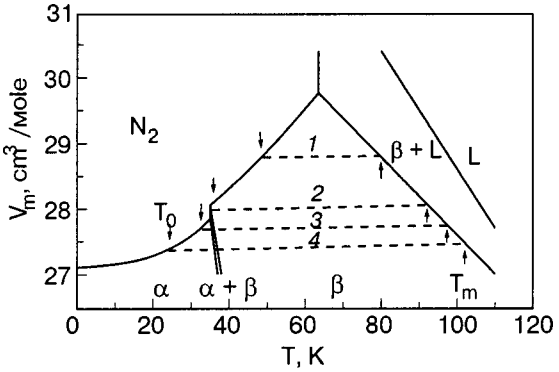

FIG. 1. $V-T$ phase diagram of solid N_2 according to:[1,2] molar volumes (----); arrows show the onset of $V=$const condition and melting.

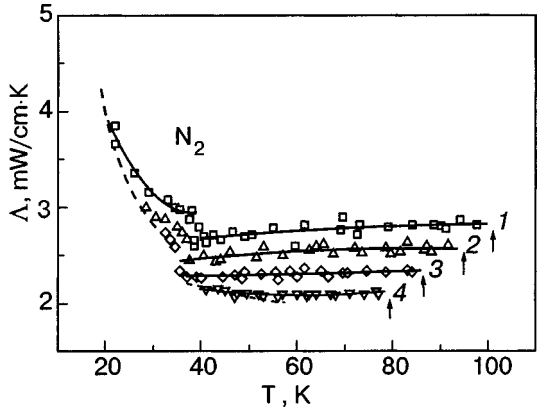

FIG. 2. Isochoric thermal conductivity of four solid N_2 samples of different densities (see Table I): smoothed values (—), measurement under saturated vapor pressure according to Refs. 2, 5–7 (---); the arrows indicate the onset of melting.

The investigation was made using a steady-state technique in a coaxial-geometry setup. The measuring beryllium bronze cell was 160 mm long, with an inner diameter of 17.6 mm. The maximum permissible pressure in it was 800 MPa. The inner measuring cylinder was 10.2 mm in diameter. Temperature sensors (platinum resistance thermometers) were placed in special channels of the inner and outer cylinders to keep them unaffected by high pressure. Duing the growth process the temperature gradient over the measuring cell was 1–2 K/cm. The pressure in the inflow capillary was varied in the range 50–200 MPa to grow samples of different densities. When the growth was completed, the capillary was blocked by freezing it with liquid hydrogen, and the samples were annealed at premelting temperatures for one to two hours to remove density gradients. After measurement the samples were evaporated into a thin-walled vessel and their masses were measured by weighing. The molar volumes of the samples were estimated from the known volume of the measuring cell and the sample masses. The total (dominant) systematic error of measurement was no more than 4% for the thermal conductivity and 0.2% for the volume. The purity of N_2 was no worse than 99.97%.

RESULTS AND DISCUSSION

The isochoric thermal conductivity of solid N_2 was investigated on four samples of different densities in the temperature interval from 20 K to the onset of melting. The experimental thermal conductivities are shown in Fig. 2 with solid lines for smoothed values and a dashed line for measurement under saturated vapor pressure.[2,5–7] Under the same P, T conditions, the discrepancy between our data and data in the literature was no more than 5%. The molar volumes V_m, temperatures T_0 (onset of $V=$const condition) and T_m (onset of sample melting) are shown in Table I. This information is also available in Fig. 1.

In α-N_2 the temperature dependence of the isochoric thermal conductivity is weaker than $\Lambda \propto 1/T$ and is similar to that observed[3] for CO_2 and N_2O. The thermal conductivity is practically constant immediately before the $\alpha \rightarrow \beta$ transition. Earlier, the thermal conductivity was observed to grow in orientationally disordered phases of some molecular crystals.[8] The Bridgman coefficients $g=-(\partial \ln \Lambda/\partial \ln V)_T$ calculated from the experimental results are 6.0 ± 0.8 for α-N_2 at $T=35$ K and 4.3 ± 0.5 for β-N_2 at $T=60$ K.

The orientational motion of the molecules in α-N_2 manifests itself as large-angle librations (immediately before the $\alpha \rightarrow \beta$ transition the rms libration amplitudes $\langle \vartheta^2 \rangle^{1/2}$ exceed 30°) accompanied by hopping over a limited set of equivalent orientations related by elements of the symmetry group.[1] The frequency of reorientations approaches 10^{-11} s^{-1} near the $\alpha \rightarrow \beta$ transition.[9] Analysis of the heat capacity data suggests that practically free precession of the molecules is observed in β-N_2 after the phase transition, which is accompanied by axial vibration through an angle θ with respect to the hexagonal axis of the cell.[1] In the β phase of N_2 the frequency of reorientations varies from 9.5×10^{11} s^{-1} immediately after the $\alpha \rightarrow \beta$ transition to 5.5×10^{12} s^{-1} before melting.[9] This is considerably in excess of the Debye frequency 1.5×10^{12} s^{-1}. No distinct libration modes were detected in β-N_2 in inelastic neutron scattering experiments, and even the observed translational acoustic phonons were broadened considerably due to the translation–orientation interaction, excluding the case of the smallest wave vectors.[10]

Since the orientational motion of the molecules in α-N_2 is essentially librational in character, the thermal conductivity can be calculated within a model in which the heat is transferred by low-frequency phonons or ''diffusive'' modes above the mobility edge. This model was used earlier to calculate the thermal conductivity of CO_2 and N_2O.[11]

Let us describe the thermal conductivity as

$$\Lambda(T)=3nk_B v\left(\frac{T}{\Theta_D}\right)^3\int_0^{\Theta_D/T} l(x)\frac{x^4e^x}{(e^x-1)^2}\,dx, \qquad (1)$$

TABLE I. Molar volumes V_m, temperatures T_0 (onset of $V=$const condition), and temperatures T_m (onset of melting).

Sample No	V_m, cm^3/mole	T_0, K	T_m, K
1	27.36	24	102
2	27.68	33	96
3	27.98	36	92
4	28.76	48	80

where $\Theta_D = v(h/k_B)(6\pi^2 n)^{1/3}$, n is the number of atoms (molecules) per unit volume, v is the polarization-averaged sound velocity, and $l(x)$ is the phonon mean free path. At $T \geqslant \Theta_D$ the mean free path is mainly determined by the umklapp processes $l(x) = l_u$, where:

$$l_u = \frac{\lambda^2}{CT}, \quad C = (12\pi^3/\sqrt{2}) n^{-1/3} (\gamma^2 k_B / m v^2). \tag{2}$$

Here λ is the phonon wavelenth, γ is the Grüneisen constant, m is the atomic (molecular) mass, and C is a numerical coefficient. In the first approximation, the translation–orientation interaction in molecular crystals leads to extra scattering which can be taken into account through simple renormalization of the coefficient C.[12] Since the smallest phonon mean free path is about half the wavelength: $l(x) = \alpha\lambda/2$, where $\alpha \approx 1$, the "diffusivity" edge λ^* can be found as

$$\lambda^* = \frac{\alpha C T}{2}, \tag{3}$$

which corresponds to an effective temperature $\Theta^* = 2hv/\alpha k_B C T$. (It is assumed that $\Theta^* \leqslant \Theta_D$; otherwise we set $\Theta^* = \Theta_D$.) Below, the term "diffusive" is applied to the modes whose mean free paths reached the smallest values.[11] The integral of thermal conductivity is subdivided into two parts describing the contributions to the thermal conductivity from the low-frequency phonons and the "diffusive" modes:

$$\Lambda = \Lambda_{\text{ph}} + \Lambda_{\text{dif}}, \tag{4}$$

$$\Lambda_{\text{ph}}(T) = 3nk_B v \left(\frac{T}{\Theta_D}\right)^3 \left[\int_0^{\Theta_*/T} l(x) \frac{x^4 e^x}{(e^x-1)^2} dx\right], \tag{5}$$

$$\Lambda_{\text{dif}}(T) = 3nk_B v \left(\frac{T}{\Theta_D}\right)^3 \left[\int_{\Theta_*/T}^{\Theta_D/T} \alpha \frac{vh}{2k_B x T} \frac{x^4 e^x}{(e^x-1)^2} dx\right]. \tag{6}$$

The results were computer-fitted by the least-squares technique to the smoothed thermal conductivity values for the sample in the α phase using $n = 2.21 \times 10^{22}$ cm^{-3} and $v = 1.17 \times 10^3$ m/s (Ref. 2) and varying the parameters C and α. The best agreement with experiment was obtained with $C = 3.0 \times 10^{-9}$ cm/K and $\alpha = 1.8$. Correspondingly, $C = 0.9 \times 10^{-9}$ cm/K and $\alpha = 2.7$ for CO_2 and $C = 1.5 \times 10^{-9}$ cm/K and $\alpha = 2.3$ for N_2O (Ref. 11). The fitting to smoothed experimental thermal conductivities and the contributions from the low-frequency phonons Λ_{ph} and the "diffusive" modes Λ_{dif} (calculated by Eqs. (5) and (6)) are shown in Fig. 3.

It is seen that the "diffusive" behavior of the oscillatory modes appears above 20 K, and immediately before the $\alpha \rightarrow \beta$ transition nearly half of the heat is transported by the "diffusive" modes. The curves Λ_{ph} and Λ_{dif} calculated for the α phase of N_2 were extrapolated to the existence region of the β phase. The change from one structure to another may cause a jump of the partial contributions to the thermal conductivity, but it will not be too large because a major part of the heat is transported by the "diffusive" modes, and they are only slightly sensitive to the structure of the crystal. The

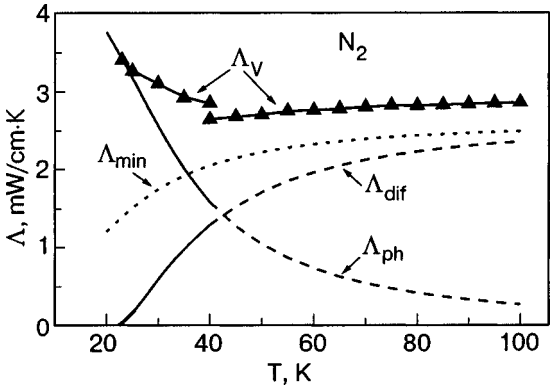

FIG. 3. Fitting to smoothed values of experimental thermal conductivity and contributions to the thermal conductivity from low-frequency phonons Λ_{ph} and "diffusive" modes Λ_{dif} calculated according to (5),(6); the lower limit of lattice thermal conductivity Λ_{min} obtained as an asymptote of the dependence $\Lambda_V(T)$ (---).

lower limit of thermal conductivity Λ'_{min} (Fig. 3, broken line) was calculated assuming that all the modes were "diffusive":

$$\Lambda'_{\text{min}} = 3\alpha \left(\frac{\pi}{6}\right)^{1/3} n^{2/3} k_B v \left(\frac{T}{\Theta_D}\right)^2 \int_0^{\Theta_D/T} \frac{x^3 e^x}{(e^x-1)^2} dx. \tag{7}$$

Note that Λ'_{min} is again independent of structure and determined only by the crystal density, and hence the Debye temperaturs were invariant for the constant volume. The lower limit of thermal conductivity Λ'_{min} fitted as an asymptote of the dependence $\Lambda_V(T)$ is $\alpha = 1.8$ times higher than the value calculated according to Cahill and Pohl.[4] The discrepancy can partly be accounted for by the imperfection of the model. Nevertheless, there is a certain correlation between α and the number of degrees of freedom (three translational and z rotational degrees) of the molecules: $\alpha \propto (3+z)/3$ (Ref. 11). Cahill and Pohl considered amorphous substances and strongly disordered crystals consisting of atoms having no rotational degrees of freedom.

The discussion of the lower limit of thermal conductivity of molecular crystals brings up the inevitable question: should the site-to-site transport of the rotational energy of the molecules be taken into account? The above correlation suggests that the answer is in the affirmative.

In this context, the heat transfer in molecular crystals, solid nitrogen in particular, can be interpreted as follows. At low temperatures, when the phonon and libron branches are well separated, the phonons forming the heat flow are scattered by both phonons and librons.[12] As a result, the thermal resistance increases in comparison with the situation, e.g., in inert gases.[3] As the temperature rises, the phonon–libron interaction is enhanced, and the mixed translation–orientation modes start to transport the heat. The heat transfer increases and extra scattering evolves due to the strong anharmonicity of the librational vibrations. Finally, under very strong scattering, when the heat is transported directly from molecule to molecule (Einstein model), both the rotational and translational energies should equally be taken into account.

In β-N_2 the isochoric thermal conductivity increases slightly with temperature. The absolute value of the thermal conductivity is only 10–12% higher than its lower limit

$\Lambda'_{\min}$. This means that in β-N_2 most of the heat is transported by the ''diffusive'' modes. The concept of the ''lower limit'' of thermal conductivity postulates its ''saturation'' rather than its growth. An increase in the isochoric thermal conductivity with temperature was observed earlier in orientationally disordered phases of some molecular crystals.[8] This effect may be due to the ''rotational'' component of the total thermal resistance, which decreases as the rotational correlations between the neighboring molecules become weaker.

The dependence of the thermal conductivity on the molar volume can also be interpreted within this model. The Bridgman coefficient $g=-(\partial \ln \Lambda/\partial \ln V)_T$ is the weighted mean with respect to the phonons and ''diffusive'' modes whose volume dependences are considerably different:[11]

$$g=\frac{\Lambda_{\rm ph}}{\Lambda}g_{\rm ph}+\frac{\Lambda_{\rm dif}}{\Lambda}g_{\rm dif}. \tag{8}$$

Equation (8) describes the general tendency of the Bridgman coefficient to decrease as more of the heat is being transported by ''diffusive'' modes. The calculation using the procedure of Ref. 11 and the mean Grüneisen coefficient $\gamma=2.2$ for nitrogen[1,2] gives $g=5.2$ at $T=35$ K and $g=3.4$ at $T=60$ K, which are in reasonable agreement with the experimental values.

CONCLUSIONS

The isochoric thermal conductivity of solid N_2 has been investigated on four samples of different densities in the temperature interval from 20 K to the onset of melting. In α-N_2 the isochoric thermal conductivity varies following a dependence weaker than $\Lambda \propto 1/T$; in β-N_2 it increases slightly with temperature. It is shown that the experimental results can be explained within a model in which the heat is transported by low-frequency phonons and by ''diffusive'' modes above the boundary of mobility. In β-N_2 most of the heat is transported by the ''diffusive'' modes. The weak growth of the thermal conductivity in β-N_2 can be attributed to the decrease in the ''rotational'' component of the total thermal resistance due to the relaxing rotational correlations between the neighboring molecules.

This study was supported by the Ukrainian Ministry of Education and Science, Project (F7/286-2001 ''Novel quantum and anharmonic effects in mixtures of cryocrystals.''

*E-mail: konstantinov@ilt.kharkov.ua

[1] V. G. Manzhelii and Yu. A. Freiman (eds.), *Physics of Cryocrystals*, AIP, New York (1996).
[2] V. G. Manzhelii, A. I. Prokhvatilov, V. G. Gavrilko, and A. P. Isakina, *Structure and Thermodynamic Properties of Cryocrystals*, Begell House, New York, Walingford, U.K. (1999).
[3] V. A. Konstantinov, V. G. Manzhelii, S. A. Smirnov, and A. M. Tolkachev, Fiz. Nizk. Temp. **14**, 189 (1988) [Sov. J. Low Temp. Phys. **14**, 104 (1988)].
[4] D. G. Cahill, S. K. Watson, and R. O. Pohl, Phys. Rev. B **46**, 6131 (1992).
[5] H. M. Roder, Cryogenics **2**, 302 (1962).
[6] L. A. Koloskova, I. N. Krupskii, V. G. Manzhelii, and B. Ya. Gorodilov, Fiz. Tverd. Tela **15**, 1913 (1973) [Sov. Phys. Solid State **15**, 1278 (1973)].
[7] P. Stachoviak, V. V. Sumarokov, J. Mucha, and A. Jezowski, Phys. Rev. B **50**, 543 (1994).
[8] O. I. Purskii, N. N. Zholonko, and V. A. Konstantinov, Fiz. Nizk. Temp. **29**, 1021 (2003) [Low Temp. Phys. **29**, 771 (2003)].
[9] T. A. Scott, Phys. Lett. C **27**, 89 (1976).
[10] B. M. Powell, G. Doling, and H. F. Nieman, J. Chem. Phys. **79**, 982 (1983).
[11] V. A. Konstantinov, Fiz. Nizk. Temp. **29**, 567 (2003) [Low Temp. Phys. **29**, 442 (2003)].
[12] V. G. Manzhelii, V. B. Kokshenev, L. A. Koloskova, and I. N. Krupskii, Fiz. Nizk. Temp. **1**, 1302 (1975).

This article was published in English in the original Russian journal. Reproduced here with stylistic changes by AIP.

EPR spectra of deuterated methyl radicals trapped in low temperature matrices

Yu. A. Dmitriev*

A. F. Ioffe Physico-Technical Institute, 26 Politekhnicheskaya St., St. Petersburg 194021, Russia
(Submitted August 2, 2004; revised November 2, 2004)
Fiz. Nizk. Temp. **31**, 558–564 (May 2005)

EPR spectra of CHD_2 and CD_3 radicals are investigated in low-temperature matrices of H_2, D_2, and Ne at temperatures of 1.6–4.2 K. A method of condensation from the gas phase on a cold substrate is used. With decreasing sample temperature, a transformation of the shape of the CD_3 spectrum in H_2, D_2, and Ne matrices and CHD_2 spectrum in H_2 and Ne is observed. This transformation was reversible in the above temperature range. The temperature effects are explained as reflecting a change in the populations of the lowest rotational states of the radicals. The temperature behavior of the EPR spectra for radicals trapped in various matrices are compared on the basis of the present data and known results for deuterated methyl radicals in Ar obtained in photolytic experiments. As a result the existence of a hindering barrier for the radical rotation is suggested. © *2005 American Institute of Physics.*
[DOI: 10.1063/1.1925370]

INTRODUCTION

The methyl radical (CH_3) trapped in low-temperature matrices has been extensively studied by EPR.[1–8] It was shown that at low temperatures near 4.2 K, the EPR spectrum of the radical consists of four lines with equal intensity 1:1:1:1, reaching the high-temperature binomial intensity distribution 1:3:3:1 with increasing temperature. In explaining the EPR spectrum shape and its transformation, two theoretical approaches are used: one treating the CH_3 radical as a restricted rotor and the other, as a free rotor. In contrast to CH_3, few studies have been devoted to deuterated methyl radicals (CD_3, CH_2D, and CHD_2). A spectrum of seven components with ''non-binomial'' distribution has been predicted for the CD_3 radical[9] at low enough temperatures. The septet has been actually registered in the CD4 matrix[10] at 4.2 K and solid Ar at 13 K.[4] Though these experimental results are consistent with the above theoretical scheme, another observation has been published[5] for CD_3 in Ar at 4.2 K showing a strong singlet superimposed on a weak septet. The authors explained their results with a new model of a three-dimensional, free quantum rotor with no hindering barrier present. They pointed out that the electronic state has to be included in the application of the Pauli principle in order to obtain the correct overall exchange symmetry for bosons.

In Ref. 11, results were presented on deuterated methyl radicals trapped from the gas phase in solid H_2. The temperatures at which the CHD_2 and CD_3 spectrum changed to the low-temperature shape turned out to be surprisingly low in H_2 matrix as compared to solid Ar.[5] The present study is aimed at obtaining new information about deuterated methyl radicals in H_2 and studying these radicals in solid D_2 and Ne in order to clarify whether the effect found in Ref. 5 is common to other matrices and to correlate new results with each other, which would help to obtain new data about the matrix effect on the radical rotation.

RESULTS AND DISCUSSION

The experimental technique and a schematic of the setup have been presented elsewhere (e.g., Ref. 12).

In our experiment, molecular deuterium, D_2, mixed with 4 mol. % methane, CH_4, was prepared in a glass vessel and passed through a discharge zone onto a low temperature substrate. Simultaneously, the D_2 was fed onto the same substrate through a separate inlet tube to avoid the gas discharge. The latter flow was much larger than the discharge flow. We estimated the admixture of CH_4 in the D_2 matrix to be about 0.5–1%. A pulsed discharge with an off-duty factor of 7 was used. The substrate temperature during the deposition was 4.2 K. Figure 1 shows the EPR spectrum of a sample of solid D_2 with trapped radicals. For reference, a scheme of EPR transitions for CH_2D, CHD_2, and CD_3 radicals at high temperatures (all rotation levels are populated)

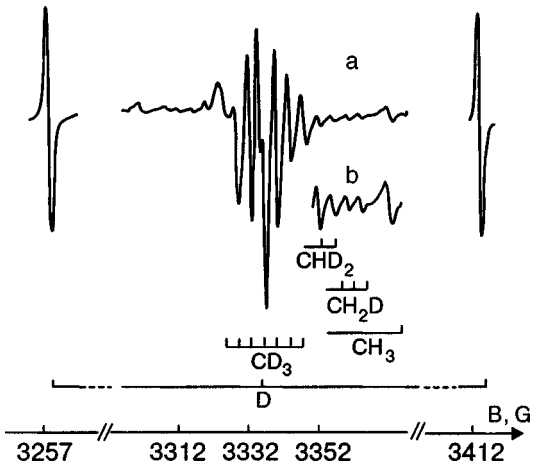

FIG. 1. The EPR spectrum of a solid D_2 sample at 4.2 K with trapped methyl radicals. Also shown are the D-atom transitions (a). The high-field part of the spectrum with higher gain (b). The substrate temperature during deposition $T_{sub}=4.2$ K. Deposition duration, $\tau_{dep}\approx 75$ min. The EPR resonance frequency $f_{res}=9348.22$ MHz.

and low temperatures (only the lowest rotational level is populated) is shown in Fig. 2, according to Ref. 5.

The experimental spectrum reveals seven strong lines of the CD_3 radical and several weak lines for CH_3, CH_2D, and CHD_2 radicals. Superimposed is a record of the high-field lines with a higher gain. Due to the rather large broadening of the lines (the peak-to-peak linewidth $\Delta H = 1.15(5)$ G) only some components of the CH_3, CH_2D, and CHD_2 spectra can be resolved. The CH_3 spectrum is supposedly composed of four lines of equal intensity, like the CH_3 spectrum in the H_2 matrix studied earlier.[6] The CH_2D spectrum is a triple triplet due to the hyperfine (hf) splittings of the two hydrogen nuclei (the major triplet) and one deuterium (the minor triplets). At high enough temperatures, the CHD_2 spectrum is a double quintet.

We have found that two adjacent CD_3 lines are spaced with $\delta H = 3.56(4)$ G. It was observed in Ref. 5 that at temperatures above 10 K the intensity distribution for CD_3 in Ar is practically a ''binomial'' one, 1:3:6:7:6:3:1, originating not only from the population of $J=0$ but also of higher rotational levels. As the temperature was lowered to 4.1 K the central line increased while the other six lines decreased rapidly. As a result, the intensity of the central peak relative to the adjacent one reached 15. It was shown that the spectrum corresponding to the $J=0$ rotational level is a singlet. Turning to our study, it is hard to estimate the relative intensity ratio because the lines are mostly superimposed. However, the amplitude ratio of two ''pure'' CD_3 lines, i.e., the third to the second (counting from the left) equals 2, which is expected for the binomial distribution. The line superimposed on the central CD_3 peak in Fig. 1 is a central transition of the D-atom triplet. We have also recorded two other D-atom lines which appeared alone, i.e., not as a mixture with any transitions. These lines (shown in Fig. 1) were used to extract the ''pure'' CD_3 central line by subtracting the D-atom transition (Fig. 3).

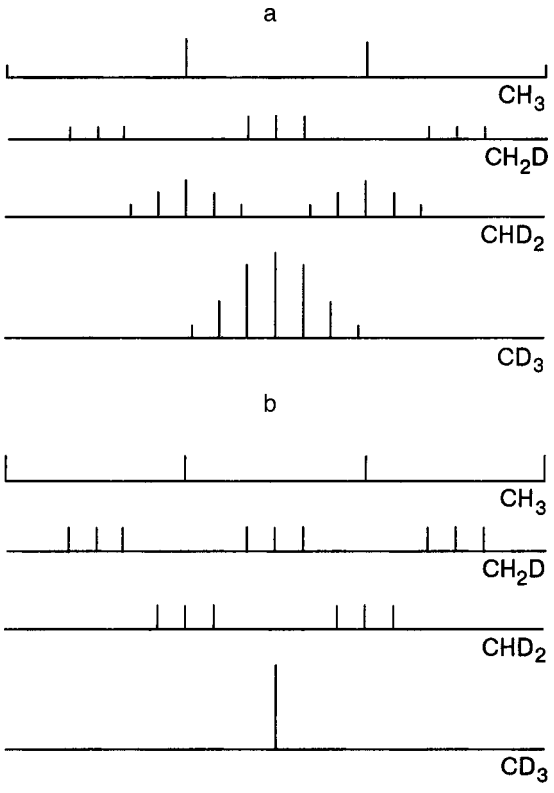

FIG. 2. The scheme of CH_3, CH_2D, CHD_2, and CD_3 transitions at (a) high and (b) low temperatures.

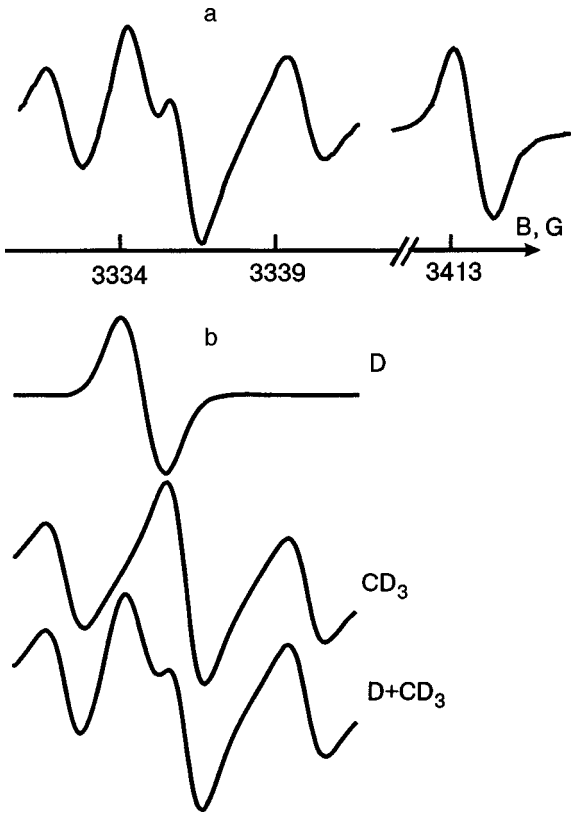

FIG. 3. Central part of the EPR spectra of the CD_3 radical and D-atom lines in a D_2 matrix. The substrate temperature during deposition, $T_{sub} = 4.2$ K. The substrate temperature during registration, $T_{reg} = 2.85$ K (a). The simulated central part of the CD_3 spectrum with the central D-atom transition superimposed (b).

As a result, the amplitude ratio of the central line to its nearest neighbor was estimated to be 1.32, which is a bit larger then the binomial 7:6. Thus the spectrum of CD_3 in D_2 at 4.2 K is a high-temperature nearly ''binomial'' spectrum with possibly a small admixture of the low-temperature singlet. The above-mentioned CH_3 spectrum of four equal lines corresponds to $J=0$, thus being a low-temperature one. Such a difference between the appearances of the CH_3 and CD_3 spectra is not surprising because the energy gap between the $J=0$ and $J=1$ rotational states for the free CH_3 is twice as large as that for the free CD_3. Therefore, the $J=1$ state of the CH_3 radical is not populated at low temperatures close to 4 K. We have found a change in the appearance of the CD_3 spectrum with varying temperature. The high-field D-atom transition was used as a reference signal. Figure 4 shows a plot of the amplitudes of the central CD_3 line and its nearest high-field neighbor versus temperature. One can readily see that the central peak with $m_F = 0$ increases with decreasing temperature, while the amplitude of the other line decreases. Plotting these data, we took special care to avoid line saturation due to microwave power. Such a difference in the temperature behavior between the lines is proof that the central peak is actually a superposition of transitions due to different rotational states: $J=0$ and $J=1$. The population of

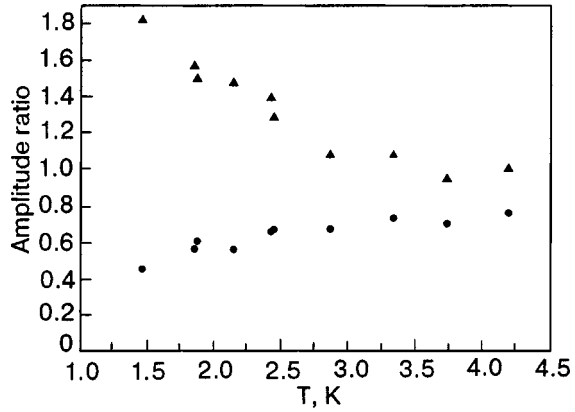

FIG. 4. Amplitudes of the CD_3 central line (▲) and its nearest high-field neighbor (●) versus temperature. The D-atom transition is used as a reference signal.

the lowest $J=0$ level increases with decreasing temperature, while the population of higher rotational levels decreases. This temperature behavior also manifests itself in Fig. 5, which shows the amplitude ratio of the central line to its nearest neighbor.

An investigation was undertaken into the correlation between the temperature change of the EPR spectrum shape and the saturation behavior for the CHD_2 and CD_3 in the molecular hydrogen matrix. Figure 6 shows the saturation curves, that is, the intensities of the central and adjacent lines versus microwave power. The high-temperature spectrum experienced no saturation in the power range used at both 4.2 K and 1.6 K, whereas the central peak starts to saturate at 4.2 K, reaching a pronounced saturation at 1.6 K. Such a difference in the saturation behavior between the lines is further proof that the central peak is actually a superposition of transitions due to different states.

The solid Ne sample with trapped methyl radicals was prepared by co-condensation on a substrate at 4.2 K of two flows: a Ne flow with 1/3 impurity of D_2 mixed with 5 mol. % methane, and a pure Ne flow through the matrix channel. The impurity concentration in the Ne matrix was estimated to be 1–1.5%. A pulsed discharge was employed. The substrate temperature during deposition was 4.2 K. As a result, we obtained a well-resolved spectrum (Fig. 7) of rather narrow lines of the radicals, with a linewidth of about 0.2–0.25 G. The relative intensity ratio for the CD_3 radical, 1:2.9:5.4:7.5:4.8:2.8:1, is close to the ''binomial'' intensity distribution 1:3:6:7:6:3:1. In these experiments, we observed an increase of the central line amplitude relative to intensities of other six lines. The ratio of the central line amplitude to the amplitude of its nearest high-temperature neighbor is presented in Fig. 5. Figure 8 shows the central part of the CD_3 spectrum in Ne taken at several temperatures. One can readily see that the central peak at $m_F=0$ increases rapidly with decreasing temperature in relation to the neighboring transitions.

The investigation with the Ar matrix is still in progress, because in our attempts to study CD_3 trapped in a solid Ar sample we encounter the problem of a very strong central line of the D-atom triplet superimposed on a weaker CD_3

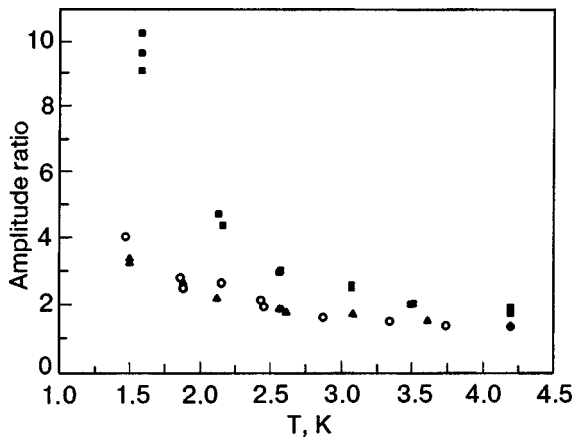

FIG. 5. The temperature dependence of the relative intensity of the CD_3 central component ($m_F=0$) to the neighbor transitions ($m_F=\pm1$) for the CD_3 radical trapped in low-temperature solids: H_2 (●), D_2 (○), and Ne (▲).

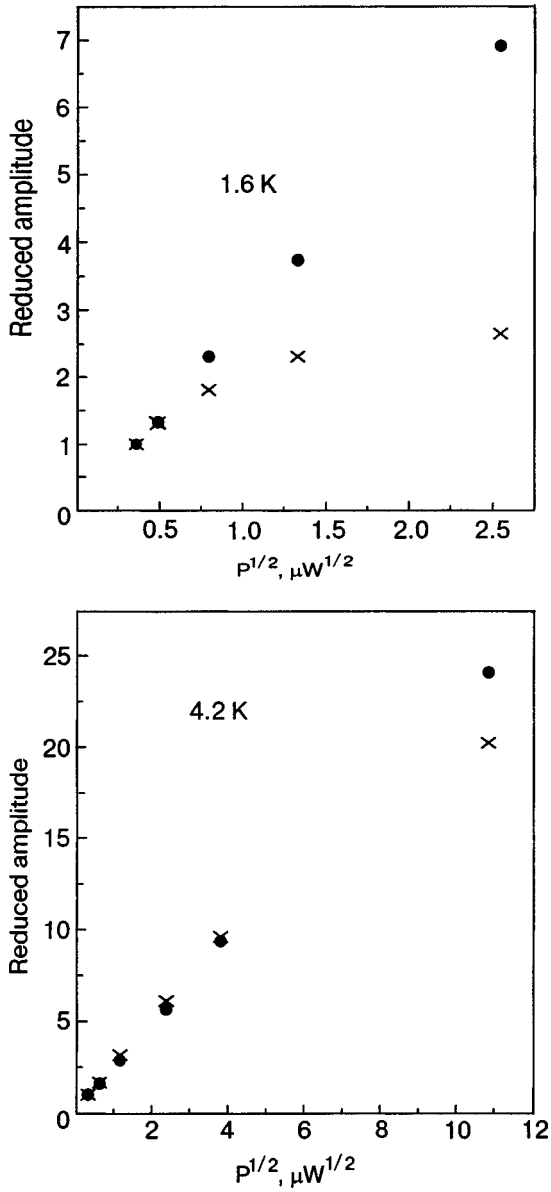

FIG. 6. The amplitudes of the CD_3 central, $m_F=0$ (×) and neighbor, $m_F=\pm1$ (●) transitions versus microwave power for the radical trapped in solid H_2. For convenience of comparison, the amplitudes of the components are set equal at the lowest microwave power.

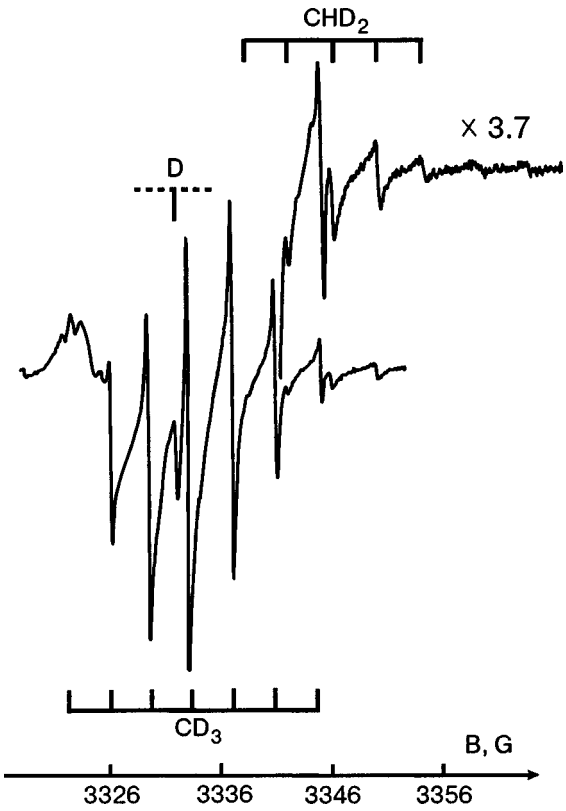

FIG. 7. The EPR spectrum of a solid Ne sample at 4.2 K with trapped methyl radicals. Also shown is the high-field part of the spectrum with higher gain. The substrate temperature during deposition $T_{sub}=4.2$ K, $\tau_{dep}\approx 1$ h, $f_{res}=9353.43$ MHz.

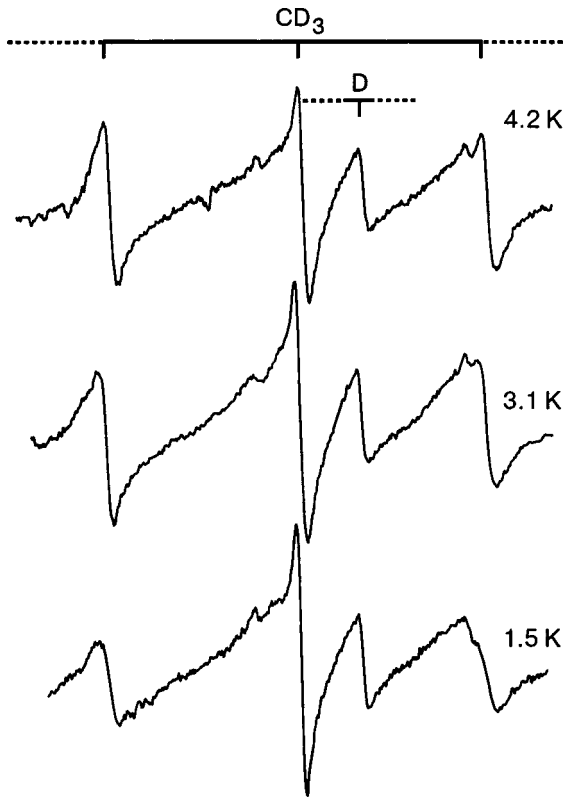

FIG. 8. Temperature-dependent central part of the CD_3 radical matrix-isolated in solid Ne. The substrate temperature during deposition $T_{sub}=4.2$ K at different sample temperature T_{samp}, K.

spectrum. In this situation, any measurements would be of insufficient reliability. We did not face this difficulty with the Ne and D_2 matrices because D atoms are usually trapped in Ne and D_2 in much lower concentrations than in Ar. With the H_2 matrix, the D atoms cannot be seen in the spectrum at all because of the fast tunneling reaction $H_2+D\rightarrow HD+H$.

It is well known that the high-temperature CHD_2 spectrum exhibits a ''binomial'' relative intensity ratio 1:2:3:2:1 for the quintet components. It has been found previously[5] that in the argon matrix the quintet transforms into a triplet with decreasing temperature from 10 K to 4.2 K. In our experiments, the spectrum of CHD_2 in D_2 and Ne was still a double quintet at 4.2 K. In Ne particularly, this spectrum showed, though, an intensity distribution different from the binomial one, which was evident from the fact that the ratio of the line amplitude at $m_F(D)=-1$ to the outermost one at $m_F(D)=-2$ was about 3. This deviation from the binomial distribution is particularly evident in the H_2 matrix. At sample temperatures as low as 1.5 K the transition at $m_F(D)=-2$ disappeared in both matrices, while the next two took similar amplitudes. Such a transformation of the shape of the spectrum suggests a transition from a mixture of the high- and low-temperature spectrum to the low-temperature double triplet. This change from the high-temperature to the low-temperature spectrum for CHD_2 corresponds very well to the case of the CD_3 radical in Ne and H_2.[11] We could draw no conclusion about the CHD_2 temperature behavior in solid D_2 because of the poorly resolved spectrum. We have also failed to draw a conclusion about the appearance of the CH_2D spectrum in both D_2 and Ne matrices, because the central CH_2D triplet could not be seen against the strong CD_3 transitions superimposed on it.

CONCLUSION

The present results verify the effect of temperature on the shape of the CD_3 and CHD_2 spectra first observed in argon[5] with samples obtained by x-ray radiolysis of a matrix containing 0.2 mol. % CH_4. Our data also give new information when comparing the temperature ranges of the spectrum transformation observed in Ref. 5 and here: 10–4.2 K and 4.2–1.5, respectively. Since the spectrum changes we discuss are due mainly to changes in the populations of the lowest $J=0$ and $J=1$ states of trapped radicals, the difference in the range suggests that the energy interval between the above rotational states is significantly larger for radicals trapped in argon[5] than in H_2, D_2, or Ne. In turn, a decrease in this interval for a trapped molecule in comparison with a free one is due to hindering of the rotation of the molecule in the matrix. Because the interaction energies for the CD_3-H_2, CD_3-D_2, and CD_3-Ne pairs are lower than that of the CD_3-Ar pair, one may expect a free rotation of CD_3 in H_2, D_2 and Ne, i.e., a smaller effect on the radical rotation than in Ar. Then the present result suggests the phonon–rotation coupling for CHD_2 and CD_3 molecules in H_2, D_2, and Ne to be surprisingly higher than in Ar. On the other hand, the results for condensed samples are consistent with each other. Actually, a greater increase of the amplitude ratio with decreasing temperature for the H_2 matrix as compared with that of D_2, and Ne suggests that the CD_3-H_2 pair potential is lower than the other two: CD_3-D_2 and CD_3-Ne.

One might suppose that the difference between our results and those of Ref. 5 originates from the greater impurity concentrations in the present study. However, there are several reasons which make this unlikely. First, the major impurity (about 3 mol. %) in the H_2 matrix experiments was another hydrogen isotope, D_2, which caused almost no shift of the lattice parameters and in the CH_3–host molecule interaction. The concentration of CH_4 was less than 0.1 mol. %. Thus, the experiments with the molecular hydrogen matrix with a very small impurity concentration show a different temperature range for the EPR spectrum shape transformation as compared to Ref. 5. Second, the narrow EPR lines in Ne matrices suggest rather regular surroundings. In our experiments, with CH_4-doped Ne (about 0.1 mol. %) we obtained lines with peak-to-peak widths of 0.12–0.15 G. The broadening observed in the present study (about 0.2–0.25 G) cannot be considered dramatic. Third, suppose the impurity concentration to be 1–2 mol. %. Then approximately 10% of the radicals would have an admixture molecule in the nearest neighborhood, which could disturb the rotational motion of the radicals. The other 90% of radicals are trapped in the fine-grain crystallites. Thus, the first group exhibits hindered rotation, while the larger second group undergoes free rotation.[5] Even so, we would not see a nearly binomial distribution at 4.2 K, based on the temperature region determined in Ref. 5. Indeed, the amplitude of the low-temperature singlet is so large that the above freely rotating radicals, even at a considerably lower concentration than suggested above, would transform the spectrum shape into the low-temperature one.

Another conclusion which could be drawn is that the difference between our results and those of Ref. 5 lies in the difference of the sample preparation techniques: radiolysis in Ref. 5 and condensation from a gas discharge in the present study. This may lead to different matrix surroundings in these experiments, that is, a larger matrix cage for the CH_3 obtained by radiolysis. With this technique, the great amount of energy being absorbed locally may lead to a significant local lattice distortion. It was pointed out in Ref. 5 that the EPR line shape of CH_3 below 40 K was reversibly changed with temperature. It is well known that annealing of an Ar matrix at 30 K gives rise to relaxation of structural defects. Although the same supposedly holds for CD_3, it is not stressed in the text that deuterated methyl radicals also showed reversible changes in the same large temperature range of 4.2 through 40 K.

It cannot be ruled out completely that the difference in the matrix preparation techniques would contribute to the difference in the temperature ranges. On the other hand, this contribution is unlikely a deciding factor, because both techniques utilize condensation of a gaseous sample onto a cold surface.

We suggest that the key to this question of different temperature ranges for the spectrum shape transformation lies with the integral intensity of the spectra. If we take this into account, then the results in Ref. 5 and the present data become consistent. Indeed, it is pointed out in Ref. 5 that at the temperature of 4.1 K the linewidth of the central singlet is 0.06 G, whereas the high-temperature transitions are about 4 times broader than the central singlet. Given the relative amplitude of the singlet to the outermost transitions of 105:1 (Ref. 5) and that the integral intensity is proportional to the product of the amplitude and the square of the linewidth, we estimate the integral intensity ratio of the singlet to the high-temperature septet as 1:4. Since the relative population of rotational levels is determined by ratio of integral intensities of lines corresponding to different states, the above result suggests that the majority of the CH_3 radicals are at higher rotational levels. Now, let the EPR lines be of the same width, i.e., broadened due to certain mechanisms: superhyperfine interaction in the H_2 and D_2 matrices and, possibly, structural defects in Ne. Then a relative amplitude ratio of the singlet to its nearest neighbor transition would be about 13:6 at 4.2 K, which is comparable with our results: 12:6.5 in H_2,[11] 8:6 in D_2, and 7.5:5.4 in Ne.

One more conclusion which stems from the above integral intensity ratio of 1:4 concerns the temperature range for the spectrum shape transition. It is obvious that the population of the lowest rotational level is far from saturation at 4.1 K, and it should keep rising with further decrease of temperature. Given lines of equal width, the most prominent spectrum shape transformation would be expected at temperatures below 4.1 K, which is the case in the present study. Because of the unchanged spectrum linewidth with changing temperature, the temperature dependence of the amplitudes in Fig. 5 reflects the relative population of different states. It follows from Fig. 5 that there is a difference between matrices in population of levels at a given temperature. Thus, the results suggest a hindered rotation. This follows both from the low temperature range for the spectrum transformation as compared to the energy gap between the two lowest rotational levels of the free CH_3 radical and from the distinction in the temperature dependence of the level populations for different matrices.

It is of interest now to study an effect of matrix deposition conditions as well as impurity concentration on the rotational barrier. The quench-condensed films of Ar and Kr are known to contain an appreciable number of structural defects. For pure Kr quench-condensed onto a 5 K substrate, the average number of planes between stacking faults is estimated as equal to 11 ± 3, which is a very high density.[13] The matrices studied in the present work have considerably lower annealing temperatures then Kr and Ar, and would contain a much lower density of structural defects. As for impurities, it is not a direct effect on the rotation of the molecule that is interesting, because it is hard to observe (see above), but an indirect effect through the influence on the matrix morphology.[13] In turn, this influence is more prominent for mixtures of two substances differing strongly in molecular parameters,[13] like $Kr:D_2$ and $Ar:D_2$, but not $Ne:D_2$.

*E-mail: dmitriev.mares@pop.ioffe.rssi.ru

[1] R. L. Morehouse, J. J. Christiansen, and W. Gordy, J. Chem. Phys. **45**, 1751 (1966).
[2] G. S. Jackel and W. Gordy, Phys. Rev. **176**, 443 (1968).
[3] C. K. Jen, S. N. Foner, E. L. Cochran, and V. A. Bowers, Phys. Rev. **112**, 1169 (1958).
[4] E. Ya. Misochko, V. A. Bendersii, A. U. Goldschleger, A. V. Akimov, A. V. Benderskii, and C. A. Wight, J. Chem. Phys. **105**, 3146 (1997).

[5] T. Yamada, K. Komaguchi, M. Shiotani, N. P. Benetis, and A. R. Sornes, J. Chem. Phys. **103**, 4823 (1999).
[6] Yu. A. Dmitriev and R. A. Zhitnikov, J. Chem. Phys. **122**, 163 (2001).
[7] H. M. McConnel, J. Chem. Phys. **29**, 1422 (1958).
[8] J. H. Freed, J. Chem. Phys. **43**, 1710 (1965).
[9] A. M. Bass and H. P. Broida (eds.), *Formation and Trapping of Free Radicals*, Academic Press, New York and London (1960).
[10] K. Toriyama, M. Iwasaki, and K. Nunome, J. Chem. Phys. **71**, 1698 (1979).
[11] Yu. A. Dmitriev and R. A. Zhitnikov, Fiz. Nizk. Temp. **29**, 595 (2003) [Low Temp. Phys. **29**, 519 (2003)].
[12] R. A. Zhitnikov and Yu. A. Dmitriev, Astron. Astrophys. **386**, 129 (2002).
[13] M. A. Strzhemechny, N. N. Galtsov, and A. I. Prokhvatilov, Fiz. Nizk. Temp. **29**, 699 (2003) [Low Temp. Phys. **29**, 522 (2003)].

This article was published in English in the original Russian journal. Reproduced here with stylistic change by AIP.

LATTICE DYNAMICS

On the polyamorphism of fullerite-based orientational glasses

A. N. Aleksandrovskii,* A. V. Dolbin,† V. B. Esel'son, V. G. Gavrilko, and V. G. Manzhelii

B. Verkin Institute for Low Temperature Physics and Engineering of the National Academy of Sciences of Ukraine, 47 Lenin Ave., Kharkov 61103, Ukraine

A. S. Bakai

National Science Center "Kharkov Institute of Physics and Technology," Kharkov 61108, Ukraine

D. Cassidy, G. E. Gadd, and S. Moricca

Australian Nuclear Science and Technology Organization, Menai, NSW 2234, Australia

B. Sundqvist

Department of Experimental Physics, Umea University, SE—901 87 Umea, Sweden
(Submitted June 30, 2004; revised March 10, 2005)
Fiz. Nizk. Temp. **31**, 565–584 (May 2005)

A dilatometric investigation in the temperature range 2–28 K shows that a first-order polyamorphous transition occurs in the orientational glasses based on C_{60} doped with H_2, D_2 and Xe. A polyamorphous transition is also detected in C_{60} doped with Kr and He. It is observed that the hysteresis of thermal expansion caused by the polyamorphous transition (and, hence, the transition temperature) is essentially dependent on the type of doping gas. Both positive and negative contributions to the thermal expansion are observed in the low-temperature phase of the glasses. The relaxation time of the negative contribution turns out to be much longer than that of the positive contribution. The positive contribution is found to be due to phonon and libron modes, while the negative contribution is attributed to tunneling states of the C_{60} molecules. The characteristic time of the phase transformation from the low-T phase to the high-T phase is found for the $C_{60}-H_2$ system at 12 K. A theoretical model is proposed to interpret these observed phenomena. The theoretical model proposed includes a consideration of the nature of polyamorphism in glasses, as well as the thermodynamics and kinetics of the transition. A model of noninteracting tunneling states is used to explain the negative contribution to the thermal expansion. The experimental data obtained are considered within the framework of the theoretical model. From the theoretical model the order of magnitude of the polyamorphous transition temperature is estimated. It is found that the late stage of the polyamorphous transformation is described well by the Kolmogorov law with an exponent of $n=1$. At this stage of the transformation, the two-dimensional phase boundary moves along the normal, and the nucleation is not important. © *2005 American Institute of Physics.*
[DOI: 10.1063/1.1925371]

INTRODUCTION

In fullerite C_{60}, the molecules form a face-centered cubic (fcc) lattice. Below the temperature of the glass transition ($T<T_g\approx 90$ K) fullerite is an orientational glass. At present, the short- and intermediate-range orientational ordering in glasses has not been investigated in detail. A two-level model[1,2] is useful for estimating the fractions of the "pentagonal" and "hexagonal" mutual orientations of two molecules in the orientational liquid state. In this model cooperative interactions are ignored. Besides, it has been speculated theoretically[3,4] and found experimentally[5,6] that the orientational structure of a two-dimensional layer of C_{60} molecules consists of domains (clusters) with narrow boundaries. Conceivably, the formation of C_{60} clusters with certain short- or intermediate-range orientational ordering is possible in the three-dimensional case as well. The short-range orientational order (SRO) is broken at the cluster boundaries. For comparison, in metal glasses with topological or structural (rather than orientational) disorder, the polycluster structure and cluster boundaries are detected by the methods of field-emission microscopy.[7–9]

The absence of long-range orientational order (LRO) and orientational structure frustrations leads to the formation of two- or many-level tunneling states (TS) in glassy fullerites. The distribution of the levels and characteristic tunneling times is presumably wide,[10] but our main interest here is with the states which at low temperatures can make an appreciable or even dominant contribution (as compared to the phonon one) to the thermodynamic coefficients such as the heat capacity and thermal expansion coefficient. Owing to

thermally nonactivated tunnel transitions, the TS system attains thermodynamic equilibrium within quite short times, no matter how low the temperature is. In this case the temperature coefficients are mainly contributed to by the those TS in which the spacings between the lowest energy levels are comparable with the thermal energy and the tunneling time does not exceed the time of the experiment.

The potential relief of the cluster boundaries in C_{60} has been considered within a two-dimensional model.[3,4] It was found that in the 2D case the double-well states are separated by low rotational potential barriers with characteristic heights that are about 10^2 times lower at the boundary than in the bulk cluster.

This indicates that within the orientational polycluster there exist low-energy TS at the cluster boundaries, which can generate significant low-temperature effects.

Several low-temperature anomalies were detected while investigating the thermal expansion coefficients of pure C_{60} and C_{60} doped with inert gases (He, Ne, Ar, Kr).[11–15] The most important of them are as follows:

(i) The coefficient of thermal expansion $\alpha(T)$ of pure C_{60} and C_{60} doped with Ne, Ar, Kr is nonmonotonically dependent on temperature and becomes negative in a finite interval at helium temperatures.

(ii) Hysteresis of $\alpha(T)$ is observed in fullerites doped with He and Kr.

Investigation of the time dependence of the thermal expansion upon a jump-like change in temperature shows that a negative contribution to $\alpha(T)$ appears even when the coefficient itself remain positive.

In view of the fact that (i) the TS contribution to $\alpha(T)$ is negative,[11–15] (ii) the positive lattice (phonon and libron) contribution α_L decreases rapidly at low temperatures $T \ll \theta_D, \theta_E$ (where the Debye temperature θ_D and effective Einstein temperature θ_E are 54 and 40 K, respectively[15]) and, (iii) the negative $\alpha(T)$ is caused by the dominant TS contribution, we can obtain at $|\alpha_{TS}| > |\alpha_L|$

$$\alpha(T) = \alpha_{TS}(T) + \alpha_L(T) < 0, \tag{1}$$

where α_{TS} is the contribution of the TS system to the coefficient of thermal expansion.

The hysteresis of $\alpha(T)$ suggests[15] the existence of at least two phases in the orientational He–C_{60} and Kr–C_{60} glasses, and that the phase transition is of the first order.[15] A transformation of phases which leaves the composition of glasses unaltered is conventionally called polyamorphous. The term ''polyamorphism'' was first used in Ref. 16 and subsequently in Ref. 17 to describe the polyamorphous transformation in the amorphous state of the substance. The phenomenon has also been observed in certain liquids and structural glasses.[18,19] It was found also by numerical simulation[20] that amorphous carbon α-C exists in two amorphous phases, graphite-like and diamondlike α-C. It was revealed that at ambient temperature and pressure changes, the graphite-like phase transforms to the diamond-like one.

Fullerite doped with inert gases is the first substance among orientational glasses in which a polyamorphous transition has been detected. It is important to emphasize the diffusion-free kinetics of such transformations. Investigation of the thermodynamics and kinetics of polyamorphous transformations in glasses runs up against certain problems which are inherent due the nature of glasses.

Since the glass is a system with broken ergodicity, the Gibbs's phase determination and, hence, the methods of conventional statistical physics and equilibrium thermodynamics do not hold.

Besides, the state of a nonergodic system is essentially dependent on the thermal history, and the measurement results can greatly be influenced by the duration of the experiment.

For this reason the observed polyamorphous transformations are attributed to the rapidly (in comparison with the time of observation) relaxing and interconverting quasi-equilibrium states of the system.

This paper reports experimental and theoretical results on low-temperature anomalies in the thermal expansion and polyamorphism of C_{60}-based orientational glasses. The objects of dilatometric investigations were solutions of Xe, H_2 and D_2, in C_{60}. This is the first inquiry into the thermal expansion of these solutions.

We propose a theory that includes both a general approach to polyamorphous transformations and a consideration of thermal expansion and phase transformation kinetics (Sec. 2), which allows us to analyze the experimental data (Sec. 3). Comments and conclusions complete the paper.

1. EXPERIMENTAL TECHNIQUE AND RESULTS

The linear thermal expansion coefficient $\alpha(T)$ was investigated using a high-sensitivity capacitance dilatometer[21] and the technique described in Ref. 11.

Since the pure C_{60} and gas-saturated C_{60} used have a cubic lattice, their thermal expansion is isotropic and is characterized by a scalar $\alpha(T)$.

1.1. Xe–C_{60} system

The C_{60} powder (99.99%) with an average grain size of about 100 μm (SES Co., USA) was intercalated with xenon and then compacted. The intercalation was performed for 36 hours at a Xe pressure of $\sim$200 MPa and a temperature of 575 °C. According to the thermal gravimetric analysis (TGA), about 30% of the octahedral cavities of C_{60} were filled with Xe, in agreement with previous studies.[22]

Since the process of Xe–C_{60} dissolution produces considerable deformation of the C_{60} lattice,[22] extreme care was taken to prepare the Xe–C_{60} samples for dilatometric investigation.

In our previous studies[11,13–15] polycrystalline specimens were formed by pressing fullerene powder in a cylindrical die for 30–45 minutes at an effective pressure between 0.5 and 1 GPa. The die consisted of an inner ring with a cylindrical bore and a conical outer surface, fit into an outer cylinder of hardened steel which provided support for the inner pressure. The inner ring was split into four sections. After pressing, the conical inner part was carefully forced out of the outer ring, after which the four sections of the inner ring could be removed with minimum damage to the specimen. The piston used was also made from hardened steel.

The present compound was rather more difficult to press into cylinders than those previously studied.

Pure C_{60} is a soft solid which easily deforms by plastic flow, and many high-pressure studies have been carried out using the material itself as a pressure transmitting medium.[23] Thin solid polycrystalline plates are easily produced by applying a nominal (force-over-area) pressure of up to 1 GPa to C_{60} in the powder form, which then deforms much like a hard wax.

However, because C_{60} hardens appreciably when deformed, in order to produce homogeneous cylindrical specimens with a height approximately equal to the diameter, as used in our measurements of the thermal expansion, it was necessary to fill the cylinder gradually.

In all experiments we have filled the cylinder in ten or more steps, packing the powder well before the next batch was poured in.

Even then, when using this method, it has been necessary to handle the specimen carefully when removing it from the die, since rough handling usually resulted in the breaking of the specimen.

The most common form of fracture observed were cracks perpendicular to the axis, but sometimes conical fractures also occurred, producing low cones with the end surfaces as base.

These difficulties were much more pronounced in the present experiments with the Xe-doped material.

The first attempt to form a cylindrical specimen failed; after pressing, the specimen broke into several pieces. After crushing the material, a second attempt was made, this time successfully. The cylindrical sample was then sent from Sweden to Ukraine for study, but on arrival it had broken into several pieces and was subsequently returned to Umea. A third, very careful attempt was then made, with a newly cleaned die to minimize friction and again with great care in handling. This resulted in a final specimen which was allowed to rest for more than 24 h to see if spontaneous cracks would appear. Since no cracks were observed, the specimen was placed between two teflon cylinders and wound with thin Teflon film until it fitted perfectly in a glass tube. Cotton wool was added to give a slight pressure on the specimen during transport to the B. Verkin Institute of Low Temperature Physics and Engineering of the National Academy of Sciences of Ukraine, Kharkov.

Despite the precautions, the specimen mailed to Ukraine broke into two unequal pieces nearly in parallel to the base. The larger piece was used for thermal expansion investigation. The final sample was a cylinder 5 mm high and 10 mm in diameter. Before measuring, it was kept in a Xe atmosphere (760 Torr) in a glass ampoule at room temperature. The sample was then transferred to the measuring cell of the dilatometer.

The procedure was performed in the air and took 20 minutes. The cell with the sample was then successively evacuated, filled with Xe at 760 Torr and sealed. The sealed measuring cell with the sample in the Xe atmosphere was cooled to 160 K. At this temperature, the measuring cell was evacuated again and cooled down to liquid helium temperature. The vacuum in the cell was maintained at 1×10^{-5} Torr during the whole experiment. The cooling from room temperature to liquid helium temperature took 12 hours.

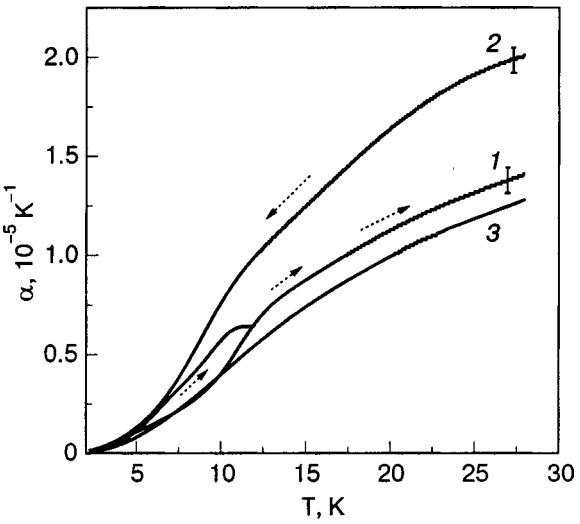

FIG. 1. Temperature dependence of the linear thermal expansion coefficient of $(Xe)_{0.3}-C_{60}$ and pure C_{60}: *1*–heating of $(Xe)_{0.3}-C_{60}$; *2*–cooling of $(Xe)_{0.3}-C_{60}$; *3*—pure C_{60}.

The temperature dependence of $\alpha(T)$ measured on the $Xe-C_{60}$ sample in the range 2–28 K is shown in Fig. 1 (the broken arrows point to the direction of the temperature change during the experiment). It is seen that on heating and subsequent cooling of the sample, $\alpha(T)$ has a considerable hysteresis. As mentioned above, the hysteresis of the temperature dependence $\alpha(T)$ of Xe-doped C_{60} indicates the existence of two phases of the orientational glass. For comparison, the same figure illustrates the thermal expansion of a pure C_{60} sample (broken curve 3) compacted from the pure C_{60} powder that was used for preparing the $(Xe)_{0.3}-C_{60}$, by an identical procedure.

In pure C_{60} the behavior of $\alpha(T)$ is similar on heating and cooling. In both cases, the step-like change in the sample temperature, ΔT, was kept approximately the same. On increasing temperature, the step changed from 0.3 to 1.5 K.

At 5 and 12 K, curve *1* (Fig. 1) is branching. The upper branch appeared with rising temperature immediately after the first cooling of the sample from room temperature to 4.2 K. The lower branch emerged after repeated cooling to 2.2 K and subsequent heating. It is evident that the hysteresis observed in curves *1* and *2* is determined by the temperature prehistory of the sample.

It is seen in Fig. 1 that the thermal expansion of $(Xe)_{0.3}-C_{60}$ is always positive over the range of temperatures studied. However, on heating the sample by ΔT, the time dependence of the thermal expansion exhibits two processes (see Fig. 2) with different characteristic times. The contribution of the faster process to the thermal expansion was positive while that of the slower process was negative. In Ref. 15 the positive contribution was attributed to low-frequency excitations (phonons and librons), while the negative contribution was attributed to tunnel reorientations of the C_{60} molecules.

The positive contribution to the thermal expansion of the $(Xe)_{0.3}-C_{60}$ sample exceeded the negative one over the whole temperature range of the experiment. As a result, the total thermal expansion coefficient is always positive.

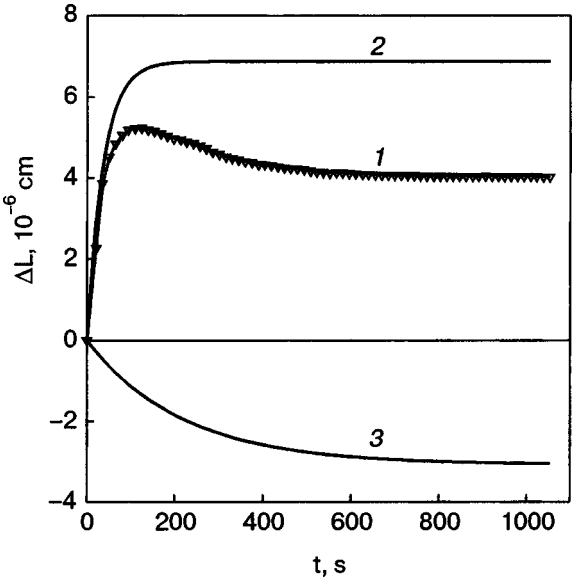

FIG. 2. Characteristic time dependence of the sample length on heating $(Xe)_{0.3}-C_{60}$ by ΔT: experimental results (*1*); positive (*2*) and negative (*3*) contributions to thermal expansion.

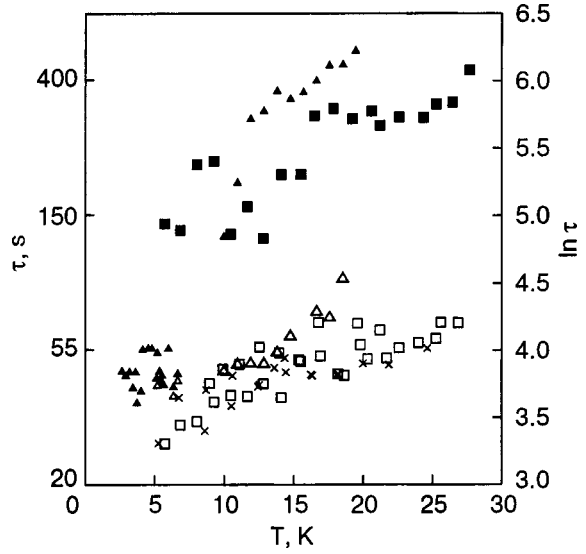

FIG. 3. Characteristic times of positive (□,△,×) and negative (■,▲) contributions to the thermal expansion of C_{60} samples intercalated with xenon (□,■) and krypton (△,×,▲); △—on heating, ×—on cooling.

On cooling of the $(Xe)_{0.3}-C_{60}$ sample there is only a positive contribution to the thermal expansion.

At constant temperature the $\alpha(t)$ dependence can be described by

$$\alpha(t)=\frac{1}{\Delta T}\frac{\Delta L}{L}=A[1-\exp(-t/\tau_1)]+B[\exp(-t/\tau_2-1)], \tag{2}$$

where the first and second terms on the right-hand side of the equation describe the positive and negative contributions, respectively; A and B are the absolute values of the corresponding contributions at $t\to\infty$; and τ_1 and τ_2 are the characteristic relaxation times for these contributions. The B/A value is the ratio of the negative to positive contributions to $\alpha(T)$.

Using the data processing procedure of Ref. 15, we can evaluate the characteristic times of the processes responsible for the thermal expansion of the $(Xe)_{0.3}-C_{60}$ sample and evaluate the positive and negative contributions as a function of temperature. The characteristic times of the positive and negative contributions, τ_1 and τ_2, are shown in Fig. 3. For comparison, the figure includes the characteristic times of the positive and negative contributions to the thermal expansion of the $(Kr)-0.625-C_{60}$ sample.[15] It is seen that in interval 12–22 K the characteristic times of the negative contribution to the thermal expansion of the $(Xe)_{0.3}-C_{60}$ sample are smaller than those for the $(Kr)-0.625-C_{60}$ sample. The characteristic times of the positive contributions in these samples coincide within the measurement error.

The temperature dependence of the ratio B/A of the $(Xe)_{0.3}-C_{60}$ and $(Kr)-0.625-C_{60}$ samples[15] is shown in Fig. 4. For $(Xe)_{0.3}-C_{60}$ the highest value of the ratio is considerably smaller in comparison with what is observed for $(Kr)-0.625-C_{60}$, and is shifted towards higher temperatures. We believe that the reason may be as follows. The gas-kinetic diameter of Xe atoms is larger than that of Kr atoms. When impurity atoms penetrate into the octahedral cavities of fullerite, the distance between the C_{60} molecules surrounding the impurity atom increases, and for the case of fullerite saturation with Xe atoms, results in a larger spacing than in the Kr case. Correspondingly, for $Xe-C_{60}$ solutions, the rotational barrier for the C_{60} molecules is lower. As a result, the tunnel splitting of the energy levels of C_{60} rotation increases and the manifestation of this is that the negative thermal expansion effect shifts towards higher temperatures (see Sec. 2). Our investigations on the $(Xe)_{0.3}-C_{60}$ (this study) and $(Kr)-0.625-C_{60}$, $He-C_{60}$, $Ne-C_{60}$, $Ar-C_{60}$ systems[13–15] lead to the following conclusions. The positive (phonon and libron) contribution to the thermal expansion of the above solutions depends comparatively weakly on the type and concentration of the inert gas dissolved in fullerite. These factors, however, influence significantly the negative contribution caused by tunnel reorientation of the C_{60} molecules

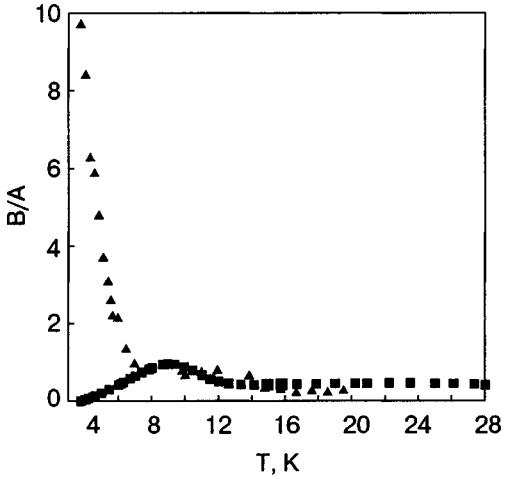

FIG. 4. The absolute value of the ratio between the negative and positive contributions to the thermal expansion of $(Xe)_{0.3}-C_{60}$ (■) and $(Kr)_{0.625}-C_{60}$ (▲) solutions. The coefficient of thermal expansion becomes negative when $B/A>1$.

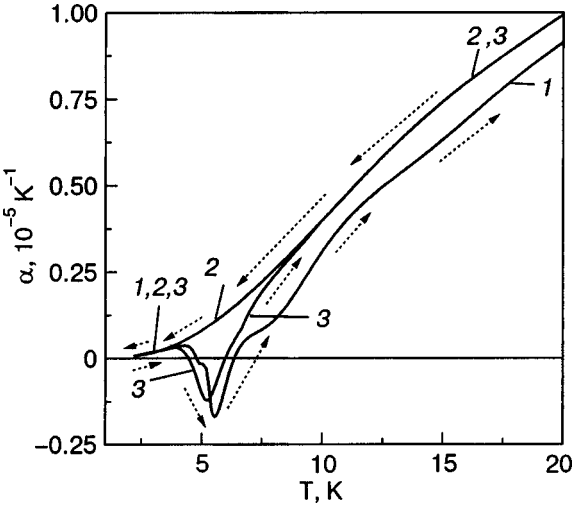

FIG. 5. Temperature dependence of linear thermal expansion coefficient of D_2-doped C_{60}: *1*—heating D_2-C_{60}; *2*—cooling D_2-C_{60}; *3*—heating D_2-C_{60} after five months D_2—desaturation at room temperature. The broken arrows show the directions of temperature variations in the experiment.

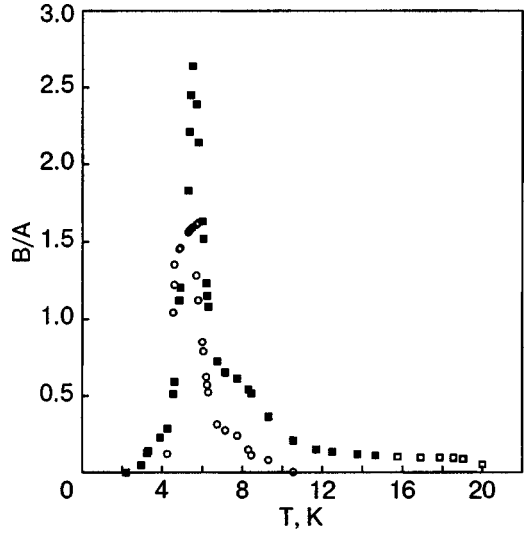

FIG. 6. Absolute values of the ratio of negative and positive contributions to the thermal expansion of D_2-C_{60} (■—before desaturation, ○—after D_2 desaturation for 5 months at room temperature). The thermal expansion coefficient becomes negative when $B/A>1$.

and the $\alpha(T)$ hysteresis caused by phase transformations of the orientational glasses.

1.2. D_2-C_{60} system

The initial sample of pure C_{60} was compacted from C_{60} powder (Term, USA, Berkeley, CA). Before saturation with D_2, the sample was dynamically evacuated (1×10^{-3} Torr, $T=250\,^{\circ}$C) for 48 hours to remove the gas impurities. Thereupon the linear thermal expansion coefficient of pure C_{60} was measured. It was positive in the whole temperature interval (2.2–24 K). No hysteresis in the temperature dependence of the thermal expansion coefficient was observed on heating or cooling the sample. The negative contribution to the thermal expansion was also absent in the whole T range. When these measurements were completed, the measuring cell with the sample was filled with D_2 at room temperature up to 760 Torr. Under this condition, the sample was saturated with D_2 for 15 days. Then the measuring cell with the sample was slowly cooled down to 25 K for 8 hours.

On reaching $T=25$ K, the cell with the sample was evacuated to no less than 1×10^{-5} Torr and the cooling was continued down to $T=2.2$ K, at which the sample was kept for 5 hours before the dilatometric measurement.

The temperature dependence of $\alpha(T)$ of D_2-saturated C_{60} is shown in Fig. 5. It is seen that on heating (curve *1*) and subsequent cooling (curve *2*) of the D_2-C_{60} sample there was a hysteresis in $\alpha(T)$ above 3.5 K (an indication of phase transformations in the orientational glass).

On heating of D_2-C_{60}, both negative and positive contributions to the expansion were detected. The temperature dependence of the ratio B/A of the D_2-C_{60} sample is shown in Fig. 6. A sharp B/A maximum is observed near 5 K. On heating of D_2-C_{60}, the absolute value of the negative contribution is higher in the interval 4.5–6.3 K.

As was stated earlier,[15] the hysteresis in the temperature dependence of thermal expansion, and hence, orientational polyamorphism, appear when the size of the introduced particle exceeds that of the interstitial cavity. In this case, the hysteresis even appears when comparatively small D_2 molecules are introduced into the fullerite lattice. This may indicate that unlike Ne, Ar, Kr and Xe atoms,[22] D_2 molecules occupy not only the octahedral cavities of C_{60}, but also the much smaller tetrahedral ones as well.

Note that earlier in Ref. 15, we also detected a hysteresis in the temperature dependence of the thermal expansion of the He–C_{60} solution. The assumption that He atoms occupy both octahedral and tetrahedral interstitial cavities in C_{60} is substantiated in Ref. 25.

The temperature dependences of the characteristic times of the negative and positive contributions, A and B, of the D_2-C_{60} sample are shown in Fig. 7. It is seen that the largest characteristic times of the negative contribution are observed at 5 K.

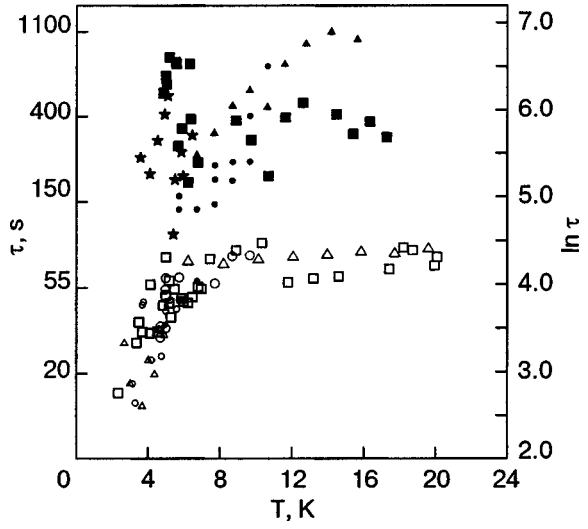

FIG. 7. Characteristic times of positive (□,△,○) and negative (■,⋆,▲) contributions to the thermal expansion of C_{60} doped with D_2 (□,■,⋆) and He (△,○,▲): △—before partial desaturation; ○—after partial desaturation; □—after 5-months desaturation at room temperature.

Recall the sharp maximum in the temperature dependence of the ratio B/A just at this temperature (see Fig. 6).

When the dilatometric investigation was completed, the D_2-C_{60} sample was partly desaturated. To do this, a vacuum no worse than 10^{-1} Torr was maintained in the dilatometric cell with the sample for 150 days at room temperature. Under these conditions the desaturation temperature also corresponded to the temperature at which the sample was saturated with D_2. The desaturation took an order of magnitude more time than the exposure in the D_2.

A further dilatometric investigation showed that the removal of D_2 was not complete even after the above procedure. The hysteresis reappeared in the temperature dependence of the thermal expansion coefficient (Fig. 5, curve *3*). But now the hysteresis and the temperature region of its existence were considerably smaller. In contrast to the D_2-saturated sample, in which the negative contribution to the thermal expansion persisted over the whole T range investigated, the negative component of the thermal expansion of the partly desaturated sample was observed only in the temperature interval of hysteresis 3.5–9 K, and its absolute values were lower than in the case of D_2-C_{60} (see Fig. 6). The positive contribution remained unaltered within the experimental error.

At room temperature and atmospheric pressure, fullerite does not form chemical bonds to hydrogen molecules.[24] The incomplete removal of D_2 from C_{60} during a prolonged desaturation at room temperature supports the aforesaid assumption that D_2 penetrates into the tetrahedral cavities of C_{60}. We can expect that the energy of the interaction between the D_2 and C_{60} molecules is higher in the comparatively small tetrahedral cavities than in the octahedral ones. The D_2 molecules therefore have a lower chance to leave the tetrahedral cavities.

Our assumption that D_2 occupies the tetrahedral cavities of C_{60} is in conflict with the conclusions in Ref. 24, where a neutron scattering investigation detected hydrogen and deuterium only in the octahedral cavities of C_{60}. But the gas saturation of C_{60} powder in Ref. 24 only lasted for 5 hours, which might be insufficient to saturate the tetrahedral interstitial cavities of the subsystem with hydrogen and deuterium. Note that in Ref. 25 the intercalation of C_{60} powder with helium at normal temperature and pressure lasted for 4000 hours. It was concluded that the time taken to saturate the tetrahedral subsystem of interstitial sites with helium was two orders of magnitude longer than that needed to saturate the octahedral subsystem.

1.3. H_2-C_{60} system

After D_2 desaturation at 250 °C, the resultant C_{60} sample was used to investigate the thermal expansion of a H_2-C_{60} solution. The C_{60} sample was saturated directly with H_2, in the measuring cell held at 20 °C and a pressure of 760 Torr, for 13 days. The sample was then cooled down to liquid helium temperature using the procedure described in the previous Section. The thermal expansion of H_2-C_{60} was investigated in the temperature interval 2.2–22 K. The results are shown in Fig. 8.

It is seen that the hysteresis in the temperature dependence of the $\alpha(T)$ of H_2-C_{60} persists over the whole temperature interval. As in the case of D_2-C_{60}, on heating H_2-C_{60}, both negative and positive contributions with different characteristic times are present in the thermal expansion. On cooling, however, only a positive contribution is observed. Curves *1* and *2* in Fig. 8 were obtained by a polynomial approximation of the experimental $\alpha(T)$ values, using a least-squares fit technique. Curve *3* is the difference between curves *1* and *2*. The positive (squares) and negative (circles) contributions to the thermal expansion on heating of the sample were evaluated through processing the time dependences of the length variations of the H_2-C_{60} sample, using Eq. (1). The heating-induced positive contributions to the thermal expansion of H_2-C_{60} (open squares), and the $\alpha(T)$ measured on cooling agree within the experimental error over the whole temperature interval. This supports our assumption that the phonon and libron contributions to the $\alpha(T)$ are insensitive to the type of orientational glass. Besides, the negative contribution measured on heating (filled circles) of H_2-C_{60} agrees, within the experimental error, with curve *3* in Fig. 8, which is the difference between curves *1* and *2*. This means that the negative contribution is precisely responsible for the decrease in the $\alpha(T)$ obtained on heating the sample (Fig. 8, curve *1* as compared to curve *2*).

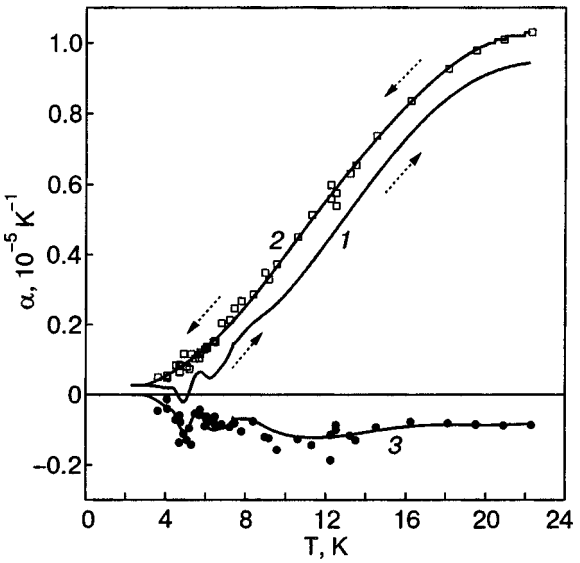

FIG. 8. Temperature dependence of the linear thermal expansion coefficient of H_2-C_{60}: data taken on heating (*1*) and on cooling (*2*) the sample, and the difference between curves *1* and *2* (curve *3*); □ and ● are positive and negative contributions to the thermal expansion of H_2-C_{60}, respectively.

The $\alpha(T)$'s of D_2-C_{60} (solid lines *1,2*) and H_2-C_{60} (broken curves *3,4*) are shown in Fig. 9. The curves taken on cooling of H_2-C_{60} and D_2-C_{60} agree within the experimental error over the whole temperature range. On heating, the H_2-C_{60} and D_2-C_{60} samples exhibit quite different behavior of $\alpha(T)$ in the interval 5–9 K. The temperature dependences of the ratio between the negative and positive contributions to the thermal expansion of the H_2-C_{60} sample are shown in Fig. 10.

The characteristic times of the positive and negative contributions to the thermal expansion of H_2-C_{60} and D_2-C_{60} are shown in Fig. 11. They are seen to coincide for both the solutions within the experimental accuracy. The dynamics of the processes responsible for the hysteresis in the tempera-

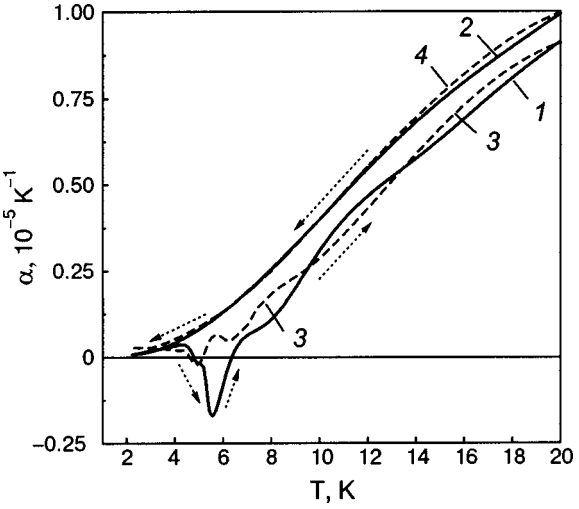

FIG. 9. Temperature dependences of $\alpha(T)$ for D_2-C_{60} (heating (*1*) and cooling (*2*)) and H_2-C_{60} (heating (*3*) and cooling (*4*)).

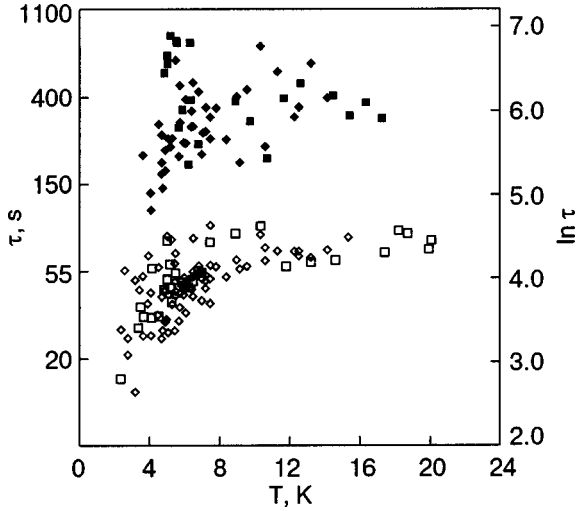

FIG. 11. Characteristic times of positive (◇,□) and negative (◆,■) contributions to the thermal expansion of H_2-C_{60} (◇,◆) and D_2-C_{60} (□,■).

ture dependence of the $\alpha(T)$ of H_2-C_{60}, was investigated in the following experiment. After keeping the sample at 4.2 K for four hours, its temperature was raised to 9.5 K during 20 min. The sample was then thermocycled in the interval 9.5–13.5 K at a step of 2 K. The duration of one step was half an hour.

The thermocycling procedure thus involved two heating steps followed by two cooling steps. In doing so, we obtained the $\alpha(T)$ values at 10.5 and 12.5 K. As the temperature increased, the negative contribution decreased with time while the positive contribution did not vary. On lowering the temperature, only the positive contribution was present.

It was thus possible to extract the time dependence of the normalized negative contribution B' to the thermal expansion of H_2-C_{60} at 10.5 and 12.5 K, and as shown by the triangles and circles, respectively, in Fig. 12. The normalized B' values are the ratios of the negative contribution at the time t to the negative contribution at the initial instant of time ($t=0$ is the time corresponding to stabilization of $T=11.5$ K).

The time dependence of the experimentally measured negative contributions to the thermal expansion of H_2-C_{60} was approximated by an exponential (see Fig. 12). The characteristic time τ' of this process found by the exponential approximation is 4700 s. The time τ' is actually the characteristic time of the phase transformation in the investigated orientational glass. Note that the characteristic time of reorientation of the C_{60} molecules in the H_2-C_{60} system at T $=11.5$ K is an order of magnitude shorter (≈ 400 s; see Fig. 11).

2. THEORY

2.1. Phase transition in systems with broken ergodicity

2.1.1. Specific features of systems with broken ergodicity

Statistical physics based on the Gibbs microcanonical distribution postulates that any system is ergodic, i.e., its

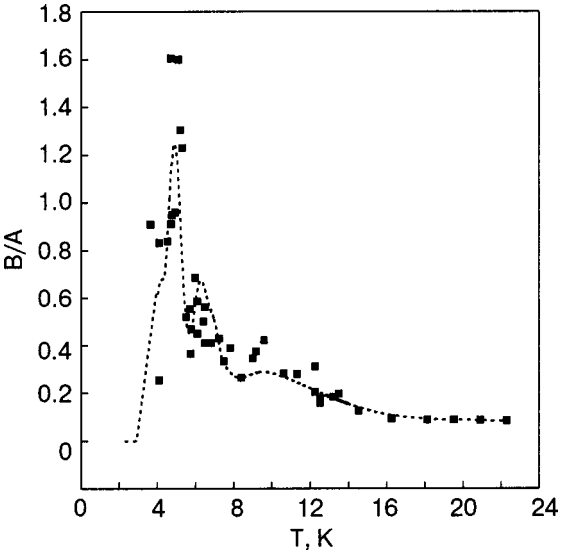

FIG. 10. The absolute values of the ratio between the negative and positive contributions to the thermal expansion of C_{60} saturated with H_2 (■). The curve in fact corresponds to the ratio of the absolute value of curve *3* to that of curve *2* shown previously in Fig. 8.

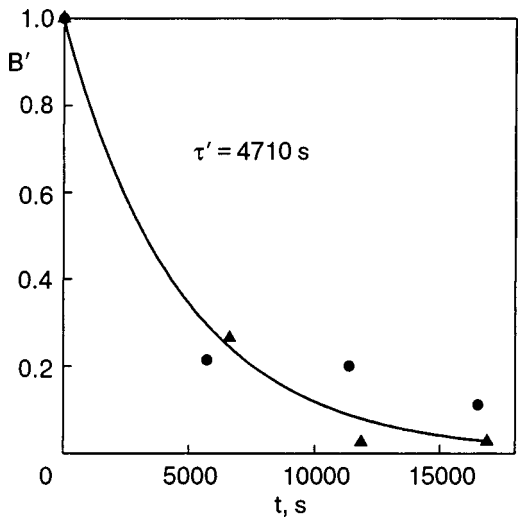

FIG. 12. Dependence of the normalized negative contributions at 10.5 K (▲) and at 12.5 K (●) to the $\alpha(T)$ of H_2-C_{60} upon the current time point of the experiment obtained during thermocycling and within the temperature range 9.5–13.5 K. The solid curve is the exponential approximation of the results.

phase trajectory covers the isoenergetic surface, $E=\varepsilon(p,q)$, densely and throughout, and along the phase trajectory, the time average is equal to the average over the isoenergetic surface.

On using the canonical distribution, the averaging over the isoenergetic surface is replaced by ensemble averaging. In systems with broken ergodicity,[26] the isoenergetic surface can be subdivided into simply connected regions (basins) in which, on the one hand, a given phase trajectory may never go beyond the boundaries of the basin it has been introduced into, during the observation time τ_{obs} and, although on the other hand, it may still have enough time to cover densely the whole basin.

It is seen that the definition of a basin inherently has to consider the parameter τ_{obs}. Sometimes (e.g., in systems with spontaneous broken symmetry) the barriers separating the basins are infinitely large in the thermodynamic limit. In this case, the phase trajectory would never leave the basin into which it was brought, by the process of evolution. The subdivision of the isoenergetic surface into basins corresponding to various possible states in this case would therefore be independent of τ_{obs}.

Glasses are typical systems with broken ergodicity whose properties depend on the time of observation. This statement itself implies the existence of finite barriers between the basins. Nevertheless, the properties of aged and annealed (at $T<T_g$) glasses vary very little with time, and such changes can usually be neglected. It can therefore be assumed that the phase trajectory of such a glass system and during the period of observation belongs to one invariable basin. As for the total number of basins possible, or equivalently the number of structural states of the glass available, this turns out to be exponentially large and is given by:

$$W(N)=\exp(\zeta N). \tag{3}$$

Here N is the number of molecules in the given system and $\zeta>0$ (ζ is usually of the order of unity).

In an ergodic system, the quantity ζ would describe the configuration entropy (assuming that the Boltzmann constant is unity). In the glass, where the system is arrested in one of the basins, ζ describes the complexity of the structure.[26]

The free energy of a glass arrested in the ith basin, $G_i(P,T)$, can be calculated taking into account the states belonging only to this basin. Since the system has no symmetry, its states, possessing a unique energy, are not equivalent thermodynamically. The numerous deepest minima of the free energy found in the isoenergetic layer in themselves make up a metabasin of states of which the glass is found invariably in one of these states.

2.1.2. Short- and intermediate-range order, isoconfigurational states

Short-range order. The glass structure has no long-range order and is therefore characterized by the short-range and intermediate-range orders. The short-range order (SRO) is determined by the correlation in the mutual arrangement of the neighboring molecules (mutual orientation). Let us consider the SRO in a certain site of a fcc lattice. Because of the short-range interaction of the molecular forces, the highest contribution to the free energy is made by the interactions with the nearest surroundings, i.e., with those molecules forming a coordination polyhedron. The mutual orientation of the molecules within the coordination polyhedron is definitely responsible for the SRO.

There are a finite number of nonequivalent orientational configurations of molecules in the coordination polyhedron that correspond to the free energy minima. Hence, there are a finite number of SRO types, which can undergo thermally activated rearrangements.

Although the coordination polyhedron is a natural structural element, the molecular associates forming significant many-particle orientational correlations can be inconsistent with the coordination polyhedra.

For simplicity, we assume that these orientational associates are equal in size to the coordination polyhedra.

The associativity of molecules in terms of the SRO is also taken into account in the description of the cooperative phenomena in ordinary vitrifying liquids (see Refs. 8, 27, 28). In this case the description of the thermodynamic properties is reasonable if we assume that the average number of molecules in the associate, k_0, is about 10, i.e., the associates include the molecules of the first coordination sphere. Assuming that the orientational associates having different types of SRO are independent statistically, we can estimate their equilibrium concentration in the melt using Gibbs statistics. In the cell approximation, the partition function of the melt $Z(P,T;N,k_0)$ is

$$Z(P,T;N,k_0)=[z(P,T;k_0)]^{N/k_0},$$

$$z(P,T;k_0)=\sum_i \exp[-k_0 g_i(P,T)\beta], \quad \beta=1/T. \tag{4}$$

Here $z(P,T;k_0)$ is the partition function of a cell consisting of k_0 molecules; $g_i(P,T)$ is the mean free energy per molecule in the ith type associate, and N is the number of molecules. Also, Boltzmann's constant is taken as 1 in Eq. (4) and below in this paper.

According to Eq. (4), the fraction of the ith type of orientational associate out of a considered total number possible of n_s is

$$c_i(P,T)=\exp[-k_0 g_i(P,T)\beta]z^{-1}(P,T;k_0). \tag{5}$$

The number of the associate types, n_s, is a characteristic of the substance.

Remember that this expression holds only for the melt (ergodic), where Gibbs statistics (Eq. (4)) are valid. If we assume that the loss of ergodicity during the glass transition does not cause significant changes in the SRO, then at a temperature $T<T_g$, the corresponding fraction of the ih type of orientational associate in the glass is given by

$$c_{i,g}=c_i(P,T_g). \tag{6}$$

Intermediate-range order. In accordance with the approximation used, the glass structure is considered as consisting of N/k_0 cells. Each of the cells possesses one of the possible SRO's correlations of orientational order that can exist. Although the orientational pair correlations become weaker with distance, the correlations between the mutual positions of various types of associates can extend to large (as compared to associate sizes) distances. This phenomenon is observed in ordinary glass forming liquids and

polymers.[28,29] Since the interaction with the molecules of the neighboring associate is weaker than that inside the associate, the formation of long-range pair correlations has only a slight effect on the free energy and, hence, on the fraction of a particular type of associate in the glass as determined by Eq. (6). However, these correlations are still important structural characteristics of the glass. The pair correlations of the mutual positions of various types of associates are

$$w_{ik}(r)=\langle c_{i,g}(x)c_{k,g}(x+r)\rangle, \quad r>r_a\approx a k_0^{1/3}. \tag{7}$$

Here r_a is the size of cell (size of associate) specified by a SRO and a is the size of the molecule; the local orientational order and the angle brackets indicate spatial averaging. When correlations are absent, then $w_{ik}(r)=\overline{c}_{i,g}\overline{c}_{k,g}$ ($\overline{c}_{k,g}\equiv\langle c_{k,g}(x)\rangle$). The first maximum of $w_{ik}(r)$ evidently is at $r_p\approx 2r_a$. The values of pair correlation functions at r_p are therefore important structural characteristics. Let us denote them as $w_{ik}(r_p)$. The number of the neighboring associates is $k\approx 2^3\sim 10$. For the ith type associate, within the sphere of radius r_p the fraction $c_{i,g}$ is nearly equal to $w_{ii}(r_p)$ provided that the associate of this type occupies the position at the center of the sphere.

On the intermediate scale, the orientational structure is characterized, along with $w_{ik}(r_p)$, by higher-order correlators.

Isoconfigurational structures. The static properties of orientational configurations are determined by the magnitudes $\{c_{i,g}, w_{ik}(r)\}$ and by higher-order correlators. Two states of the glass will be considered isoconfigurational in the mth order if their first m correlators coincide. Differences between correlators higher than m reflect the distinctions between the structures and properties of the two states of the glass. On the other hand two isoconfigurational structures are considered as being isomorphic if $m\to\infty$.

The free energy of the glass can be represented as an expansion in which the first two terms are determined by the $\overline{c}_i$ and $w_{ik}(r_p)$ values:

$$G_0(P,T)=N\left[\sum_i \overline{c}_{i,g}g_i(P,T)+\sum_{i,k}\overline{c}_{i,g}w_{ik}(r_p)g_{ik}(P,T)\right]. \tag{8}$$

Here we put $w_{ik}(r>r_p)=0$ assuming that the pair correlations at $r>r_p$ are negligible; $g_{ik}(P,T)$ is the mean free energy contribution from the pair interaction of the associate i with k. In operations with Eq. (8) it has to be taken into account that $\Sigma_i c_{i,g}=1$ and $\Sigma_k w_{ik}=1$.

In the approximation of Eq. (8) all structural states of the glass with identical $\overline{c}_i$ and $w_{ik}(r_p)$ are taken as isoconfigurational states having the same free energies. The expression for free energy should also allow for the contribution from the intercluster boundaries

$$G(P,T)=G_0(P,T)+G_s(P,T),$$

$$G_s(P,T)=N_s[\overline{g}_s(P,T)-\overline{g}_0(P,T)], \tag{9}$$

where N_s is the number of molecules in the cluster boundaries; $\overline{g}_s(P,T)$ and $\overline{g}_0(P,T)$ are the mean free energy per molecule within boundary and bulk, respectively. The contributions of other defects to the free energy can be included, too, but it is reasonable to separate these contributions explicitly only if we are interested in their related phenomena.

2.1.3. Polyamorphous transformations

The free energy of the glass represented in the form of Eqs. (8) and (9) enables us to construct the phenomenology of polyamorphous transformations. First note that the expression for the free energy includes both the free energies $g_i(P,T)$ and $g_{ik}(P,T)$ describing the thermodynamic properties of associates, as well as the ''frozen in'' concentrations $\overline{c}_i$ and correlations $w_{ik}(r_p)$. The nth-order phase transition entails a jump-like change in the nth-order derivative of the free energy with respect to pressure and temperature.

If $\overline{c}_i$ and $w_{ik}(r_p)$ are considered to be constant, while P, T are considered as independent variables, a polyamorphous transition is possible only on discontinuity of the derivatives of the functions $g_i(P,T)$ and $g_{ik}(P,T)$. Such a phase transition is *isoconfigurational*. The isoconfigurational transition is caused by changes in the associates which leave their concentrations and mutual positions unaltered. During the isoconfigurational phase transition the system remains in the same basin but the derivatives of the free energy are not smooth, at least for some types of associates or associate correlations. Isoconfigurational phase transitions are reversible, since the topology of associates remains unaltered. Isoconfigurational polyamorphism is a special case of the general polyamorphism during which both the derivations of $g_i(P,T)$ and $g_{ik}(P,T)$, as well as the magnitudes $\overline{c}_i$ and $w_{ik}(r_p)$, change in a jump-like manner.

Transformability of the glass structure stems from the nature of the ''frozen in'' configurations. Indeed, the parameters $\overline{c}_i$ and $w_{ik}(r_p)$ correspond to the free energy minimum only at $T>T_g$. This is not truly correct any more at $T<T_g$ because Eqs. (4) and (5) do not hold in this case. The degree of the glass nonequilibrium is evident in the deviation of the free energy from the minimum,

$$\Delta G(P,T)\approx N\sum_i [c_i(P,T)-c_{i,g}]g_i(P,T). \tag{10}$$

Here $c_i(P,T)$ stands for equilibrium fractions (5). Equation (10) is a simplified form of $\Delta G(P,T)$, since it does not allow for the contribution from pair interactions of the associates.

It is clear that the structure relaxation induced by the thermodynamic driving force, Eq. (10), is retarded only by the slow kinetics of structural rearrangements. The slowing down of the thermally activated relaxation processes with decreasing temperature is the reason why the polyamorphous transformation to a glass manifests itself as a jump-like change of physical quantities and is observed only when the kinetic requirement is met so that

$$\tau_{12}<\tau_{\text{obs}}. \tag{11}$$

Here τ_{12} is the time during which phase 1 transforms into phase 2. The kinetic requirement of Eq. (11) can be fulfilled only if the activation barriers controlling the phase transformation decrease considerably or if the phase nonequilibrium is large enough and there is a mechanism of athermic relaxation similar to martensitic transformations (see, e.g., Ref. 30).

Since we have to deal with the multiplicity of structural states, it is appropriate to specify the meaning of τ_{12}. We can denote the sets of isoconfigurational states of two compositionally identical glass phases as

$$\{S_1\}=(s_1^{(1)},s_1^{(2)},\ldots s_1^{(W_1)}),$$

$$\{S_2\}=(s_2^{(1)},s_2^{(2)},\ldots s_2^{(W_2)}). \tag{12}$$

The numbers of structural states of the phases, W_1 and W_2, are determined by Eq. (2).

Each of the structural states $s_i^{(l)}$ $(i=1,2)$ has a free energy

$$G_{1,2}(P,T)=N\mu_{1,2}(P,T), \tag{13}$$

$$\mu_1(P,T)=\sum_i c_{1,i}\left[g_{1,i}(P,T)+\sum_k w_{1,ik}g_{1,ik}(P,T)\right],$$

$$\mu_2(P,T)=\sum_i c_{2,i}\left[g_{2,i}(P,T)+\sum_k w_{2,ik}g_{2,ik}(P,T)\right], \tag{14}$$

which is dependent only on the upper index indicating the number of the structure state.

Assume that the glass transition leads to the formation of the state $s_1^{(l)}$ with the chemical potential $\mu_1(P,T)$. After crossing the phase coexistence curve given by the equation

$$\mu_1(P,T)=\mu_2(P,T), \tag{15}$$

the states of phase 2 have lower free energy than those of phase 1. As a result, a polyamorphous phase transformation is advantageous thermodynamically and conceptually the state $s_1^{(l)}$ can transform into any of the states $\{S_2\}$. It is clear that in the approximation of Eq. (8), the thermodynamic driving force of the transformation $\Delta\mu=\mu_1(P,T)-\mu_2(P,T)$ is independent of which of the states of $\{S_2\}$ is realized by the transition. However, the time of transformation is essentially dependent on the microscopic structure of the final state because the transition causes rearrangement of the SRO. We take τ_{lm} as the characteristic time of the $s_1^{(l)}\rightarrow s_2^{(m)}$ transformation. Among a large body of τ_{lm} values, there is the smallest one

$$\tau_l^*=\min_m\tau_{lm}. \tag{16}$$

The condition in Eq. (16) determines which of the states $\{S_2\}$ will result from the transformation of $s_1^{(l)}$. The resulting state is numbered $m(l)$. τ_l^* averaged over all states $\{S_1\}$ determines the characteristic time of the phase transformation in Eq. (11)

$$\tau_{lm}\tau_{12}=\langle\tau_l^*\rangle. \tag{17}$$

It is obvious that the time is the shorter the fewer structural rearrangements that are required for the polyamorphous transformation and the lower the barriers of these rearrangements. The proportions of structural changes during the $s_l(l)\rightarrow s_2^{(m)}$ transformation are characterized by $c_{i,g}$ variations,

$$\Delta c_i=c_{1,i}^{(l)}-c_{2,i}^{(m)}, \tag{18}$$

and by the overlapping parameter

$$q_{lm}=\sum_i c_{1,i}^{(l)}\langle c_{1,i}^{(l)}(x)c_{2,i}^{(m)}(x+r_p)\rangle. \tag{19}$$

The quantity $\Delta c=(\Delta c_1,\Delta c_2,\ldots,\Delta c_{n_s})$ is the vector of n_s components in the space of Δc_i components.

Choosing the space metric in the form

$$|\Delta c|=\frac{1}{2}\sum_i|\Delta c_i| \tag{20}$$

we can estimate the extent of the difference between the two structures. The metric in Eq. (20) is suitable because it includes the relation $0\leqslant|\Delta c|\leqslant 1$ similar to the relation $0\leqslant c_i\leqslant 1$, that applies for the fraction c_i of orientational associate type i.

The overlapping parameter q_{lm} describes changes of the pair correlators. During the isoconfigurational transformation, when $|\Delta c|=0$, the overlapping parameter q_{lm} is equal to unity. Contrarily, it is a small quantity if the structure of the state $s_2^{(m)}$ is essentially different from that of $s_1^{(l)}$.

The τ_l^* value is expected to be independent l in the thermodynamic limit. This means that each of the states $s_1^{(l)}$ has a $|\Delta c|$-spaced neighboring state $s_2^{(m)}$ with the overlapping parameter q_{lm} and at that the magnitudes $|\Delta c|$ and q_{lm} are independent of the index l.

2.2. Low-temperature polyamorphous transformations in orientational glasses based on doped fullerite C_{60}

Using the results of the previous Section, we can now analyze the polyamorphous transformations revealed experimentally in the orientational glasses based on doped fullerite C_{60}. At low temperatures the free energy of the molecule with the ith orientational SRO (or associate type) can be written as (disregarding the associate interaction)

$$g_i(P,T)=u_{0i}+\sum_{l=1}^{n_\Omega}\frac{1}{2}[\hbar\Omega_i^{(l)}-T\exp(-\hbar\Omega_i^{(l)}\beta)]$$

$$+g_{\rm ph}(P,T)+Pv. \tag{21}$$

Here u_{0i} is the energy of the molecule disregarding the zero-point vibrations, whose contributions are described by the first terms under the summation sign in Eq. (21); $\Omega_i^{(l)}$ are the frequencies of libration and intramolecular vibrations; n_Ω is the number of their frequencies; $g_{\rm ph}(P,T)$ is the phonon contribution, presumably independent of the type of orientational SRO and minor changes in the lattice parameter during phase transformation; v is the specific volume. Of all the terms with $\sim\exp(-\hbar\Omega_i^{(l)}\beta)$, only those with frequencies close to the lowest $\Omega_i^{(l)}$ can contribute appreciably. The number of significant terms $\sim\exp(-\hbar\Omega_i^{(l)}\beta)$ can be denoted as n_Ω. Since the frequencies of intramolecular vibrations are much higher than the libration frequencies and the number of the latter frequencies is 3, we obtain $n_\Omega=3$.

Assume that $\overline{\Omega}_i$ is the mean value of the frequencies for the ith orientational SRO, and $(\delta\Omega)_i^2$ is the variance of these frequencies. We consider the low-temperature region where $T\ll\hbar\overline{\Omega}_i$. At the same time we assume that $(\hbar\delta\Omega_i/4T)^2\ll 1$. Taking into account only the second-order corrections in the parameter $(\hbar\delta\Omega_i/T)$, we can write Eq. (20) as

$$g_i(P,T)=u_{0i}(P,T)-Tn_\Omega \exp(-\hbar\overline{\Omega}_i\beta) \times[1+(\hbar\delta\Omega_i/4T)^2]+g_{\rm ph}(P,T)+Pv. \quad (22)$$

Substituting the expression for $g_i(P,T)$ into Eq. (8) and neglecting the contribution of the associate interaction, we can obtain with the most minimal loss in accuracy

$$G(P,T)=N\{\overline{\varepsilon}(P,T)-Tn_\Omega \exp(-\hbar\overline{\Omega}\beta) \times[1+(\hbar\delta\Omega/T)^2]+g_{\rm ph}+Pv\}, \quad (23)$$

where

$$\overline{\varepsilon}(P,T)=\sum_i c_i u_{0i}(P,T), \quad (24)$$

$$\exp(-\hbar\overline{\Omega}\beta)=\sum_i c_i \exp(-\hbar\overline{\Omega}_i\beta)_i,$$

$$\delta\Omega^2=\sum_i c_i(\overline{\Omega}_i-\overline{\Omega})^2. \quad (25)$$

Equations (22)–(25) show that the approximation chosen is an effective medium approximation. Inclusion of the associate interactions will naturally lead to renormalization of $\overline{\varepsilon}$ and $\overline{\Omega}$.

The above expression suggests that the phase transition is possible if there are two minima of free energy, Eq. (23), as a function of $\{c_i\}$. We use $\mu_1(P,T)$ and $\mu_2(P,T)$ to denote the chemical potentials of the phases (as previously used in Eq. (14)), and given by the braced terms in Eq. (23), at minima 1 and 2, respectively. The transition temperature T_e is then determined by the Gibbs equation

$$\mu_1(P,T)=\mu_2(P,T), \quad (26)$$

which after cancelling of the phonon contributions, disregarding the term $P(v_1-v_2)$ and the corrections quadratic in $\hbar\delta\Omega\beta$, gives

$$\overline{\varepsilon}_1(P,T)-T_e n_\Omega \exp(-\hbar\overline{\Omega}_1\beta)=\overline{\varepsilon}_2(P,T)-T_e n_\Omega \times\exp(-\hbar\overline{\Omega}_2\beta). \quad (27)$$

To get solution (27) one should note that the temperature dependence of the energies $\overline{\varepsilon}_1$, $\overline{\varepsilon}_2$ and frequencies $\overline{\Omega}_1$, $\overline{\Omega}_2$ can be neglected at low temperatures, where $\overline{\varepsilon}_{1,2}(P,T)\approx\overline{\varepsilon}_{1,2}(P,0)\equiv\overline{\varepsilon}_{1,2}$ and $\overline{\Omega}_{1,2}(P,T)\approx\overline{\Omega}_{1,2}(P,0)\equiv\overline{\Omega}_{1,2}$. As result we have

$$T_e n_\Omega[\exp(-\hbar\overline{\Omega}_2\beta)-\exp(-\hbar\overline{\Omega}_1\beta)]\approx n_\Omega\hbar \times(\overline{\Omega}_2-\overline{\Omega}_1)\exp[-\hbar(\overline{\Omega}_1+\overline{\Omega}_2)\beta/2]=\overline{\varepsilon}_2-\overline{\varepsilon}_1$$

or

$$T_e=-\frac{\hbar(\overline{\Omega}_1+\overline{\Omega}_2)}{2}\left(\ln\frac{\overline{\varepsilon}_2-\overline{\varepsilon}_1}{n_\Omega\hbar(\overline{\Omega}_2-\overline{\Omega}_1)}\right)^{-1} =-\frac{\hbar(\overline{\Omega}_1+\overline{\Omega}_2)}{2}\left(\ln\frac{\overline{\varepsilon}_2-\overline{\varepsilon}_1}{3\hbar(\overline{\Omega}_2-\overline{\Omega}_1)}\right)^{-1}. \quad (28)$$

2.3. Thermal expansion coefficient

In the previous Section our attention was focused on the thermodynamics of a low-temperature transition. The contribution from the cluster boundaries was neglected. Indeed, this contribution is negligible at high (near T_g) temperature. However, at low temperatures when the phonon contribution is small (see the Introduction), the tunneling states situated at the cluster boundaries start to play a significant role.

An important feature of the low-temperature excitations of the tunneling states is a weak temperature dependence of the relaxation time. Owing to this feature, the system of tunneling states (TS) can be considered thermodynamically as an equilibrium subsystem of the glass. On polyamorphous transformation, the cluster boundary structure, the number of tunneling states and the density of their low-energy states all change. These changes come as evidence of the polyamorphous transition at low temperatures when it is possible to separate the TS contribution to the temperature coefficients. In this Section we analyze the component $\alpha_{TS}(T)$ of the thermal expansion coefficient $\alpha(T)$. Existence of polyamorphism in orientational glasses based on doped C_{60} was detected from the hysteresis of $\alpha(T)$.

Let us consider an isolated TS. The free energy of the TS with the level splitting E can be written as

$$g_{TS}(T,v)=\varepsilon_0(v)-T\ln 2\cosh(E(v)\beta/2)+\varepsilon_{\rm el}(v). \quad (29)$$

Here $\varepsilon_0(v)$ is the sum of energies of the well bottom and zero oscillations; v is the TS volume; $\varepsilon_{\rm el}(v)$ is the elastic deformation energy,

$$E^2(v)=\Delta^2+\Delta_0^2(v),$$

$$\Delta_0=\hbar\Omega e^{-\lambda}, \quad \lambda\sim(2IV_0/\hbar)^{1/2}\varphi, \quad (30)$$

where Ω is the libration frequency, I is the moment of inertia, V_0 is the height of the hump separating two potential well minima, φ is the angle of rotation to get from one minimum to the other, and Δ is the difference between the minima depths.

The two-well potential at $\Delta=0$ can be represented as a sine curve within the interval $-\varphi<0<\varphi$

$$U(\theta)=U_0(v)[\cos(2\pi\theta/\varphi)-1]+\text{const} \quad (31)$$

and supplemented with infinitely high walls at $\theta=\pm\Delta D$. In this case

$$\varepsilon_0(v)=-2U_0(v)+\hbar\Omega_0/2+\text{const} \quad (32)$$

and the hump height is $V_0=2U_0(v)-\hbar\Omega_0/2$. Here Ω_0 is the zero oscillation frequency.

The origin of the elastic energy $\varepsilon_{\rm el}(v)$ is as follows. If the tunneling barrier is very high and $\Delta_0\to 0$, the TS gains a volume v_0 which can be found from the condition of equilibrium between the TS and the surrounding molecules. At finite Δ_0 the correction Δv_{TS} appears. As a result,

$$v=v_0+\Delta v_{TS}. \quad (33)$$

(The necessity of including this correction in the TS contribution to the thermal expansion coefficient was first considered in Ref. 31. Using special assumptions, Δv_{TS} for methane was calculated in Ref. 32.)

When the addition Δv_{TS} appears, the tunneling state becomes a dilatation center whose elastic energy is[33]

$$\varepsilon_{\rm el}(v)=\frac{1}{2}f_{\rm el}v_0\left(\frac{\Delta v_{TS}}{v_0}\right)^2, \tag{34}$$

where

$$f_{\rm el}=\frac{4}{9}\mu\frac{1+\nu}{1-\nu}. \tag{35}$$

Here μ is the shear modulus and ν is the Poisson coefficient.

Now Δv_{TS} can be found by minimizing the free energy of Eq. (29) in v. From the requirement of the minimum

$$\frac{\partial g_{TS}(v)}{\partial v}=0 \tag{36}$$

we have

$$2\left(1-\frac{1}{4}\frac{\lambda\Delta_0^2}{EV_0}\tanh\frac{E\beta}{2}\right)\frac{\partial U_0}{\partial v}=f_{\rm el}\frac{\Delta v_{TS}}{v_0}. \tag{37}$$

Hence,

$$\frac{\Delta v_{TS}}{v_0}=2\,f_{\rm el}^{-1}\left(1-\frac{1}{4}\frac{\lambda\Delta_0^2}{EV_0}\tanh\frac{E\beta}{2}\right)\frac{\partial U_0}{\partial v}. \tag{38}$$

We may state that the derivative $\partial U_0(v)/\partial v$ is negative, since the well depths in Eq. (30) and the height of the hump between the wells should decrease when the volume increases. Note that Eqs. (37) and (38) were derived neglecting the dependence of Δ on the volume, because we assumed that the $E(v)$ variation was mainly caused by the changes in the depths of the wells and the separating barrier [see Eqs. (31), (32)].

Taking into account that the second term in brackets in Eq. (38) is always less than unity (since $\Delta_0\leqslant E<U_0$ and $\tanh(E\beta/2)\leqslant 1$), we can find that $\Delta v_{TS}<0$, i.e., the tunneling states compress the sample. Since $\tanh(E\beta/2)$ decreases with rising temperature, then

$$\begin{aligned}\alpha_{TS}(E,\Delta_0,T)&=\frac{1}{v_0}\frac{\partial\Delta v_{TS}}{\partial T}\\&=\frac{1}{4T^2}\frac{\lambda\Delta_0^2}{f_{\rm el}V_0}\frac{1}{\coth^2(E\beta/2)}\frac{\partial U_0}{\partial v}\\&<0.\end{aligned} \tag{39}$$

To estimate the total contribution of the tunneling states to the thermal expansion coefficient, Eq. (39) should be integrated with respect to all the TS. Using $f_{TS}(E,\Delta_0)$ for the distribution function of TS as a function of both E and Δ_0, and denoting the TS concentration (the number of TS per molecule) as c_{TS}, we obtain

$$\alpha_{TS}(T)=c_{TS}\int_0^\infty\int_0^\infty f_{TS}(E,\Delta_0)\alpha_{TS}(E,\Delta_0,T)dE\Delta_0. \tag{40}$$

The distribution function $f_{TS}(E,\Delta_0)$ is assumed to be normalized to unity.

The low-temperature ($T\leqslant 1$ K) contribution of TS to the thermodynamic coefficients is usually described using a function homogeneous over the finite interval of Δ and λ values. In terms of the variables E and and Δ_0 it is

$$f_{TS}(E,\Delta_0)\sim\frac{\overline{P}E}{\Delta_0\sqrt{E^2-\Delta_0^2}}. \tag{41}$$

Here $\overline{P}$ is a constant. We are interested in how the TS system influences the thermal expansion coefficient in the temperature interval of about 20 K, i.e., far from the region where the low-temperature anomalies are observable. In this case the distribution function of Eq. (41) can be invalid for a reasonable interpretation of experimental results. The phonon contribution into the thermal expansion coefficient can be found using the phenomenological expression

$$\alpha_{\rm ph}(T)=\Gamma C_{\rm ph}(T), \tag{42}$$

where Γ is the Grüneisen coefficient and $C_{\rm ph}(T)$ is the phonon contribution to the heat capacity. It is known that at low temperatures $C_{\rm ph}(T)\sim T^3$. As a result, $\alpha_{\rm ph}(T)$ becomes comparatively low. The total thermal expansion coefficient is

$$\alpha(T)=\alpha_{\rm ph}(T)+\alpha_{TS}(T), \tag{43}$$

where $\alpha_{TS}(T)$ is determined by Eqs. (39) and (40), and can become negative in the low temperature region, where $\alpha_{\rm ph}(T)<\alpha_{TS}(T)$.

2.4. Relaxation process

The dilatometric technique applied to orientational C_{60}-based glasses permits investigation of the relaxation processes whose characteristic times are no longer than $\tau_{\rm obs}\sim 10^3$ s. Three important relaxation processes can be distinguished in the orientational glasses studied. One of them is the polyamorphous transformation time τ_{12} included in the kinetic criterion of Eq. (10). The other two are the times during which the distribution functions of elementary excitations in the phonon-libron system and in the TS system come to equilibrium. We start with the polyamorphous transformation.

The phase transformation during the first-order phase transitions can be described within the framework of the Avrami—Kolmogorov model.[34] According to this model, after crossing the phase coexistence curve, the fraction of the new phase changes by the law

$$V_2(t)=V_0[1-\exp(-At^n)]. \tag{44}$$

Here V_0 is the total volume, A is a constant dependent on the rates of the new phase nucleation and growth, n is the Kolmogorov exponent, which depends on the system dimensions. For example, with uniform nucleation at the rate I and the growth constant u_g in the 3-dimensional space $A=Iu_g^3$ and $n=4$.

If nucleation is nonuniform occurring mostly in special regions (e.g., at the grain boundaries) and the nucleation rate is high, the time of the phase transformation is determined by the growth rate of the new-phase precipitates. In this case we can put in Eq. (44)

$$A\approx Bu_g,\quad n=1, \tag{45}$$

where B is the density of the sites where the new phase nucleates. If nucleation occurs at the grain boundaries, $B\approx 2/l$, where l is the average linear grain size.

To identify the scenario of phase transformation, we estimate the bulk thermodynamic driving ''force'' controlling the rate of the transformation. Under a constant low pressure in the first order of $T-T_e$, we have

$$\Delta\mu_{12}(T)=\mu_1(T)-\mu_2(T)=-\Delta\varepsilon_{12}(T_e)(T-T_e)/T_e,$$
$$\Delta\varepsilon_{12}=\varepsilon_1-\varepsilon_2. \quad (46)$$

Since in the general case the phase transformation entails changes in the volume and in SRO, we can separate these contributions to $\Delta\varepsilon_{12}$:

$$\Delta\varepsilon_{12}=\Delta\varepsilon_{\rm el}+\Delta\varepsilon_{\rm or}+\Delta\varepsilon_{\rm intra}, \quad (47)$$

where

$$\Delta\varepsilon_{\rm el}=\frac{K}{2}\left(\frac{\Delta v}{v}\right)^2 v, \quad (48)$$

K is the bulk elastic modulus, v is the specific volume; $\Delta\varepsilon_{\rm el}$ shows what amount of energy is stored in the sample due to the volume variation in the transformation process; $\Delta\varepsilon_{\rm or}$ takes into account the energy changes due to the orientational order difference, and $\Delta\varepsilon_{\rm intra}$ allows for the changes in the intramolecular structural state.

Since the free energy and entropy decrease during phase transformation, the energy per molecule in the low-temperature phase (phase 1) is lower than that in the high-temperature phase. Thus, $\Delta\varepsilon_{12}<0$. Since $\Delta\varepsilon_{\rm el}$ is always positive, the sum $\Delta\varepsilon_{\rm or}+\Delta\varepsilon_{\rm intra}$ should be negative, and its absolute value exceeds $\Delta\varepsilon_{\rm el}$.

It is beyond reason to expect that the intramolecular ground state can change as $T\to 0$. Otherwise, the phase transition could occur in pure C_{60}, since the mutual positions and orientations of molecules (essential for molecular interactions) are less important. Therefore, in Eq. (47) we can put $\Delta\varepsilon_{\rm int}=0$. It is quite simple to estimate $\Delta\varepsilon_{\rm el}$. Since in fullerites $K\approx 10.3$ GPa, $v\sim 10^3$ Å^3 and, as is seen from our data, $\Delta v/v\sim 10^{-3}$, we have $\Delta\varepsilon_{\rm el}\sim 10^{-1}$ K.

$\Delta\varepsilon_{\rm or}$ is related to the changes in SRO. According to Eq. (24),

$$\Delta\varepsilon_{\rm or}=\sum \Delta c_i\varepsilon_i. \quad (49)$$

Taking into account that $\Delta c_i<1$ (e.g., $\Delta c_i\sim 10^{-1}$) and the energy difference between two neighboring molecules can amount to $\sim 10^2$ K due to the change of the mutual orientation,[1,2] we can put $\Delta\varepsilon_{\rm or}\sim 10$ K.

The above estimates suggest that no isoconfigurational transition (for such transition $\Delta\varepsilon_{\rm or}=0$) occurs in the investigated orientational glasses. In our case the phase transformation is a cooperative change of the SRO and the lattice parameter. Since the phase transformation is accompanied by a change in the volume, it is most likely that the transformation process starts at the sample surface or at the grain boundaries. In this case elastic relaxation is possible where the new phase nucleates. The ensuing quasi-one-dimensional growth of the nuclei changes the lattice parameter at the phase interface. In this scenario of the phase transformation, the SRO is disturbed at the phase interface and this suppresses the potential barriers for orientational rearrangements. It is therefore quite easy to overcome the barriers under the action of local inner elastic stresses and weak thermal fluctuations. The diffusion-free mechanism of relaxation of the elastic stresses at the transformation front caused by an inconsistency between the lattice parameters deserves special attention and will be considered elsewhere. Here we can conclude that the phase transition in the orientational glasses studied can be described by Eqs. (44), (45), the structural transformation is a nondiffusive process, and the transformation rate is determined mainly by $\Delta\varepsilon_{\rm or}$. As is seen in Eq. (45), the characteristic time of phase transformation is

$$\tau_{12}\sim l/u_g. \quad (50)$$

If the above estimate $\Delta\varepsilon_{\rm or}\sim 10$ K is correct, then a considerable amount of heat is released at the front of the phase 2→phase 1 transformation at $|T-T_e|\sim T_e$. This causes local heating and accelerates the transformation process. On a reverse transformation, above T_e, the heat is absorbed at the transformation front, which hampers a thermoactivated overcoming of even low potential barriers. We should expect slowing down of the reverse transformation in this case.

The relaxation time $\tau_{\rm ph}$ of the phonon—libron system is determined by the free path of the phonons that are scattered at these excitations and are responsible for their thermalization and the equilibration of the distribution function. This is obviously the shortest of all the relaxation times under consideration, $\tau_{\rm ph}\ll\tau_{12},\tau_{TS}$. This relaxation process therefore produces very little effect on the polyamorphous transformations of interest to us.

The relaxation time of the TS system is mainly determined by the tunneling time,[10]

$$\tau_{TS}^{-1}=A\Delta_0^2 E\coth(E\beta). \quad (51)$$

Here A is a certain constant. At low temperatures, when $E\beta\leqslant 1$, the last factor on the right-hand side of the equation has a value of the order of unity. As a result, τ_{TS} is only slightly dependent on temperature in this case.

3. COMPARISON WITH EXPERIMENT

It is noteworthy that the phase transition is revealed in fullerites doped by gases while in pure fullerite this phenomenon is not observed. The dopants change molecular interactions and the potential energy landscape. As result structural, thermodynamic and kinetic properties are changed. For this reason the thermodynamic quantities and kinetic coefficients are dependent on the dopant concentrations. The proposed theoretical model is valid despite the fact that these dependences are not known. It was hardly possible in this study to find experimental coexistence temperatures T_e of the glass phases (phase transformation temperature) in the investigated materials. This is because phase transformations are inevitably smeared. T_e is expected to be somewhere within the region of the thermal expansion hysteresis.

In our experiments the upper boundary of the hysteresis for Xe–C_{60} was not reached. It seems plausible that the hysteresis and T_e depend on the type of the doping gas. The x-ray diffraction measurement[35] of the lattice parameter a of Xe–C_{60} in a wide temperature interval (7–300 K) also revealed a hysteresis of $\alpha(T)$ in the region 7–65 K. The largest width of the hysteresis loop was observed at $T\approx 20$ K. Like in our experiments, in Ref. 35 $\alpha(T)$ was lower on cool-

ing from high temperature and higher on heating from 7 K. This counts in favor of polyamorphism, which we detected in Xe–C_{60}. Besides, it shows that the phase coexistence temperature T_e is above 7 K, presumably being $T_e \approx 20$ K.

When using Eq. (28) to estimate T_e, we should remember that according to Refs. 36 and 37, the characteristic frequency of libron vibrations is about $\hbar\Omega_1 \approx \hbar\Omega_2 \approx 40$ K. Taking $\varepsilon_1 - \varepsilon_2 \approx 10$ K and $|\Omega_1 - \Omega_2|/\Omega_1 \sim 10^{-4}$ (which seems quite reasonable), we get $T_e \sim 10$ K (according to Eq. (28)). This is a rough estimate, but since the difference quotient $(\varepsilon_1 - \varepsilon_2)/(\Omega_1 - \Omega_2)$ appears in Eq. (28) in logarithmic form, T_e has only a weak dependence on the choice of these quantities.

We were able to separate the positive (A) and negative (B) contributions to the thermal expansion coefficients owing to their considerably different relaxation times under jump-like changes of temperature.

The positive contribution $A(T)$ to $\alpha(T)$, made by the low-frequency lattice excitations (phonons and librons), and its relaxation time $\tau(T)$ are little dependent on the type of the doping gas. $A(T)$ and $\tau(T)$ are practically insensitive to polyamorphous transformations.

The negative contribution to the thermal expansion, $B(T)$, is in our opinion connected with the TS system, which undergoes significant restructuring during the polyamorphous transformation. $B(T)$ and its relaxation time are strongly dependent on the type of doping gas. The negative contribution to $\alpha(T)$ of C_{60} doped with gases is described below.

Taking

$$B(T) = \alpha_{TS}(T) \tag{52}$$

and assuming that α_{TS} is described by Eqs. (38), (39), we can understand from the analysis of experimental results how the TS system changes during the polyamorphous transformation. First note that the temperature dependence of the contribution to $\alpha(T)$ from the TS system on splitting of the energy levels E, $\alpha_{TS}(E, \Delta_0, T)$, has a maximum at $T \approx E/2$. This function decreases quite rapidly with decreasing temperature and falls off slowly, $\sim T^{-2}$, at high temperatures. A linear superposition of these functions, Eq. (40), tends rapidly to zero at $T < E_{\min}/2$ and decreases as $\sim T^{-2}$ at high temperatures $T > E_{\max}/2$. $E_{\min}$ and $E_{\max}$ are the lowest and highest values of E.

Equation (40) holds for an equilibrium stationary TS system and can be used when its relaxation time τ_{TS} is much shorter than the time of observation. In Eq. (50) τ_{TS} is inversely proportional to Δ_0 squared. As a result, two-level systems with $\tau_{TS}\overline{\Omega\Delta} < 1$ do not contribute to thermodynamic quantities, in particular, to $\alpha(T)$. Thus, the coefficient c_{TS} in Eq. (40) has to include only the concentration of ''active'' TS coming to equilibrium during the time of observation. Therefore, the negative contribution $B(T)$ appearing during the polyamorphous transformation at $T < T_e$ should be attributed to a change in the concentration of active TS undergoing level splittings E comparable with the temperature.

The structural transformations during the reverse orientational transition at $T > T_e$ are very slow near T_e. Therefore, the parameter c_{TS} is assumed to be temperature-independent

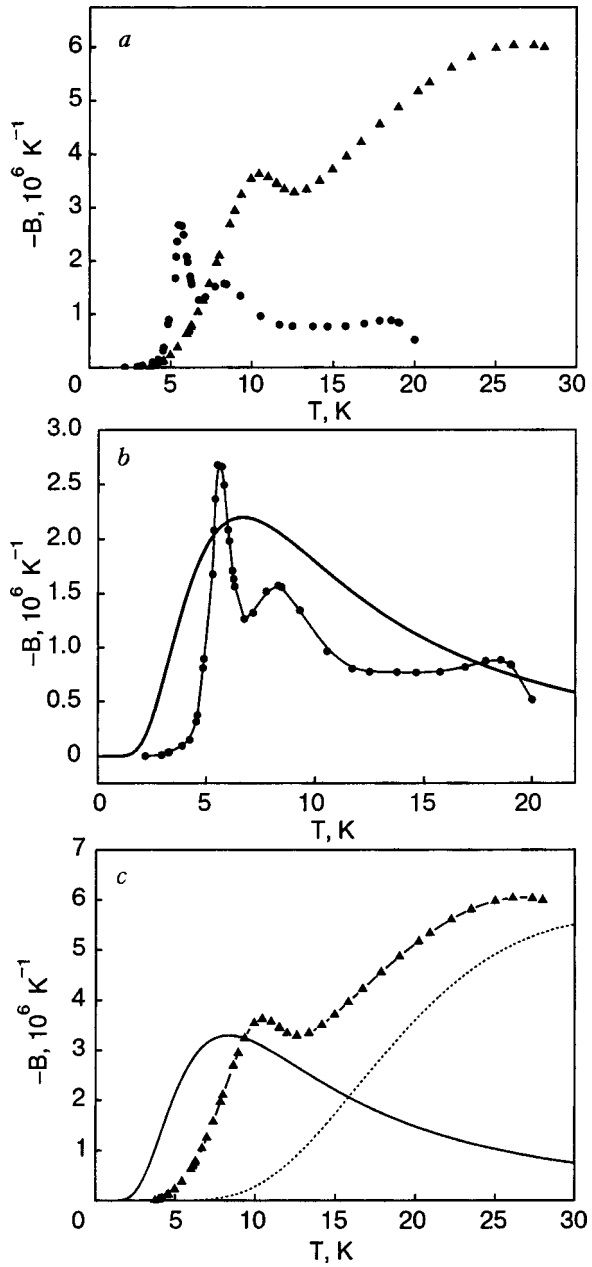

FIG. 13. Temperature dependence of $B(T)$: a—experimental data for D_2–C_{60} (●) and Xe–C_{60} (▲); b—fitting by Eq. (53) (solid line) for experimental data D_2–C_{60} (●); c—fitting by Eq. (54) (dashed line) for experimental data Xe–C_{60} (▲) and fitting by Eq. (53) (solid line) for experimental data D_2–C_{60}.

at $T \approx T_e$, but away from T_e it depends both on time and on thermal prehistory, which is important for the analysis of experimental data.

We lack information to take into account the polyamorphous transformation in the relaxation kinetics of the TS system, but Eqs. (38) and (39) seem to be good for an adequate analysis of the experimental results in a wide temperature interval near T_e.

The $B(T)$ curves measured on Xe–C_{60} and D_2–C_{60} are shown in Fig. 13a. These values correspond to the low-temperature phase having an increased specific volume. In both the samples, the $B(T)$ behavior has characteristic features: (i) the presence of maxima and (ii) a sharp decrease in the low-temperature region below the lower maximum. Be-

sides, the $B(T)$ peak at $T=6$ K in D_2-C_{60}, it is narrower than that following from Eq. (38), as is shown in Fig. 13b.

The temperature dependence of the negative contribution can be analyzed in terms of Eqs. (38), (39) and (52). We can put $f(E,\Delta)=f_1\delta(E-E_1)$ because with an equilibrium stationary density of TS, a distinct $\alpha_{TS}(T)$ peak is possible only for a narrow distribution of $f(E,\Delta_0)$ concentrated near a certain value E_1. In this case

$$\alpha_{TS}(T)=c_{TS}(E_1)\alpha(E_1,\Delta_0,T). \tag{53}$$

The $B(T)$ values fitted by Eq. (53) for the D_2-C_{60} sample are shown in Fig. 13b. It is seen that Eq. (53), in which c_{TS} comes as independent of temperature and time, offer a rather rough description of experimental data. If T_e is close to the peak, $T_1\approx E_1/2$ and the fast decrease in $B(T)$ at $T>T_1$ can be attributed to the reverse polyamorphous transformation. This explanation seems quite reasonable, considering that the time of the reverse transformation at $T=10.5$ K is about 5×10^3 (Fig. 12), i.e., comparable to the time of measuring $B(T)$. But the experimental results available are not sufficient for a more detailed analysis.

The more dramatic [than the assignment of Eq. (53)] decrease in $B(T)$ at $T<T_1$ suggests that the distribution of TS levels is temperature-dependent at $T<T_e$ as well. In the case of an equilibrium TS system in this T interval (like the low-temperature phase of an orientational glass) this behavior can be explained through a deeper insight into the thermodynamics of the TS system. If the TS density is nonequilibrium and varies with time during measurement, it is necessary to analyze the relaxation kinetics of the system, which is beyond the scope of this study.

The data on the kinetics of the reverse polyamorphous transformation (Fig. 12) show that at least the long-time asymptotic of Eq. (43) can be described by the simple exponential $\sim[1-\exp(t/\tau))]$, i.e., the Kolmogorov exponent is equal to unity at least at the late stage of the phase transformation [see Eq. (44)]. This means that at this stage the polyamorphous transformation proceeds as a one-dimensional growth of the stable phase at a two-dimensional interphase boundary with the metastable (nonequilibrium) phase.

The dependence $B(T)$ for C_{60} doped with Xe should be analyzed taking into account the two peaks with a slight dip in between that are observed in this case. Following the reasoning used for the D_2-C_{60} system, we arrive at the conclusion that in $Xe-C_{60}$ the TS density is concentrated near $E_1\approx10$ K and $E_2\approx40$ K. Figure 13c shows the experimental results fitted by the expression

$$\alpha_{TS}(T)=c_{TS}(E_1)\alpha_{TS}(E_1,\Delta_0,T)+c_{TS}(E_2)\alpha_{TS}(E_2,\Delta_0,T), \tag{54}$$

where $c_{TS}(E_1)$ and $c_{TS}(E_2)$ are the fitting constants, and $\varepsilon_{TS}(E,T)$ is described by Eq. (38). The data obtained are in good qualitative and quantitative agreement. The better fitting in this case (compared to that for D_2-C_{60}) suggests that in $Xe-C_{60}$ the TS density is weakly dependent on temperature in a wide interval. This conclusion is supported by the measurement in Ref. 35, where it was shown that on heating $Xe-C_{60}$ the reverse polyamorphous transformation was complete only at $T\approx60$ K. The process is rather slow and cannot manifest itself in the temperature interval of our measurements, at $T<28$ K.

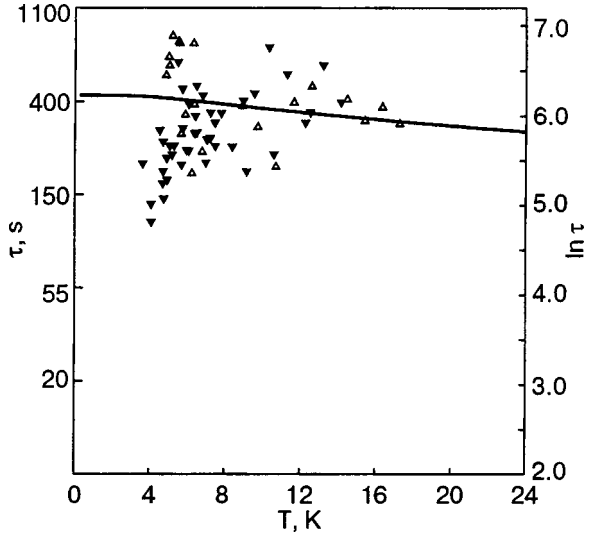

FIG. 14. Characteristic time $\tau(T)$ of the negative contribution of the thermal expansion of H_2-C_{60} (▼) and D_2-C_{60} (△). The solid line is a description by Eq. (51).

However, at low temperatures the coefficient $B(T)$ decreases faster than is implied by Eq. (54) containing the best fitting parameters. Like in the case of D_2-C_{60}, this behavior is not yet clear.

The relaxation times $\tau(T)$ fitted by Eq. (51) for the H_2-C_{60} and D_2-C_{60} systems are shown in Fig. 14. The scatter in the experimental data is too large to expect satisfactory agreement. But it should be noted that the TS system cannot be considered as independent of temperature and time as Eq. (51) requires.

CONCLUSIONS

A dilatometric investigation in the temperature range 2–28 K has shown that a first-order polyamorphous transition occurs in orientational glasses based on C_{60} doped with H_2, D_2, and Xe. A polyamorphous transition was also detected in our earlier[15] study on C_{60} doped with Kr and He. The hysteresis of thermal expansion caused by the polyamorphous transition (and, hence, the transition temperature) is essentially dependent on the type of the doping gas.

Both positive and negative contributions to thermal expansion were observed in the low-temperature phase of the glasses. Within the investigated temperature interval the relaxation time of the negative contribution is considerably longer than that of the positive contribution. This fact has permitted us to separate and analyze both the contributions to the thermal expansion. The positive contribution is found to be due to the low-frequency excitations of the lattice (phonon and librons) and its value is weakly dependent on the type of the doping gas. Arguments are advanced that the negative contribution is due to the tunnel reorientations of some of the C_{60} molecules.

The relaxation time of the negative contribution is strongly dependent on the type of the doping gas. This means that the molecules (atoms) of the doping gas affect apprecia-

bly the penetrability of the potential barriers separating different orientations of the tunneling C_{60} molecules.

In the high-temperature glassy phase, only the positive contribution to thermal expansion is observed. Its value and relaxation time coincide, within the experimental accuracy, with the corresponding values for the positive contribution in the low-temperature phase. This means that the polyamorphous transition discussed here is accompanied first of all by rearrangement of the tunnel state system.

A theoretical model is proposed to interpret these phenomena. The order of magnitude of the polyamorphous transition temperature has been estimated. The estimate agrees with the experimental results. The characteristic time of the phase transformation from the low-T phase to the high-T phase has been found for the C_{60}-H_2 system at 12 K. Its value is an order of magnitude higher than the characteristic time of the tunnel reorientation of C_{60} molecules.

The late stage of the polyamorphous transformation is described well by the Kolmogorov law with the exponent $n=1$. This means that at this stage of tranformation the two-dimensional phase boundary moves along the normal, and the nucleation of the new phase is of no importance.

Evidence is obtained in favor of the assumption that the H_2 and D_2 molecules dissolved in C_{60} occupy both the octahedral and the smaller tetrahedral interstitial cavities in the C_{60} lattice.

This study was supported by the Science and Technology Center of Ukraine (STCU, project Uzb-116(j)) and National Academy of Sciences of Ukraine (comprehensive program of fundamental research ''Nanosystems, nanomaterials and nanotechnologies'').

We would like to thank Profs. V. D. Natsik, M. A. Strzhemechnyi, and A. I. Prokhvatilov for valuable and critical discussion.

Note added in proof: After this paper had been sent for publication, we became aware of the results[38] on the low-temperature microhardness of Xe-intercalated fullerite C_{60} which pointed to a considerable increase in the microhardness of C_{60} on its intercalation with Xe. This result agrees with the increase of brittleness of C_{60} when Xe is solved in it.

*E-mail: dolbin@ilt.kharkov.ua
†Deceased.

[1] V. D. Natsik and A. V. Podolskiy, Fiz. Nizk. Temp. **24**, 689 (1998) [Low Temp. Phys. **24**, 523 (1998)].
[2] N. P. Kobelev, Fiz. Tverd. Tela **44**, 188 (2002) [Phys. Solid State **44**, 195 (2002)].
[3] V. M. Loktev, J. N. Khalack, and Yu. G. Pogorelov, Fiz. Nizk. Temp. **27**, 539 (2001) [Low Temp. Phys. **27**, 397 (2001)].
[4] J. M. Khalack and V. M. Loktev, Fiz. Nizk. Temp. **29**, 577 (2003) [Low Temp. Phys. **29**, 429 (2003)].
[5] H. Wang, C. Zeng, B. Wang, J. G. Hou, Q. Li, and J. Yang, Phys. Rev. B **63**, 085417–1 (2001).
[6] J. G. Hou, Y. Jinlong, W. Haiqian, L. Qunxiang, Z. Changgan, Y. Lanfeng, W. Bing, D. M. Chen, and Z. Qingshi, Nature (London) **409**, 304 (2001).
[7] A. S. Bakai, *Polycluster Amorphous Solids* [in Russian], Energoatomizdat, Moscow (1987).
[8] A. S. Bakai, in *Glassy Metals III*, Vol. 72 of Topics in Applied Physics, H. Beck and H.-J. Guentherodt (eds.), Springer, Heidelberg (1994), p. 209.
[9] A. S. Bakai, I. M. Mikhailovskiy, T. I. Mazilova, and N. Vanderka, Fiz. Nizk. Temp. **28**, 400 (2002) [Low Temp. Phys. **28**, 279 (2002)].
[10] S. Hunklinger, in *Amorphous Insulators and Semiconductors*, M. F. Thorpe and M. I. Mitkova (eds.), Kluwer, Netherlands (1997), p. 469.
[11] A. N. Aleksandrovskii, V. B. Esel'son, V. G. Manzhelii, A. Soldatov, B. Sundqvist, and B. G. Udovidchenko, Fiz. Nizk. Temp. **23**, 1256 (1997) [Low Temp. Phys. **23**, 943 (1997)].
[12] A. N. Aleksandrovskii, V. B. Esel'son, V. G. Manzhelii, A. Soldatov, B. Sundqvist, and B. G. Udovidchenko, Fiz. Nizk. Temp. **26**, 100 (2000) [Low Temp. Phys. **26**, 75 (2000)].
[13] A. N. Aleksandrovskii, V. G. Gavrilko, V. B. Esel'son, V. G. Manzhelii, B. Sundqvist, B. G. Udovidchenko, and V. P. Maletskiy, Fiz. Nizk. Temp. **27**, 333 (2001) [Low Temp. Phys. **27**, 245 (2001)].
[14] A. N. Aleksandrovskii, V. B. Esel'son, V. G. Gavrilko, V. G. Manzhelii, B. Sundqvist, B. G. Udovidchenko, and V. P. Maletskyi, Fiz. Nizk. Temp. **27**, 1401 (2001) [Low Temp. Phys. **27**, 1033 (2001)].
[15] A. N. Aleksandrovskii, A. S. Bakai, A. V. Dolbin, V. B. Esel'son, G. E. Gadd, V. G. Gavrilko, V. G. Manzhelii, S. Moricca, B. Sundqvist, and B. G. Udovidchenko, Fiz. Nizk. Temp. **29**, 432 (2003) [Low Temp. Phys. **29**, 324 (2003)].
[16] L. S. Palatnik, A. A. Nechitailo, and A. A. Koz'ma, Dokl. Akad. Nauk SSSR **36**, 1134 (1981) [Sov. Phys. Dokl. **26**, 889 (1981)].
[17] C. A. Angell, Science **267**, 1924 (1995).
[18] P. H. Pool, T. Grande, F. Scortino, H. E. Stanley, and C. A. Angell, Comput. Mater. Sci. **4**, 373 (1995).
[19] O. Mishima and Y. Suzuki, Nature (London) **419**, 599 (2002).
[20] A. S. Bakai, M. P. Fateev, and Yu. A. Turkin, in *Nanostructured Carbon for Advanced Applications*, G. Benedek *et al.* (eds.), Kluwer, Netherlands (2001), p. 185.
[21] A. M. Tolkachev, A. N. Aleksandrovskii, and V. I. Kuchnev, Cryogenics **15**, 547 (1975).
[22] G. E. Gadd, S. Moricca, S. J. Kennedy, M. M. Elcombe, P. J. Evans, M. Blackford, D. Cassidy, C. J. Howard, P. Prasad, J. V. Hanna, A. Burchwood, and D. Levy, J. Phys. Chem. Solids **58**, 1823 (1997).
[23] B. Sundqvist, Adv. Phys. **48**, 1 (1999).
[24] S. A. FitzGerald, T. Yildirim, L. J. Santodonato, D. A. Neuman, J. R. D. Copley, J. J. Rush, and F. Trouw, Phys. Rev. B **60**, 6439 (1999).
[25] Yu. E. Stetsenko, I. V. Legchenkova, K. A. Yagotintsev, A. I. Prokhvatilov, and M. A. Strzhemechnyi, Fiz. Nizk. Temp. **29**, 597 (2003) [Low Temp. Phys. **29**, 445 (2003)].
[26] R. Palmer, Adv. Phys. **31**, 669 (1982).
[27] A. S. Bakai, J. Non-Cryst. Solids **307–310**, 623 (2002).
[28] A. S. Bakai and E. W. Fischer, J. Chem. Phys. **120**, 5235 (2004).
[29] E. W. Fischer, Physica A **201**, 183 (1993).
[30] G. V. Kurdyumov, L. I. Utevski, and R. I. Entin, *Transformations in Iron and Steel* [in Russian], Moscow (1977).
[31] F. W. Sheard, in *Thermal Expansion—1971*, AIP Conference Proceedings, No. 3, M. G. Graham and H. E. Hagy (eds.), New York (1972), p. 151.
[32] Yu. A. Freiman, Fiz. Nizk. Temp. **9**, 657 (1983) [Sov. J. Low Temp. Phys. **9**, 335 (1983)].
[33] J. Eshelby, Proc. Roy. Soc. A **241**, 376 (1957).
[34] J. W. Christian, The Theory of Transformations in Metals and Alloys, Pergamon Press, Oxford, New York (1965).
[35] A. I. Prokhvatilov, N. N. Galtsov, I. V. Legchenkova, M. A. Strzhemechny, D. Cassidy, G. E. Gadd, S. Moricca, B. Sundqvist, and N. A. Aksenova, Fiz. Nizk. Temp. **31**, 585 (2005).
[36] W. P. Beyermann, M. F. Hundley, J. D. Thompson, F. N. Diederich, and G. Gruner, Phys. Rev. Lett. **68**, 2046 (1992).
[37] W. P. Beyermann, M. F. Hundley, J. D. Thompson, F. N. Diederich, and G. Gruner, Phys. Rev. Lett. **69**, 2737 (1992).
[38] L. S. Fomenko, S. V. Lubenets, V. D. Natsik, D. Cassidy, G. E. Gadd, S. Moricca, and B. Sundqvist, Fiz. Nizk. Temp. **31**, 596 (2005) [Low Temp. Phys. **31**, 454 (2005)].

This article was published in English in the original Russian journal. Reproduced here with stylistic changes by AIP.

Hysteretic phenomena in Xe-doped C_{60} from x-ray diffraction

A. I. Prokhvatilov, N. N. Galtsov,* I. V. Legchenkova, and M. A. Strzhemechny

B. Verkin Institute for Low Temperature Physics and Engineering of the National Academy of Sciences of Ukraine, 47 Lenin Ave., Kharkov 61103, Ukraine

D. Cassidy, G. E. Gadd,** and S. Moricca

Australian Nuclear Science and Technology Organisation, Private Mail Bag 1, Menai, NSW 2234, Australia

B. Sundqvist

Department of Physics, Umea University, S-901 87 Umea, Sweden

N. A. Aksenova

Rail Way Transport Academy, 23 Moskovski Ave., Kharkov, Ukraine

(Submitted August 4, 2004; revised August 10, 2004)
Fiz. Nizk. Temp. **31**, 585–589 (May 2005)

Polycrystalline fullerite C_{60} intercalated with Xe atoms at 575 K and a pressure of 200 MPa was studied by powder x-ray diffraction. The integrated intensities of a few brighter reflections have been utilized to evaluate the occupancy of the octahedral interstitial sites in C_{60} crystals, which turned out to be $(34\pm4)\%$, and in good agreement with another independent estimate. It is found that reflections of the $(h00)$ type become observable in Xe-doped C_{60}. The presence of xenon in the octahedral sites affects both the orientational phase transition as well as the glassification process, decreasing both characteristic temperatures as well as smearing the phase transition over a greater temperature range. Considerable hysteretic phenomena have been observed close to the phase transition and the glassification temperature. The signs of the two hysteresis loops are opposite. There is reliable evidence that at the lowest temperatures studied the thermal expansion of the doped crystal is negative under cool-down. © *2005 American Institute of Physics.* [DOI: 10.1063/1.1925372]

INTRODUCTION

The cubic crystals of fullerite C_{60} comprise almost spherical molecules with a diameter of 10.2 Å. The lattice has quite large interstitial cavities with octahedral (4.12 Å) and tetrahedral (2.2 Å) point symmetry, which can be stuffed with various atoms or molecules with sizes comparable to the void diameters. This circumstance was utilized at the very beginning of the fullerene era resulting in the high-T_c superconductivity of an organic crystal (C_{60} doped with alkali metals).[1] Afterwards, C_{60} was intercalated with rare gas atoms[2–7] and molecules of different symmetries and sizes.[8–14] It is commonly accepted that changes in the physical properties of fullerite C_{60} brought about by intercalation with neutral species are mainly due to the doping-related change in the molar volume. In the particular case under study the doped crystal can be considered either to be under a negative pressure or, in the opposite sense, to exhibit a positive internal pressure.

The most interesting phenomena caused by intercalation are observed within the regions where the orientational phase transition ($T_c=260$ K) occurs or the orientational glass forms ($T_g=90$ K). Usually, when the voids are filled with the larger rare gas atoms such as Xe or with simpler closed-shell molecules, the anisotropic interaction between C_{60} molecules weakens; and the rotation of the C_{60} molecules loosens up, resulting in lower critical temperatures for both transformations.[6,7] Moreover, when the dopant species are certain molecules, for example, CO or NO, there are indications[15,16] that no freezing into an orientational glass state is observed. In regards to doping with rare gas species, both large negative expansivity as well as temperature hysteresis of the thermal expansion are observed at low temperatures.[17]

In this paper, we report detailed powder x-ray studies of the structural characteristics of Xe-doped C_{60}, with temperature cycling around the orientational phase transition (150–300 K) as well as in the region where orientational glass states tend to form (7 to 100 K).

EXPERIMENTAL

C_{60} powder was saturated with xenon at a pressure and temperature of about 200 MPa and 575 °C, respectively, for a period of 36 hours. When intercalated at high pressure but at 300 °C, only 10% of the octahedral voids are filled; the filling can reach 66% if C_{60} is saturated at 575 °C.[6] In the present case, thermogravimetric analysis (TGA) showed a weight loss between 6 and 7%, indicating a stoichiometry of $Xe_{0.39-0.45}C_{60}$. The powder of Xe-doped C_{60} was subsequently compacted for dilatometric studies in cylindrical dies by quasi-hydrostatic compression with pressures of up to 1 GPa, as described elsewhere.[17] The sample used in our x-ray experiments was a chunk taken from the larger compacted specimen, the smooth surface of which served as the reflection plane in the x-ray experiments.

Powder x-ray studies were carried out on a DRON-3M diffractometer equipped with a special liquid-helium cryostat. The temperature of samples was varied over the range of 7 to 300 K. The temperature was stabilized to within ± 0.05 K at every measurement point. In the orientational glass domain ($T<70$ K) and below the orientational phase transition point ($T_c=260$ K), the temperature was varied in warm-up and cool-down regimes with the intention of looking for possible hysteretic phenomena of the lattice parameters and thermal expansivities. The intensities, widths, and angular positions of the relevant reflections as functions of temperature were used for analysis of the phenomena under study. The lattice parameter error was $\pm 0.02\%$ and the intensity of the x-ray reflections was measured to within 1%.

RESULTS AND DISCUSSION

A typical x-ray pattern is shown in Fig. 1. It can be seen that our fine-grain samples, in addition to the fcc phase of Xe-doped fullerite C_{60}, contain about 10% of another phase which could in no way be indexed as fcc. It should be noted that in the ''as-prepared'' Xe-doped powder samples, no phases other than the fcc phase were detected[6] either in x-ray or neutron diffraction experiments. The reflections belonging to this new phase are indicated in Fig. 1 with arrows. It is possible that the new phase is a result of a partial polymerization caused by the previous compacting. Notwithstanding the known polymerization-related structure[18,19] we failed to find a space group that could fit the extra reflections mentioned.

We observed substantial changes in the scattered intensities compared to pure fullerite. To mention first, the reflections of the type ($h00$) became clearly distinguishable (in pure C_{60} their intensities are virtually zero because of the specific molecule/lattice size relation and the shape of C_{60} molecule[20]). Some other reflections, such as (111) and (220), are lower in intensity as compared to pure C_{60}, while others, such as (420) and (422), are brighter.

The absolute lattice parameter values as a function of temperature were determined as follows. At two reference points, viz., at room temperature and at 7 K, full-profile diffraction patterns were recorded in order to obtain the rms averaged reference cubic lattice parameter values for those two reference points and in each case with the lattice parameter averaged over all the observed reflections. Then, between those two reference points, the lattice parameters at other temperatures were determined from the (311) reflection and scaled appropriately to the reference values.

Using these lattice parameters, we calculated how the intercalation with Xe has changed the room-temperature diffraction intensity ratios for specifically chosen reflections compared to the most intense (311) reflection, as a function of the occupancy of octahedral voids by Xe atoms and assuming a uniform distribution of the dopant throughout the sample. In the calculations we used the following expression for the scattering amplitude of reflection (hkl):

$$F(q)\propto 60 f_C(\mathbf{q})(\sin qr/qr + f_{RG}(\mathbf{q})X_{RG}(-1)^{h+k+l}. \quad (1)$$

Equation (1) generally applies for the case of atoms of any rare gas randomly distributed over octahedral cavities. The first term in the right-hand side of Eq. (1) is the contribution from the randomly rotating C_{60} molecules; the second term is the contribution from the interstitial rare gas (RG) atoms. The quantities $f_C(\mathbf{q})$ and $f_{RG}(\mathbf{q})$, both functions of the momentum transfer vector, are respectively the carbon and RG atomic scattering factors and $f_{\mathrm{Xe}}(\mathbf{q})$ will be used for the latter. The absolute magnitude of the vector $\mathbf{q}$ is given by $4\pi \sin(\theta)/\lambda$, where 2θ is the deflection angle of the incident x-rays with wavelength λ. Finally, X_{RG} is the rare gas occupancy of the octahedral voids, which is assumed to be uniform throughout the sample. The square of $F(\mathbf{q})$ in Eq. (1) is proportional to the intensity of the actual x-ray reflections at the respective angles 2θ; the values were calculated using the lattice parameter determined as described from the room-temperature value $a=14.246\pm 0.003$ Å. Integrated intensities were determined using the Gaussian function, which turned out to be a little better than the Lorentzian. All calculated integrated intensities were normalized to that of the brightest reflection (311). The experimentally determined integrated intensity ratios for the chosen reflections are plotted in Fig. 2 to evaluate the occupancy of octahedral voids by xenon. Using the four occupancies thus found (see Fig. 2), we calculated the weighted average of the occupancy to be $X_{\mathrm{Xe}}=(34\pm 4)\%$, in good agreement with previously found TGA data $(41.5\pm 2.5)\%$, see the Experimental Section above). We ascribe the uncertainty in the value to two fac-

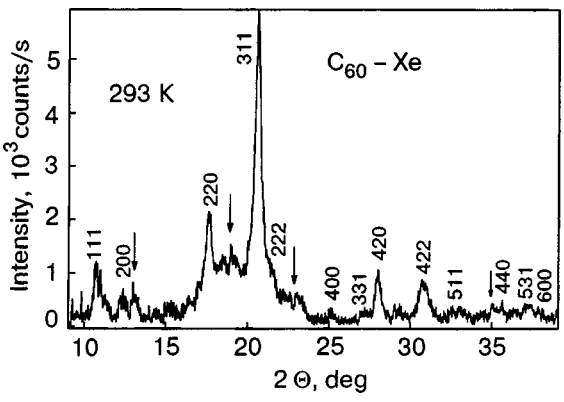

FIG. 1. A typical x-ray diffraction pattern from polycrystalline C_{60}–Xe samples, recorded at room temperature. The indexed reflections belong to the orientationally disordered fcc phase of Xe-doped fullerite C_{60}. The arrows indicate reflections of an unknown phase.

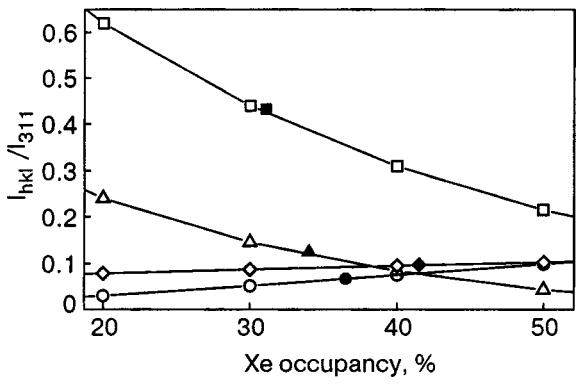

FIG. 2. Calculated intensity ratios for a few fcc reflections versus the Xe occupancy of octahedral voids at room temperature with the lattice parameter equal to $a=14.246$ Å: 220 (□), 222 (△), 420 (◇), 200 (○). The filled symbols indicate the corresponding experimental intensity ratios.

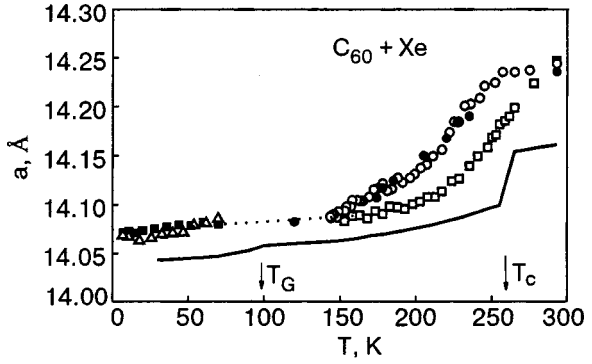

FIG. 3. Temperature dependence of the lattice parameter of the $C_{60}-Xe$ sample, as measured under cool-down or warm-up regimes: warm-up (□), (■); cool-down (○), (●), (△); pure C_{60} (–). The lower solid curve is for pure fullerite C_{60}.[22]

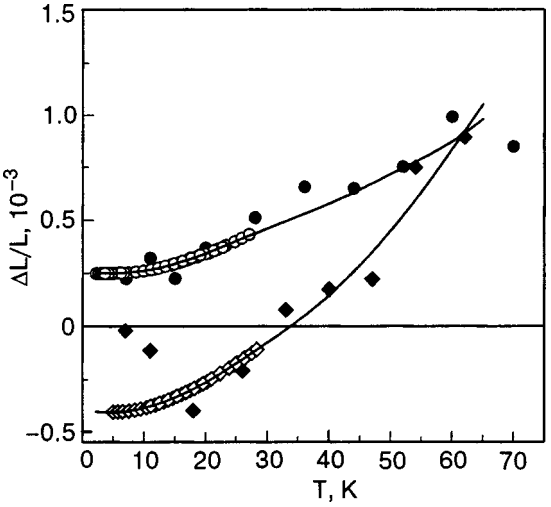

FIG. 4. Relative elongation versus temperature for polycrystalline $C_{60}-Xe$ samples under warm-up and cool-down, according to dilatometric[24] and x-ray diffraction measurements; cool-down: this work (♦), Ref. 24 (◇); warm-up: this work (●), Ref. 24 (○).

tors, viz., the inhomogeneity of the distribution of Xe over the grain volume and the errors in absolute intensity values for the weaker lines (see Fig. 2).

Variations of the lattice parameter $a(T)$ of Xe-doped C_{60} with temperature under warm-up and cool-down are plotted in Fig. 3. One can see that the path $a(T)$ depends essentially on the direction of temperature variation. Two hysteresis loops were observed and it is noteworthy that the signs of the warm-up/cool-down hystereses are opposite to each other. At temperatures below the orientational phase transition in pure fullerite ($T_c = 260$ K), the cool-down lattice parameters are appreciably higher than those found with warm-up. In the temperature range where the orientational glass is observed in pure C_{60} the hysteresis loop has a narrower span and, as mentioned above, its sign is opposite to that of the hysteresis at higher temperatures, or in other words, the cool-down lattice parameter values are smaller than the warm-up ones.

Repeated cool-down of the sample had virtually no effect on the situation, and the lattice parameter $a(T)$ followed the same path as found during the first cool-down run. What is striking is the strong ''smearing'' and shift of the orientational transition to lower temperatures, as compared to that for pure C_{60}, as well as the huge temperature span of the hysteresis loop, which stretches from 150 K up to room temperature. The largest lattice parameter difference at 230 K amounts to $\Delta a = 0.055$ Å, which exceeds by far the experimental error in $a(T)$. The hysteretic effect observed at lower temperatures affects the crystal lattice to a lesser extent. The loop is found to be far from symmetric; the upper bifurcation point is at $T = 60 \pm 5$ K, while the maximum lattice parameter difference $\Delta a = (0.007 \pm 0.003)$ Å is reached at ~ 20 K. A pronounced instability was observed for the cool-down regime, which manifested itself in a greater scatter of lattice parameter values. The cool-down curve is steeper than the warm-up curve at the high-temperature end of the hysteresis loop. What is equally striking is that at the low-temperature end there is a definite indication that the thermal expansivity has become negative. A very rough estimate from the three lowest points yields unusually large negative expansivities of the order of -5×10^{-4} K^{-1}. Negative linear thermal expansion coefficients at low temperatures have already been documented for pure fullerite[21] and also for fullerite intercalated with neon, argon, and krypton[17,23] and now, in conjunction with this work, with Xe as well.[23] The dilatometric measurements of thermal expansion coefficients in the orientational glass region of the $C_{60}-Xe$ system have been carried out up to 28 K, which allowed comparison between the dilatometric[24] and x-ray data, as shown in Fig. 4. The solid curves are drawn through dilatometry points and smoothly extrapolated to higher temperatures. The good qualitative agreement is evident.

We tried to observe relaxation processes in the domain of the high-temperature hysteresis at fixed temperatures of 150, 180, 220 and 250 K on both the warm-up and cool-down branches. Contrary to our expectations, no changes in lattice parameter values were recorded and this was even after quite long waiting times (10 hours).

The cause behind the anomalies observed in this report (two hystereses, large negative expansivities at low temperatures) is not completely clear. A qualitative explanation of both low-temperature anomalies (the hysteresis and the negative expansivities) was suggested by Aleksandrovskii *et al.*[24] The negative expansion coefficients, found dilatometrically at low temperatures,[24] are related to the tunnel nature of the low-energy levels. The hysteresis is ascribed to a polyamorphic phase transition between two different orientational glass phases, in which case the non-ergodic character of the glass system can lead to hysteretic phenomena. As regards the high-temperatures hysteresis, we can make the following remarks. Of course, since the orientational phase transition is a first-order one, it is quite natural that it occurs with a hysteresis. We are well aware that because the distribution of Xe atoms inside the crystallites most likely should be highly inhomogeneous, the span of the hysteresis could be much larger than in pure C_{60}.[22] However, first, the temperature span is too broad and, second, the high-temperature bifurcation point is (contrary to expectations) above T_c in the pure material. Thus the nature of the high-temperature hysteresis is not completely understood.

Considering the lattice parameter of C_{60} doped with Xe as a function of the occupancy X_{Xe} (see Fig. 5) we note that the specific occupancy as estimated from our x-ray diffrac-

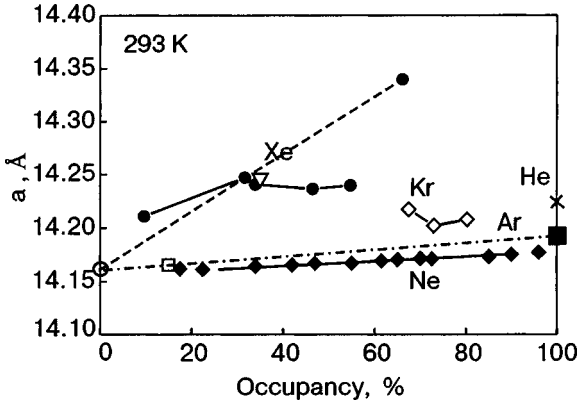

FIG. 5. The lattice parameter of RG-doped cubic fullerite C_{60} as a function of the RG occupancy of octahedral voids: Ref. 6 (●) and the present study (▽) for Xe; Ref. 3 (◆) for Ne; Ref. 6 (◇) for Kr; Refs. 5 and 6 (■) and the present study (□) for Ar; Refs. 26 and 27 (×) for He; Ref. 22 for pure C_{60} (○).

tion data (Fig. 2) falls close to the points from other reports[6] that deal with the $C_{60}-Xe$ system. However, if taken in their completeness the points of the $a(X_{Xe})$ dependence do not fall on a straight line. For other rare gas species as dopants of C_{60}, and where the lattice parameter versus occupancy is known, it appears to follow a linear $a(X_{RG})$ relationships. This is clearly seen in Fig. 5 for Ne.[25] Indirect evidence from our findings on the $C_{60}-He$ system,[26,27] also suggests is a linear function, whereas for Ar the span of X_{Ar} is too narrow to make a sound judgment at this stage. The reason behind the nonlinearity of the $a(X_{Xe})$ relationship is not clear at present.

CONCLUSIONS

We have performed x-ray powder diffraction studies of a Xe-doped C_{60} sample over the temperature range from 7 to 300 K.

The sample is found to contain two phases. One is the fcc phase, quite common for fullerite C_{60} but with the lattice parameter slightly increased due to the xenon present. The structure of the other phase (of approximately 10% content) was not determined. Its presence might result from partial polymerization brought about by handling during sample preparation.

The room temperature reflection intensities allowed us to evaluate the weighted average Xe occupancy as (34 ± 4) mol %, in good agreement with the TGA estimates performed upon saturation.

The variation of the fcc lattice parameter with temperature depends strongly on the sign of the temperature increment. Two hysteresis loops have been observed in the temperature dependence of the lattice parameter. The wider and more pronounced one is below the orientational transition point; the other hysteresis loop is below the orientational glassification point ($Tg < 70$ K). The nature of the hysteresis, especially of the high-temperature one, is not completely clear.

The lattice parameters measured at the lowest temperature points under cool-down give an indication of unusually large negative thermal expansivities.

The authors thank A. N. Aleksandrovskii and V. G. Manzhelii for valuable discussions and for providing us with their experimental results prior to publication.

This work was partially supported by the STCU, Grant No 2669.

*E-mail: galtsov@ilt.kharkov.ua
**E-mail: geg@ansto.gov.au

[1] O. Zhou and D. E. Cox, J. Phys. Chem. Solids **11**, 1373 (1992).
[2] J. E. Schirber, G. H. Kwei, J. D. Jorgensen, R. L. Hitterman, and B. Morosin, Phys. Rev. B **51**, 12014 (1995).
[3] B. Morosin, J. D. Jorgensen, S. Short, G. H. Kwei, and J. E. Schirber, Phys. Rev. B **53**, 1675 (1996).
[4] G. E. Gadd, P. J. Evans, S. Moricca, and M. James, J. Mater. Res. **12**, 1 (1997).
[5] G. E. Gadd, S. J. Kennedy, S. Moricca, C. J. Howard, M. M. Elcombe, P. J. Evans, and M. James, Phys. Rev. B **55**, 14794 (1997).
[6] G. E. Gadd, S. Moricca, S. J. Kennedy, M. M. Elcombe, J. Evans, M. Blackford, D. Cassidy, C. J. Howard, P. Prasad, J. V. Hanna, A. Burchwood, and D. Levy, J. Phys. Chem. Solids **58**, 1823 (1997).
[7] M. Gu and T. B. Tang, J. Appl. Phys. **93**, 2486 (2003).
[8] J. E. Schirber, R. A. Assink, G. A. Samara, B. Morosin, and D. Loy, Phys. Rev. B **51**, 15552 (1995).
[9] S. A. Meyers, R. A. Assink, J. E. Schirber, and D. Loy, Mater. Res. Soc. Symp. Proc. **359**, 505 (1995).
[10] B. Morosin, R. A. Assink, R. G. Dunn, T. M. Massis, and J. E. Schirber, Phys. Rev. B **56**, 13611 (1997).
[11] M. James, S. J. Kennedy, M. M. Elcombe, and G. E. Gadd, Phys. Rev. B **58**, 14780 (1998).
[12] G. H. Kwei, F. Troun, B. Morosin, and H. F. King, J. Chem. Phys. **113**, 320 (2000).
[13] S. A. FitzGerald, T. Yildirim, L. J. Santodonato, D. A. Neuman, J. R. D. Copley, J. J. Rush, and F. Trouw, Phys. Rev. B **60**, 6439 (1999).
[14] I. Holleman, G. von Helden, A. van der Avoird, and G. Meijer, Phys. Rev. Lett. **80**, 4899 (1998).
[15] S. Van Smaalen, R. Dinnebier, I. Holleman, G. von Helden, and G. Meijer, Phys. Rev. B **57**, 6321 (1998).
[16] M. Gu, T. B. Tang, and D. Feng, Phys. Rev. B **66**, 073404 (2002).
[17] A. N. Aleksandrovskii, A. S. Bakai, A. V. Dolbin, G. E. Gadd, V. G. Gavrilko, V. G. Manzhelii, S. Moricca, B. Sundqvist, and B. G. Udovidchenko, Fiz. Nizk. Temp. **29**, 432 (2003) [Low Temp. Phys. **29**, 324 (2003)].
[18] S. Amelinks, C. Van Henrich, D. van Dyck, and G. Van Tendeloo, Phys. Status Solidi A **131**, 589 (1992).
[19] B. Sundqvist, Adv. Phys. **48**, 1 (1999).
[20] R. Moret, P. Launois, T. Wagberg, B. Sundqvist, V. Agafonov, V. A. Davydov, and A. V. Rakhmanina, Eur. Phys. J. B **37**, 25 (2004).
[21] A. N Aleksandrovskii, V. B. Esel'son, V. G. Manzhelii, A. V. Soldatov, B. Sundqvist, and B. G. Udovidchenko, Fiz. Nizk Temp. **23**, 1256 (1997) [Low Temp. Phys. **23**, 943 (1997)]; Fiz. Nizk. Temp. **26**, 100 (2000) [Low Temp. Phys. **26**, 75 (2000)].
[22] N. A. Aksenova, A. P. Isakina, A. I. Prokhvatilov, and M. A. Strzhemechny, Fiz. Nizk. Temp. **25**, 964 (1999) [Low Temp. Phys. **25**, 724 (1999)].
[23] A. N. Aleksandrovskii, V. G. Gavrilko, V. B. Esel'son, V. G. Manzhelii, B. G. Udovidchenko, and V. P. Maletskiy, Fiz. Nizk Temp. **27**, 1401 (2001) [Low Temp. Phys. **27**, 1033 (2001)].
[24] A. N. Aleksandrovskii, A. S. Bakai, A. V. Dolbin, V. B. Esel'son, G. E. Gadd, V. G. Gavrilko, V. G. Manzhelii, S. Moricca, and B. Sundqvist, Fiz. Nizk. Temp. **31**, 565 (2005) [Low Temp. Phys. **31**, 565 (2005)].
[25] B. Morosin, J. D. Jorgensen, S. Short, G. H. Kwei, and J. E. Schirber, Phys. Rev. B **53**, 1675 (1996).
[26] I. V. Legchencova, A. I. Prokhvatilov, Yu. E. Stetsenko, M. A. Strzhemechny, K. A. Yagotintsev, A. A. Avdeenko, V. V. Eremenko, P. V. Zinoviev, V. N. Zoryansky, N. B. Silaeva, and R. S. Ruoff, Fiz. Nizk. Temp. **28**, 1320 (2002) [Low Temp. Phys. **28**, 942 (2002)].
[27] Yu. E. Stetsenko, I. V. Legchenkova, K. A. Yagotintsev, A. I. Prokhvatilov, and M. A. Strzhemechny, Fiz. Nizk. Temp. **29**, 597 (2003) [Low Temp. Phys. **29**, 445 (2003)].

This article was published in English in the original Russian journal. Reproduced here with stylistic changes by AIP.

Phonon spectrum and electron-phonon interaction in technetium

S. M. Sichkar* and V. N. Antonov

G. V. Kurdyumov Institute of Metal Physics, National Academy of Sciences of Ukraine, pr. Vernadskogo 36, Kiev 03142, Ukraine

(Submitted August 12, 2004)
Fiz. Nizk. Temp. **31**, 590–595 (May 2005)

Ab initio calculations of the phonon spectrum, spectral function of the electron-phonon interaction, and transport properties (resistivity) of technetium are carried out in the framework of linear response theory. Good agreement with the experimental data is obtained. © *2005 American Institute of Physics.* [DOI: 10.1063/1.1925373]

INTRODUCTION

It is well known that the electron-phonon interaction governs a number of important physical properties of metals. The electrical and thermal resistivities, superconductivity, softening of phonon modes, renormalization of the low-temperature electronic component of the heat capacity ($\sim T$), and a number of other physical phenomena can be interpreted correctly only with knowledge of the spectral distribution function of of the electron-phonon interaction in each particular substance. An *ab initio* calculation of the latter is best, since it avoids the artificial approximations typical in phenomenological models. Moreover, calculations from first principles in cases where the ''physics'' of the process can be governed by different mechanisms enable one to obtain a correct picture of the phenomena. For example, a detailed microscopic calculation of the electron-phonon interaction makes it considerably easier to elucidate the origins of a superconducting phase (which can be due, e.g., to electron-exciton or electron-plasmon interaction).[1] Some other examples are the mechanism of softening of phonon modes, structural phase transitions, and anomalies of the phonon spectrum. These phenomena can be explained as resulting from a strong interaction of electrons with an ''anomalous'' phonon branch (this can be determined only as a result of a detailed calculation), or by strong anharmonicity of the material, or by the presence of impurities and various defects in the crystal.[2]

The goal of the present study was to investigate the dynamic and transport properties of technetium. We note that this element is of independent theoretical interest by virtue of a number of unique physical properties. Technetium, the lightest artificial element of the periodic table (atomic number 43) was obtained in 1937 by the Italian scientists Segre and Perrier by bombarding molybdenum nuclei with deuterons. Technetium has the highest temperature of transition to the superconducting state among all of the metals with the hcp structure, $T_c = 7.86$ K, and is second among all the elements of the periodic table only to the fcc metal Nb, with $T_c = 9.25$ K. Furthermore, the transition temperature is increased substantially in alloys of technetium with an extremely small admixture of Nb (Ref. 3) or Mo (Ref. 4): $T_c(Nb_{0.03}Tc_{0.97}) = 12.8$ K; $T_c(Mo_{0.12}Tc_{0.88}) = 13.0$ K. (For comparison, in the bcc alloys NbZr the critical temperature $T_c = 9.3$ K.[5])

A broad anomalous ''dip'' of the longitudinal optical (LO) branch in the direction of the hexagonal axis (00ξ) and strong temperature dependence of the LO branch were observed in Ref. 6. The value of the phonon frequency at the Brillouin zone center [$\omega_{LO}(k=0)$] decreased from 3.7 THz at room temperature to 2.4 THz at $T = 30$ K. Such temperature dependence is not observed in any other hcp metal, and its ''amplitude'' is comparable only to the analogous temperature dependence of the phonon anomalies in high-T_c superconductors with the A15 structure: Nb_3Sn and V_3Si.

CALCULATION TECHNIQUE

The dispersion curves of the phonon spectrum and the electron-phonon interaction matrix element were calculated by a scalar-relativistic linear method of MT orbitals (LMTO) with non-MT corrections taken into account.[7,8] We used the $3k$-spd LTMO basis set (27 orbitals per atom) with a one-center decomposition of the wave function inside the MT sphere to $l_{max} = 6$. In the intersphere region the wave function was decomposed into plane waves to energies of 13.4, 19.6, and 21.4 Ry (120, 145, and 169 waves for the s, p, and d orbitals, respectively). The variations of the charge density and potential were expanded in spherical harmonics inside the MT sphere (to $l_{max} = 6$) and in plane waves in the intersphere region (82.7 Ry, 2430 waves).

The radius of the MT sphere was chosen equal to 2.552 a.u. The von Barth-Hedin approximation[9] of the exchange-correlation potential was used. The lattice constant $a = 5.1698$ a.u.; $c/a = 1.6022$.

The integration in k space necessary for finding the induced electron density and the dynamic matrix was carried out at 50 points in the irreducible part of the Brillouin zone (BZ). This is quite sufficient, since the improved tetrahedron method[10] that we used for calculation of the bulk (surface) integrals allows one to refine the calculation substantially (in particular, to make accurate allowance for the real shape of the Fermi surface) by using weighting coefficients obtained on a denser mesh. The weighting factors were found using electron bands ε_{kj} calculated at 793 irreducible points of the BZ.

The spectral function of the electron-phonon interaction (the Eliashberg function) expressed in terms of the phonon line broadenings $\gamma_{q\nu}$ (characterizing the partial contribution of each phonon) has the form[11]

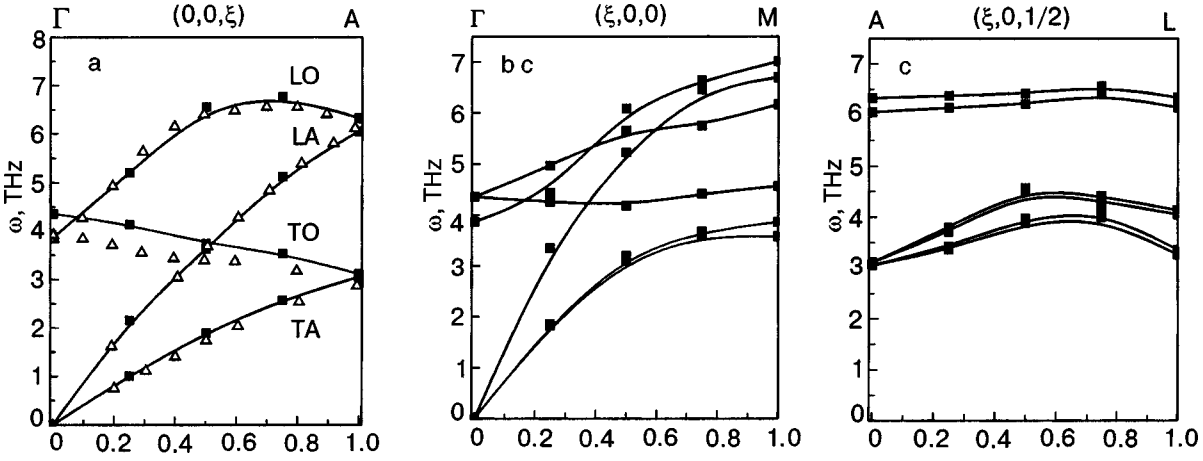

FIG. 1. Dispersion curves of the phonon spectrum of technetium for the directions ΓA(0,0,ξ), ΓM(ξ,0,0), and AL (ξ,0,1/2) in the Brillouin zone. The unfilled triangles are the experimental points from Ref. 7.

$$\alpha^2F(\omega)=\frac{1}{2\pi N(\varepsilon_F)}\sum_{q\nu}\frac{\gamma_{q\nu}}{\omega_{q\nu}}\delta(\omega-\omega_{q\nu}), \tag{1}$$

$$\gamma_{q\nu}=2\pi\omega_{q\nu}\sum_{kjj'}|g^{q\nu}_{k+qj',kj}|^2\delta(\varepsilon_{kj}-\varepsilon_F)\delta(\varepsilon_{k+qj'}-\varepsilon_F). \tag{2}$$

The electron-phonon interaction constant is defined as

$$\lambda=2\int_0^\infty\frac{d\omega}{\omega}\alpha^2F(\omega). \tag{3}$$

It can also be expressed in terms of the phonon line broadenings:[14]

$$\lambda=\sum_{q\nu}\frac{\gamma_{q\nu}}{\pi N(E_F)\omega^2_{q\nu}}, \tag{4}$$

were $N(\varepsilon_F)$ is the phonon density of states on the Fermi surface ε_F, and $g^{q\nu}_{k+qj',kj}$ is the electron-phonon interaction matrix element.

The double summation over the Fermi surface in (2) was carried out on a dense mesh (793 points in the irreducible part of the BZ).

PHONON SPECTRUM

Figure 1 shows the dispersion curves of the phonon spectrum calculated in the directions ΓA (0, 0, ξ), ΓM (ξ,0,0), and AL (ξ,0,1/2). Values of the phonon branches in the ΓA direction were obtained by the inelastic incoherent neutron scattering method in Ref. 6. It is seen that our calculation reproduces the experimental data rather well. In particular, it accurately reproduces the broad anomaly of the LO branch. A slight difference is observed only for the TO branch. Our calculation overestimates the experimental spectrum by a small amount ($\sim$0.4 THz). It should be noted that we did some test calculations using different exchange-correlation potentials (including one with a general gradient correction[12]) and were unable to improve the agreement with the experimental data. The cause of this discrepancy apparently lies in the local electron density approximation (LDA) itself. We think that the LDA can lead to errors in the calculation in those regions of reciprocal space where the electron-phonon interaction is large.

Phonon densities of states $F(\omega)$ in technetium were obtained in Ref. 13 for two values of the temperature: 300 and 150 K. A comparison of the low-temperature data with our calculation (Fig. 2) shows rather good agreement of the three main values of the maxima on the $F(\omega)$ curve. Experiment: 14.5, 18, and 27 meV; theory: 15.2, 19, and 27 meV.

ELECTRON-PHONON INTERACTION

Figure 3 shows a plot of our calculated values of the Eliashberg function $\alpha^2F(\omega)$ [Eq. (1)].

The calculated electron-phonon interaction constant was found to be $\lambda=0.9039$.

Comparing $\alpha^2F(\omega)$ and $F(\omega)$, we see that there are no material differences caused by integrating over the real Fermi surface and the presence of the electron-phonon interaction matrix element in the integrand. The coefficient $\alpha^2(\omega)$ [where $\alpha^2\equiv\alpha^2F(\omega)/F(\omega)$] is practically constant over the whole region of integration (we are not considering the initial part $<$10 MeV because of the limited set of calculated data in the low-energy region of the phonon spectrum). The slight increase of $\alpha^2(\omega)$ in the 22 meV region and also the broadening of the high-energy peak of $\alpha^2F(\omega)$

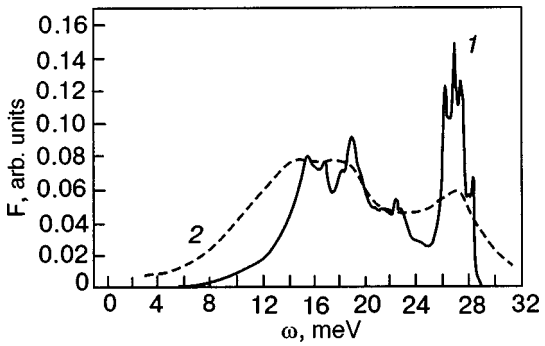

FIG. 2. Phonon density of states: calculation (*1*); experiment[13] (*2*).

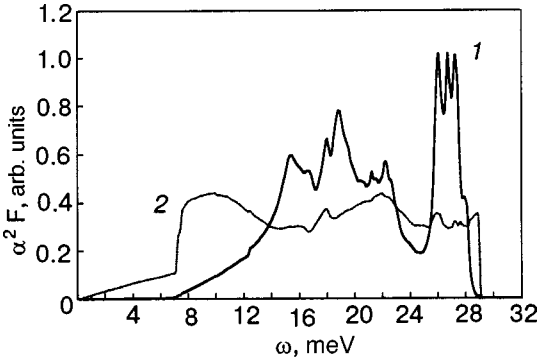

FIG. 3. Eliashberg function (*1*) and the coefficient $\alpha^2(\omega)$ (*2*).

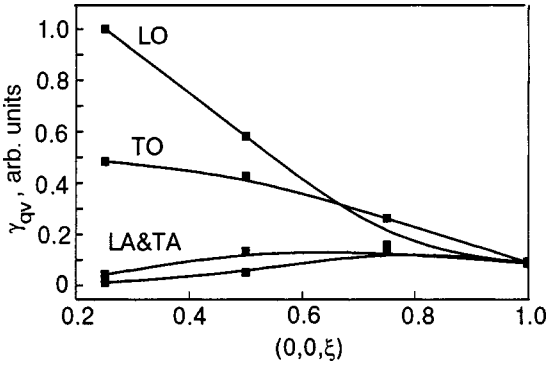

FIG. 4. Partial broadenings of the phonon lines in the $\Gamma(A(0,0,\xi)$ direction.

in the 26–28 meV region can be explained by a stronger interaction of the longitudinal branches of the phonon spectrum with the electronic subsystem.

Since for technetium $\alpha^2(\omega) \approx$ const, one expects that it will be correct to use the McMillan approximation,[15] according to which the electron-phonon interaction constant factorizes into the product of an electron part and a phonon part: $\lambda = \eta / M\langle\omega^2\rangle$, where the Hopfield parameter η (Ref. 16) is determined entirely by the band structure of the substance.

We obtained the values $\eta = 0.164$ a.u. and $\langle\omega^2\rangle^{1/2} = 224.08$ K and, hence, $\lambda_H = 0.9001$. We see that this value of λ agrees well with that obtained earlier.

Let us now compare our calculated value of the Hopfield parameter with the result of Ref. 17, where in the approximation of a rigid MT shift and in the framework of the KKR method[18] a value $\eta_{\mathrm{KKR}} = 0.170$ a.u. was obtained. Thus the rigid MT shift approximation works quite well in our case.

For the phonon part the situation looks just the opposite: any simplifying assumptions as to the phonon spectrum leads to noticeable scatter in the values of $\langle\omega^2\rangle$ and, consequently, of λ. As an example, let us give some published values of the electron-phonon interaction constant of technetium: 0.65,[19] 0.78,[20] 1.01 and 1.17.[21]

In other words, calculation of the phonon spectrum from first principles is a necessary and sufficient condition for obtaining a realistic picture of the physical processes underlying the electron-phonon interaction.

Let us return to the anomaly in the phonon spectrum. Let us note first that the dynamic matrix was obtained by us in the harmonic approximation.[8] The fact that the anomaly is clearly reproduced in the calculation speaks to the fact that the main mechanism of its formation is the strong influence of the electronic subsystem on the motion of the technetium ions. (We are talking about low temperatures. As to the high-temperature dependence of the LO branch, the causes of this effect may include phonon-phonon interaction.)

Figure 4 shows the values of $\gamma_{q\nu}$ corresponding to different phonon modes. It is clearly see that as the Γ point is approached, the broadening corresponding to the LO mode is substantially greater than the value for the other branches. For example, at the point $\mathbf{q}(0,0,0.25)$: $\gamma_{\mathrm{LO}}/\gamma_{TO} = 2$, $\gamma_{LO}/\gamma_{LA} = 23.9$, $\gamma_{LO}/\gamma_{TA} = 105.6$. Thus strong interaction of the electronic subsystem with longitudinal optical vibrations is indeed observed in the $(0,0,\xi)$ direction. (Note that we have eliminated the Γ point itself from consideration, since the matrix element appearing in expression (2) is equal to zero. This becomes obvious if one examines the functions appearing in the integrand of the expression for the matrix element in Ref. 21. At $k = 0$ they are all periodic with the period of the direct lattice. The integration, in turn, is also over a whole period of the direct lattice.)

POINT-CONTACT SPECTRA

Figure 5 shows the experiment electron-phonon interaction function $G_{pc}(\omega)$ obtained by the method of point-contact (PC) spectroscopy.[22] The theoretical shape of the latter differs from $\alpha^2F(\omega)$ only by the presence of an additional form factor $K(\mathbf{k},\mathbf{k}')$ (Ref. 22) in Eq. (1), which specifies the geometry of the contact and the conditions of current flow. It is assumed that $K(\mathbf{k},\mathbf{k}')$ cannot materially alter the structure of the features occurring in $\alpha^2F(\omega)$. Thus $G_{pc}(\omega)$ should be close to $\alpha^2F(\omega)$.

Nevertheless, for technetium these functions are substantially different in the region >18 MeV. The peaks at 19 and 22.5 meV are absent in the experiment, and the peak at 27 meV is strongly suppressed.

Such a marked "cutoff" of the high-energy region in $G_{pc}(\omega)$ in fact means that the interaction of the electronic subsystem with high-energy phonons (including the longitudinal acoustic and optical) is almost completely suppressed. If this were indeed the case, then technetium should not exhibit any superconducting properties. We note that many PC spectra exhibit a significantly lower intensity ratio of the high-energy peak (G_2) to the low-energy peak (G_1) in comparison with the neutron-scattering phonon spectra. This is explained by the heating of the contact by the current and the

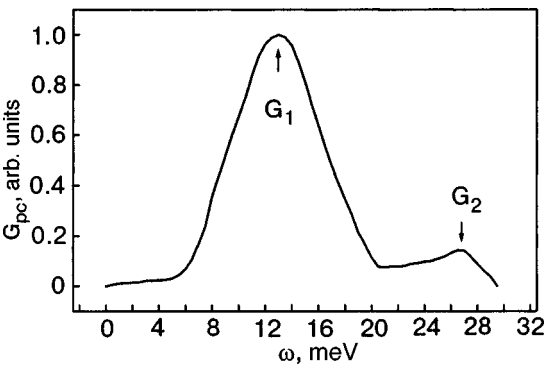

FIG. 5. Experimental point-contact function of the electron-phonon interaction in technetium.[22]

resulting broadening of the spectral lines[23] and also significant plastic deformation of the metal in the contact region.[24]

The cleanliness of the surface of the sample also has a substantial influence on the result of an experiment. For example, in Ref. 13 spectra were taken for a bulk polycrystal in addition to the film sample on which the results for $G_{pc}(\omega)$ plotted in Fig. 5 were obtained. In the latter case the high-energy peak was absent altogether, and the level of the zero-point anomalies and the noise level were significantly lower.

Interestingly, a similar situation with the suppression of the high-energy peak was also observed in experiments to determine the electron-phonon interaction function but by the method of tunneling spectroscopy in Nb.

The high-energy peak obtained in Refs. 14 and 19 was completely suppressed on the experimental curve.[25] This difference has been discussed in detail in the literature, and a number of arguments have been advanced to explain it. First it was noted that Nb forms oxides on the surface rather easily, and they give rise to a proximity effect that suppresses the high-energy peak in tunneling microscopy experiments. The experimental and theoretical functions $\alpha^2F(\omega)$ for Ta were adduced in support of this hypothesis in Ref. 21. Tantalium is known for being practically inactive in forming compounds with oxygen. For that metal extremely good agreement of theory and experiment was achieved. In Ref. 14 it was also hypothesized that the tunneling spectroscopy technique does not reflect the whole ''volume'' of the electron-phonon interaction, especially in the high-energy region. Indeed, the area under the high-energy part of the spectrum is several times smaller than the area for the lower-frequency region (cf. Fig. 5). As was shown in Ref. 26, the mean free path of the electrons participating in the electron-phonon interaction decreases as the phonons advance up the energy scale (moreover, since $l(\omega)=v_F\tau(\omega)$, this effect is additionally enhanced for d electrons, the Fermi velocity of which is low.

Thus one expects a smaller contribution of the high-energy phonons to the total integrated tunneling current and, as a consequence, strong suppression or even the complete absence of high-energy features in $\alpha^2F(\omega)_{\exp}$.

The aforementioned causes of the distortion of the high-energy part of the experimental spectral function of the electron-phonon interaction in Nb mentioned above can apparently also operate in the PC spectroscopy of technetium.

Let us say a few words about the low-energy peak G_1. The value given by experiment is 13 meV. In Ref. 13 it was conjectured that by virtue of the features of the matrix element and the shape of the Fermi surface a substantial displacement of the central peak to lower energies occurs in the experiment. This can explain the participation of all the ''low-energy'' groups of phonons (14–20 meV) in the formation of the low-energy peak G_1 of the function $G_{pc}(\omega)$. However, as we have said, $\alpha^2(\omega)$ is practically constant in the region of interest to us. Responsibility for the formation of G_1 peak is left to the lowest-energy phonon peak at 15.2 meV. The difference of 2.2 meV between them can be explained by the fact that it is in this energy part that our calculated phonon spectrum gives a somewhat overestimated value (for example, the aforementioned TO branch in Fig. 1a).

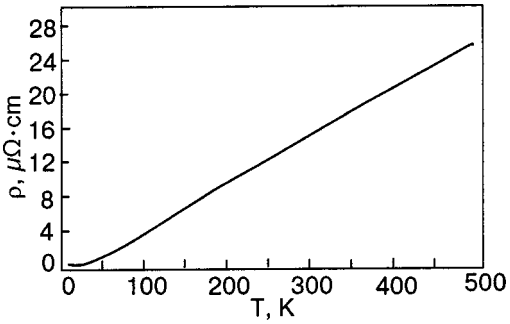

FIG. 6. Theoretically calculated behavior of the lattice resistivity of technetium.

ELECTRICAL CONDUCTIVITY

In pure metals except in the low-temperature region the electron-phonon interaction is the dominant factor governing the electrical conductivity of the substance.

The variational solution of the Boltzmann equation[27] gives the following formula for the temperature dependence of $\rho_z(T)$:

$$\rho_z(T)=\frac{\pi\Omega_{\text{cell}}k_BT}{N(\varepsilon_F)\langle v_z^2\rangle}\int_0^\infty\frac{d\omega}{\omega}\frac{x^2}{\sinh^2 x}\alpha_{\text{tr}}^2F(\omega). \tag{5}$$

The transport spectral function $\alpha_{\text{tr}}^2F(\omega)$ differs form $\alpha^2F(\omega)$ (1) only by the presence of an additional factor of $[1-v(k)v(k')/|v(k)|^2]$ in the integrand, which specifies the geometry of the scattering process. The subscript z specifies the direction of flow of the electrical current in the sample. Formula (5) remains valid in the range $\Theta_{\text{tr}}/5<T<2\Theta_{\text{tr}}$, where

$$\Theta_{\text{tr}}\equiv\langle\omega\rangle_{\text{tr}}^{1/2}, \tag{6}$$

$$\langle\omega^2\rangle_{\text{tr}}=\frac{1}{\lambda_{\text{tr}}}\int_0^\infty\omega\alpha_{\text{tr}}^2F(\omega)d\omega, \tag{7}$$

$$\lambda_{\text{tr}}=2\int_0^\infty\alpha_{\text{tr}}^2F(\omega)\frac{d\omega}{\omega}. \tag{8}$$

The upper boundary of the temperature range is due to the fact that at higher temperatures it is necessary to take into account the effects of anharmonicity and the smearing of the Fermi surface. The low-temperature electrical conductivity, on the contrary, is governed by the electron-electron interaction, size effects, scattering on impurities, etc.

In our calculation $\Theta_{\text{tr}}=225.8$ K. Thus $T\in(45\text{ K}, 451.6\text{ K})$.

Figure 6 shows the function $\rho(T)$ averaged over three directions. The latter is obtained as $\rho(T)=(1/3)[\rho_x(T)+\rho_y(T)+\rho_z(T)]$ and can be used directly for comparison with the experimental measurements of the conductivity on technetium polycrystals. In Ref. 28 a value $\sigma=0.067\times10^6/(\Omega\cdot\text{cm})$ was measured for the conductivity (the reciprocal of the resistivity) under standard conditions. Thus we obtain $\rho_{\exp}(293.2\text{ K})=14.9\ \mu\text{O}\cdot\text{cm}$. The calculated value is $\rho_{\text{th}}(293.2\text{ K})=14.7\ \mu\Omega\cdot\text{cm}$.

CONCLUSION

We have studied the dynamic and electron-phonon properties of technetium. With the use of linear response theory implemented in the framework of the LMTO method with allowance for non-MT corrections, we were able to achieve good agreement with the experimental data. This is particularly true for the phonon spectrum [including the reproduction of the anomaly for the $(0,0,\xi)$ direction], the photon density of states, and the electrical conductivity. The theoretically calculated spectrum of the electron-phonon interaction (the Eliashberg function) has a much higher intensity of the high-energy peak at 27 meV in comparison with the analogous maximum in the point-constant spectra. This may be due to features of the experimental conditions (heating of the contact by the current, plastic deformation of the metal in the contact region, possible contamination of the surface of the sample, and other factors) and also the limited accuracy of the computational scheme (finite number of points at which the computation is done; the local electron density approximation).

Taking all these arguments into consideration, we think that it would be extremely interesting to continue the experimental and theoretical study of the high-energy part of the point-contact function of the electron-phonon interaction.

*E-mail: sichkar@imp.kiev.ua

[1] V. L. Ginzburg, in *Proceeding of the Adriatico Research Conference on High Temperature Superconductors*, ICTP, Trieste, Italy, July 5–8, 1987, p. 3.
[2] N. H. March and M. Parrinello, *Collective Effects in Solids and Liquids*, Hilger, Bristol, England (1982), Mir, Moscow (1986).
[3] A. L. Giorgi and E. G. Szklarz, J. Less-Common Met. **20**, 173 (1970).
[4] A. L. Giorgi and B. T. Matthias, Phys. Rev. B **17**, 2160 (1978).
[5] W. L. McMillan, Phys. Rev. B **167**, 331 (1968).
[6] H. G. Smith and N. Wakabayashi, Solid State Commun. **39**, 371 (1981).
[7] S. Yu. Savrasov, Phys. Rev. Lett. **69**, 19 (1992).
[8] S. Y. Savrasov, Phys. Rev. B **54**, 16 470 (1996).
[9] U. von Barth and L. Hedin, J. Phys. C **5**, 1629 (1972).
[10] P. Blochl, O. Jensen, and O. K. Andersen, Phys. Rev. **49**, 16223 (1994).
[11] P. B. Allen, Phys. Rev. B **6**, 2577 (1972).
[12] J. P. Perdew, K. Burke, and Y. Wang, Phys. Rev. B **54**, 16533 (1996).
[13] A. A. Zakharov, M. G. Zemlyanov, M. N. Mikheeva, G. F. Syrykh, and M. B. Tsetlin, Zh. Éksp. Teor. Fiz. **88**, 1402 (1985) [Sov. Phys. JETP **61**, 836 (1985)].
[14] W. H. Butler, H. G. Smith, and N. Wakabayashi, Phys. Rev. Lett. **39**, 16 (1977).
[15] W. L. McMillan, Phys. Rev. **167**, 331 (1968).
[16] J. J. Hopfield, Phys. Rev. **186**, 443 (1969).
[17] W. H. Butler, Phys. Rev. **15**, 11 (1977).
[18] V. V. Nemoshkalenko and V. N. Antonov, *Computational Methods in Solid State Physics*, Gordon and Breach, London (1999), Naukova Dumka, Kiev (1985).
[19] R. J. Trainor and M. B. Brodsky, Phys. Rev. B **12**, 4867 (1975).
[20] J. S. Faulker, Phys. Rev. B **16**, 736 (1977).
[21] S. Y. Savrasov and D. Y. Savrasov, Phys. Rev. B **54**, 16 487 (1996).
[22] I. K. Yanson, Fiz. Nizk. Temp. **9**, 676 (1983) [Sov. J. Low Temp. Phys. **9**, 343 (1983)].
[23] J. Caro, R. Coehorn, and D. G. de Groot, Solid State Commun. **39**, 267 (1981).
[24] B. Keck and A. Schmid, J. Low Temp. Phys. **24**, 611 (1976).
[25] J. Bostock, V. Diadiuk, W. N. Cheung, K. H. Lo, R. M. Rose, and M. L. A. MacVicar, Phys. Rev. Lett. **36**, 603 (1976).
[26] P. B. Allen, *Phonons and Superconducting Transition Temperature*, North-Holland (1980).
[27] O. Madelung, *Introduction to Solid-State Theory*, Springer-Verlag, Berlin (1978), Nauka, Moscow (1980).
[28] http://environmentalchemistry.com/yogi/periodic/Tc.html.

Translated by Steve Torstveit

LOW-TEMPERATURE PHYSICS OF PLASTICITY AND STRENGTH

Low-temperature microhardness of Xe-intercalated fullerite C_{60}

L. S. Fomenko,* S. V. Lubenets, and V. D. Natsik

B. Verkin Institute for Low Temperature Physics and Engineering of the National Academy of Sciences of Ukraine, 47 Lenin Ave., Kharkov 61103, Ukraine

D. Cassidy, G. E. Gadd, and S. Moricca

Australian Nuclear Science and Technology Organization, NSW 2234, Australia

B. Sundqvist

Department of Experimental Physics, Umea University, SE-90187 Umea, Sweden
(Submitted July 28, 2004)
Fiz. Nizk. Temp. **31**, 596–601 (May 2004)

The Vickers microhardness of Xe-intercalated polycrystalline fullerite C_{60} (Xe_xC_{60}, $x \simeq 0.35$) is measured in a moderately low temperature range of 77 to 300 K. A high increase in the microhardness of the material (by a factor of 2 to 3) as compared to that of pure C_{60} single crystals is observed. It is shown that the step-like anomaly in the temperature dependences of the microhardness of pure C_{60} single crystals recorded under the orientational fcc-sc phase transition ($T_c \simeq 260$ K) is also qualitatively retained for Xe_xC_{60}, but its onset is shifted by 40 K towards lower temperatures and the step becomes less distinct and more smeared. This behavior of $\overline{H_V}(T)$ correlates with x-ray diffraction data, the analysis of which revealed a considerable influence of xenon interstitial atoms on the peculiar features of fullerite thermal expansion due to orientational phase transitions (see the paper by A.I. Prokhvatilov *et al.* in this issue). [DOI: 10.1063/1.1925374]

INTRODUCTION

The physical and mechanical properties of crystalline C_{60} are considerably affected by intercalation of the crystal by different impurities, where the environment itself may be considered as an impurity source.[1] This is related to the weak van der Waals interaction between the C_{60} molecules as well as the presence of comparatively large interstitial sites in the fullerite lattice. As a result, the crystal easily absorbs impurities and is easily amenable to intercalation. The most dramatic effect due to intercalation is the superconductivity that occurs with alkali metals.[2]

Of possible intercalants, gases occupy a highly important place for C_{60}. The high interest in this type of impurity is dictated by several facts.[1] Gases are commonly used to transmit pressure to solid C_{60}. In this case gas atoms and molecules can diffuse into the cavities of the fullerite lattice and form interstitial solutions. Considering the arrangement of the centers of gravity of its molecules, fullerite C_{60} forms a face-centered cubic (fcc) lattice through the whole range of existence of its solid phase. For each C_{60} molecule in the lattice there are two tetrahedral sites as well as one octahedral site, which may be occupied by impurity atoms or molecules. Besides their occupation, chemical interaction between impurities and the C_{60} molecules (including polymer bond formation) is possible.

This paper is concerned with the influence of interstitial gaseous impurities on the mechanical properties of solid C_{60}. In particular, xenon was selected because being a rare gas eliminates the intercalant-matrix chemical interaction. The atomic diameter of Xe (3.92 Å) is almost two times larger than the effective diameter of a tetrahedral site (2.2 Å) and close to that of an octahedral one (4.1 Å), so that one might expect xenon to only occupy the octahedral sites of the C_{60} lattice. The large diameter of the Xe atom makes its entry into the lattice difficult and possible only at elevated pressure and temperature.[3] The effect of xenon on the mechanical properties of fullerite C_{60} has not previously been studied. In fact the only related study so far has been that in Ref. 4, which has shown the remarkable result of almost a hundredfold increase in the microhardness of a C_{60} single crystal grown in vacuum and kept in an argon atmosphere.

The mechanical properties of Xe_xC_{60} were studied by using the microindentation technique. As was shown in the previous papers,[5–8] the temperature dependence of the microhardness of pure C_{60} single crystals displays a step-like anomaly, the position of which is correlated with the temperature $T_c \simeq 260$ K of the fcc-sc phase transition. It is known[9,10] that intercalation of an impurity into the C_{60} lattice results, as a rule, in a decrease of T_c and a broadening of the phase transition temperature range. The research reported in this paper concerns the influence of xenon saturation of the C_{60} lattice on both the microhardness value and the anomaly of its temperature dependence in the vicinity of the phase transition point.

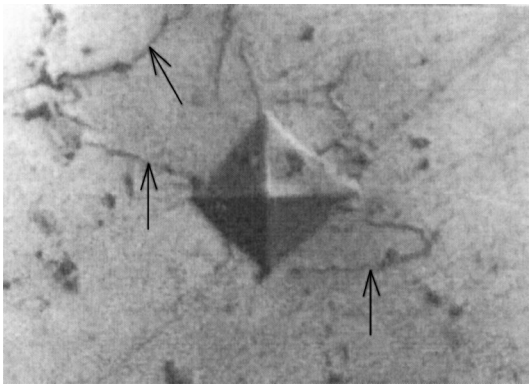

FIG. 1. The impression on the Xe_xC_{60} polycrystal surface for indenter load $P \simeq 0.2$ N and room temperature. The area of brittle fracture in the form of lateral (secondary) cracks is marked by arrows. The impression diagonal is about 30 μm.

EXPERIMENTAL PROCEDURE

C_{60} powder was saturated with xenon at a Xe pressure $p \simeq 200$ MPa and a temperature $T \simeq 575\,^{\circ}$C, for 36 hr.[3] To prepare the specimens for micro-indentation studies, the saturated powder of Xe_xC_{60} was pressed into tablet-shaped samples ~ 10 mm in diameter and ~ 5 mm in height, using hydrostatic pressure ($p \simeq 0.5$–1.0 GPa).[11,12] From the x-ray structural data,[13] the degree of filling of the octahedral sites with xenon amounted to $(35 \pm 5)\%$ ($x \simeq 0.35$). Prior to measuring, the tablet surface was polished on a benzol-moistened chamois leather.

The Vickers microhardness at room temperature was measured with a standard unit PMT-3 and in the temperature range of 77–300 K with a freely suspended indenter system.[14] The time of load endurance was 10 s. To reveal the relation between microhardness and indentation load, the load P was varied between 0.005 and 0.2 N, at room temperature. The temperature dependence $H_V(T)$ was measured at $P \simeq 0.05$ N as it was found that there was no influence of indentation load on microhardness in the vicinity of this load. The measurement was made in the course of cooling. The microhardness was calculated by the expression $H_V = 1.854P/(2a)^2$, where $2a$ is the impression diagonal. For each temperature or load 10 indents were applied to the surface, and then the values of microhardness were averaged over those indentations. The averaged value, $\overline{H_V}(T)$, was considered statistically to be a representative mechanical property of the material studied.

EXPERIMENTAL RESULTS

A typical impression on the polished surface of a Xe_xC_{60} polycrystal is shown in Fig. 1. The impression exhibited good faceting, indicating a high microplasticity of the material in question. The impressions remained sharp with decreasing temperature down to 77 K. At the same time cracks were commonly formed round the observed impressions, even at low load. These are mainly lateral (secondary) cracks, dipping at a low angle to the sample surface (clearly seen in Fig. 1). One may speculate that the cracks propagate along the grain boundaries which are the weakest sites of the pressed material due to a high density of defects, particularly pores, in them. The average values of the microhardness,

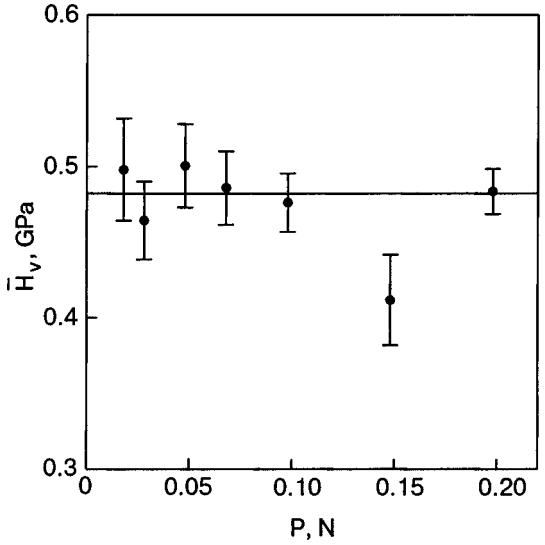

FIG. 2. The dependence of average microhardness $\overline{H_V}$ of Xe_xC_{60} on indenter load P at room temperature. The standard deviations for $\overline{H_V}$ are indicated as bars.

$\overline{H_V}(T = 300\ \text{K})$, of the Xe_xC_{60} polycrystal for different loads are shown in Fig. 2. As is evident, $\overline{H_V}(T = 300\ \text{K})$ is almost independent of indentation load, and only at a high value of $P \geqslant 0.15$ N can one observe reduced microhardness, supposedly due to active crack propagation. To avoid the influence of crack formation and consider $\overline{H_V}(T)$ as a characteristic of plasticity, measurements of the temperature dependence of microhardness were made at a low load of $P \simeq 0.05$ N.

The temperature dependences of microhardness for the Xe_xC_{60} polycrystal and for the pure C_{60} single crystal studied in Ref. 6 (indentation plane (001)) are illustrated in Fig. 3. A comparison of these curves allows us to recognize the prin-

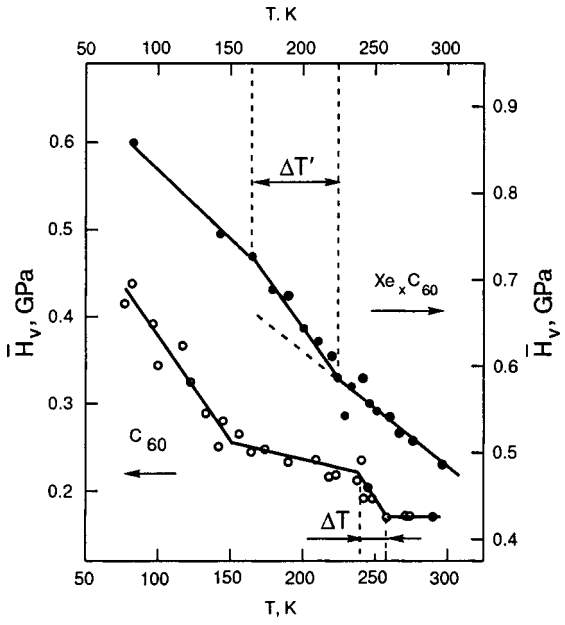

FIG. 3. The temperature dependence of $\overline{H_V}$ for the Xe_xC_{60} polycrystal (upper curve) and pure C_{60} single crystal (lower curve).[6] The standard deviations for $\overline{H_V}$ are about 3%.

cipal differences in the micromechanical behavior between the two materials. These differences are:

1. At room temperature the microhardness of the Xe_xC_{60} polycrystal is approximately three times higher than that of the pure C_{60} single crystal; and as the temperature is decreased down to 77 K, this discrepancy reduces to a factor of two.

2. As the temperature is decreased from 300 to 225 K, the microhardness of the Xe_xC_{60} polycrystal increases linearly by $\sim 20\%$, while for the fcc single crystal of pure C_{60} it remains almost unchanged (down to 260 K).

3. The step-like anomaly in the dependence $\overline{H}_V(T)$ for pure C_{60}, clearly seen under the transition from fcc to the sc phase below 260 K, changes significantly. Such an anomaly is observed for Xe_xC_{60} too, but the step edge is shifted towards lower temperatures (down to 220 K) and the step itself becomes less steep and highly smeared ($\Delta T' \simeq 60$ K for the intercalated fullerite as compared to $\Delta T \simeq 20$ K for pure C_{60}).

4. In the case of pure crystalline C_{60}, the low temperature edge of the step in the $\overline{H}_V(T)$ curve is adjacent to an area of rather slight variations in microhardness. Below 150 K this area turns into a region of drastic growth in $\overline{H}_V(T)$. As to the Xe_xC_{60} polycrystal, an analog of the first area can also be observed below 160 K, but we could not detect the second range because of lack of a microhardness measuring technique for temperatures below 77 K.

DISCUSSION

Before proceeding to a discussion of the anomalies observed in the microhardness of C_{60} on its saturation with xenon, some important results obtained in comparative x-ray diffraction studies of pure C_{60} and Xe_xC_{60} polycrystals should be mentioned.[13] Introduction of Xe preserves the fcc structure of the greater part of the material (90%), but in Xe_xC_{60} there also exists $\sim 10\%$ of another phase (most likely polymerized C_{60} molecules). Besides, considerable distortions of the fcc lattice by the Xe atoms cause the fcc-sc transition temperature, T_c, and the glass transition point, T_g, to decrease. This correlates with the anomalies in the temperature dependence of microhardness: saturation with xenon results in a substantial hardening and an embrittlement of the fullerite and, similarly, in a shift of the anomalies in the $\overline{H}_V(T)$ curve.

Investigations performed by several teams of researchers (see Ref. 8 and the references therein) have revealed that macro- and microplastic deformation of fullerite C_{60} at room and at moderately low temperatures is determined by the glide of dislocations in the $\{111\}\langle 110\rangle$ slip system; the system is kept efficient even after the fcc-sc transition. As the saturation of fullerite with xenon produces no change in its lattice structure, the scientific treatment of the observed difference in microhardness between the pure C_{60} single crystals and Xe_xC_{60} polycrystals should be limited to a discussion of some possible differences in those structural factors and mechanisms which dictate the dislocation mobility in these materials.

On the qualitative level, one should distinguish two effects caused by the influence of intercalation. These are (1) a rather substantial increase in the absolute values (background) of microhardness $\overline{H}_V$ and (2) a certain transformation of subtle peculiarities in the temperature dependence $\overline{H}_V(T)$ under the fcc-sc transition. The origin of these effects may generally be accounted for by different physical and structural factors. The first effect may be caused by the different morphology of the Xe-intercalated sample and by the influence of Xe atoms on the elastic properties and the mobility of the dislocations. The other one is probably connected with the influence of the Xe impurity on the dynamics of the orientational degrees of freedom of the C_{60} molecules, and therefore, on the dislocation-orientational interaction. The influence of these factors is discussed in detail below.

First of all, we shall consider a possible influence of the morphologies of the materials compared. One of these is a reasonably perfect single crystal, while the other is a polycrystal with inclusions of another phase. The difference in morphology between the two materials is due to the specific features of the intercalation technology;[3,12] unfortunately, at present there is no other way of preparing macroscopically homogeneous single crystals adequately saturated with xenon. The very high microhardness of the Xe_xC_{60} polycrystal as compared to that of the C_{60} single crystal may be caused by two factors: (i) the hardening effects of both the intergrain boundaries and secondly (ii) the minor second phase particles within the crystalline grains. By the Hall–Petch relation,[15] the yield stress and microhardness of a polycrystal are higher than those of a single crystal by an amount inversely proportional to the square root of polycrystal grain size. The second-phase fine particles form local barriers which impede dislocation slip, reducing appreciably the plastic compliance and increasing the microhardness of the material (that mechanism of hardening is well known in the physics of ageing alloy plasticity[16]). It should also be noted that any porosity induced from pressing the specimens should have an opposite effect, deteriorating the mechanical properties.[17,18] The softening due to this factor appears to be slight. We now turn to the effect of gaseous impurities on dislocation mobility in the bulk of a separate crystalline grain. A high Xe concentration in the lattice, as well as its almost identical size with that of the octahedral site which it occupies, suggest that as a first approximation by concentration, the intercalation does not disturb the macrostructural homogeneity of the material inside the grains. Because of this, separate impurity atoms produce no effective local barriers to dislocation slip in the sense of the term ''local barrier'' used in the physics of plasticity of weakly and moderately concentrated solid solutions.[16] At the same time, in a highly concentrated solid solution effects of second order in the concentration and, in particular, the presence of microclusters with a short-range order of impurities, are supposed to be of a certain importance. For example, in some unit cells of the lattice the impurity atoms occupy all octahedral sites while other unit cells remain unoccupied.

Such microclusters may be effective centers of dislocation drag, thus enhancing the material's microhardness. One more thing should be mentioned: for fullerite C_{60} and many atomic cubic crystals, a significant influence on the plastic compliance may be exerted by dislocation drag by the Peierls relief which becomes essential for a low density of local

barriers with low height.[19] It may therefore appear that the effect of gaseous impurities on the microhardness of fullerite is partially due to the change of the Peierls relief caused by the influence of a great number of interstitial atoms on the lattice parameter and intermolecular interaction. Unfortunately, even the sign of that influence cannot be predicted without detailed microscopic calculations.

Finally, one more important factor should be pointed out, namely, a considerable enhancement in the elastic moduli at the transition from pure crystals to highly concentrated solid solutions. According to a well known law in materials science,[20] the basic value of the microhardness of a material as a local characteristic of plasticity is proportional to the Young modulus. Independent measurements of the elastic moduli of intercalated fullerites (for example, by acoustic techniques or by Brillouin light-scattering measurements) would enable one to determine the individual contributions to enhancement of their hardness, but at present such data are not available.

Above we have discussed the principal factors that dictate the order of magnitude of the yield stress and microhardness and the general background of their temperature dependences in a wide range of moderately low temperatures for both pure and atomic impurity-intercalated fullerite C_{60}. From the general conclusions of the theory of thermally activated dislocation motion,[21,22] the background should be rather smooth and involve no distinct features like kinks which are seen in the dependences $\overline{H}_V(T)$ for pure and intercalated fullerites C_{60}. It would therefore appear reasonable that these observed anomalies are caused by the effect of the orientational degrees of freedom of the C_{60} molecule on the dislocation mobility.[6,23] Direct support for this suggestion may come from the correlations between the anomalies in the $\overline{H}_V(T)$ dependences and the anomalies of thermal and acoustic properties, which may be considered as an indicator of the orientational phase transitions in fullerite C_{60}: the fcc-sc phase transition and the orientational glass transition. The absolute contribution of dislocation-orientation interaction to dislocation drag forces is not high but it has peculiarities as mentioned above and therefore can be qualitatively identified in the background of contributions from other factors. In conclusion, the effect of interaction on subtle anomalies like kinks in the temperature dependences of the lattice parameter, $a(T)$, and the microhardness, $\overline{H}_V(T)$, is considered to be caused by the influence of gaseous impurities on the libration and rotation dynamics of C_{60} molecules.

It is evident that intercalation of the fullerite lattice by a great number of interstitial atomic impurities has an appreciable effect on the dynamics of the orientational degrees of freedom of the C_{60} molecules, producing a shift along the temperature scale and a smearing of the orientational fcc-sc and orientational glass transitions. This is supported by the x-ray diffraction data for Xe_xC_{60},[13] testifying that the values of temperature T_c and the glass transition point T_g decrease by 30–40 K. The comparison between the dependences $\overline{H}_V(T)$ for pure and Xe-saturated fullerites shown in Fig. 3 and their correlation with the x-ray diffraction data for the temperature dependences of the lattice parameter, $a(T)$,[13] indicate that the dislocation-orientational interaction determines the characteristic anomalies in the temperature dependence of the microhardness even in the presence of gaseous impurities. The influence of gaseous impurities on the orientation dynamics of the C_{60} molecules and the parameters of the lattice-orientation interaction can be estimated quantitatively by analyzing simultaneously x-ray diffraction, thermal, mechanical and acoustic data.[24] Although such data are available for pure C_{60} fullerite,[25] no such data is available for Xe_xC_{60}, making these estimations difficult at present.

The authors would like to express their gratitude to V. G. Manzhelii, M. A. Strzhemechny, and A. I. Prokhvatilov for their helpful discussion of the results and to the STCU for partial financing of the research under Project No. 2669.

*E-mail: fomenko@ilt.kharkov.ua

[1] B. Sundqvist, Fiz. Nizk. Temp. **29**, 590 (2003) [Low Temp. Phys. **29**, 440 (2003)].
[2] A. F. Hebard, M. J. Rosseinsky, R. C. Haddon, D. W. Murphy, S. H. Glarum, T. T. M. Palstra, A. P. Ramirez, and A. R. Kortan, Nature (London) **370**, 600 (1991).
[3] G. E. Gadd, S. Moricca, S. J. Kennedy, M. M. Elcombe, P. J. Evans, M. Blackford, D. Cassidy, C. J. Howard, P. Prasad, J. V. Hanna, A. Burchwood, and D. Levy, J. Phys. Chem. Solids **58**, 1823 (1997).
[4] M. Haluska, M. Zehetbauer, M. Hulmann, and H. Kuzmany, in *Materials Science Forum* **210–213**, *Part 1. Nondestructive Characterization of Materials 11*, A. L. Bartos, R. E. Green Jr., and C. O. Ruud (eds.), Transtec Publ., Zürich (1996), p. 267.
[5] M. Tachibana, M. Michiyama, K. Kikuchi, Y. Achiba, and K. Kojima, Phys. Rev. B **49**, 14945 (1994).
[6] L. S. Fomenko, V. D. Natsik, S. V. Lubenets, V. G. Lirtsman, N. A. Aksenova, A. P. Isakina, A. I. Prokhvatilov, M. A. Strzhemechny, and R. S. Ruoff, Fiz. Nizk. Temp. **21**, 465 (1995) [Low Temp. Phys. **21**, 364 (1995)].
[7] V. D. Natsik, S. V. Lubenets, and L. S. Fomenko, Fiz. Nizk. Temp. **22**, 337 (1996) [Low Temp. Phys. **22**, 264 (1996)].
[8] S. V. Lubenets, V. D. Natsik, L. S. Fomenko, A. P. Isakina, A. I. Prokhvatilov, M. A. Strzhemechny, N. A. Aksenova, and R. S. Ruoff, Fiz. Nizk. Temp. **23**, 338 (1997) [Low Temp. Phys. **23**, 251 (1997)].
[9] N. A. Aksenova, A. P. Isakina, A. I. Prokhvatilov, M. A. Strzhemechny, and V. N. Varyukhin, in *Fullerenes. Proceedings of the Symposium on Recent Advances in the Chemistry and Physics of Fullerenes and Related Materials*, K. M. Kadish and R. S. Ruoff (eds.), The Electrochemical Society, Inc., Pennington, (1994), Vol. **94–24**, p. 1543.
[10] X. D. Shi, A. R. Kortan, J. M. Williams, A. M. Kini, B. M. Savall, and P. M. Chaikin, Phys. Rev. Lett. **68**, 827 (1992).
[11] A. N. Aleksandrovskii, A. S. Bakai, A. V. Dolbin, V. B. Esel'son, G. E. Gadd, V. G. Gavrilko, V. G. Manzhelii, S. Moricca, B. Sundqvist, and B. G. Udovidchenko, Fiz. Nizk Temp. **29**, 432 (2003) [Low Temp. Phys. **29**, 324 (2003)].
[12] A. N. Aleksandrovskii, A. S. Bakai, A. V. Dolbin, V. B. Esel'son, G. E. Gadd, V. G. Gavrilko, V. G. Manzhelii, S. Moricca, and B. Sundqvist, Fiz. Nizk. Temp. **31**, 565 (2005) [Low Temp. Phys. **31**, (2005)].
[13] A. I. Prokhvatilov, N. N. Galtsov, I. V. Legchenkova, M. A. Strzhemechny, D. Cassidy, G. E. Gadd, S. Moricca, B. Sundqvist, and N. A. Aksenova, Fiz. Nizk. Temp. **31**, 585 (2005) [Low Temp. Phys. **31**, (2005)].
[14] B. Ya. Farber, N. S. Sidorov, V. I. Kulakov, Yu. A. Iunin, A. N. Izotov, G. A. Emelchenko, V. S. Bobrov, L. S. Fomenko, V. D. Natsik, and S. V. Lubenets, Sverkhprovodimost' **4**, 2393 (1991) [Superconductivity **4**, 2296 (1991)].
[15] E. O. Hall, Nature (London) **173**, 948 (1954).
[16] J. Friedel, *Dislocations*, Pergamon Press, Oxford (1964).
[17] W. D. Kingery, *Introduction to Ceramics*, Wiley, New York (1960) Stroiizdat, Moscow (1967).
[18] V. V. Demirskii, S. V. Lubenets, V. D. Natsik, M. M. Sorin, L. S. Fomenko, and N. M. Chaykovskaya, Sverkhprovodimost' **3**, 84 (1990) [Superconductivity **3**, 80 (1990)].
[19] A. Seeger, Z. Metallkd. **72**, 369 (1981).
[20] E. R. Petty and H. O'Neill, Metallurgia (January 25, 1961).

[21] T. Suzuki, H. Yoshinaga, and S. Takeuchi, *Dislocation Dynamics and Plasticity*, Springer-Verlag, New York (1991), Mir, Moscow (1989).
[22] E. Nadgornyi, *Dislocation Dynamics and Mechanical properties of Crystals*, Vol. 31 of Progress in Materials Science, J. W. Christian, P. Haasen, and T. B. Massalski (eds.), Pergamon Press (1988).
[23] V. D. Natsik and A. V. Podolskii, Fiz. Nizk. Temp. **26**, 304 (2000) [Low Temp. Phys. **26**, 225 (2000)].
[24] V. D. Natsik, S. V. Lubenets, and L. S. Fomenko, Fiz. Nizk. Temp. **31**, (2005) [Low Temp. Phys. **31**, (2005)].
[25] V. D. Natsik and A. V. Podolskii, Fiz. Nizk. Temp. **26**, 1155 (2000) [Low Temp. Phys. **26**, 857 (2000)].

This article was published in English in the original Russian journal. Reproduced here with stylistic changes by AIP.